Nonlinear light propagation and self-inscription processes in a photopolymer doped with Ag nanoparticles

By

Liqun Qiu, B. Sc., M. Sc.

A Thesis

Submitted to the School of Graduate Studies in Partial Fulfillment of the Requirements for the Degree

Doctor of Philosophy in Chemistry

McMaster University

DOCTOR OF PHILOSOPHY (2012) **MCMASTER UNIVERSITY**

(Chemistry) Hamilton, Ontario

TITLE: Nonlinear light propagation and self-inscription processes in a photopolymer doped with Ag nanoparticles

AUTHOR: Liqun Qiu, B. Sc, M. Sc. (Soochow University, China)

SUPERVISOR: Dr. Kalaichelvi Saravanamuttu

Number of pages: xxiii, 216

Abstract

The resonance of surface plasmons on metal nanoparticles can be excited at visible wavelengths. The extraordinary enhancement of a variety of optical phenomena in the vicinity of metal nanoparticles has been attributed to the strong fields generated under resonance conditions. As a result, extensive research has been carried out to incorporate the extraordinary optical properties of metal nanoparticles into optical devices and applications, ranging from spectroscopy (e.g, surface enhanced Raman, IR and Fluorescence), optical sensing and imaging, to photovoltaic cells, photonic crystals and optical switches. Particular effort has been directed towards producing stable dispersion of metal nanoparticles within soft dielectric matrices and their subsequent construction into different device geometries.

This thesis describes a method to photolytically generate Ag nanoparticles within organosiloxane sols, which can subsequently be photopolymerized in the presence of photoinitiators and therefore, be patterned through a variety of photo-inscription processes. The mechanism of Ag nanoparticle growth and evolution is described in detail followed by the fabrication of periodic metallodielectric gratings through photomask and laser interference lithography. Studies also showed that three different forms of nonlinear light propagation, optical self-trapping, modulation instability and spatial self-phase modulation could be elicited in the Ag nanoparticle-doped systems. Detailed experimental examination of these phenomena elucidated significant differences in their dynamics in the metallodielectric systems compared to non-doped samples. These included variations in the dynamics of self-trapped beams such as the excitation of optical modes, critical thresholds for modulation instability and self-phase modulation. The potential of these nonlinear processes for the self-inscription of 3-D

metallodielectric structures including cylindrical multimode waveguides and waveguide lattices has also been studied.

Acknowledgements

Firstly I would like to thank my supervisor, Dr. Kalaichelvi Saravanamuttu, for providing me the opportunity to be a student in her research group, for her ongoing direction, guidance, and encouragement.

I would also like to thank my committee members, Dr. Harald Stöver and Dr. Adam. Hitchcock, for their help and support, and their invaluable insights and advice for my research.

I would like to thank Dr. Daniele Blanc and Dr. Janyce Franc, for their advice and assistance on optical lithography, and for making my short stay in France enjoyable.

I would like to thank people from the Canadian Centre for Electron Microscopy (CCEM), specifically, Dr. Glynis Silveira, Dr. Steve Koprich, Fred Pearson, Julia Huang and Chris Butcher for their assistances on SEM, TEM and optical microscopy. I would like to thank Dr. Harald Stöver for letting me use his optical microscope, and Dr. Alex Adronov for letting me use his UV-Vis spectrometer. I am grateful to Dr. Nick Burke for training me on his group's optical microscope and other instruments.

I can't be luckier than to be working with such a great group of people in the lab. Many thanks to Abhitej Rewari for assisting me in mask lithography. Special thanks to Ana, who established the optical assembly for laser experiments and conducted work on optical self-trapping and diffraction rings in non-Ag doped samples, from where I could easily initiate work on optical self-trapping and diffraction rings in Ag nanoparticle doped samples. Also thanks to Ian, Whitney and Matt, who conducted work on modulation instability in non-Ag doped samples, which also greatly helped me with my work on modulation instability in Ag nanoparticle doped samples. Great

thanks to Ana, Kailash and Matt for uncountable discussion, suggestions and supports on my research. More than those, thanks for all the good times brought by my group members, besides those names just mentioned, Jihua, Alex, Dinesh, Cindy, Natalie, Idlir, Czerysh, Rachel, and many others.

Finally, I greatly thank my parents, Jun Gong and Yongfu Qiu, my brother Liyu Qiu, my sister in law, Li Zhu, and my nephew Qi Qiu for their continued support.

Table of Contents

List of Figures

List of Tables

List of Abbreviations

CVD	Chemical vapor deposition
CTAB	Cetyl trimethylammonium bromide
DDA	Discrete dipole approximation
EDX	Energy-Dispersive X-ray
FIB	Focused ion beam
MAPTMS	3-Methacryloxypropyltrimethoxysilane
MI	Modulation instability
PVA	Poly(vinylalcohol)
PAA	Poly(acrylic acid)
PAH	Poly(allylamine hydrochloride)
PDMS	Polydimethylsiloxane
SEM	Scanning electron microscopy
SPRs	Surface plasmon resonances
TEM	Transmission electron microscopy
TOAB	Tetraoctylammonium bromide

ω_o	Natural oscillation frequency of an object
ξ	Displacement of an oscillating object
t	Time
n_f	Free electron density
m	Free electron mass
ω_p	Volume(or bulk) plasmon frequency
$\hbar$	The reduced Plank constant
ε	Dielectric constant
k	Wave vector
ω	Optical frequency
c	Speed of light in vacuum
n	Refractive index
κ_{ext}	Extinction coefficient
λ	Optical wavelength
ω_R	Frequency of surface plasmons
α	Attenuation coefficient

Chapter 1 Introduction

When downsized to subwavelength scales, metal particles behave strikingly different than metals in bulk. Especially, the efficient confinement of free electrons enables surface plasmons to be optically excited, which in turn introduces a completely new set of optical properties. Metallo-dielectric composites, where metal nanoparticles are dispersed in a soft dielectric medium, hold promise in applications ranging from spectroscopy [1;2;3], photovoltaic cells [4;5;6;7], photonics [8;9;10;11;12;13] to optical sensing and imaging [14;15;16]. Motivated by this, various methods have been developed to stabilize metal nanoparticles in dielectric matrices; however the controlled and efficient transformation of soft metallo-dielectric composites into device geometries necessary for real applications remains challenging. One efficient approach is to incorporate metal nanoparticles into photopolymerisable materials that can be subsequently structured into necessary device geometries through photo-inscription methods.

Besides conventional photo-lithographic techniques, photopolymers can also be structured through nonlinear light propagation processes. In a medium where changes of refractive index can be photoinduced as a function of optical intensity, incident beams self-adjust their propagation paths while traveling through the medium. As described through differential equations (*vide infra*), such self-action processes can be classified as nonlinear light propagation processes. These have been mostly studied in conventional optical nonlinear materials, where the photoinduced refractive index change originates from high order susceptibility terms. In a photopolymerisable medium, nonlinear light propagation arises from refractive index changes

due to a permanent polymerisation reaction and therefore leaves an indelible imprint on the medium.

The contents of this introductory chapter are presented in two parts, respectively regarding metal nanoparticles (Section 1.1~1.4) and nonlinear forms of light propagation (Section 1.5). In part one, surface plasmon is introduced with a review of the unique optical properties of metal nanoparticles at the wavelengths of surface plasmon resonances; synthesis/fabrication of metal nanoparticles (specifically, Ag nanoparticles) and nanoparticle doped metallo-dielectric composites are also reviewed. In part two, nonlinear forms of light propagation are introduced, followed by a review of nonlinear forms of light propagation in a variety of media, with emphasis on studies in photopolymerisable materials. Research objectives of this thesis are presented in section 1.6.

1.1 Surface plasmons on metal nanoparticles

Surface plasmon is a kind of collective electron-oscillation that exists on the surface of a metal which is surrounded by dielectric media. On metal particles with nanometer-sized dimensions, surface plasmons can be optically excited. Properties of surface plasmons are determined by many factors, including particle material, particle size and shape, dielectric environment and interparticle coupling. In the following sections, a further explanation of surface plasmons will be provided. Studies of surface plasmons on metal nanoparticles will be reviewed.

1.1.1 Plasmons

Surface plasmon is a type of plasmon, which is used to describe the collective movement of electrons. Here, "collective" is emphasized to distinguish it from the case of individual electrons. It is a kind of cooperative

movement (oscillation) due to the mutual interactions of a number of electrons.

"Plasmon" was derived from the word "plasma", which is an ionized gas[17], in which the positive ions can be assumed to be stationary relative to the fast moving electrons, because the former are much heavier than the latter. Between the late 1940s and the early 1950s, Bohm and Pines initiated systematic studies on plasmons and proposed models based on Coulomb interactions between electrons [18; 19; 20]. They observed that in the electron gas, electrons behave both "individually" and "collectively": In short distances (i.e., shorter than the Debye-length), the electron gas can be considered as an ensemble of individual electrons, as Coulomb forces between the electrons are mostly screened by the surrounding electron cloud. Whereas, in long distances, collective fields caused by Coulomb interactions lead to the collective oscillations of electrons, which can be described with the harmonic oscillation model:

$$\frac{\partial^2 \xi}{\partial t^2} + \omega_o{}^2 \xi = 0, \qquad \textbf{1-1}$$

Where ξ is the displacement of an oscillating object, ω_o is the natural frequency of the oscillation, and t is the time.

For free electron gas with free electron density n_f and free electron mass m, its harmonic oscillation equation (**equation 1-1**) can be written as follows:

$$\frac{\partial^2 \xi}{\partial t^2} + \frac{4\pi n_f e^2}{m} \xi = 0, \qquad \textbf{1-2}$$

where the frequency of the collective oscillation of free electrons (i.e. the frequency of plasmons) is:

$$\omega_p = (\frac{4 n_f e^2}{m})^{\frac{1}{2}} \qquad \textbf{1-3}$$

Equation 1-3 also applies to collective oscillations of free electrons in solids, especially in metals with free conduction electrons [21]. ω_p is usually called the volume (or bulk) plasmon frequency of the material.

One way to experimentally measure the plasmon frequency ω_p is by measuring the energy loss ΔE of a fast electron passing through the sample film. As $\Delta E = \hbar\omega_p$, ω_p can be calculated. [21]

1.1.2 Surface plasmons

When experimentally studying plasmons in metal films, it was found that besides energy loss corresponding to volume plasmon frequency ω_p, there also exist low-lying losses at $\sim \omega_p / \sqrt{2}$. Ritchie [22] attributed this to plasma oscillations of electrons near the metal surface, as a result of the surface boundary effect. Such surface charge oscillation is named “surface plasmon” as opposed to “volume plasmon”. Later, it was found that such low-lying losses due to surface plasmons further shifted towards lower frequencies when the metal film had a layer of oxide coating [23;24]. According to Stern and Ferrella’s explanation [23], in contrast to volume plasmon oscillations, part of the restoring electric field from the oscillating surface plasmon waves extends beyond the metal boundary; surface plasmons are therefore strongly affected by the boundary dielectric medium.

By solving Maxwell's equations with boundary conditions on the metal-dielectric interface, dispersion of surface plasmons can be expressed as [25]:

$$k_{zd} = -i(k_x^2 - \varepsilon_d k_0^2)^{1/2}, \qquad \textbf{1-4 a}$$

$$k_{zm} = i(k_x^2 - \varepsilon_m(\omega) k_0^2)^{1/2}, \qquad \textbf{1.4 b}$$

and

$$k_x = k_{sp} = \frac{\omega}{c}\sqrt{\frac{\varepsilon_d \varepsilon_m(\omega)}{\varepsilon_d + \varepsilon_m(\omega)}}, \qquad \textbf{1-5}$$

Here, the metal-dielectric interface is assumed as the x-y plane, and the direction from the dielectric to the metal as the z direction; ε_d is the dielectric constant of the bounding dielectric medium; $\varepsilon_m(\omega)$ is the dielectric function of the metal; $k_x = k_{sp}$ is the wave vector of the surface plasmon along the interface; $k_0 = \frac{\omega}{c}$ is the free space wave vector of the incident optical field; k_{zd} and k_{zm} are wave vectors of surface plasmon waves normal to the interface, which are, respectively, in the dielectric medium and in the metal. Both k_z from **Equation 1-4** are imaginary, indicating the nonradiative nature of surface plasmons [25; 26].

Usually, the dielectric function of metal $\varepsilon_m(\omega)$, as a function of the frequency ω of the incident beam, can be approximated to that of an ideal plasma:

$$\varepsilon_m(\omega) = 1 - \omega_p^2 / \omega^2 \qquad \textbf{1-6}$$

When the optical frequency ω is larger than ω_p (for many metals, ω_p is in the ultraviolet region), $\varepsilon_m(\omega)$ is positive, and the metal behaves like a dielectric. Below that frequency region, which is mostly considered, $\varepsilon_m(\omega)$ is largely negative, i.e. $\varepsilon_m(\omega) < 0$, and $|\varepsilon_m(\omega)| > |\varepsilon_d|$. According to **Equation** 1-5, this leads to k_{sp} that is always larger than $\sqrt{\varepsilon_d} k_0$, as shown in the surface plasmon dispersion curve (Figure 1.1). In other words, the momentum of surface plasmon $\hbar k_{sp}$ is always beyond the maximum momentum that could be provided by the incident beam $\hbar\sqrt{\varepsilon_d} k_0$ [25;26].

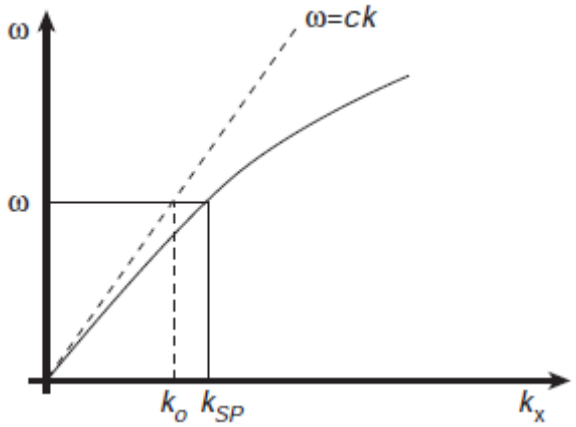

Figure 1.1 Surface plasmon dispersion curve, showing that, at frequency ω, the surface plasmon wave vector k_{sp} is larger than the free space wave vector k_0, causing a momentum mismatch between the surface plasmon and the incident light. Reprinted by permission from Macmillan Publishers Ltd:[Nature] [26], Copyright (2003)

1.1.3 Optical coupling of surface plasmons

As mentioned in the previous section, there is a mismatch between the momentum of surface plasmon $\hbar k_{sp}$ and the momentum from the incident light $\hbar k_0$. This makes it impossible to directly generate surface plasmons from metal by incident light. Two key approaches are used to compensate such momentum mismatch.

The first approach is by coupling the incident beam to the metal-dielectric interface with a prism [25;27;28], The prism has a refractive index n_{prism} that is larger than that of the boundry dielectric medium n_d; when the incident angle θ_i at the interface of the prism dielectric medium boundary satisfies $(n_{prism}/n_d)\sin\theta_i > 1$, total internal refraction occurs, and the resulting evanescent wave has a momentum of $n_{prism}\hbar k_0 \sin\theta_i$ along its propagation. Obviously, the momentum of the evanescent wave ($n_{prism}\hbar k_0 \sin\theta_i$) is larger than the momentum of the free-space light ($n_d \hbar k_0$) in the dielectric medium, making it possible to couple the momentum of surface plasmons and therefore to excite surface plasmons along the metal-dielectric interface.

The other approach is by phase modulating the incident light to reach a larger wave vector, from gratings or roughness of the metal surface [28;29;30;31]. For example, when the periodicity of metal surface variation is d, a wave vector of $K = 2\pi/d$ is created. For incident light with an incident angle θ_i, which has a surface component of the wave vector $k_s = \frac{\omega}{c}\sin\theta_i$, due to the surface modulation, its effective wave vector along the surface is enhanced to $k_s + nK$. Here, n is an integer. Such wave-vector compensation can also be realized by scattering from subwavelength structures [32; 33; 34;

35]. A typical example is the direct optical excitation of surface plasmons from metal nanostructures.

1.1.4 Optical responses of metal nanoparticles

Optical excitation and resonance of surface plasmons on metal nanoparticles causes extinction of incident photons with corresponding frequencies, resulting in specific colors that can be tuned with particle composition, size/shape, boundary dielectric media and inter-particle coupling [36; 37; 38; 39; 40, 41]. Application of gold/silver nanoparticles as pigments for colored glass and ceramics can be dated back to early centuries. The most famous example is the Lycurgus Cup, which was created in the 4th century A.D. in the Roman Empire. Due to the presence of gold/silver nanoparticles (50-100 nm in diameter), the cup appears translucent ruby in transmitted light and opaque green-yellow in reflected light [42]. However, it was not until the 17th century that people started to relate the unique color to the colloidal form of metal [43], and the initial scientific research on metal nanoparticles can be dated to the 19th century, when Michael Faraday obtained the ruby red gold colloids through chemical reduction of $AuCl^{4-}$. In addition, Faraday observed reversible color changes of films made from dried colloidal solutions, by exerting mechanical compressions on the films [44].

A great triumph of theoretical study on optical properties of metal nanoparticles was achieved in 1908 by Mie, who presented the first nationalized explanation of unique colors of metal nanoparticles, by giving exact solution to Maxwell's equations for spherical particles with appropriate boundary conditions [45].

1.1.4.1 Mie's theory

Mie's theory applies to an ensemble of well dispersed and randomly located sphere particles, so that optical responses of individual particles are not affected by the fields induced by other particles. In Mie's theory, energy loss of the incident beam caused by N spherical particles of volume V is expressed in terms of the extinction coefficient κ_{ext} [1][46]:

$$\kappa_{ext} = \frac{3\pi NV\varepsilon_d^{3/2}}{\lambda a^3}\sum_{l}^{\infty}(2l+1)\,\mathrm{Re}(A_l + B_l) \qquad \textbf{1-7}$$

where λ is the incident wavelength, ε_d is the dielectric constant of the surrounding dielectric, and $a = 2\pi r\sqrt{\varepsilon_d}/\lambda$, where r is the radius of the spheres. A_l and B_l are the series expansion of the involved electric and magnetic fields, in terms of the l -th spherical harmonic functions.

When surface plasmons are excited on metal nanoparticles, collective oscillations of conduction electrons result in displacement of the negative electron cloud relative to the positive nuclei, restoring forces therefore, arise from the Coulomb attraction between the positive nuclei and the negative electron cloud. For metal spherical particles whose diameter is much smaller comparing to the wavelength of the incident light, at surface plasmon resonances, all the free electrons oscillate coherently. When the negative electron cloud is displaced relative to the positive nuclei, an electric dipole is

[1] The extinction coefficient κ_{ext} is defined by the relation $\ln\frac{I_0}{I} = \kappa_{ext}x$, where I_o and I are intensity of incident and transmission light beam, respectively; x is the pathlength of the medium.

formed. Such collective electron oscillation is called a dipole mode surface plasmon, where only the 1st spherical harmonic needs to be considered. Mie's solution (**Equation 1-7**) is then reduced to [46]:

$$\kappa_{ext} = \frac{18\pi NV\varepsilon_d^{3/2}}{\lambda} \frac{\varepsilon_i(\omega)}{[\varepsilon_r(\omega) + 2\varepsilon_d]^2 + (\varepsilon_i(\omega))^2} \qquad \textbf{1-8}$$

where $\varepsilon_r(\omega)$ and $\varepsilon_i(\omega)$ are respectively the real and imaginary parts of the metal dielectric function, i.e. $\varepsilon_m(\omega) = \varepsilon_r(\omega) + i\varepsilon_i(\omega)$.

1.1.4.2 Surface plasmon resonances (SPRs)of metal particles

Assuming that $\varepsilon_i(\omega)$ is small and has no direct wavelength dependence, the resonance condition of **Equation 1-8** can be approximated as below:

$$\varepsilon_r(\omega) + 2\varepsilon_d = 0 \qquad \textbf{1-9}$$

Substituting **Equation 1-6** to **Equation 1-9**, the resonance frequency becomes:

$$\omega_R = \frac{\omega_p}{\sqrt{1 + 2\varepsilon_d}} \qquad \textbf{1-10}$$

A general expression of resonance condition can be written as [47],

$$\varepsilon_m(\omega) + \frac{l+1}{l}\varepsilon_d = 0 \qquad \textbf{1-11}$$

For dipole mode surface plasmon, $l = 1$ gives the same expression as **Equation 1-9**. For larger particles, higher modes of electron oscillations can occur. For example, in quadrupole surface plasmons, half of the free electron

cloud moves parallel to the incident field, while half moves anti parallel. In this case, $l = 2$, and the resonance condition becomes:

$$\varepsilon_r(\omega) + \frac{3}{2}\varepsilon_d = 0, \qquad \textbf{1-12}$$

and, the resonance frequency is then

$$\omega_R = \frac{\omega_p}{\sqrt{1+\frac{3}{2}\varepsilon_d}}. \qquad \textbf{1-13}$$

Comparing **Equation 1-10** and**1-13**, it is obvious that higher order modes of surface plasmons are located at higher frequencies with respect to the dipolar mode. In addition, the latter is usually red-shifted due to the disturbance from the electric fields induced by the former.

Surface plasmon resonances (SPRS): Effects of particle composition

The plasmon resonance frequency is determined by the surface charge distribution which is affected by particle size, shape, and more importantly, electron density, which is unique for different materials. Their effects on surface plasmon resonance are reflected by the volume plasmon frequency ω_p in **Equation 1-10** and **1-13**. For example, while the SPRs (dipole mode surface plasmon) of small Ag nanospheres usually locate at around 400 nm, SPRs of gold nanospheres occurs at over 500 nm. In a study of gold-silver alloy nanoparticles with a diameter of 18 nm, it was found that the extinction band blue shifted from 520 nm to 423 nm when the mole fraction of gold in the particles decreased from 1 to 0.27 [48].

SPRs: Effects of dielectric surrounding

It is also obvious from numerical expressions (**Equation 1-8~1-13**) that SPRs has a direct dependence on the dielectric constant of the surrounding medium. As mentioned in **Section 1.1.2**, this is because part of the restoring field of surface plasmons extends beyond the metal boundary to the dielectric surrounding. Generally, an increase in dielectric constant of the surrounding medium results in redshifting SPRs.

SPRs: Effects of particle shape

For non-spherical metal nanoparticles, the symmetry of the surface-charge distribution is broken, and different plasmon modes can be excited along different axes.

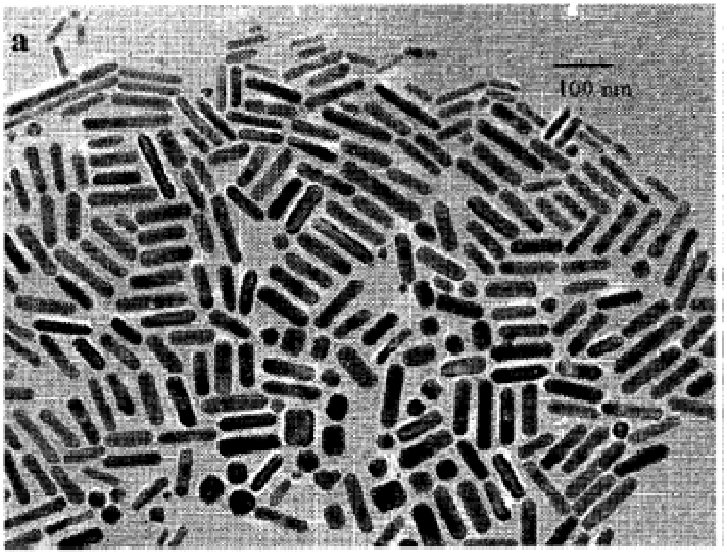

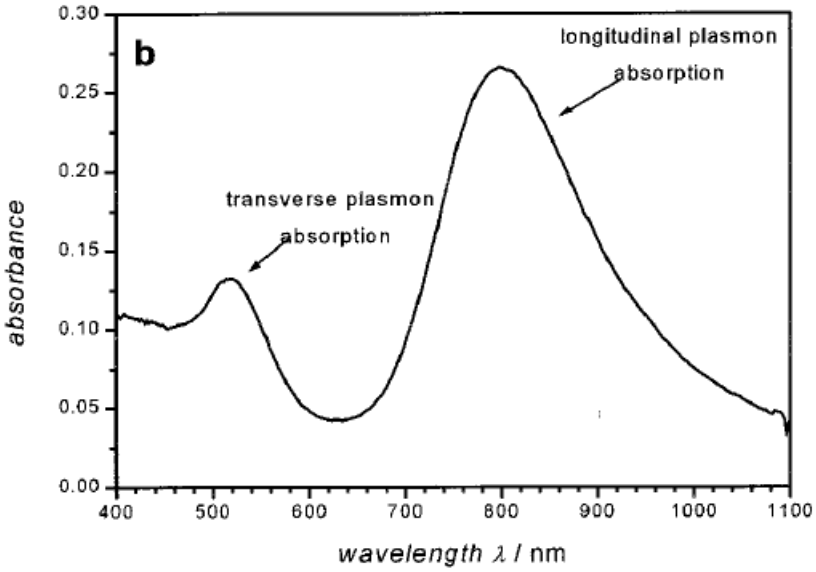

Figure 1.2 (a) TEM image of gold nanorods with an average aspect ratio of 4:1; (b) is the corresponding UV-Vis absorption spectrum of the gold nanorods solution. Reprinted with permission from [48]. Copyright (1999) American Chemical Society.

As shown in **Figure 1.2**, the absorption spectrum of a gold-nanorod colloidal solution has both a longitudinal and a transverse plasmon absorption, which correspond to the collective oscillation of free electrons along and perpendicular to the primary axis of the rods, respectively [48]. According to Gans, who extended Mie's theory to ellipsoidal particles in 1912, the extinction coefficient for N randomly orientated metal nanoparticles with aspect ratio R and volume V is given by [46]:

$$\kappa_{ext} = \frac{2\pi NV\varepsilon_d^{3/2}}{3\lambda}\sum_j \frac{(1/P_j^2)\varepsilon_i(\omega)}{(\varepsilon_r(\omega)+\frac{1-P_j}{P_j}\varepsilon_d)^2+(\varepsilon_i(\omega))^2}, \qquad \textbf{1-14}$$

where, P_j are the depolarization factors along the three axes X, Y and Z of the particles. For prolate spheroids, Z > Y = X,

$$P_Z = \frac{1-e^2}{e^2}[\frac{1}{2e}\ln(\frac{1+e}{1-e})-1], \qquad \textbf{1-15 a}$$

and

$$P_X = P_Y = \frac{1-P_Z}{2}. \qquad \textbf{1-15 b}$$

For oblate or flat spheroids, Z = Y > X,

$$P_X = \frac{1}{e^2}[1-(\frac{1-e^2}{e^2})^{1/2}\sin^{-1}e], \qquad \textbf{1-16 a}$$

and

$$P_Z = P_Y = \frac{1-P_X}{2}. \qquad \textbf{1-16 b}$$

For both cases,

$$e = \sqrt{1-\left(\frac{X}{Z}\right)^2} = \sqrt{1-\frac{1}{R^2}} \qquad \textbf{1-17}$$

Both experimental and theoretical studies show a significant red shift of the longitudinal SPRs with increasing aspect ratio [48]. For example, comparing to plasmon resonance at ~ 550 nm for gold nanospheres (i.e. $R=1$), the longitudinal plasmon of gold nanorods ($R=4$) is red shifted to over 800 nm [48].

In Gan's model, mainly the dipole mode plasmon is considered. In fact, higher multipolar modes can occur for large spheroids. However, exact

electrodynamic calculations shows that they are "quenched" by asymmetry and become less important with increasing aspect ratio (Figure 1.3) [49].

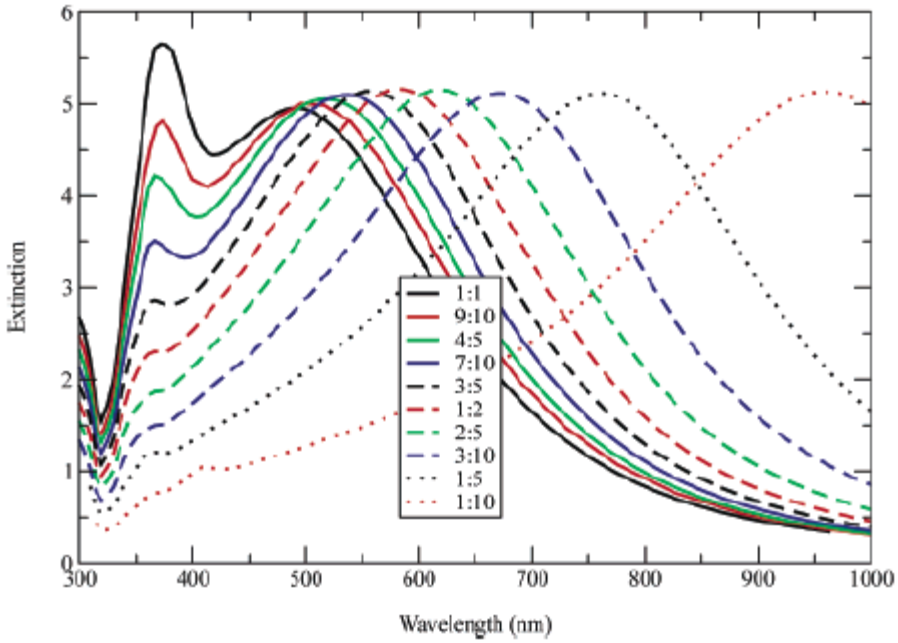

Figure 1.3 Extinction spectra obtained by exact electrodynamic calculation of oblate spheroids with different aspect ratios. All particles are of the same equivalent volume as a sphere with a diameter of 80 nm. It is assumed that the incident field polarization is along the major axis of the spheroid. Reprinted with permission from **[49].** Copyright (2003) American Chemical Society.

For particles of shapes other than spheroids, the electron confinement varies not only along different directions, but also, for many cases, at different sites (e.g. the corner or the edge of a triangular particle), resulting in complex SPRs that can not be solved by simple models. Nowadays, highly developed computational methods have enabled accurate calculation of SPRs of non-spherical particles [49;50].

DDA (discrete dipole approximation) simulations of randomly oriented Ag triangular prisms (edge size=100 nm, thickness=16 nm) (**Figure 1.4**) show resonance bands corresponding to plasmon oscillations along different axes. The two bands beyond 450 nm are due to in-plane mode plasmons, and bands at shorter wavelengths are due to out-of-plane modes. In addition, simulations show that the red-most maximum (corresponding to the primary dipole oscillation) blue shifts dramatically with increasing truncation of the corner (**Figure 1.4**). Furthermore, a significant blue shift of the primary dipole mode due to corner truncation occurs for all polyhedral shapes [50].

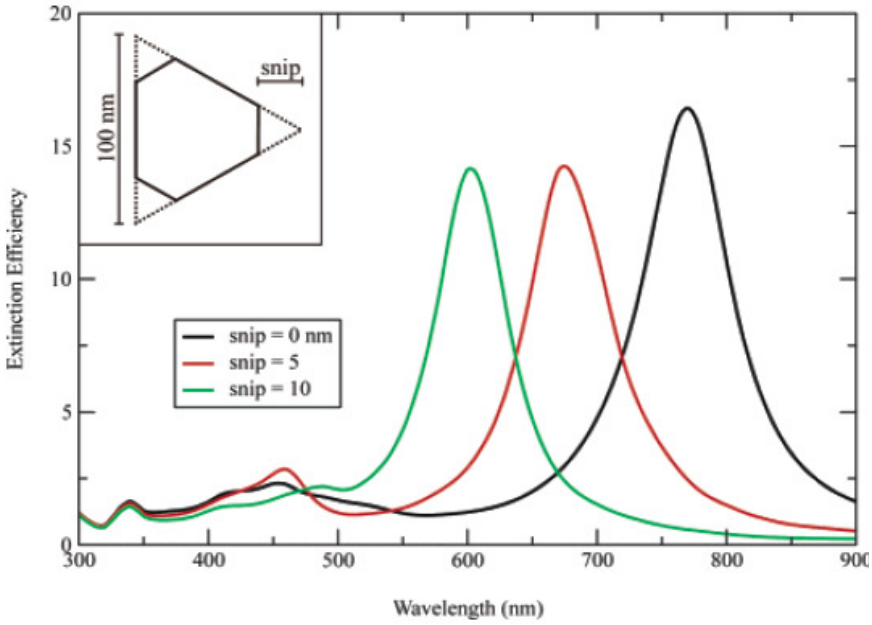

Figure 1.4 Spectrum of the extinction efficiency obtained through DDA calculations for randomly orientated triangular prisms with 100 nm long edges and 16 nm thickness. Also included are spectra of extinction efficiency of prisms with their corners truncated by 10 nm and 20 nm, respectively (as illustrated in Inset). Reprinted with permission from [49]. Copyright (2003) American Chemical Society.

SPRs: Effects of particle size

In numerical expressions cited in previous sections, particle size is not directly included to determine the wavelength of SPRs. Experimentally, however, size-effects have been observed.

For metal particles with diameters smaller than the electron mean free path, particle size has little impact on the frequency of plasmon resonance. But smaller particle size causes wider resonance due to surface dispersion effects [48;50]. A $1/R$ dependence of the bandwidth has been observed. [48;51;52; 53;54].

For larger metal particles, whose sizes become more comparable to the wavelength of the incident light, free electrons can't move all in phase, resulting in retardation of plasmon oscillations. Furthermore, phase coherence of the dipole-mode-electron oscillation is disturbed when higher multipolar modes are excited. Meanwhile, as optical scattering becomes increasingly significant in larger particles (*vide infra*), collective oscillations of free electrons are more damped by the re-radiation field. All these effects cause red-shifting of the resonance bands, which become wider, weaker, and more asymmetric [48;50;51].

SPRs: Effects of inter-particle coupling

When metal nanoparticles are very closely located, inter-particle coupling of surface plasmons occurs. Further enhanced fields can be induced at the junction between particles. For example, a theoretical calculation showed a >10 times increase of the SPRs-induced field at the junction of two adjacent Ag nanoparticles with a separation of 2 nm, compared with the non-coupled SPR field of an individual particle [**55**].

1.1.4.3 Decay of surface plasmons

Excited surface plasmons decay either radiatively through a scattering process, or non-radiatively through an absorption process. For N small spherical particles of volume V, the scattering coefficient κ_{sca} is [46]:

$$\kappa_{sca} = \frac{24\pi N V^2 \varepsilon_d^2}{\lambda^4} \frac{(\varepsilon_r(\omega) - \varepsilon_d)^2 + (\varepsilon_i(\omega))^2}{[\varepsilon_r(\omega) + 2\varepsilon_d]^2 + (\varepsilon_i(\omega))^2}, \qquad \textbf{1-18}$$

and the absorption coefficient

$$\kappa_{abs} = \kappa_{ext} - \kappa_{sca}. \qquad \textbf{1-19}$$

By comparing with **Equation 1-8** (which shows $\kappa_{ext} \propto V$), **Equation 1-18** (which shows $\kappa_{sca} \propto V^2$) indicates that the scattering process becomes more dominant with increasing particle size.

1.2 Applications of surface plasmons on metal nanoparticles

Selective absorption induced by SPRs brings unique colors of metal nanoparticles. The use of metal nanoparticles as decorative pigments started since as early as the time of the Romans [56]. Nowadays, many more applications of metal nanoparticles have emerged due to the better scientific understanding of SPRs on metal nanoparticles.

Firstly, as SPRs of metal nanoparticles are affected by many factors, including boundary dielectrics [57;58;59;60], particle size/shape, and inter-particle coupling, detectors and sensors based on shifts of SPRs have been developed [61;20;62;63]. Especially, extensive research has been carried out

to apply metal nanoparticles (especially Ag and Au nanoparticles) as probes in bio-systems [64;65;66;67;68;69].

Secondly, as described above, surface plasmons are electromagnetic waves bound to the metal surface. When optically excited at resonance, incident light is efficiently trapped/localized, which makes metal nanoparticles promising in light-harvesting for photovoltaic cells [4;5;6;7;70;71].

Furthermore, surface plasmon resonances results in highly concentrated and enhanced electric field (The maximum E-field enhancement factor $\left|E^2\right|$ has been found to be in the order of 10^3-10^6 [55]). Especially, extremely strong electric fields happen in highly curved surfaces with radii of several nanometers (such as the corner of a triangular plate or the tip of a sharp pin) where the surface mode is highly localized; further enhanced fields occur at the junction part between closely located metal nanoparticles [55;72]. Such field enhancement has been applied to improve the efficiency of various optical excitation processes, most notably, surface enhanced Raman scattering (SERs) [55; 73 ; 74 ; 75] and surface enhanced fluorescence [76;77;78], with the best enhancement factors in the order of 10^{10}-10^{12} and 10^3, respectively. Extraordinary enhancement in photoluminescence through multiphoton –absorption by metal nanoparticles near SPRs has also been reported [79].

Besides, the effective dielectric constant of a dielectric matrix can be modified by doping with metal nanoparticles [80]. There has been great interest in including metal nanoparticles in dielectric photonic crystals, to enhance the dielectric contrast between different blocks, which is very important to achieve sufficient photonic band gap within the photonic crystals [8;9;10;11;12;81]. Compared with all-metal photonic crystals, metal

nanoparticle doped metallodielectric photonic crystals show lower absorption at visible and near-Infrared wavelengths [8;9;82].

Furthermore, at SPRs, conduction electrons under collective oscillations are quickly "heated" and lose their thermal equilibrium with the lattice; the absorption coefficient and dielectric function of metal nanoparticles are therefore modified, leading to a nonlinear refractive response [83]. Enhancement (up to ~10^7 times) of the ultrafast (picoseconds) third- order nonlinear response has been observed at near SPRs of metal nanoparticles [84;85]. Photonic switches can be fabricated by doping metal nanoparticles into optical components (e.g. optical fibers) [83;86;87].

1.3 Metals supporting surface plasmons

Free conduction electrons on metals enable optical excitation of surface plasmons. Numerically, according to **Equation 1-8**, the extremely large value of extinction coefficient, which occurs at surface plasmon resonance, can be achieved when the denominator is close to zero. Metals are essential because they usually have a negative $\varepsilon_r(\omega)$ at optical wavelengths, so that the condition $\varepsilon_r(\omega)+2\varepsilon_d=0$ can be satisfied. At the same time, the image part of the dielectric function $\varepsilon_i(\omega)$ has to be small to support strong surface plasmons. Strength of surface plasmons can be described by the quality factor [88]:

$$Q=\frac{\omega(d\varepsilon_r(\omega)/d\omega)}{2(\varepsilon_i(\omega))^2} \qquad \textbf{1-20}$$

In general, Q should be larger than ~10 to support strong surface plasmons. Ag has a large Q across a broad range of wavelengths from 300 nm

to 1200 nm. Interband transitions also play an important role in dampening surface plasmons. For Ag, they occur at short wavelengths below 300 nm, whereas for Au and Cu, interband transitions expand into the visible range and strong surface plasmons can be excited only above 500 nm and 600 nm, respectively [88;89]. For Al, large Q can be obtained only in UV region. Li also has a large Q factor over a large range of wavelengths. However, it is too reactive for plasmonic applications.

Overall, Ag and Au are the best materials for supporting surface plasmons and have been the most studied over the years. They have been prepared in many different nanostructures by various synthesis approaches [88;90;91]. Whereas Au nanoparticles are better suited for in vivo applications within humans for its low toxicity, Ag is more competitive in other plasmonic applications for its lower cost.

1.4 Methods to produce Ag nanoparticles and Ag-nanoparticle doped metallodielectric composites

1.4.1 Preparing Ag nanoparticles

The 50~100 nm Au and Ag nanoparticles in the famous Lycurgus Cup were created during heat-treatment of the glass, through chemical reduction of the pre-dissolved monovalent gold and silver. The created particles were finely dispersed and stabilized in the silica matrix [92]. People in the 17th century found that gold colloids could be stabilized by using boiled starch [93;43]. The first controlled synthesis was reported in 1857 by Faraday, who prepared Au colloids in a two phase system, through reduction of $AuCl_4^-$ (in aqueous phase) by phosphorus (in CS_2) [44]. Ever since, various synthesis methods for preparing metal nanoparticles have been developed [43;88;94]. Most synthesis methods share the same principles: metal precursors are well dispersed in the medium and then reduced into elemental metal atoms,

which nucleate and grow into colloidal particles; at the same time, the reaction medium enables formed nanoparticles to be stabilized, for example, through electrostatic or steric effects. The following discussion is focused on the synthesis of Ag nanoparticles.

Silver precursors

Usually, soluble silver salts are used as precursors for making Ag nanoparticles. $AgNO_3$ is the most commonly used. Other silver salts, such as $AgClO_4$ [95], silver 2-ethylhexonate [96] have also been used. Recently, efficient control of particle growth has also been achieved with CF_3COOAg as the precursor [97]. Ag nanoparticles can also be prepared from precursors with low solubility, such as silver halides [98;99] and Ag_2O [100], when they are initially well dispersed in the medium.

Reducing methods and agents

The large reduction potential (0.7996 V) of monovalent silver [101] enables it to be reduced by various inorganic and organic chemicals.

Both citrate salts [102;103] and sodium borohydride [98;104;105] are commonly used as reducing agents for making Ag nanoparticles. Specifically, citrate ions serve not only as a reducing agent, but also as a stabilizer for Ag nanoparticles. Citrate-ion reduction is easy and fast, and has been often used in preparing large quantities of Ag colloids for commercial applications. Sodium borohydride has been applied in a two-phase synthesis. The method requires a phase transfer agent (such as tetraoctylammonium bromide (TOAB)) to transport the metal ions from the aqueous phase to the organic phase, and a capping agent (such as thioalkanes or aminoalkanes) to stabilize the formed Ag particles.

Organic solvents, such as ethylene glycol, 1,2-propanediol, and 1,5-pentanediol represent another category of reducing agents [88; 106; 107; 108]. In polyol methods, a separate capping agent (such as, poly(vinyl pyrrolidone) (PVP)) is used, making it possible to achieve controlled particle growth. In recent years, this method has been extensively investigated, and well controlled Ag nanostructures have been synthesized with abundant shapes by varying reaction conditions, such as temperature, reaction time, concentration of precursors, type and concentration of stabilizers, and concentration of trace ions [88;108].

Other chemicals, such as N,N-dimethylformamide [109], hydrazine [110], dimethyl sulfoxide [96] and potassium bitartrate [111] have all been used as reducing agents. Mild reducing agents, such as ascorbic acid, have been used to reduce Ag^+ on preformed Ag seeds [112;113]. In addition, hydrogen gas has also been used as a "clean" reducing agent, leaving no chemical residuals in the reaction system [100; 114; 115; 116; 117].

Besides using chemical reducing agents, Ag particles have also been prepared through photolytic methods, either by directly reducing photosensitive silver halides [99], or by reducing monovalent Ag by photo-excited radicals [118;119]. Furthermore, recent studies show that in the presence of appropriate chemicals, Ag nanoparticles can be shaped with the irradiation light: Excitation of localized surface plasmon modes causes inhomogeneous electric-fields over the particle, which affects the binding states of capping agents, and therefore causes different growth rates at different facets of the particle [120;121;122;123;124;125;126; 127;128].

Capping agents

In terms of stabilizers, Ag particles stabilized through electrostatic effect, for example, by citrate ions, are usually very sensitive to the electrolyte environment. Aggregations can be easily induced when the electrolyte balance is broken. Better stability can be achieved through a two-phase synthesis with amphiphile surfactants, such as thioalkanes, aminoalkanes[98;104;105], sodium di(2-ethyl-hexyl)sulfosuccinate (NaAOT) [110] and cetyltrimethylammoniun bromide (CTAB) [129; 130]. Besides, soft dielectric matrices, such as polymers [88;106;107;108; 131 ; 132;133;134;135], dendrimers [136], and sol-gel composites [137;138] have also been used as efficient stabilizers for Ag nanoparticles.

Lithographic fabrication of Ag nanoparticles

Besides chemical synthesis, Ag nanoparticles/nanostructures have also been fabricated through various forms of lithography techniques (such as electron beam lithography (EBL), focused ion beam lithography (FIB), nanosphere lithography (NSL), and nanoskiving), which are in many cases combined with physical or chemical vapor depositions [88]. These methods provide precise control over the shape and placement of the Ag nanoparticles, though many of them require high costs associated with fabrication equipments.

1.4.2 Fabrication of Ag nanoparticle doped metallodielectric composites

Incorporation of Ag nanoparticles into dielectric matrices such as polymers results in metallodielectric composites, which have both the advanced mechanical properties from the polymers and the unique physicochemical properties (e.g., optical and catalytic properties) from Ag nanoparticles.

Ag nanoparticles can be incorporated in polymers through various in-situ and ex-situ [139] synthetic methods. For example, a Ag-nanoparticle doped PVA (Poly(vinylalcohol)) film was made by solvent evaporation of the PVA water solution containing Ag nanoparticles [140]. Ag-nanoparticle doped [poly(styrene)]-dibenzo-18-crown-6-[poly(styrene)] was obtained by photochemically reducing Ag^+ cations that were initially induced (through the complex effect of crown ether) in the polymer matrix [141]. Similarly, Ag nanoparticles were formed in-situ in a poly (acrylic acid) (PAA)-poly(allylamine hydrochloride) (PAH) multilayered film by reducing Ag^+ cations that were initially bonded to carboxylic acid groups in the polymer matrix [142]. Furthermore, metallodielectric photonic crystals with periodically confined metal nanoparticles have been fabricated within the self-segregated microdomains of diblock copolymers [12].

Besides chemical synthesis, metallodielectric composites can be achieved through other processing techniques. Plasma polymerization, which is widely used in polymer film coating, when combined with metal sputtering or metal evaporation, can result in polymer films doped with metal nanoparticles. [143] Various chemical vapor depositions, which are widely used in fabricating high-pure solid materials in optics and semiconductor industry, have been used to simultaneously include metal components during vapor depositions. For example, optical fibers doped with Ag or Au nanoparticles have been fabricated through a modified chemical vapor deposition (MCVD) [144] combined with a solution doping process [13;145].

1.4.3 Fabrication of metallodielectric composites with device geometries

Devices for optics, electronics, optoelectronics and sensors, etc. require materials with specific functional geometries. Films can be achieved through casting, spin-coating, or dip-coating of soft materials [146;147] or through

physical processes such as plasma polymerization [143] or chemical vapor deposition. 1-D nano-fibers and micro-fibers have been fabricated through electronspinning (3 nm to 1000 nm in diameter) [148;139;149;150] and modified chemical vapor deposition [13;144;145], respectively. Metal nanoparticles can be incorporated either in-situ or ex-situ into the dielectric matrices. 2-D patterned metallodielectric structures have been achieved through a soft lithography where desired patterns were transferred from a polymer (e.g. polydimethylsiloxane, PDMS) stamp to a polymer film; metal nanoparticles were then selectively absorbed onto the desired domains [151;152]. Besides, based on the self-segregation and micro-phase-separation of diblock copolymers, 2D photonic crystals with periodically confined metal nanoparticles have been fabricated [12;153]. 3D metallo-dielectric microstructures with Ag nanoparticle have been inscribed into dielectric matrix through a 2-photon lithography [154]; 3D periodic photonic crystal structures with doped Ag nanoparticles have been attempted with holographic intereference[155].

1.5 Spontaneous structure formation due to optical self-trapping and modulation instability in photopolymerisable organosiloxanes

1.5.1 An introduction to nonlinear forms of light propagation

1.5.1.1 Optical self-focusing and self-trapping

In a dispersive linear medium, due to natural diffraction, light beams tend to broaden as they propagate(**Figure 1.5b**). This can be understood by considering the beam as a linear superposition of plane-waves, each traveling in a slightly different direction. Despite that each wave may have an identical wavevector (e.g. monochromatic light), they propagate at a different phase velocity with respect to the propagation axis. Hence, phase differences arise over distance, resulting in broadening and weakening (in intensity) of

the beam [156]. One commonly used approach to counteract diffraction of beam is by using a waveguide, where the beam is confined and guided within a high refractive-index medium based on total internal refraction. Alternatively, confining and guiding of light can be realized by passing light through a medium where a change of refractive index (Δn) is photo-induced as a function of optical intensity. Specifically, propagation of a narrow beam of light induces a refractive gradient corresponding to the beam intensity profile, which then acts as an effective positive lens (i.e. refractive index maximizes at the center of the beam and decreases towards the beam's edge), focusing the beam along the propagation axis. (**Figure 1.5a**) Natural diffraction can thus be cancelled by the light-induced *self-focusing*. At the balance of these two effects, the light beam propagates over distance without broadening and becomes *self-trapped* within the self-induced waveguide. (**Figure 1.5c**) Theoretically, self-trapping can be described by the nonlinear Shrödinger equation [157;158]:

$$ik_0 n_0 \frac{\partial E}{\partial z} + \frac{1}{2}\nabla_{\perp}^2 E + k_0^2 n_0 \Delta n E + \frac{i}{2} k_0 n_0 \alpha E = 0, \qquad \textbf{1-21}$$

which indicates that E (the light field amplitude) is the effect from the dynamic competition between the natural broadening of the beam in the transverse direction ($\nabla_{\perp}^2 = (\partial^2/\partial x^2) + (\partial^2/\partial y^2)$) and the self-induced refractive index change Δn along the beam propagation path (z). Here, α is the attenuation coefficient of the medium, n_0 is the refractive index in the medium before light exposure, and k_0 is the free space wave vector.

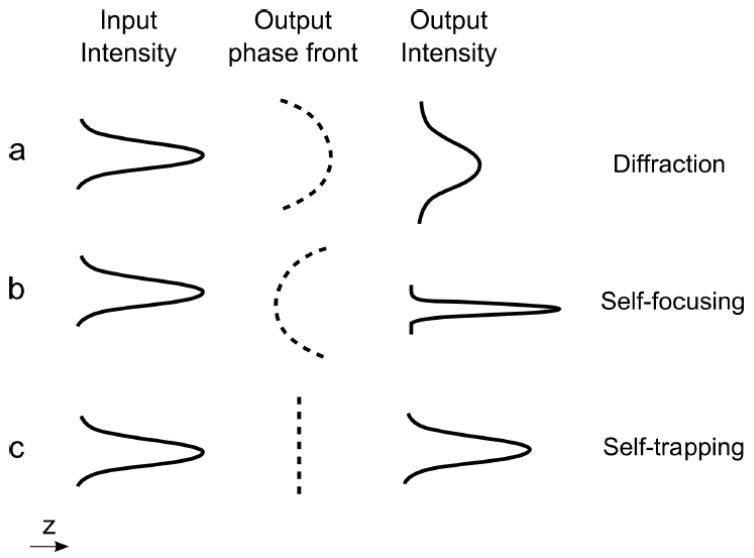

Figure 1.5 Schematic illustration of the spatial beam profiles (solid lines) and phase front (dashed line) of a propagating beam undergoes (a) natural diffraction, (b) self-focusing and (c) self-trapping, respectively. Schematic illustration reprinted from [159] with permission from Elsevier.

1.5.1.2 Spatial self-phase modulation: diffraction rings

The optical beam induced refractive index change $\Delta n(\rho)$ gives rise to the corresponding spatial phase shift across the beam $\Delta\psi(\rho)$ as expressed by [160]:

$$\Delta\psi(\rho)=\frac{2\pi}{\lambda}\int_{z_0}^{z_0+d}\Delta n(\rho,z)dz \qquad \textbf{1-22}$$

Here ρ represents the transverse position in a beam, which is propagating along the axis z. z_0 represents the incidence position of the beam in the medium, d is the propagation distance of the beam within the medium,

and λ is the wavelength of the light in free space. Specifically, the spatial phase shift profile given by a Gaussian beam is:

$$\Delta\psi(\rho) = \Delta\psi_0 \exp(-\frac{2\rho^2}{\omega^2}), \qquad \textbf{1-23}$$

where $\Delta\psi_0$ is the maximum value of phase shift and ω is the beam radius at the entrance face of the medium.

Based on **Equation 1-23,** Durbin *et al.* plotted the phase shift profile across a Gaussian beam propagating in a nonlinear medium (**Figure 1.6)** [160] **.** The slope at each spot along the curve corresponds to the transverse wavevector, $k_t = \left(\frac{d\Delta\psi}{d\rho}\right)_\rho$. As illustrated in **Figure 1.6**, along the curve, radiation at spots ρ_1 and ρ_2 share the same value of transverse wavevector, and therefore interfere with each other. The maximum constructive interference occurs when $\Delta\psi(\rho_1) - \Delta\psi(\rho_2) = 2m\pi$, where m is an integer. For a Gaussian beam with a cylindrical symmetry, constructive interference result in concentric *diffraction rings* when the beam is observed at a transverse plane in far-field. The number of rings can be estimated by the following equation:

$$N \approx \frac{\Delta\psi_0}{2\pi}. \qquad \textbf{1-24}$$

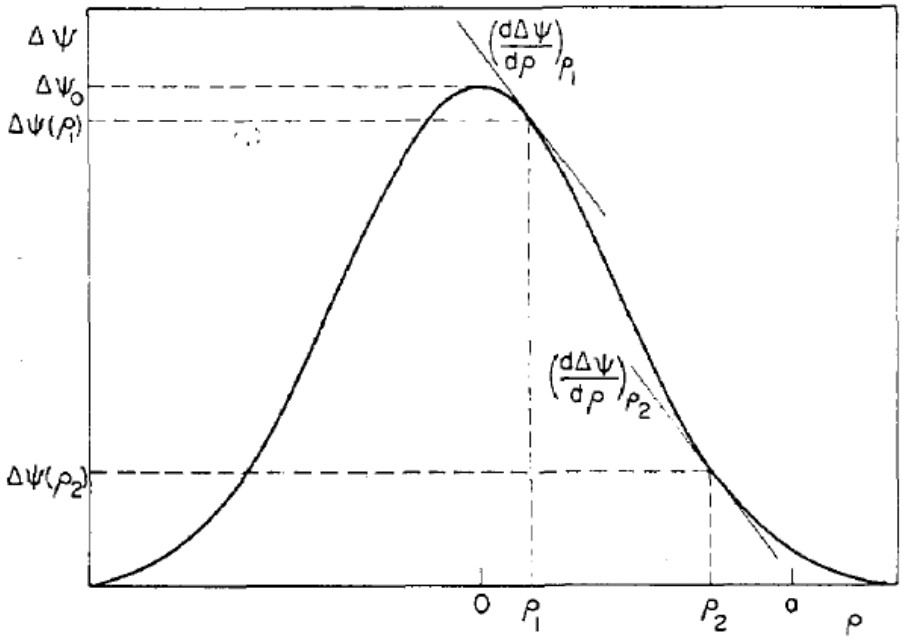

Figure 1.6 The phase shift profile that is derived from **Equation 1-23 by** Durbin *et al.*, for a Gaussian beam propagating in a nonlinear medium. Here, Light diffracted at position ρ_1 and ρ_2 have the same transverse wavevector (as indicated by their identical value of slope), and therefore interfere. Figure is reprinted from [160]. Reprinted with permission from OSA.

1.5.1.3 Optical modulation instability

During optical self-trapping/self-focusing, the propagating beam is more concentrated and confined in the high intensity region, leaving less light in the low intensity region. In other words, the initial inhomogeneity of the optical field is amplified during the nonlinear light propagation. For a broad uniform beam, no matter how perfect it is, during its propagation, noises always exist due to the refractive index inhomogeneity of the medium. Growth and amplification of the perturbations lead to strong intensity modulations across the beam. As a result, the beam becomes unstable and

spontaneously divides into multiple self-trapped filaments. This phenomenon is called *Modulation Instability* (MI). Increase of beam intensity could also increase instability of the propagating beam, causing filamentation(i.e. MI) of a narrow beam, which otherwise undergoes single beam self-trapping/focusing [161; 162].

The growth rate $g(k_\perp)$ of MI can be described as [163]:

$$\frac{g(k_\perp)}{k_0} = -(k_{x_0}/k_0)(|k_\perp|/k_0) + (|k_\perp|/k_0)\sqrt{\frac{\kappa I_0}{n_0} - (\frac{k_\perp}{2k_0})^2}\,, \qquad \textbf{1-25}$$

where $k_\perp$ is the spatial wave vector of the perturbation, I_0 is the intensity of the incident beam, $\kappa = d(\Delta n)/dI$ represents how big the refractive change is affected by the optical intensity; and (k_{x_0}/k) represents the coherence of the beam. This equation shows that the growth rate of MI is a function of $k_\perp$ of the perturbation. Under specific condition, MI of certain $k_\perp$ grows faster than any other MI and becomes dominant [164].

1.5.2 Materials supporting nonlinear forms of light propagation

As described above, nonlinear forms of light propagation requires a medium where the change of refractive index is induced locally by the optical field. Primary study in this field has been carried out mainly in conventional nonlinear materials such as Kerr media and photorefractive crystals, where refractive index changes arise from nonlinear dielectric susceptibilities [165].

In general, in a bulk material, the electric polarization P induced by an electric/optical field E can be expressed as below [166]:

$$P = \varepsilon_0(\chi^{(1)}E + \chi^{(2)}EE + \chi^{(3)}\left|E\right|^2 E + \cdots), \qquad \textbf{1-26}$$

where ε_0 is the permittivity in vacuum, and $\chi^{(n)}$ is the susceptibility with the order of $n = 1, 2, 3\cdots$. In a linear medium, only the first term in this equation dominates, corresponding to the linear response of the polarization P to the electric/optical field E.

In a Kerr medium, the 3rd term in **Equation** 1-26 becomes non-negligible. Its refractive index can be expressed as $n = n_0 + n_2\left|E\right|^2$, where n_0 is the linear refractive index which has no dependence on the incident optical intensity, n_2 is the Kerr nonlinear refractive index coefficient, and the optically induced refractive index change $\Delta n = n_2\left|E\right|^2$ is the one responsible for the nonlinear light propagation. The mostly studied Kerr media are semiconductors (e.g. AlGaAs [167]) and glasses [168;169; 170]. Usually, a Kerr medium has a femtosecond response. Since n_2 is quite small (e.g. $n_2 \approx 2\times10^{-13}\,\mathrm{cm}^2/\mathrm{W}$ in AlGaAs), high incident intensities on the order of GW/cm^2 are required for efficient nonlinear light propagation [171]. In addition, the refractive index change in a Kerr medium is nonsaturable, and the beam grows infinitely with intensity. Materials are therefore easily damaged. In a Kerr medium, stable self-trapping occurs only in (1+1)-dimensional (i.e. a planar waveguide), but not in (2+1)-dimensional (i.e. a propagating beam with both transverse direction self-confined) [171].

In photorefractive crystals, the nonlinear polarization from the second term in **Equation** 1-26**,** has a mechanism very different from that in Kerr media. Photorefractive crystals are electro-optic materials (typically dielectric or semiconductor crystals) that contain a small amount of

photosensitive impurities that can be photoionized. Optical illumination generates an out-of equilibrium concentration of mobile charges which redistribute throughout the crystal to reach a stable electrostatic status, and the resulting space-charge field causes changes of the refractive index. An external electric field is usually required to control the drift of the photoexcited charges, which determines the direction of the induced field. Generally, the refractive index change induced by a low frequency electric field E is $\Delta n = -\frac{1}{2} n_0^3 r_{eff} E$, where n_0 is the unperturbed (linear) refractive index of the material and r_{eff} is the effective electro-optic tensor. The refractive gradient that is responsible for the nonlinear light propagation is caused by the spatial inhomogeneity of the charge distribution induced by optical illumination. Photoionized electrons move statistically towards the positive electrode, giving rise to a double layer that screens the external field, resulting in a higher refractive index in the irradiated region [172]. Refractive index changes induced in photorefractive crystals are saturable, rendering possible stable self-trapping in (2+1)-dimensional. The photo-response time, which varies from nanoseconds to minute, is in a reverse proportion to the optical intensity. Required intensities for self-trapping are of the order of mW/cm^2 and MW/cm^2 for slow and fast response times, respectively [173]. While the self-trapping beam has to be highly coherent in nonlinear media with instantaneous refractive responses, in nonlinear media with non-instantaneous refractive responses, the media only see a time-averaged intensity profile of the beam, allowing the self-trapping of a beam with a low level of coherence [174]. The first observation of self-trapping of a beam of incoherent white light was reported by Mitchell and Segev in 1997 in a photorefractive crystal [174].

Besides Kerr media and photorefractive crystals, nonlinear light propagation has also been studied in liquid crystals (especially nematic ones), which exhibit large birefringence and thus significant nonlinear responses in their dielectric properties. The characteristic reorientational response times of liquid crystals give rise to large refractive index changes on the order of 10^{-1} that can be induced at an intensity of W/cm^2, but with relatively slow response (on the order of 10 to 100 milliseconds) [175;176]. The photoinduced refractive index change Δn is intensity dependent, saturable and polarization sensitive, but independent of wavelength from visible to mid-infrared regions [175].

Changes of refractive index in Kerr media, photorefractive crystals and liquid crystals, are all due to optical-field induced physical changes, i.e., change in molecular polarization, charge transfer, and molecular orientation, respectively. Change of refractive index also occurs upon chemical reactions/changes, as the bonding status within the material is changed. Therefore, optical self-written behavior, which has mainly been observed and studied in conventional nonlinear materials, is also possible in photochemically reactive (i.e. photosensitive) materials. One of the typical photosensitive materials studied in this field are photopolymers. Discussion below is focused on refractive index changes and the resulting nonlinear forms of light propagation through free-radical photopolymerizations.

Photopolymers exhibit refractive index changes through photopolymerizations, in which bonding of monomers results in a cumulative increase in local density and a corresponding localized increase in the refractive index. Refractive index changes due to photopolymerization are intensity dependent, with the empirically obtained expression [177]:

$$\Delta n(x,y,z,t) = \Delta n_s \left\{ 1 - \exp[-\frac{1}{U_0}\int_0^{t-\tau} \left| E(x,y,z,t) \right|^2 dt] \right\}. \qquad \textbf{1-27}$$

Where Δn_s is the maximum refractive index change (at the saturation of polymerization), U_0 is the critical exposure required to initiate photopolymerization, τ is the monomer radical lifetime, t is the irradiation time, and $E(x,y,z,t)$ is the amplitude of the optical field at a particular point in time and space. This equation indicates that the refractive index change Δn increases with light exposure, until the maximum refractive index change of Δn_s is reached (Figure 1.7). It takes a short (long) time to reach the maximum refractive index change Δn_s with high (low) intensity beams. Saturable Δn allows stable self-trapping in (2+1)D. The response time through photopolymerization ranges from milliseconds to seconds; refractive index changes can be as high as 0.15 [177]. In photopolymers, a self-action effect can be triggered with extremely low intensities on the order of tens of μW/cm^2 [178]. In fact, for free-radical photopolymerization, a relatively low optical intensity is preferred. Too intense irradiation causes a large concentration of free radicals produced in a short time; reactive free radicals therefore combine with each other instead of initiating polymerization; in other words, the sample would be bleached by the intense illumination without polymerization, or refractive index change. Functional groups, such as acrylate (or acrylic acid), that undergo free-radical polymerization, are usually involved in the photopolymerisable materials for optical self-writting through nonlinear light propagation [177;178; 179 ; 180 ; 181 ; 182 ; 183 ; 184]. One unique property of photopolymeizable materials is that photo-induced refractive index changes are irreversible and the self-formed optical structures are retained after the optical source is removed.

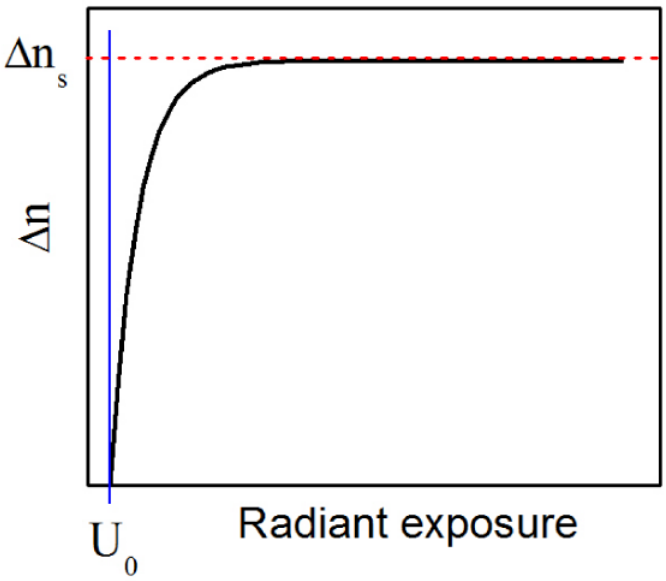

Figure 1.7 Plot of change in refractive index Δn as a function of radiation exposure given by equation (**1-27**). Reprinted from Ref [178]. Copyright (2008) American Chemical Society.

1.5.3 Studies of self-written structures induced by nonlinear-light-propagation in photopolymers

Photosensitivity was first applied to form a self-induced waveguide by Frisken in 1993 in a UV-cured epoxy [185]. Self-trapping in photosensitive materials was then theoretically described by Monro *et al.* in 1995. Almost at the same time, Yariv *et al.* produced optical fibers 10-50 micron wide and up to several millimeters long through a free-radical-photopolymerization induced optical self-trapping in liquid diacrylate monomer by irradiating the sample with a laser beam of 325 nm [177;186]. By measuring the refractive index changes during free-radical polymerization, Yariv *et al.* derived a numerical expression of the refractive index response (**Equation** 1-27) and used this to simulate beam self-trapping in free radical photopolymerization

[177], Kagami *et al.* then took this one step further by fabricating 20 mm long optical fibers with both core and cladding by using a mixture of two kinds of photopolymerisable materials, with the core of the fiber formed by self-trapping of a laser beam through selective photopolymerization of the high refractive index polymer [187]. Dorkenoo et al. observed filamentation of the propagating beam when the self-trapping experiment was performed at a high intensity [161]. Then they noted that in simulations, multimode waveguides can form when the intensity is increased, and inhomogenities due to the oscillating multimodes cause diffusion (filamentation) of the propagating beam at certain points [188]. The interactions of self-written waveguides in photopolymer were studied both theoretically and experimentally by Shoji *et al.* [189]. They found that two self-trapping beams interacting with each other, can merge to form one single waveguide when the collision is small enough (e.g. <6.4°, in their experiment) and the merged single beam tilted toward the optical axis of the beam with higher intensity. Lonin and coworkers found numerically that the criterion for stable beam self-trapping in photopolymerisable media is that the beam's half-width is smaller than the size of self-formed inhomogeneities. Out of this stable regime, filamentation (i.e. MI) of the beam occurs. Besides, sizes of self-formed inhomogeneities have been found to increase with both decreasing radiation intensities and decreasing medium viscosities [190].

Permanent waveguides through optical self-trapping in photopolymers have potential applications in the field of integrated optics. Optical interconnects have been fabricated through self-writting in photopolymers for both single-mode and multimode fibers (**Figure 1.8a**) [191;192]. A polymer waveguide module for visible wavelength division multiplexing has been made through a self-written process (**Figure 1.8b**) [193]. Self-written waveguides have been applied to rebuild diced waveguides [194]. Micro-

sized polymer molds with various morphologies corresponding to specific optical modes were formed at the extremity of optical fibers through self-writing at the emitting end of fibers carrying corresponding optical modes. With a molded polymerized tip as an extension of the fiber core, the fiber can be applied either to collect light for optical imaging with submicrometer resolution, or to achieve controlled excitation of selective optical modes. [195]. An array of self-written waveguides has been fabricated on a vertical-cavity surface-emitting laser diode-emitting window by using a mask, to increase the efficiency of beam output and optical coupling from the laser [196]. Furthermore, bio-mimetic artificial compound eyes with a 3-D array of self-written polymeric waveguides have been demonstrated with potential applications such as data storage/reading, medical diagnostics, surveillance imaging, and light-field photography (**Figure 1.8c**) [197].

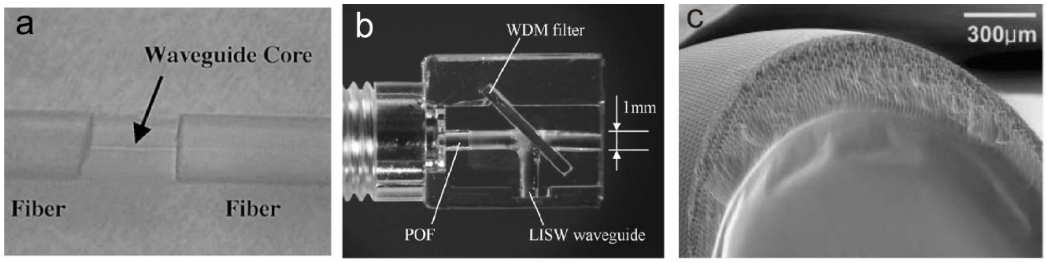

Figure 1.8 Example applications of self-written waveguides through photopolymerization in a) optical interconnects [192], b) polymer waveguide module for visible wavelength division multiplexing[193], and c) fabrication of biomimetic artificial compound eyes [197].

1.5.4 Optical self-written in photopolymerisable organosiloxanes

In this thesis, organosiloxanes with photopolymerisable methacrylate covalently bonded to a silica network (**Figure 1.9**) were used as the dielectric matrix to grow and stabilize Ag nanoparticles, and the resulting composite was then used to construct various metallo-dielectric micro-structures through both conventional optical lithography and self-writting induced by nonlinear forms of light propagation.

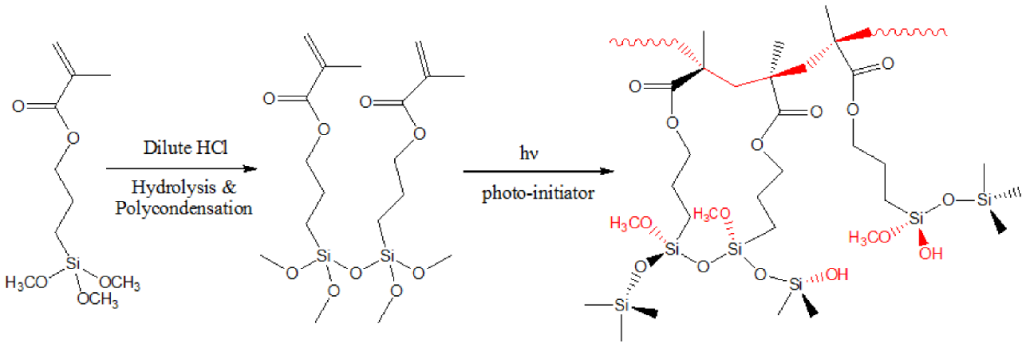

Figure 1.9 Schematic illustration showing that the organosiloxane network is formed through a hydrolysis-condensation process of the inorganic siloxane part and a subsequent photopolymerization of the methacrylate moieties.

During photopolymerization of the organosiloxanes, methacrylate radicals remain attached to the siloxane network. Diffusion of the free radicals is therefore minimized, leading to localized optical response with a spatial resolution of ~ 150 nm [198]. 3-D photonic crystals with highly ordered sub-micron periodicity have been fabricated with organosiloxane through 3-D holographic lithography [198]. According to a previous study by Saravanamuttu and Andrews, the maximum refractive index change induced by photopolymerization in the organosiloxane is 0.006 [199].

Work on optical self-trapping in organosiloxanes was initiated by Saravanamuttu *et al.* by coupling a laser beam to a spin-coated film of the sample [200]. Villafranca and Saravanamuttu further conducted systematic studies (both experimentally and theoretically) to understand the dynamics of coherent beam self-trapping in the photopolymerisable media. [178;201] When conducting self-trapping in organosiloxanes over a broad range of intensities, they observed at certain intensity regimes, the existence of other forms of nonlinear light propagation besides self-trapping: while self-trapping could be induced at the low-intensity regime ($3.2 \times 10^5 \sim 1.6 \times 10^{-2}$ W/cm^2), diffraction rings were observed in the mid-intensity regime (0.19~16 W/cm^2), and single ring with filamentations were observed in the high intensity regime (159~12732 W/cm^2).

Besides, due to the slow optical response in the photopolymerisable organosiloxanes, self-trapping with incoherent white light has been demonstrated by Zhang and Saravanamuttu [179; 202]. Kasala and Saravanamuttu further studied interactions of self-trapped white-light beams in the medium [203]. Burgess, Shimmell, Ponte and Saravanamuttu have fabricated 2-D and 3-D periodic microstructures, respectively through a single-beam and a two-beam modulation instability of white light [180;181].

1.6 Research objectives: Fabrication of metallodielectric microstructures with Ag-doped photosensitive organosiloxanes, especially through optical self-written induced by nonlinear forms of light propagation

As discussed in previous sections, surface plasmons on metal nanoparticles can be optically excited. This gives metal nanoparticles unique optical properties. By dispersing metal nanoparticles into dielectric

materials, the resulting metallo-dielectric composites hold promise in various applications. However, most fabrications of the metallo-dielectric composites to functional geometries still rely on either costly devices or complex processes.

Among all the metals that support surface plasmons, Ag is probably the best as it supports strong surface plamons over a wide range of wavelengths (i.e., from UV to near-IR, 300 nm~ 1200 nm). Practically, Ag is also competitive for its high stability (comparing with many other metals, such as Li and Cu) and relatively low cost (e.g., 1/50 of Au).

In this thesis, one primary research objective is to develop simple step photochemical routes to metallodielectric microstructures doped with Ag-nanoparticles. To achieve that, Ag nanoparticles were photolytically generated and dispersed within organosiloxane sols (Chapter 1), which can be subsequently photopolymerzed in the presence of photoinitiators and therefore be photo-patterned through photoinscription processes, such as photomask and interference lithography. Besides, three different forms of nonlinear light propagation, optical self-trapping, modulation instability and spatial self-phase modulation have been able to be elicited in the Ag nanoparticle-doped organosiloxane. Detailed experimental examination has been performed in the metalldielectric system as well as in the non-doped samples to understand the effect of the embedded Ag nanoparticles on the dynamics of these nonlinear phenomena. The potential of the self-inscription induced by these nonlinear processes for 3-D metallodielectric structures, including cylindrical multimode waveguides and waveguide lattices has also been studied.

In this thesis, we first presented in Chapter 2 a simple step, room temperature method to generate stable Ag nanoparticles photolytically in the

organosiloxanes, together with a detailed discussion of the mechanisms of Ag -nanoparticle growth and evolution. We also demonstrated in this chapter the fabrication of periodic metallodielectric gratings through photomask and laser interference lithography. Then Chapter 3, 4 and 5 each deals with one form of the nonlinear light propagation in the Ag-nanoparticle doped photopolymerisable organosiloxanes, i.e. optical self-trapping, modulation instability and spatial self-phase modulation, respectively. The content in Chapter 2 and 3 have been published in J. Mater. Chem. [204] and J. Opt. Soc. Am. B. [205], respectively, and are reproduced in this thesis with permissions from the publishers. The content in Chapter 4 has been submitted to Journal of Optics and the content in chapter 5 is to be submitted. In this thesis, references are self-contained within each chapter.

---

1. R. G. Freeman, K. C. Grabar, K. J. Allison, R. M. Bright, J. A. Davis, A. P. Guthrie, M. B. Hommer, M. A. Jackson, P. C. Smith, D. G. Walter, and M. J. Natan, "Self-assembled metal colloid monolayers: an approach to SERS substrates," Science **267**, 1629-1632 (1995).

2. Y. Lu, G. L. Liu, and L. P. Lee, "High-density silver nanoparticle film with temperature-controllable interparticle spacing for a tunable surface enhanced Raman scattering substrate," Nano Lett. **5**(1), 5-9 (2005).

3. N. Horimoto, N. Ishikawa, and A. Nakajima, "Preparation of a SERS substrate using vacuum-synthesized silver nanoparticles," Chem. Phys. Lett. **413**, 78-83 (2005).

4. H. A. Atwater and A. Polman, "Plasmonics for improved photovoltaic devices," Nat. Mater. **9**, 205-213 (2010).

5. H. Choi, W. T. Chen, and P. V. Kamat, "Know thy nano neighbor. Plasmonic versus electron charging effects of metal nanoparticles in dye-sensitized solar cells," ACS nano **6**(5), 4418-4427 (2012).

6. X. Li, W. C. H. Choy, L. Huo, F. Xie, W. E. I. Sha, B. Ding, X. Guo, Y. Li, J. Hou, J. You, and Y. Yang, "Dual plasmonic nanostructures for high performance inverted organic solar cells," Adv. Mater. **24**(22), 3046-3052 (2012).

7. C. Hägglund and S. P. Apell, "Plasmonic near-field absorbers for ultrathin solar cells," Phys. Chem. Lett. **3**, 1275-1285 (2012).

8. V. Morandi, F. Marabelli, V. Amendola, and M. Meneghetti, "Colloidal photonic crystals doped with gold nanoparticles: spectroscopy and optical switching properties," Adv. Funct. Mater. Vol. **17**, pp. 2779-2786, 2007.

9. Y. Tan, W. Qian, S. Ding, and Y. Wang, "Gold-nanoparticle-infiltrated polystyrene inverse opals: A three-dimensional platform for generating combined optical properties," Chem. Mater. Vol.18, pp. 3385-3389, 2006.

10. S. Fan, P. R. Vileneuve, and J. D. Joannopoulos, "Large omnidirectional band gaps in metallodielectric photonic crystals," Phys. Rev. B **54**(16), 11245-11251 (1996).

11. Y. Yang, G.-P. Wang, J. Xie, and S. Zhang, "Metal nanoparticles-embedded three-dimensional microstructures created by single-beam holography," Appl. Phys. Lett. **86**, 173108 (2005).

12. M. Bockstaller, R. Kolb, and E. L. Thomas, "Metallodielectric photonic crystals based on diblock copolymers," Adv. Mater. **13**, 1783-1786 (2003)

13. A. Lin, X. Liu, P. R. Watekar, Y. Chung, and W.-T. Han, "Ag nanocrystal-incorporated germano-silicate optical fiber with high resonant nonlinearity,"

App. Phys. Lett. **93**, 021901 (2008); Lin, A.; Liu, X.; A. Lin, X. Liu, P. R. Watekar, W. Zhao, B. Peng, C. Sun, Y. Wang, and W.-T. Han, "All-optical switching application of germano-silicate optical fiber incorporated with Ag nanocrystals," Opt. Exp. **34**(6), 791-793 (2009); A. Lin, B. H. Kim, S. Ju, and W.-T. Han, "Fabrication and third-order nonlinearity of germano-silicate glass fiber incorporated with Au nanoparticles," Proc. SPIE **6481**, 64810M (2007).

14. A. D. McFarland and R. P. V. Duyne, "Single silver nanoparticles as real-time optical sensors with zeptomole sensitivity," Nano Lett. **3**(8), 1057-1062 (2003).

15. K.-S. Lee and M. A. El-Sayed, "Gold and silver nanoparticles in sensing and imaging: Sensitivity of plasmon response to size, shape and metal composition," J. Phys. Chem. B **110**, 19220-19225 (2006).

16. A. Lin, D. H. Son, I. H. Ahn, G. H. Song, and W.-T. Han, "Visible to infrared photoluminescence from gold nanoparticles embedded in germano-silicate glass fiber," Opt. Exp. **15**(10), 6374-6379 (2007).

17. L. Tonks and I. Langmuir, "Oscillations in ionized gases," Phys. Rev. **33**, 195-210 (1929).

18. D. Bohm and E. P. Gross, "Theory of Plasma Oscillations. B. Excitation and Damping of Oscillations," Phys. Rev. **75**, 1864 (1949)

19. D. Pines, "A Collective Description of electron interactions:II.Collectrive vs Individual particle aspects of the interactions," Physical Review **85**(2), 338 (1952).

20. D. Bohm and D. Pines, "A Collective Description of Electron Interactions:III. Coulomb Interactions in a Degenerate Electron Gas," Physical Review **92**, 609 (1953).

21. D. Pines, "Collective energy losses in solids," Reviews of Modern Physics **28**(3), 184-198 (1956).

22. R.H.Ritchie, "Plasma Losses by fast electrons in thin films," Phy. Rev. **106**(5), 874-881 (1957).

23. E. A. Stern and R. A. Ferrell, "Surface plasma oscillations of a degenerate electron gas," Phys. Rev. **120**(1), 130-136 (1960).

24. C. J. Powell and J. B. Swan, "Effect of oxidation on the characteristic loss spectra of aluminum and magnesium," Phys. Rev. **118**(3), 640-643 (1960).

25. J. R. Sambles, G. W. Bradbery, and F. z. Yang, "Optical-excitation of surface plasmons-an introduction," Contemporary physics **32**, 173 (1991).

26. W. L. Barnes, A. Dereux, and t. W. Ebbesen, "Surface plasmon subwavelength optics," Nature **424**(14), 824 (2003).

27. A. Otto, "Excitation of nonradiative surface plasma waves in silver by the method of frustrated total reflection," Zeitschrift für Physik **216**, 398 (1968).

28. D. Beaglehole, "Optical Excitation of Surface Plasmons," IEEE Transactions on electron devices **17**(3), 240 (1970).

29. R.H.Ritchie, E. T. Arakawa, J. J. Cowan, and R. N. Hamm, "Surface-plasmon resonance effect in grating diffraction," Physical review letters **21**, 1530 (1968).

30. G. Diaz and N. García, "Scattering of p-polarized light from Au and Ag gratings and the effect of surface polaritons," Surface Science **146**, 1-9 (1984).

31. F. Toigo, A. Marvin, V. Celli, and N. R. Hill, "Optical properties of rough surfaces: General theory and the small roughness limit," Phys. Rev. B **15**(12), 5618-5626 (1977).

32. B. Hecht, H. Bielefeldt, L. Novotny, Y. Inouye, and D. W. Pohl, "Local excitation, scattering, and interference of surface plasmons," Phys. Rev. Lett. **77**(9), 1889 (1996).

33. A. W. Sanders, D. A. Routenberg, B. J. Wiley, Y. Xia, E. R. Dufresne, and M. A. Reed, "Observation of plasmon propagation, redirection, and fan-out in silver nanowires," Nano Lett. **6**(8), 1822-1826 (2006)

34. H. Ditlbacher, J. R. Krenn, G. Schider, A. Leitner, and F. R. Aussenegg, "Two-dimensional optics with surface plasmon polaritons," Applied Physics Letters **81**(10), 1762-1764 (2002).

35. Z. Li, F. Hao, Y. Huang, Y. Fang, P. Nordlander, and H. Hu, "Directional light emission from propagating surface plasmons of silver nanowires," Nano Lett. **9**(12), 4383-4386 (2009).

36. S. Link and M. A. El-Sayed, "Spectral properties and relaxation dynamics of surface plasmon electronic oscillations in gold ans silver nanodots and nanorods," J. Phys. Chem. B **103**, 8410 (1999).

37. S. Link and M. A. Ei-Sayed, "Size and Temperature Dependence of the Plasmon Absorption of Colloidal Gold Nanoparticles," J. Phys. Chem. B **103**, 4212-4217 (1999).

38. K. L. Kelly, E. Coronado, L. L. Zhao, and G. C. Schatz, "The Optical Properties of Metal Nanoparticles: The Influence of Size, Shape, and Dielectric Environment," J. Phys. Chem. B **107**, 668-677 (2003).

39. C. Noguez, "Surface plasmons on metal nanoparticles: The influence of shape and physical environment," J. Phys. Chem. C **111**, 3806-3819 (2007).

40. V. I. Boev, J. Pérez-Juste, I. Pastoriza-Santos, C. J. R. Silva, M. D. J. M. Gomes, and L. M. Liz-Marzán, "Flexible ureasil hybrids with tailored optical

properties through doping with metal nanoparticles," Langmuir **20**, 10268-10272 (2004).

41. L. M. Liz-Marzán, "Nanometals formation and color," Materials Today **7**(2), 26-31 (2004).

42. I. Freestone, N. Meeks, M. Sax, and C. Higgitt, "The Lycurgus cup- a Roman nanotechnology," Gold Bulletin **40**(4), 270-277 (2007).

43 . M.-C. Daniel and D. Astruc, "Gold Nanoparticles:Assembly, supramolecular chemistry, Quantum-size-related properties, and applications toward biology, catalysis, and nanotechnology," chem. Rev. **104**, 293-346 (2004).

44. M. Fraraday, Philos. Trans. **147**, 145 (1857).

45. G. Mie, "Contributions to the optics of turbid media, particularly of colloidal metal solutions," Ann. Phys **25**, 377 (1908).

46. G. C. Papavassiliou, "Optical properties of small inorganic and organic metal particles," Prog. Solid St. Chem. **12**, 185-271 (1979)

47. J. Crowell and R.H.Ritchie, "Radiative decay of coulomb-stimulated plasmons in spheres," Phys. Rev. **172**(2), 436 (1968).

48. S. Link and M. A. El-Sayed, "Spectral properties and relaxation dynamics of surface plasmon electronic oscillations in gold ans silver nanodots and nanorods," J. Phys. Chem. B **103**, 8410 (1999).

49. K. L. Kelly, E. Coronado, L. L. Zhao, and G. C. Schatz, "The Optical Properties of Metal Nanoparticles: The Influence of Size, Shape, and Dielectric Environment," J. Phys. Chem. B **107**, 668-677 (2003).

50. C. Noguez, "Surface plasmons on metal nanoparticles: The influence of shape and physical environment," J. Phys. Chem. C **111**, 3806-3819 (2007).

51. S. Link and M. A. Ei-Sayed, "Size and Temperature Dependence of the Plasmon Absorption of Colloidal Gold Nanoparticles," J. Phys. Chem. B **103**, 4212-4217 (1999).

52. U. Kreibig and C. V. Fragstein, "The limitation of electron mean free path in small silver particles," Z. Physik **224**(4), 307-323 (1969).

53. A. Kawabata and R. Kubo, "Electronic properties of fine metallic particles. II. Plasma resonance absorption," J. Phys. Soc. Jpn. **21**, 1765-1772 (1966).

54. B. N. J. Persson, "Polarizability of small spherical metal particles: influence of the matrix environment," Surf. Sci. **281**, 153 (1993).

55. E. Hao and G. C. Schatz, "Electromagnetic fields around silver nanoparticles and dimers," J. Chem. Phys. **120**(1), 357 (2004).

56. L. M. Liz-Marzán, "Nanometals formation and color," Materials Today **7**(2), 26-31 (2004).

57. J. Zhao, L. J. Sherry, G. C. Schatz, and R. P. V. Duyne, "Molecular plasmonics: Chromophore-plasmon coupling and single-particle nanosensors," IEEE J. Sel. Top. Quantum Electron **14**(6), 1418-1429 (2008).

58. A. Das, J. Zhao, G. C. Schatz, S. G. Sligar, and R. P. V. Duyne, "Screening of type I and II drug binding to human cytochrome P450-3A4 in nanodiscs by localized surface plasmon resonance spectroscopy," Anal. Chem. **81**, 3754-3759 (2009).

59. Y. B. Zheng, Y.-W. Yang, L. Jensen, L. Fang, B. K. Juluri, A. H. Flood, P. S. Weiss, J. F. Stoddart, and T. J. Huang, "Active molecular plasmonics: controlling plasmon resonances with molecular switches," Nano Lett. **9**(2), 819-825 (2009).

60. E. H. Witlicki, S. S. Andersen, S. W. Hansen, J. O. Jeppesen, E. W. Wong, L. Jensen, and A. H. Flood, "Turning on resonant SERRS using the chromophore-plasmon coupling created by host-guest complexation at a plasmonic nanoarray," J Am Chem Soc **132**(17), 6099-6107 (2010).

61. E. Hutter and J. H. Fendler, "Exploitation of localized surface plasmon resonance," Adv. Mater. **16**(19), 1685-1706 (2004).

62. J. N. Anker, W. P. Hall, O. Lyandres, N. C. Shah, J. Zhao, and R. P. V. Duyne, "Biosensing with plasmonic nanosensors," Nat. Mater. **7**(6), 442-453 (2008).

63. M. E. Stewart, C. R. Anderton, L. B. Thompson, J. Maria, S. K. Gray, J. A. Rogers, and R. G. Nuzzo, "Nanostructured plasmonic sensors," Chem. Rev. **108**, 494-521 (2008).

64. B. M. Reinhard, S. Sheikholeslami, A. Mastroianni, A. P. Alivisatos, and J. Liphardt, "Use of plasmon coupling to reveal the dynamics of DNA bending and cleavage by single EcoRv restriction enzymes," J. Proc. Natl. Acad. Sci. **104**(8), 2667-2672 (2007).

65. Y. Choi, N.-H. Ho, and C.-H. Tung, "Sensing phosphatase activity by using gold nanoparticles," Angew. Chem. Int. Ed. **46**, 707-709 (2007).

66. G. L. Liu, Y. Yin, S. Kunchakarra, B. Mukherjee, D. Gerion, S. D. Jett, D. G. Bear, J. W. Gray, A. P. Alivisatos, L. P. Lee, and F. F. Chen, "A nanoplasmonic molecular ruler for measuring nuclease activity and DNA footprinting," Nature Nanotechnology **1**(1), 47-52 (2006).

67. G. Rong, H. Wang, and B. M. Reinhard, "Insights from a nanoparticle minuet:Two-dimensional membrane profiling through silver plasmon ruler tracking," Nano Lett. **10**, 230-238 (2010).

68. Y.-w. Jun, S. Sheikholeslami, D. R. Hostetter, C. Tajon, C. S. Craik, and A. P. Alivisatos, "Continuous imaging of plasmon rulers in live cells reveals early-stage caspase-3 activation at the single-molecule level," J. Proc. Natl. Acad. Sci. **106**(42), 17735-17740 (2009).

69. J. Aaron, N. Nitin, K. Travis, S. Kumar, T. Collier, S. Y. Park, M. José-Yacamán, L. Coghlan, M. Follen, R. Richards-Kortum, and K. Sokolov, "Plasmon resonance coupling of metal nanoparticles for molecular imaging of carcinogenesis in vivo," J. Biomed. Opt. **12**(3), 034007 (2007).

70. B. P. Rand, P. Peumans, and S. R. Forrest, "Long-range absorption enhancement in organic tandem thin-film solar cells containing silver nanoclusters," J. Appl. Phys. **96**(12), 7519-7526 (2004).

71. H. Shen, P. Bienstman, and B. Maes, "Plasmonic absorption enhancement in organic solar cells with thin active layers," J. Appl. Phys. **106**(7), 073109 (2009).

72. A. Sundaramurthy, P. J. Schuck, N. R. Conley, D. P. Fromm, G. S. Kino, and W. E. Moerner, "near-field of bowtie optical nanoantennas," Nano Lett. **6**(6), 355-360 (2005).

73. M. Moskovits, "Surface-enhanced spectroscopy," Rev. Mod. Phys. **57**(3), 783-826 (1985).

74 . M. Moskovits, "Surface-enhanced Raman spectroscopy: a brief retrospective," J. Raman Spectrosc. **36**(6-7), 485-496 (2005).

75. E. C. L. Ru and P. G. Etchegoin, "Rigorous justification of the |E|4 enhancement factor in Surface Enhanced Raman Spectroscopy," Chem. Phys. Lett. **423**(1-3), 63-66 (2006).

76. F. Tam, G. P. Goodrich, B. R. Johnson, and N. J. Halas, "Plasmonic enhancement of molecular fluorescence," Nano Lett. **7**(2), 496-501 (2007).

77. J.-W. Liaw, J.-H. Chen, C.-S. Chen, and M.-K. Kuo, "Purcell effect of nanoshell dimer on single molecule's fluorescence," Opt. Exp. **17**(16), 13532-13540 (2009).

78. A. Kinkhabwala, Z. Yu, S. Fan, Y. Avlasevich, K. Müllen, and W. E. Moerner, "Large single-molecule fluorescence enhancements produced by a bowtie nanoantenna," Nat. Photonics **3**, 654-657 (2009).

79. R. A. Farrer, F. L. Butterfield, V. W. Chen, and J. T. Fourkas, "Highly efficient multiphoton-abosorption-induced luminescence from gold nanoparticles," Nano Lett. **5**(6), 1139-1142 (2005).

80. Garnett, J. C. M., Colours in metal glasses and in metallic films. *Philos.* Trans. R. Soc. 203, 385-420**1904**.

81. A. Moroz, "Three-dimensional complete photonic-band-gap structures in the visible," Phys. Rev. Lett. **83**(25), 5274-5277 (1999).

82. I. El-Kady, M. M. Sigalas, R. Biswas, K. M. Ho, and C. M. Soukoulis, "Metallic photonic crystals at optical wavelengths," Phys. Rev. B` **62**(23), 15299-15302 (2000).

83. A. Lin, X. Liu, P. R. Watekar, Y. Chung, and W.-T. Han, "Ag nanocrystal-incorporated germano-silicate optical fiber with high resonant nonlinearity," App. Phys. Lett. **93**, 021901 (2008).

84. F. Hache, D. Richard, and C. Flytzanis, "Optical nonlinearities of small metal particles: surface-mediated resonance and quantum size effects," J. Opt. Soc. Am. B **3**(12), 1647-1655 (1986).

85. F. Hache, D. Ricard, C. Flytzanis, and U. Kreibig, "The optical Kerr effect in small metal particles and metal colloids: The case of gold," Appl. Phys. A 47, 347-357 (1988).

86. A. Lin, X. Liu, P. R. Watekar, W. Zhao, B. Peng, C. Sun, Y. Wang, and W.-T. Han, "All-optical switching application of germano-silicate optical fiber incorporated with Ag nanocrystals," Opt. Exp. **34**(6), 791-793 (2009).

87. A. Lin, B. H. Kim, S. Ju, and W.-T. Han, "Fabrication and third-order nonlinearity of germano-silicate glass fiber incorporated with Au nanoparticles," Proc. SPIE **6481**, 64810M (2007).

88. M. Rycenga, C. M. Cobley, J. Zeng, W. Li, C. H. Moran, Q. Zhang, D. Qin, and Y. Xia, "Controlling the synthesis and assembly of silver nanostructures fro plasmonic applications," Chem. Rev. **111**(6), 3669-3712 (2011).

89. H. Wang, F. Tam, N. K. Grady, and N. J. Halas, "Cu nanoshells: effects of interband transitions on the nanoparticle plasmon resonance," J. Phys. Chem. B **109**(39), 18218-18222 (2005).

90. Hu, M.; Chen, J.; Li, Z.-Y.; Au, L.; Hartland, G. V.; Li, X.; Marquez, M.; Xia, Y., Gold nanostructures:engineering their plasmonic properties for biomedical applications. Chem. Soc. Rev.**,** 35, 1084-1094 (2006).

91. Xiang, y.; Wu, X.; Liu, D.; Feng, L.; Zhang, K.; Chu, W.; Zhou, W.; Xie, S., Tuning the morphology of gold nanocrystals by switching the Growth of {110} facets from restriction to preference. J. PHys. Chem. C**,** 112, 3203-3208 (**2008)**.

92. F. E. Wagner, S. Haslbeck, L. Stievano, S. Calogero, Q. A. Pankhurst, and K.-P. Martinek, "Before striking gold in gold-ruby glass," Nature **407**, 691-692 (2000).

93. H. H. Helcher, *Aurum potabile order gold tinstur* (Johann Herbord Klossen, Breslau, 1718).

94. M. Hu, J. Chen, Z.-Y. Li, L. Au, G. V. Hartland, X. Li, M. Marquez, and Y. Xia, "Gold nanostructures:engineering their plasmonic properties for biomedical applications," Chem. Soc. Rev. **35**, 1084 (2006).

95. A. Henglein, "Formation of colloidal silver nanoparticles: Capping action of citrate," J. Phys. chem. B **103**(44), 9533-9539 (1999).

96. G. Rodríguez-Gattorno, D. D, L. Rendón, and G. O. Hernández-Segura, "Metallic nanoparticles from spontaneous reduction of silver(I) in DMSO. Interaction between nitric oxide and silver nanoparticles," J. Phys. Chem. B **106**(10), 2482-2487 (2002).

97. Q. Zhang, W. Li, L.-P. Wen, J. Chen, and Y. Xia, "Facile synthesis of Ag nanocubes of 30 to 70 nm in edge length with CF3COOAg as a precursor " Chem. - Eur. J. **16**, 10234-10239 (2010).

98. R. Lahtinen, S. Mertens, E. East, C. Kiely, and D. Schiffrin, "Silver halide colloid precursors for the synthesis of monolayer-protected clusters," Langmuir **20**(8), 3289-3296 (2004).

99. L. Qiu, J. Franc, A. Rewari, D. Blanc, and K. Saravanamuttu, "Photolytic formation of Ag nanoparticles in oligomeric organosiloxanes: new photolithographic routes to metallodielectric microperiodic structures," J. Mater. Chem. **19**, 373-378 (2009).

100. D. D. Evanoff and J. a. G. Chumanov, "Size-Controlled Synthesis of Nanoparticles. 1. “Silver-Only” Aqueous Suspensions via Hydrogen Reduction," J. Phys. Chem. B **108**, 13948 (2004).

101. R. C. Weast, ed., *CRC Handbook of Chemistry and Physics* (CRC Press, Boca Raton, FL, 1979).

102. J. Turkevich, P. C. Stevenson, and J. Hillier, "A study of the nucleation and growth processes in the synthesis of colloidal gold," Discuss. Faraday Soc. **11**, 55-75 (1951).

103. P. C. Lee and D. Meisel, "Adsorption and surface-enhanced Raman of dyes on silver and gold sols " J. Phys. Chem. B **86**(17), 3391-3395 (1982).

104. J. R. Heath, C. M. Knobler, and D. V. Leff, "Pressure/Temperature phase diagrams and superlattices of organically functionalized metal nanocrystal monolayers: The influence of particle size, size distribution, and surface passivant," J. Phys. Chem. B **101**(2), 189-197 (1997).

105. B. A. Korgel, S. Fullam, S. Connolly, and D. Fitzmaurice, "Assembly and self-organization of silver nanocrystal superlattices: ordered "soft spheres"," J. Phys. Chem. B **102**(43), 8379-8388 (1998).

106. C. Ducamp-Sanguesa, R. Herrera-Urbina, and M. Figlarz, "Synthesis and characterization of fine and monodisperse silver particles of uniform shape," J. Solid State Chem. **100**(2), 272-280 (1992).

107. P.-Y. Silvert, R. Herrera-Urbina, and N. Duvauchelle, "Preparation of colloidal silver dispersions by the polyol process. Part 1 - Synthesis and characterization," J. Mater. Chem. **6**, 573-577 (1996).

108. B. Wiley, Y. Sun, and Y. Xia, "Synthesis of silver nanostructures with controlled shapes and properties," Acc. Chem. Res. **40**, 1067 (2007).

109. I. Pastoriza-Santos and L. M. Liz-Marzán, "Formation of PVP-protected metal nanoparticles in DMF," Langmuir **18**(7), 2888-2894 (2002); I.

Pastoriza-Santos and L. M. Liz-Marzán, "Synthesis of silver nanoprisms in DMF," Nano Lett. **2**(8), 903-905 (2002).

110. M. Maillard, S. Giorgio, and M.-P. Pileni, "Tuning the size of silver nanodisks with similar aspect radios: synthesis and optical properties," J. Phys. Chem. B **107**(11), 2466-2470 (2003).

111. Y. Tan, X. Dai, Y. Li, and D. Zhu, "Preparation of gold, platinum, palladium and silver nanoparticles by the reduction of their salts with a weak reductant-potassium bitartrate," J. Mater. Chem. **13**(5), 1069-1075 (2003).

112. C. J. Murphy and N. R. Jana, "Controlling the aspect ratio of inorganic nanorods and nanowires," Adv. Mater. **14**(1), 80-82 (2002).

113. J. Zeng, Y. Zheng, M. Rycenga, J. Tao, Z.-Y. Li, Q. Zhang, Y. Zhu, and Y. Xia, "Controlling the shapes of silver nanocrystals with different capping agents," J. Am. Chem. Soc. **132**(25), 8552-8553 (2010).

114. G. Mitrikas, C. C. Trapalis, and G. Kordas, "Tailoring the particle size of sol-gel derived silver nanoparticles in SiO2," Journal of Non-Crystalline Solids **186**(1-2), 41-50 (2001).

115. V. G. Pol, D. N. Srivastava, O. Palchik, V. Palchik, M. A. Slifkin, A. M. Weiss, and A. Gedanken, "Sonochemical deposition of silver nanoparticles on silica spheres," Langmuir **18**(8), 3352-3357 (2002).

116. Y. Plyuto, J.-M. Berquier, C. Jacquiod, and C. Ricolleau, "Ag nanoparticles synthesised in template-structured mesoporous silica films on a glass substrate," Chem. Commun. **17**, 1653-1654 (1999).

117. T. C. Wang, M. F. Rubner, and R. E. Cohen, "Polyelectrolyte multilayer nanoreactors for preparing silver nanoparticle composites: controlling metal concentration and nanoparticle size," Langmuir **18**(8), 3370-3375 (2002).

118. J. P. Abid, A. W. Wark, P. F. Brevet, and H. H. Girault, "Preparation of silver nanoparticles in solution from a silver salt by laser irradiation," Chem. Commun. **7**, 792-793 (2002).

119. H. H. Huang, X. P. Ni, G. L. Loy, C. H. Chew, K. L. Tan, F. C. Loh, J. F. Deng, and G. Q. Xu, "Photochemical formation of silver nanoparticles in poly(N-vinylpyrrolidone)," Langmuir **12**(4), 909-912 (1996).

120. X. Wu, P. L. Redmond, H. Liu, Y. chen, M. Steigerwald, and L. Brus, "Photovoltage mechanism for room light conversion of citrate stabilized silver nanoxrystal seeds to large nanoprisms," J. Am. Chem. Soc. **130**(29), 9500-9506 (2008).

121. R. Jin, Y. Cao, E. Hao, G. S. Métraux, G. C. Schatz, and C. A. Mirkin, "Controlling anisotropic nanoparticle growth through plasmon excitation," Nature **425**, 487-490 (2003).

122. J. Zhang, S. Li, J. Wu, G. C. Schatz, and C. A. Mirkin, "Plasmon-mediated synthesis of silver triangular bipyramids," Angew. Chem. Int. Ed. **48**(42), 7787 (2009).

123. X. Zheng, W. Xu, C. Corredor, S. Xu, J. An, B. Zhao, and J. R. Lombardi, "Laser-induced growth of monodisperse silver nanoparticles with tunable surface plasmon resonance properties and a wavelength slef-limiting effect," J. Phys. Chem. C **111**(41), 14962-14967 (2007).

124. C. Xue, G. S. Métraux, J. E. Millstone, and C. A. Mirkin, "Mechanistic study of photomediated triangular silver nanoprism growth," J. Am. Chem. Soc. **130**(26), 8337-8344 (2008).

125. X. Zheng, W. Xu, C. Corredor, S. Xu, J. An, B. Zhao, and J. R. Lombardi, "Laser-induced growth of monodisperse silver nanoparticles with tunable

surface plasmon resonance properties and a wavelength self-limiting effect," J. Phys. Chem. C **111**(41), 14962-14967 (2007).

126. R. Jin, Y. Cao, C. A. Mirkin, K. L. Kelly, G. C. Schatz, and J. G. Zheng, "Photoinduced conversion of silver nanospheres to nanoprisms," Science **294**(5548), 1901-1903 (2001).

127. M. Maillard, P. Huang, and L. Brus, "Silver nanodisk growth by surface plasmon enhanced photoreduction of adsorbed [Ag+]," Nano Lett. **3**(11), 1611-1615 (2003).

128. K. G. Stamplecoskie and J. C. Scaiano, "Light emitting diode irradiation can control the morphology and optical properties of silver nanoparticles," J. Am. Chem. Soc. **132**, 1825-1827 (2010).

129. S. Chen, Z. Fan, and D. L. Carroll, "Silver nanodiskes: Synthesis, characterization, and self-assembly," J. Phys. Chem. B **106**, 10777 (2002).

130. S. Chen and D. L. Carroll, "Synthesis and characterization of truncated triangled silver nanoplates," Nano Lett. **2**(9), 1003-1007 (2002).

131. S. Porel, S. Singh, S. S. Harsha, D. N. Rao, and T. P. Radhakrishnan, "Nanoparticle-embedded polymer:In situ synthesis, free-standing films with highly monodisperse silver nanoparticles and optical limiting," Chem. Mater. **17**(1), 9-12 (2005).

132. B.-H. Sohn, J.-M. Choi, S. I. Yoo, S.-H. Yun, W.-C. Zin, J. C. Jung, M. Kanehara, T. Hirata, and T. Teranishi, "Directed self-assembly of two kinds of nanoparticles utilizing monolayer films of diblock copolymer micelles," J. Am. Chem. Soc. **125**, 6368-6369 (2003).

133 . D.-H. Chen and Y.-W. Huang, "Spontaneous formation of Ag nanoparticles in dimethylacetamide solution of poly(ethylene glycol)," J. Colloid Interface Sci. **255**(2), 299-302 (2002).

134. I. Sondi, D. V. Goia, and D. Matijevi, "Preparation of highly concentrated stable dispersions of uniform silver nanoparticles," J. Colloid Interface Sci. **260**(1), 75-81 (2003).

135. K. P. Velikov, G. E. Zegers, and A. v. Blaaderen, "Synthesis and characterization of large colloidal silver particles," Langmuir **19**(4), 1384-1389 (2003).

136. A. Manna, T. Imae, K. Aoi, M. Okada, and T. Yogo, "Synthesis of dendrimer-passivated noble metal nanoparticles in a polar medium: Comparison of size between silver and gold particles," Chem. Mater. **13**, 1674-1681 (2001).

137. L. M. Bronstein, D. M. Chernyshov, P. M. Valetsky, E. A. Wilder, and R. J. Spontak, "Metal nanoparticles grown in the nanostructured matrix of poly(octadecylsiloxane)," Langmuir **16**(22), 8221-8225 (2000).

138. M. Malenovska, S. Martinez, M.-A. Neouze, and U. Schubert, "Growth of metal nanoparticles in a sol-gel silica thin film," Eur. J. Inorg. Chem. **18**, 2609-2611 (2007).

139. V. Thomas, M. Namdeo, Y. M. Mohan, S. K. Bajpai, and M. Bajpai, "Review on polymer, hydrogel and microgel metal nanocomposites: A facile nanotechnological approach," Journal of Macromolecular Science Part a-Pure and Applied Chemistry **45**(1), 107-119 (2008).

140. Z. H. Mbhele, M. G. Salemane, C. G. C. E. v. Sittert, J. M. Nedeljkovic, V. Djokovic, and A. S. Luyt, "Fabrication and characterization of silver-polyvinyl alcohol nanocomposites," Chem. Mater. **15**(26), 5019-5024 (2003).

141. J. Gao, J. Fu, C. Lin, J. Lin, Y. Han, X. Yu, and C. Pan, "Formation and photoluminescence of silver nanoparticles stabilized by a two-armed polymer with a crown either core," Langmuir 20(22), 9775-9779 (2004).

142. E. Veletanlic and M. C. Goh, "Polyelectrolyte multilayer films as templates for the in situ photochemical synthesis of silver nanoparticles," J. Phys. Chem. C **113**, 18020-18026 (2009).

143.A. Heilmann, *Polymer films with embedded metal nanoparticles*, Materials Science (Springer-Verlag Berlin Heidelberg New York, 2003).

144. S. R. Nagel, J. B. Macchesney, and K. L. Walker, "An overview of the modified chemical vapor deposition (MCVD) process and performance," IEEE Transactions on Microwave Theory and Techniques **MTT-30**(4), 305-322 (1982).

145. S. Ju, P. R. Watekar, S. G. Kang, J.-K. Chung, C. J. Kim, and W.-T. Han, "Effect of TEOS addition on formation of Au metal nano-particles in the Au-doped optical fiber and its optical nonlinearity," Journal of Non-Crystalline Solids **356**(44-49), 2578-2582 (2010).

146. W. Fritzsche, H. Porwol, A. Wiegand, S. Bornmann, and J. M. Köhler, "In-situ formation of Ag-containing nanoparticles in thin polymer films," NanoStructured Materials **10**(1), 89-97 (1998).

147. S. De and G. De, "Coarsening of Ag nanoparticles in SiO2-PEO hybrid film matrix by UV light," J. Mater. Chem. **16**(31), 3193-3198 (2006).

148. S. Ramakrishna, K. Fujihara, W.-E. Teo, T.-C. Lim, and Z. Ma, *Electrospinning and nanofibers* (World Scientific Publishing Co. Pte. Ltd., 2005).

149. D. Li, J. T. McCann, M. Gratt, and Y. Xia, "Photocatalytic deposition of gold nanoparticles on electrospun nanofibers of titania," Chem. Phys. Lett. **394**(4-6), 387-391 (2004).

150. W.-J. Jin, H. K. Lee, E. H. Jeong, W. H. Park, and J. H. Youk, "Preparation of polymer nanofibers containing silver nanoparticles by using poly(N-vinylpyrrolidone)," Macromol. Rapid Commun. **26**(24), 1903-1907 (2005).

151. C. Jiang, S. Markutsya, H. Shulha, and V. V. Tsukruk, "Freely suspended gold nanoparticle arrays," Adv. Mater. 17(13), 1669-1673 (2005).

152. B. Zdyrko, M. K. Kinnan, G. Chumanov, and I. Luzinov, "Fabrication of optically active flexible polymer films with embedded chain-like arrays of silver nanoparticles " Chem. Commun. , 1284 (2008).

153. M. Aizawa and J. M. Buriak, "Block copolymer templated chemistry for the formation of metallic nanoparticle arrays on semiconductor surfaces," Chem. Mater. **19**, 5090-5101 (2007).

154. P.-W. Wu, W. Cheng, I. B. Martini, B. Dunn, B. J. Schwartz, and E. Yablonovitch, "Two-Photon Photographic Production of Three-Dimensional Metallic Structures within a Dielectric Matrix," Adv. Mater. **12**(19), 1438-1441 (2000).

155. Y. Yang, G. P. Wang, J. Xie, and S. Zhang, "Metal nanoparticles-embedded three-dimensional microstructures created by single-beam holography," Appl. Phys. Lett. **86**, 173108 (2005).

156. M. Segev, "Optical spatial solitons," Optical and Quantum Electronics **30**, 503-533 (1998).

157. T. M. Monro, C. M. De Sterke, and L. Poladian, "Topical review - Catching light in its own trap," Journal of Modern Optics **48**(2), 191-238 (2001).

158. A. W. Snyder and D. J. Mitchell, "Accessible Solitons," Science **276**, 1538-1541 (1997).

159. Y. S. Kivshar and G. P. Agrawal, *Optical solitons* (Elsevier, 2003).

160. S. D. Durbin, S. M. Arakelian, and Y. R. Shen, "Laser-induced diffraction rings from a nematic-liquid-crystal film," Opt. Lett. **6**(9), 411-413 (1981).

161. K. Dorkenoo, O. Crégut, L. Mager, and F. Gillot, "Quasi-solitonic behavior of self-written waveguides created by photopolymerization," Optics Letters **27**(20), 1782-1784 (2002).

162. N. F. Pilipetskii and A. R. Rustamov, "Observation of self-focusing of light in liquids," JETP Lett. **2**(2), 55-56 (1965).

163. Soljacic, M.; Segev, M.; Coskun, T.; Christodoulides, D. N.; Vishwanath, A., *Phys. Rev. Lett.* **2000,** 84, 467.

164. Chen, Z.; Klinger, J.; Christodoulides, D. N., *Phys. Rev. E* **2002,** 66, 66601.

165. Trillo, S.; Torruellas, W., *Spatial Solitons*. 1 ed.; Springer: New York, 2001.

166. W. Nie, "Optical nonlinearity:phenomena, applications, and materials," Adv. Mater. **5**(7/8), 520-545 (1993).

167. A. L. Lonin, S. N. Mensov, and Y. V. Polushtaitsev, "Causes of the filamentary instability of optical-beam self-channeling in photopolymerisable composites," Jetp Letters **79**(11), 515-518 (2004).

168. J. S. Aitchison, A. M. Weiner, Y. Silberberg, M. K. Oliver, J. L. Jackel, D. E. Leaird, E. M. Vogel, and P. W. E. Smith, "Observation of spatial optical solitons in a nonlinear glass waveguide," Optics Letters 15(9), 471-473 (1990).

169. I. Kang, T. D. Krauss, F. W. Wise, B. G. Aitken, and N. F. Borrelli, "Femtosecond measurement of enhanced optical nonlinearities of sulfide," J. Opt. Soc. Am. B **12**(11), 2053-2059 (1995).

170. M. Asobe, K. i. Suzuki, T. Kanamori, and K. i. Kubodera, "Nonlinear refractive index measurement in chalcogenideglass fibers by self phase modulation," Appl. Phys. Lett. **60**(10), 1153-1154 (1992).

171. B. Luther-Davies and G. I. Stegeman, "Materials for spatial solitons," in *Spatial Solitons*, S. Trillo and W. Torruellas, eds. (Springer, Berlin, 2001).

172. E. DelRe, B. Crosignani, and P. D. Porto, "Photorefractive spatial solitons," in *Spatial Solitons*, S. Trillo and W. Torruellas, eds. (Springer, Berlin, 2011).

173. M. Segev, M.-f. Shih, and G. C. Valley, "Photorefractive screening solitons of high and low intensity," Journal of the Optical Society of America B: Optical Physics **13**(4), 706 (1996).

174. M. Mitchell and M. Segev, "Self-trapping of incoherent white light," Nature **387**, 880-883 (1997).

175. G. Assanto and M. A. Karpierz, "Nematicons:self-localised beams in nematic liquid crystals," Liquid Crystals **36**(10-11), 1161-1172 (2009).

176. I. Khoo and S. Wu, *Optics and nonlinear optics of liquid crystals* (World Scientific, Singapore, 1993).

177. A. S. Kewitsch and A. Yariv, "Self-focusing and self-trapping of optical beams upon photopolymerization," Optics Letters **21**(1), 24-26 (1996).

178. A. B. Villafranca and K. Saravanamuttu, "An experimental study of the dynamics and temproal evolution of self-trapped laser beams in a photopolymerizable organosiloxane," J. Phys. Chem. C **112**, 17388-17396 (2008).

179. J. Zhang, K. Kasala, A. Rewari, and K. Saravanamuttu, "Self-Trapping of Spatially and Temporally Incoherent White Light in a Photochemical Medium," Journal of the American Chemical Society **128**, 406-407 (2006).

180. I. B. Burgess, W. E. Shimmell, and K. Saravanamuttu, "Spontaneous Pattern Formation Due to Modulation Instability of Incoherent White Light in a Photopolymerizable Medium," J. Am. Chem. Soc. **129**, 4738 (2007).

181. I. B. Burgess, M. R. Ponte, and K. Saravanamuttu, "Spontaneous formation of 3-D optical and structural lattices from two orthogonal and mutually incoherent beams of white light propagating in a photopolymerisable material," J. Mater. Chem. **18**, 4133 (2008).

182.K. Kasala and K. Saravanamuttu, "An experimental study of the interactions of self-trapped white light beams in a photopolymer," Appl. Phys. Lett. **93**(5), 051111 (2008).

183. K. D. Dorkenoo, S. Klein, J.-p. Bombenger, A. Barsella, L. Mager, and A. Fort, "Functionalized photopolymers for integrated optical components," Molecular Crystals and Liquid Crystals **446**(1), 151-160 (2006).

184. M. Kagami, T. Yamashita, and H. Ito, "Light-induced self-written three-dimensional optical waveguide," Applied Physics Letters **79**(8), 1079-1081 (2001).

185. S. J. Frisken, "Light-induced optical waveguide uptapers," Optics letters **18**(13), 1035-1037 (1993).

186. A. S. Kewitsch and A. Yariv, "Nonlinear optical properties of photoresists for projection lithography," Applied Physics Letters **68**(4), 455-457 (1996).

187. M. Kagami, T. Yamashita, and H. Ito, "Light-induced self-written three-dimensional optical waveguide," Applied Physics Letters **79**(8), 1079-1081 (2001).

188. K. D. Dorkenoo, F. Gillot, O. Cregut, Y. Sonnefraud, A. Fort, and H. Leblond, "Control of the refractive index in photopolymerizable materials for (2+1)D solitary wave guide formation," Physical Review Letters **93**(14)(2004).

189. S. Shoji, S. Kawata, A. A. Sukhorukov, and Y. S. Kivshar, "Self-written waveguides in photopolymerizable resins," Optics Letters **27**(3), 185-187 (2002).

190. A. L. Lonin, S. N. Mensov, and Y. V. Polushtaitsev, "Causes of the filamentary instability of optical-beam self-channeling in photopolymerizable composites," Jetp Letters **79**(11), 515-518 (2004).

191. K. Yamashita, T. Hashimoto, K. Oe, K. Mune, R. Naitou, and A. Mochizuki, "Self-written waveguide structure in photosensitive polyimide resin fabricated by exposure and thermosetting process," Ieee Photonics Technology Letters **16**(3), 801-803 (2004).

192. O. Sugihara, H. Tsuchie, H. Endo, N. Okamoto, T. Yamashita, M. Kagami, and T. Kaino, "Light-induced self-written polymeric optical waveguides for single-mode propagation and for optical interconnections," Ieee Photonics Technology Letters **16**(3), 804-806 (2004).

193. M. Yonemura, A. Kawasaki, S. Kato, M. Kagami, and Y. Inui, "Polymer waveguide module for visible wavelength division multiplexing plastic optical fiber communication," Optics Letters **30**(17), 2206-2208 (2005).

194. H. Ozawa, Y. Obata, Y. Mimura, O. Mikami, and T. Shioda, "Self-written waveguide connection across diced waveguide gaps," Ieee Photonics Technology Letters **18**(5-8), 880-882 (2006).

195. R. Bachelot, C. Ecoffet, D. Deloeil, P. Royer, and D. J. Lougnot, "Integration of micrometer-sized polymer elements at the end of optical fibers by free-radical photopolymerization," Applied Optics **40**(32), 5860-5871 (2001).

196. Y. Obata, M. Kanda, and O. Mikami, "Self-written waveguide on a VCSEL-emitting window using a photomask transfer method," Ieee Photonics Technology Letters **18**(9-12), 1308-1310 (2006).

197. K. H. Jeong, J. Kim, and L. P. Lee, "Biologically inspired artificial compound eyes," Science **312**(5773), 557-561 (2006).

198. K. Saravanamuttu, C. F. Blanford, D. N. Sharp, E. R. Dedman, A. J. Turberfield, and R. G. Denning, "Sol-Gel Organic-Inorganic Composites for 3D Holographic lithograpy of photonic crystals with submicron periodicity," Chemistry of Materials **15**, 2301-2304 (2003).

199. K. Saravanamuttu, X. M. Du, S. I. Najafi, and M. P. Andrews, "Photoinduced structural relaxation and densification in sol-gel-derived nanocomposite thin films: implications for integrated optics device fabrication," Can. J. Chem. **76**(11), 1717-1729 (1998).

200. K. Saravanamuttu and M. P. Andrews, "Visible laser self-focusing in hybrid glass planar waveguides," Optics Letters **27**(15), 1342-1344 (2002).

201. A. B. Villafranca and K. Saravanamuttu, "Diffraction rings due to spatial self-phase modulation in a photopolymerizable medium," J. Opt. A: Pure Appl. Opt. **11**, 125202 (2009).

202. J. H. Zhang and K. Saravanamuttu, "The dynamics of self-trapped beams of incoherent white light in a free-radical photopolymerizable medium," Journal of the American Chemical Society **128**(46), 14913-14923 (2006).

203. K. Kasala and K. Saravanamuttu, "An experimental study of the interactions of self-trapped white light beams in a photopolymer," Appl. Phys. Lett. **93**(5), 051111 (2008).

204. L. Qiu, J. Franc, A. Rewari, D. Blanc, and K. Saravanamuttu, "Photolytic formation of Ag nanoparticles in oligomeric organosiloxanes: new photolithographic routes to metallodielectric microperiodic structures," J. Mater. Chem. **19**, 373-378 (2009).

205. L. Qiu and K. Saravanamuttu, "Optical self-trapping in a photopolymer doped with Ag nanoparticles: a single-step route to metallodielectric cyclindrical waveguides," J. Opt. Soc. Am. B **29**(5), 1085-1093 (2012).

Chapter 2 Ag nanoparticle-doped organosiloxanes for photolithographic fabrication of metallodielectric microstructures

Liqun Qiu, Janyce Franc, Abhitej Rewari, Daniele Blanc, Kalaichelvi Saravanamuttu

J. Mater. Chem., 2009, (19), 373-378, DOI: 10.1039/b810566a

Work presented in this chapter was supervised by Dr. Kalaichelvi Saravanamuttu, and it was carried out in collaboration with Dr. Daniele Blanc (Laboratoire Traitement du Signal et Instrumentation, Université Jean Monnet, Saint-Etienne, France). Synthesis and characterization of Ag sols were conducted by Liqun Qiu. Major work on mask lithography and the subsequent optical micrograph characterization were conducted by Liqun Qiu, with assistances from Abhitej Rewari. Both Janyce Franc (Laboratoire Traitement du Signal et Instrumentation, Université Jean Monnet, Saint-Etienne, France) and Liqun Qiu contributed equally to experiment on interference lithography. AFM characterization was conducted by Janyce Franc.

Abstract

Ag nanoparticles in organosiloxane sols were generated through the well-established method of AgCl photoreduction. Evolution of the shape, size

and distribution of Ag nanoparticles in the fluid sols upon irradiation with white light was characterised in detail through optical extinction spectroscopy and transmission electron microscopy. The application of these Ag doped composites in the fabrication of optical gratings containing a uniform distribution of Ag nanoparticles was demonstrated through both photomask and interference lithographic techniques. While the former was based on *in situ* photoreduction of Ag(I), the latter was based on photopolymerization of the methacrylate substituents of organosiloxane oligomers.

2.1 Introduction

Several methods have been developed to stabilise metal nanoparticles in soft dielectric matrices ranging from dendrimers [1;2], polymers [3;4;5;6;7] surfactant systems [8;9] to sol-gel derived composites [10]. The collective plasmon resonance response of such an ensemble of metal nanoparticles can be elicited at visible wavelengths and moreover, tuned through their average size, shape and surrounding medium [19,20]. This holds promise in the design of optical-response based devices for applications ranging from spectroscopy [11;12;13], optical sensing [14;15], to photonic crystals [16;17]. However, the controlled and efficient transformation of soft metallodielectric composites into the device geometries necessary for such applications remains challenging.

In this Letter, a single-step, room temperature method to photolytically generate stable Ag nanoparticles is described. Employing the well-established method of the photoreduction of Ag(I) initiated in AgCl grains [21;22;23], the *in situ* formation and growth of Ag nanoparticles were carried out in a transparent sol of oligomeric organosiloxanes, which could

subsequently be processed into thin films, gels and monoliths. Detailed analyses of extinction spectra and corresponding transmission electron micrographs were carried out to understand photoinduced formation and evolution of the size, shape and distribution of Ag nanoparticles in this medium. The application of the resulting composites in the photolithographic inscription of microperiodic optical gratings was also demonstrated through both mask and interference lithographic techniques. Two different lithographic methods were developed based respectively on the *in situ* reduction of Ag particles in thin organosiloxane films and through photopolymerization of methacrylate substituents of organosiloxane oligomers.

2.2 Experimental

2.2.1 Preparation of Ag(I) doped siloxane sols

Hydrolysis and condensation of 3-methacryloxypropyltrimethoxysilane (4.75 ml, Gelest, Inc. USA) was catalyzed with acid (0.27 ml of 0.05 N HCl from standardized 0.1 N HCl, Sigma-Aldrich, Canada.) to form oligomeric siloxane sols. The majority of Cl^- ions in the sol was first removed through the addition of $AgNO_3$ (0.1 ml, of 0.1 M, Sigma-Aldrich Canada). This resulted in the precipitation of AgCl, which was filtered out through a polytetrafluoroethylene (PTFE) membrane (0.2 μm pore size, Pall Corporation, USA). The organosiloxane sol now had a Cl^- concentration of $7x10^{-4}$ M. Various amounts of $AgNO_3$ solution (0.1 N) were then added so that the sol had a constant concentration of AgCl ($7x10^{-4}$ M) and concentrations of $AgNO_3$ that ranged from 1, 3, 5 to 7 $x10^{-3}$ M. Because $[Ag^+][Cl^-]\sim10^{-6}$ in the sols is always several orders of magnitude greater than $K_{sp}=[Ag^+][Cl^-] = 1.7\times10^{-10}$ [18], AgCl existed as insoluble grains in the sol. The low saturation

ratio of AgCl however increases the free energy barrier for crystal nucleation and thus inhibits immediate formation of larger AgCl particles in the sol, which therefore remained transparent and stable for up to 2 days.

2.2.2 Extinction spectra

Extinction spectra of organosiloxanes sols and thin films doped with Ag nanoparticles were acquired with a Cary 50 Bio UV-Visible spectrophotometer.

2.2.3 Transmission electron microscopy(TEM)

Organosiloxane sols, gels and films doped with Ag-nanoparticles for TEM were first diluted 200-fold with *iso*-propanol and cast onto carbon-coated Cu TEM grids. TEMs were acquired with a Philips CM12 microscope.

2.2.4 Photolithographic inscription of microperiodic metallodielectric structures

Thin films for photolithography were cast from organosiloxane sols doped with $8x10^{-2}$ M of $AgNO_3$ and $7x10^{-4}$ M of AgCl. Microperiodic gratings with periodicities of 500 nm, 2 μm and 3 μm were then inscribed by patterning Ag(I)-doped films through a chrome-plated photomask with white light from a 60 W incandescent bulb or alternatively with a 2-beam interference pattern generated at 244 nm. Photoinscription of optical gratings was also achieved through photoinitiated free-radical polymerisation of methacrylate substituents of the organosiloxane oligomers. In this case, a small amount (3 wt.%) of a free-radical photoinitiator [bis(η^5cyclopentandienyl) bis(2,6-difluoro-3-(1H-pyrrol-yl)-phenl) titanium(IV), Ciba Specialty Chemicals Inc., Canada] was included in the organosiloxane.

2.3 Results and discussion

Ag nanoparticles were photolytically generated in an organosiloxane sol derived through acid-catalysed condensation of 3-methacryloxypropyltrimethoxysilane. The sol, which contained $AgNO_3$ ($7x10^{-3}$ M) and AgCl ($7x10^{-4}$ M), was irradiated continuously with white light (400 nm-800 nm; ~23 $mWcm^{-2}$) emitted by a 60 W incandescent lamp. The originally colourless medium turned a brownish-yellow that deepened with irradiation time. Transmission electron micrographs (TEMs) acquired after 20 minutes confirmed the presence of uniformly dispersed Ag nanoparticles with average diameter and aspect ratio of 30 nm±10 nm and 1.3±0.3, respectively (**Figure 2.1 b, c)**. Corresponding extinction spectra consisted of an absorption band maximising at ~420 nm, which originates from the dipolar plasmon resonance component of small (< 40 nm) Ag particles (**Figure 2.1** a). Contributions to extinction from scattering are small at these particle dimensions [19 ; 20]. The resonance wavelength was bathochromically shifted relative to aqueous solvents (~400 nm)[19] due to the greater dielectric constant of the organosiloxane (~ 1.47) compared to H_2O (1.33).

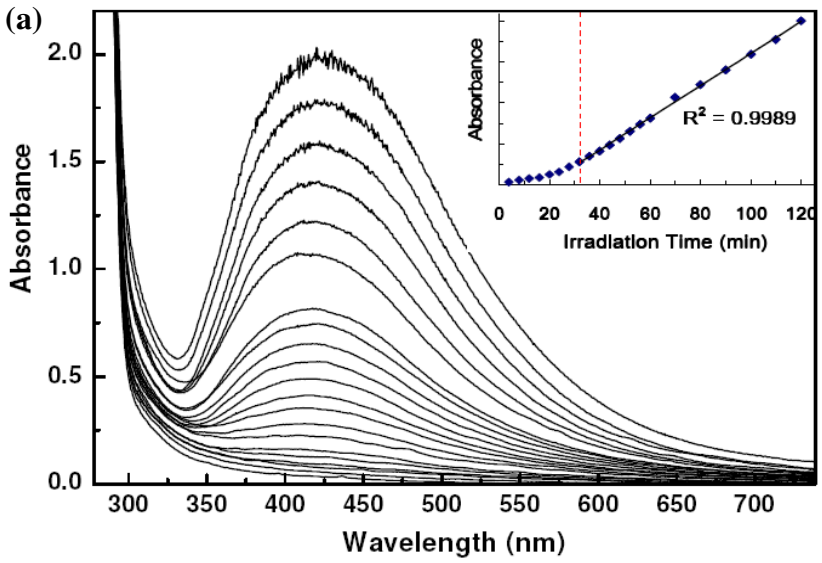
(a)
Absorbance
Wavelength (nm)
Absorbance
Irradiation Time (min)
R² = 0.9989

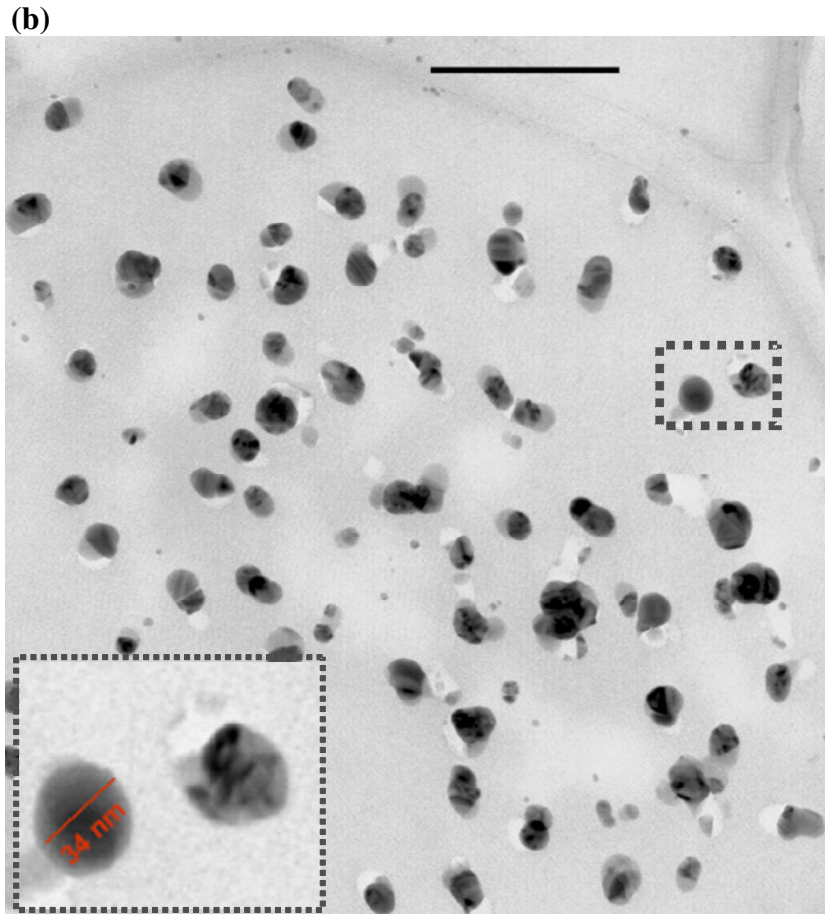
(b)
34 nm

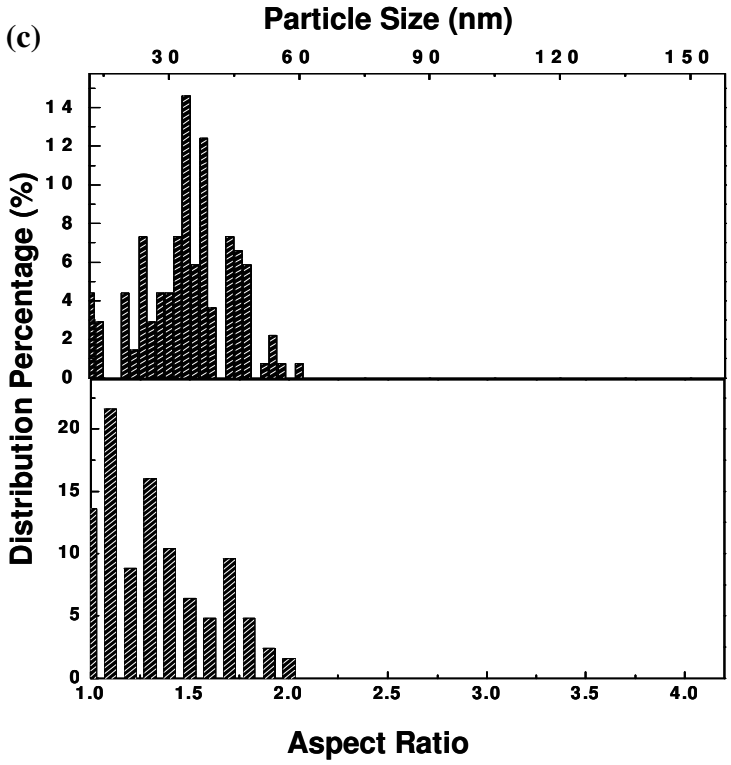

Figure 2.1 (a) Extinction spectra of organosiloxane sol with ~$8x10^{-3}$ M Ag(I) ($7x10^{-3}$ M of $AgNO_3$ and $7x10^{-4}$ M of AgCl) at increasing irradiation times over 120 mins. Inset: temporal plot of maximum extinction at ~420 nm. (b) TEM of Ag particles after 20 min. of irradiation (Scale bar=200 nm) and (c) their distributions of size and aspect ratio (population ~ 150 particles).

Ag particle-formation occurred only in the presence of AgCl grains; no particles formed in organosiloxanes with $AgNO_3$ alone. The photophysics of AgCl has been well established through solid state theory, according to which the sensitivity of AgCl grains to visible wavelengths originates from lattice defects [21;22;23]. Because the organosiloxane itself is transparent in the visible [24], the photoreduction of Ag(I) could be efficiently achieved with white light. The size and shape distribution of Ag particles did not change significantly during early times of irradiation (≤3 hrs). TEMs showed that

even after 3 hours of continued irradiation, the average particle size and aspect ratio were 40 nm±10 nm and 1.4±0.3, respectively. No significant change was therefore observed in the *wavelength* of maximum extinction in corresponding spectra (**Figure 2.1 a**). The continued increase in the *amplitude* of extinction at ~420 nm was therefore primarily due to the increasing concentration of Ag particles with approximately the same size (**Figure 2.1 a**).

A temporal plot of extinction at ~420 nm revealed two distinct stages of increase in particle concentration, an induction period followed by a highly linear region (**Figure 2.1 a, Inset**). This is consistent with the nucleation and growth mechanism of photoreduction in AgCl grains [21], which occurs through reciprocal electronic and ionic events: electrons released upon irradiation become rapidly trapped by lattice defects and coulombically attract mobile Ag^+ ions, which in turn attract additional electrons. In the nucleation stage, this process continues until stable clusters of Ag atoms (nucleating centres) are formed. This induction period is followed by a period of growth of the nuclei, which proceeds through the same mechanism [21].

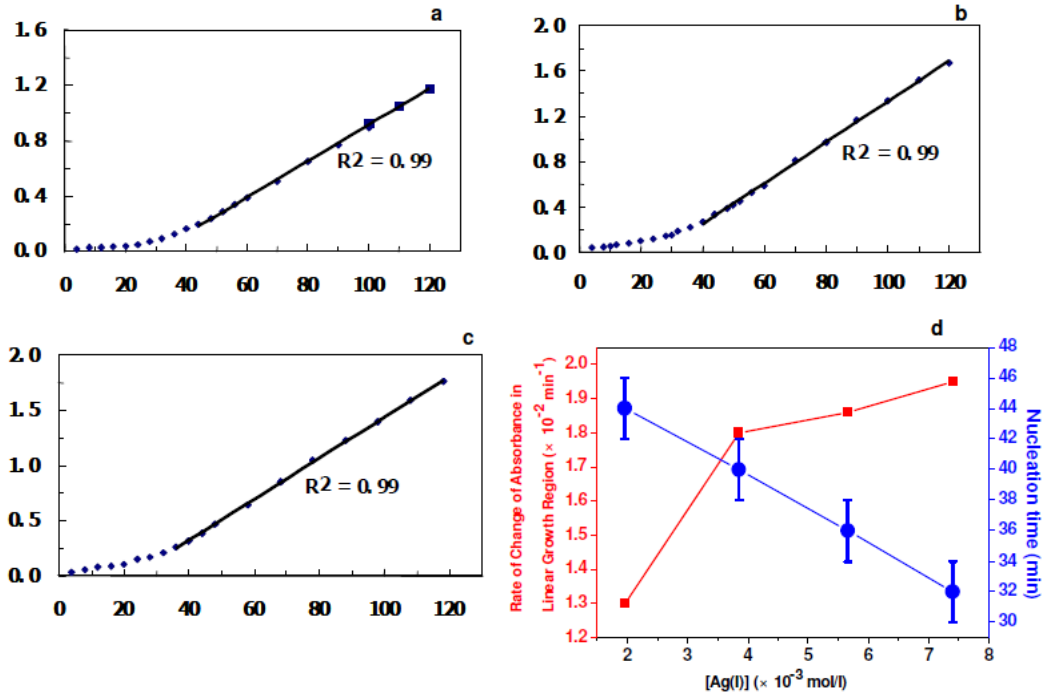

Figure 2.2 Graphs of extinction at 420 nm versus irradiation times for organosiloxane sols containing (a) $1x10^{-3}$ M (b) $3x10^{-3}$ M and (c) $5x10^{-3}$ M of $AgNO_3$. All sols contained the same concentration ($7x10^{-4}$ M) of AgCl. In (a), the large squares represents the extinctions measured after a 30 min break of light irradiation of the sample. Each curve shows an induction period followed by a highly linear region of growth in extinction. (d) Plots of the rate of growth in extinction (square), and induction time (circle), versus the total concentration of Ag(I) in the medium.

The photolytic formation of Ag particles was achieved in organosiloxanes with varying concentrations of $AgNO_3$ ($1x10^{-3}$ M, $3x10^{-3}$ M, $5x10^{-3}$ M and $7x10^{-3}$ M), all photosensitised with AgCl ($7x10^{-4}$ M). The two-stage process was observed in each system during early stages of irradiation (≤3 hrs) While the induction period varied inversely linearly with total Ag(I) concentration, the rate of increase in extinction increased in proportion to [Ag(I)] except in the case of the smallest concentration for which the rate was anomalously small. (**Figure 2.2**). This indicates that a critical Ag^+

concentration is necessary to efficiently increase the concentration of Ag nanoparticles – even if the concentration of Ag nuclei (determined by [AgCl]) is the same. It was also noted that Ag particle concentration did not increase when the same sample was placed in the dark after being irradiated for 100 min (to initiate nuclei formation). However, growth continued at the *same rate* when irradiation was resumed after 30 min. (**Figure 2.2a**) Although AgCl is electrolytically conductive at thermal equilibrium, constant irradiation and consequent steady-state generation of mobile electrons and Ag^+ ions is necessary for the growth of detectable particles.

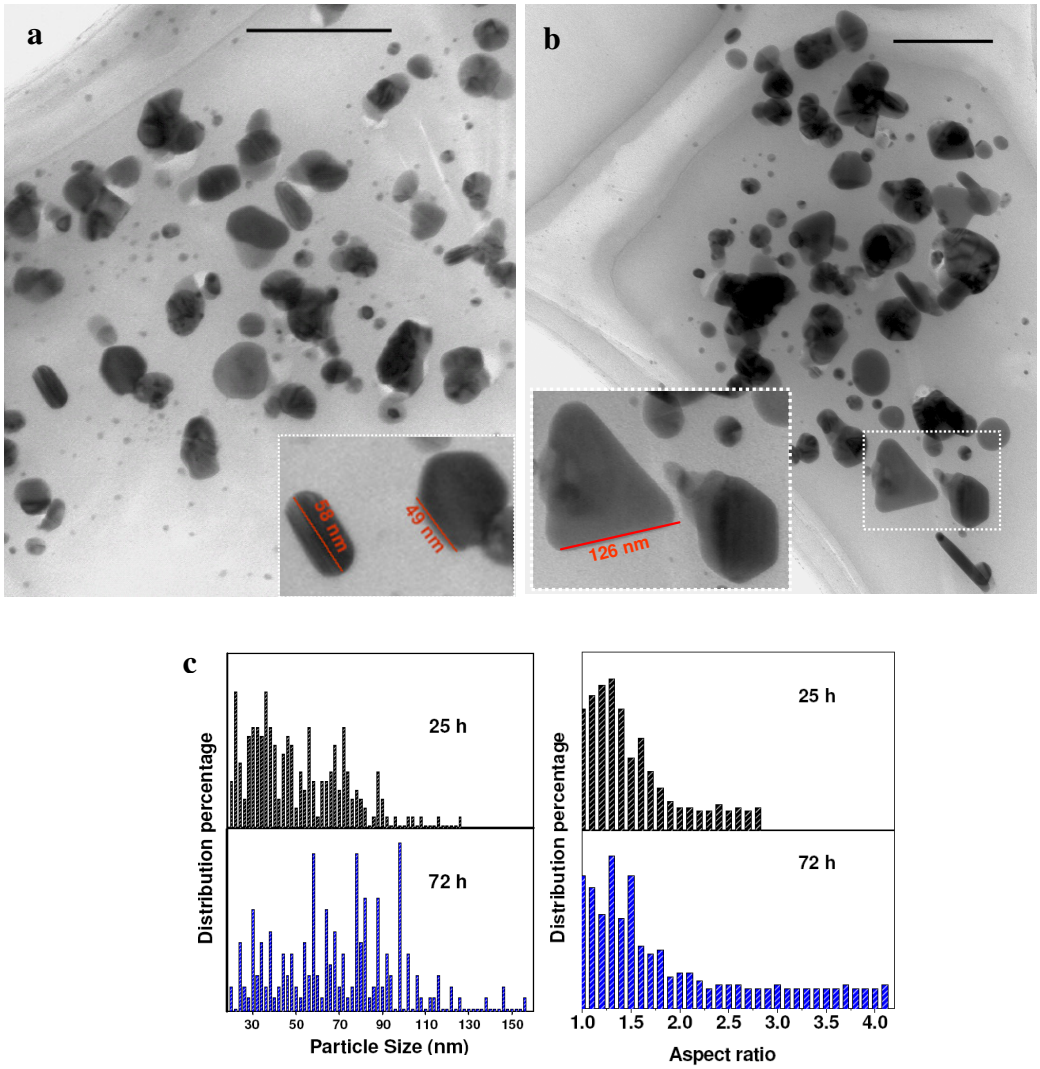
a
58 nm
49 nm
b
126 nm
c
25 h
72 h
Distribution percentage
30 50 70 90 110 130 150
Particle Size (nm)
25 h
72 h
Distribution percentage
1.0 1.5 2.0 2.5 3.0 3.5 4.0
Aspect ratio

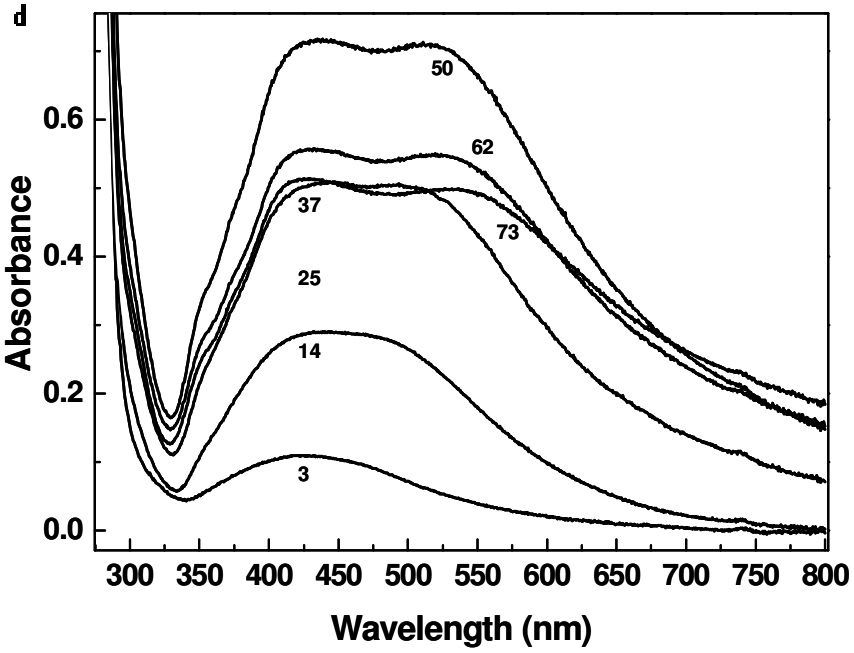

Figure 2.3 TEMs (Scale bar = 200 nm) of ~8x10^{-3} M Ag(I)-doped organosiloxane sol after irradiation for (a) 25 hrs, (b) 72 hrs, with (c) respective distributions of particle size and aspect ratio. (d) UV-Vis absorbance spectra at increasing times of irradiation (hrs indicated on each spectrum). (A general decrease in extinction was observed at later time (62 hrs, 73 hrs) due to increased scatter.)

While at early stages of irradiation (>3 hrs), small Ag particles with a narrow size distribution were produced, their polydispersity increased significantly at long times of irradiation (>10 hrs) at which particles with different length scales (20 nm to 156 nm) and aspect ratios (up to 4) were formed (**Figure 2.3 c)**. TEMs revealed rods and hexagons after 24 hrs and even a small number of triangles after 72 hrs (**Figure 2.3 a,b**). These changes were also detected in extinction spectra (**Figure 2.3 d**). After 14 hrs, the band at ~420 nm increased in width (FWHM ~200 nm) due to contributions from both quadrupolar and dipolar resonance components of large particles [19;20]. At 37 hrs, these two components resolved into maxima at 425 nm

and 520 nm, respectively. The former consists of the quadrupolar resonance component of large particles and dipolar component of small particles (< 40 nm). The maximum at 520 nm corresponds to the dipolar component of *large* particles and continued to bathochromically shift as the average particle-size increased with irradiation, shifting to 537 nm after 73 hrs of continued irradiation. The shoulder at 355 nm observed after 25 hrs has previously been attributed to a plasmon resonance component of large particles while the dampening of resonance at ~320 nm originates from interband transitions of the metal [19;20]. Fluorescent light-induced conversion of small seed particles (formed through chemical reduction) to triangular Ag-prisms in $AgNO_3$ solution has previously been reported [25]. According to the proposed mechanism, this process occurrs through photo-induced digestion of seed particles and their reprecipitation and growth as triangular prisms. In the current study, seed particles with a narrow size distribution were themselves photogenerated *in situ* at early times of irradiation (≤ 3 hrs). The formation of polygonal particles occurred at later times (>> 3 hrs) and appeared to rely on interactions between seed particles. For e.g. polygonal particles did not form in organosiloxanes with low concentration of Ag(I) (2×10^{-3} M), extinction spectra acquired over long irradiation times consisted only of the dipolar resonance component at ~ 420 nm(**Figure 2.4a**). TEMs confirmed that average particle size remained small (40 nm), even after 71 hours of irradiation. (**Figure 2.4b**) This suggests that the reduced probability of interactions at low concentration of Ag seeds inhibits the formation of polygonal particles.

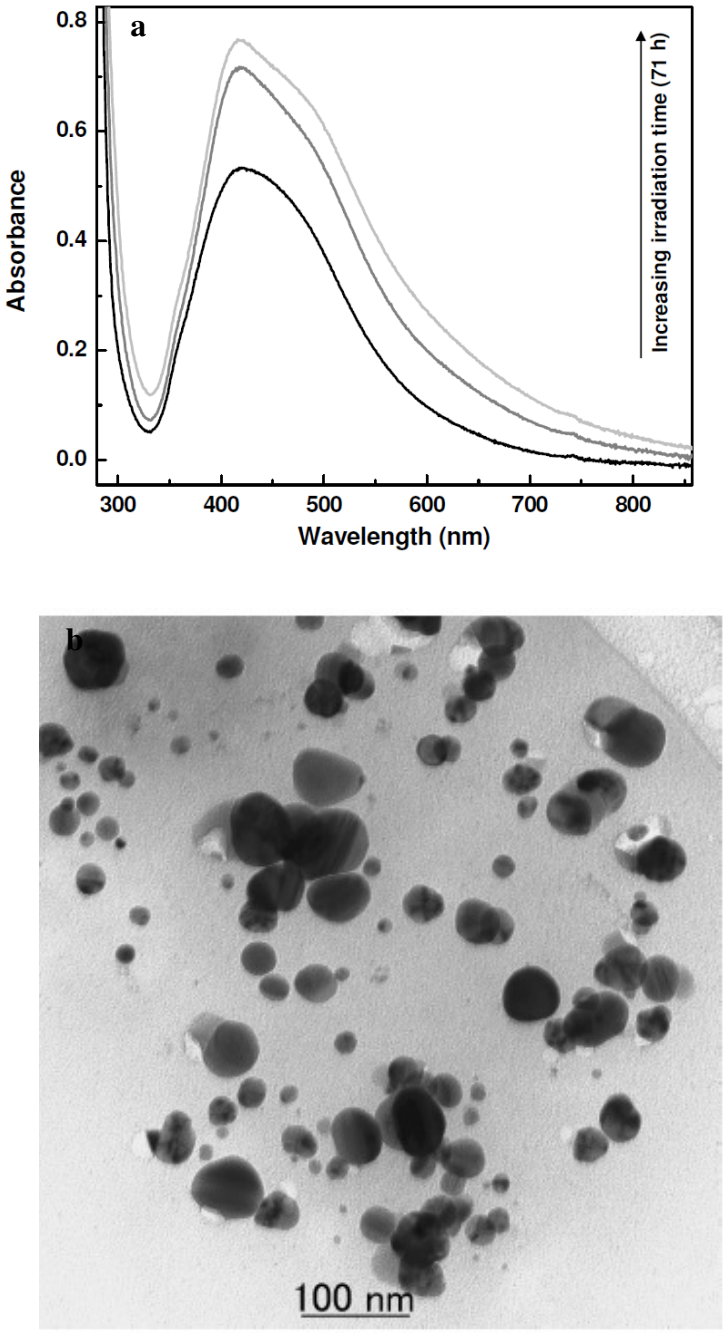

Figure 2.4 (a)Extinction spectra of the sample with 2×10^{-3} M Ag(I) with irradiation of up to 71 hours; (b) TEM image of the particles in this sample after 71 hours' irradiation.

Consistent with this hypothesis, the diffusion of particles also appeared critical for the formation of polygons. For e.g, in aqueous systems, exhaustive

irradiation completely converted seed particles to triangular ones.[25] However, in the organosiloxane sol even with a relatively large concentration of Ag (I) (~$8x10^{-3}$ M), the particle polydispersity actually increased with long times of irradiation (for 72 hrs) (**Figure 2.3**c). Here, the complete conversion of small particles into polygonal ones seemed inhibited by the increasing viscosity of the medium. The organosiloxane sol was derived through characteristically slow [26] condensation reactions of a silicon trialkoxide [24]. Residual alkoxide and hydroxy substituents therefore continued to undergo condensation over days, gradually increasing cross-linking and viscosity of the siloxane sol until it gelled after 7 days.

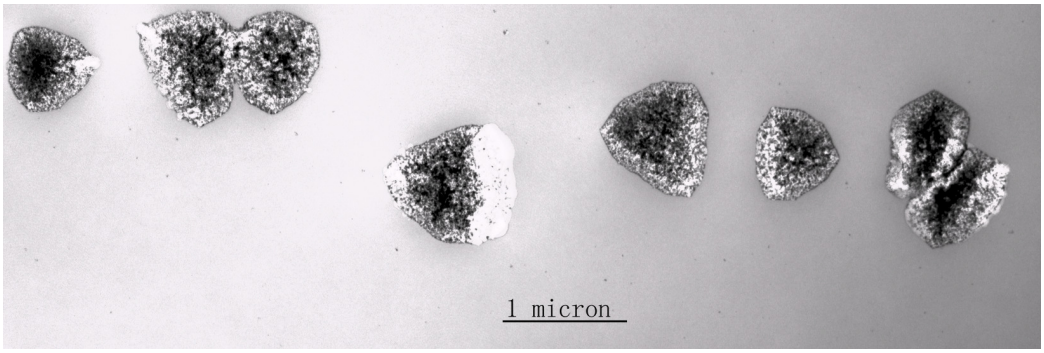

Figure 2.5 TEM of the organosiloxane gel after 7 days of irradiation. Samples for microscopy were prepared by redispersing the gel in *iso*-propanol and casting the colloid onto Cu grids.

This property also prevented the coalescence of particles and thus their phase separation from the medium. In fact, Ag particles remained uniformly distributed even in the gel phase of the organosiloxane; TEMs of the gel redispersed in alcohol revealed ~ 1 μm-sized particles densely embedded with discrete Ag nanoparticles (**Figure 2.5**). Within ~6 hrs of gellation, the gel transformed into a hard, insoluble Ag particle-doped monolith, which appeared pink in transmission (extinction due to SPRs ocurring mainly in the

green spectral region) and green in reflectance due to resonance Rayleigh scattering of Ag particles at the same wavelengths.

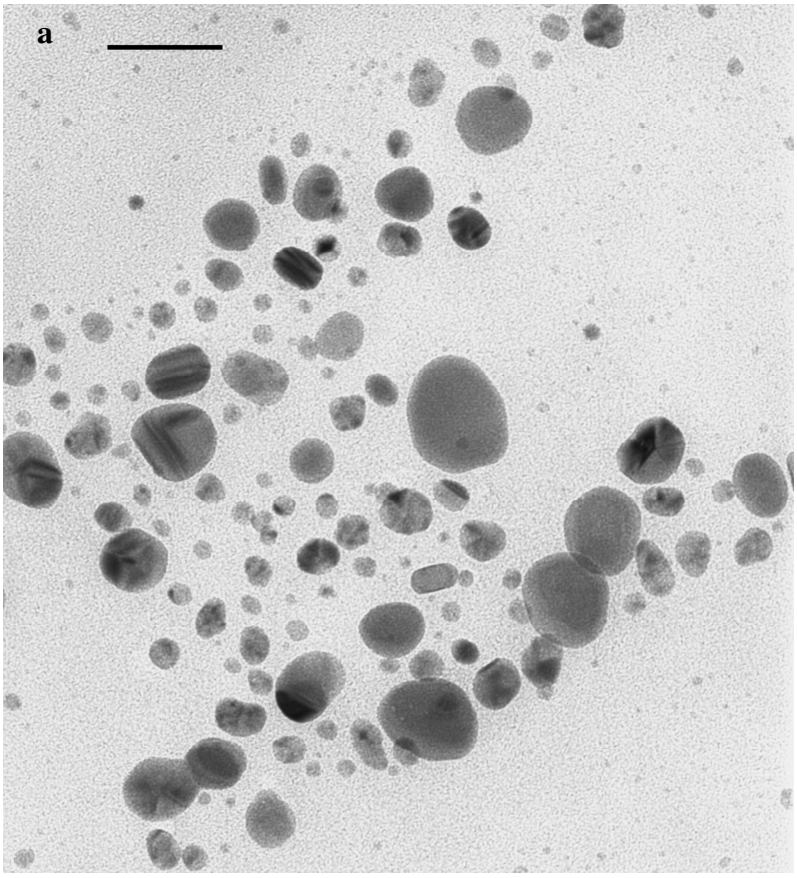

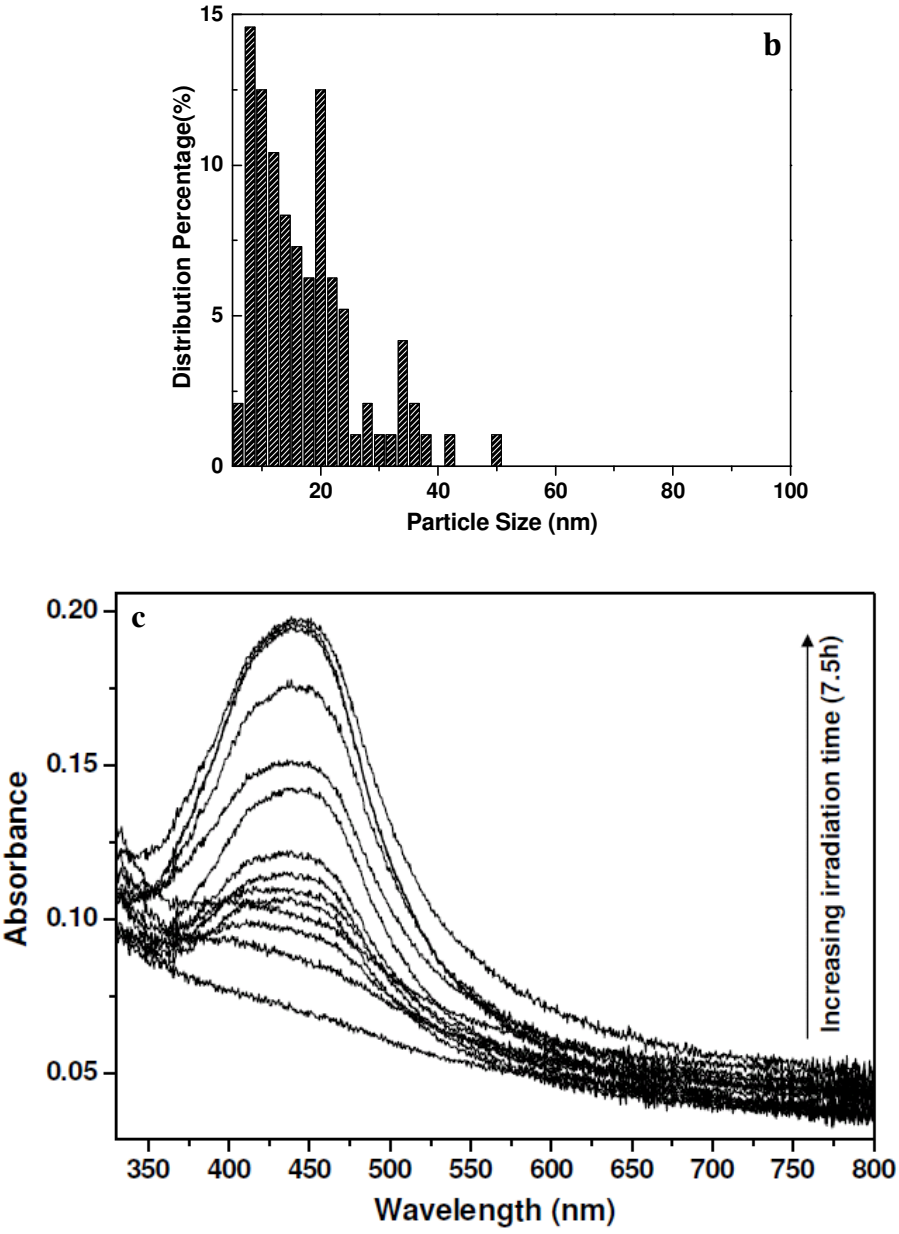

Figure 2.6 (a) TEM of Ag nanoparticles grown in the organosiloxane film with ~8x10^{-2}M Ag(I) and 48 hrs irradiation (scale bar = 50 nm), and (b) the corresponding size distribution. (c) Extinction spectra of the organosiloxane film at increasing irradiation times.

Photolytic formation of stable, uniformly dispersed Ag nanoparticles in organosiloxane sols provides convenient fabrication routes to metallodielectric microstructures. To demonstrate this, Ag particle formation in a ~1 um-thick organosiloxane film containing $8x10^{-2}$ M $AgNO_3$ and $7x10^{-4}$ AgCl was studied. When uniformly irradiated with white light, the film turned brownish yellow in colour but retained excellent transparency. Extinction spectra were dominated by a narrow band at ~440 nm [27] due to the dipolar resonance component of small particles, which increased in amplitude with irradiation (Figure 2.6 **c)**. In contrast to particles formed in the sol, the average size and distribution of those formed within the film remained small (18 nm±9 nm) even after irradiation for 48 hrs and at Ag (I) concentration ($8x10^{-2}$ M) that was ~10-fold greater than the maximum amount contained in sols (**Figure 2.6a,b**). Photoreduction of Ag(I) initiated in individual AgCl grains produced a large concentration of small Ag particles. However, interactions of these seeds and formation of polygonal particles were suppressed in the pseudo-gelatinous film medium [26], which inhibits the diffusion of particles.

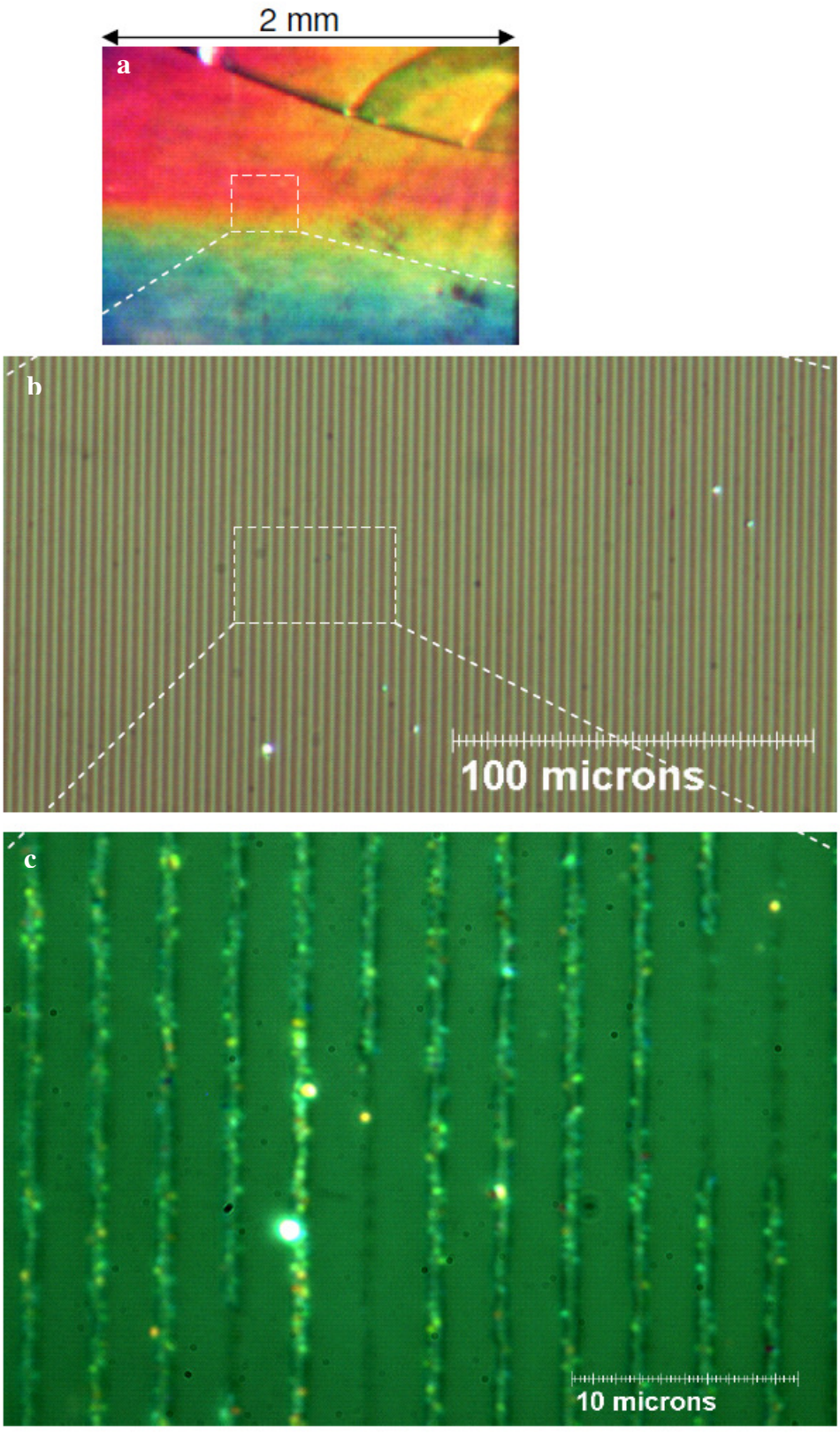
2 mm
a
b
100 microns
c
10 microns

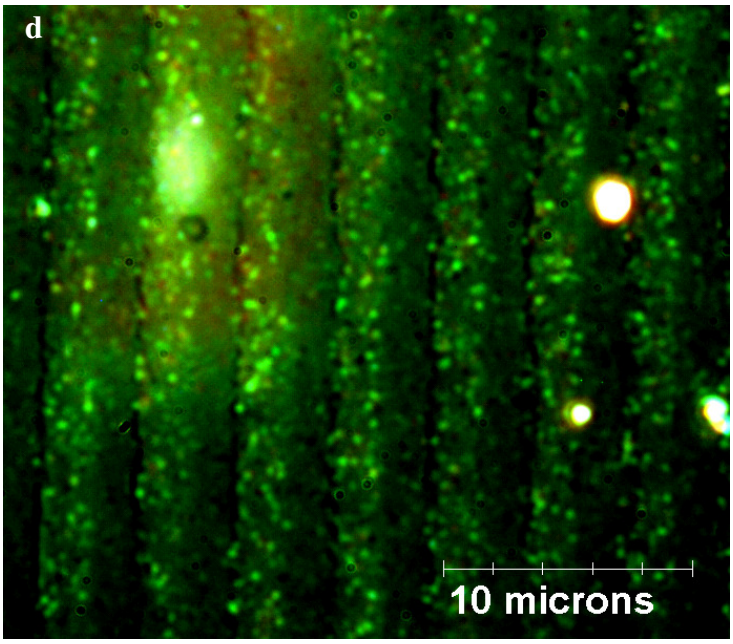

Figure 2.7 (a) Photograph and (b-d) optical reflection micrographs of gratings formed by *in situ* Ag particle formation. (a-c) are images of one same sample with different magnifications.

Optical gratings with periodicities of 2 μm and 3 μm were fabricated by irradiating the Ag(I)-containing organosiloxane films through photomasks. **Figure 2.7 b-d** contain optical reflection micrographs of resulting structures, in which Ag particles appear as bright specks due to resonance Rayleigh scattering of incident light. Particle formation was strongly localised to irradiated regions; each element of the 1-D periodic arrays contained a distribution of discrete Ag particles. Patterning was achieved over large length scales (>1 mm), restricted only by mask dimensions (**Figure 2.7a**). Photoinscription of gratings with periodicities corresponding to visible wavelengths were achieved through interference lithography, where the Ag (I) doped film was exposed to a 2-beam interference pattern (at 244 nm). At this wavelength, free-radical polymerisation of methacrylate substituents of the organosiloxane occurred in irradiated regions. Polymerisation renders

these areas insoluble; the pattern could therefore be brought into relief by immersing the film in alcohol to etch non-irradiated regions. Atomic force micrographs (AFM) of the resulting volume grating with periodicity of 500 nm and average groove-depth of 50 nm are presented in **Figure 2.8**. Similarly, interference gratings were also created in organosilxoane films doped with pre-formed Ag nanoparticles (**Figure 2.9**). Interference lithography could therefore be applied to fabricate gratings in which the size and shape distribution of Ag particles could be deliberately varied. This route employed thin films containing Ag particles, which were photolytically *pre-formed* in the sol phase of the organosiloxane (*vide supra*).

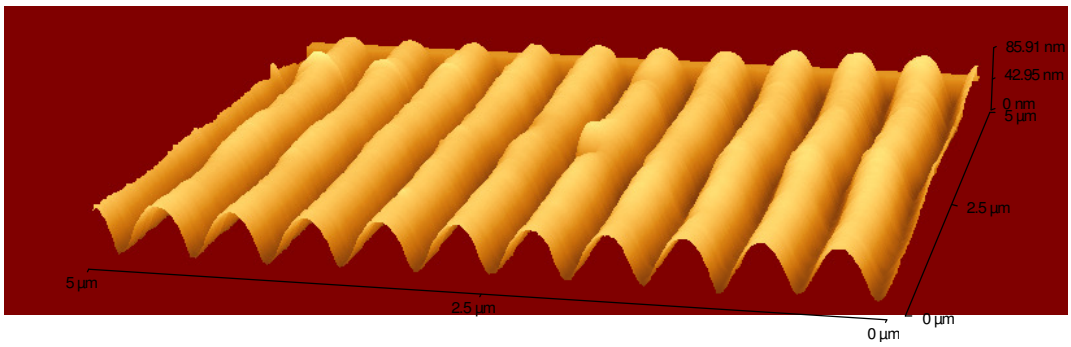

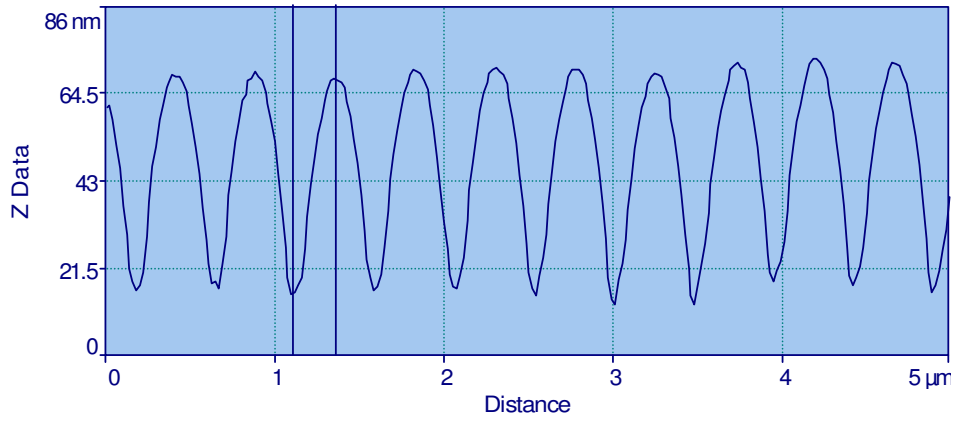

Figure 2.8 AFM of gratings constructed by interference lithography in Ag(I) doped organosiloxane films.

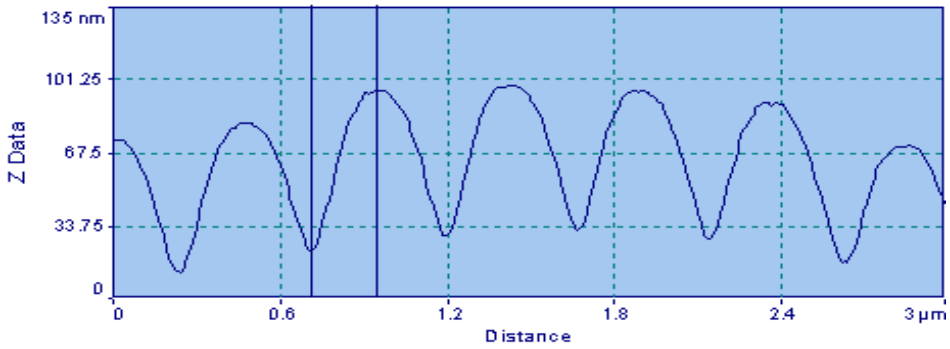

Figure 2.9 AFM profile of gratings constructed by interference lithography in organosilxoane films doped with pre-formed Ag nanoparticles.

2.4 Conclusion

In summary, uniformly dispersed, stable Ag particles were photolytically generated in organosiloxane sols, gels, monoliths and thin films. Ag particles occurred through photoreduction of Ag(I) initiated in AgCl grains; the distribution of Ag particle size and shape varied with the duration of irradiation, total concentration of Ag(I) and viscosity of the medium. Based on these findings, holographic and photo-mask lithographic fabrication of

metallodielectric gratings was demonstrated, which respectively employed *in situ* photoreduction of Ag(I) in thin films and photopolymerization in films containing pre-formed Ag particles. These single-step photolithographic routes provide convenient access to periodic metallodielectric microstructures containing a uniform dispersion of colloidal metal nanoparticles. The effect of the plasmon resonance of this ensemble of metal particles on the effective dielectric constant and thus optical properties of periodic microstructures is valuable in the design of new types of optical devices including metallodielectric photonic crystals [28;29].

2.5 Acknowledgements

Funding from NSERC, CFI, OIT, McMaster and France Canada Research Fund is gratefully acknowledged. The authors thank CIBA-Geigy for donation of photoinitiator and the Electron Microscopy Centre (McMaster University) for assistance with TEM.

---

1. A. Manna, T. Imae, K. Aoi, M. Okada, and T. Yogo, "Synthesis of dendrimer-passivated noble metal nanoparticles in a polar medium: Comparison of size between silver and gold particles," Chem. Mater. 13, 1674-1681 (2001).

2. O. M. Wilson, R. W. J. Scott, J. C. Garcia-Martinez, and R. M. Crooks, "Separation of dendrimer-encapsulated Au and Ag nanoparticles by selective extraction," Chem. Mater. **16**(22), 4202-4204 (2004).

3. L. M. Bronstein, D. M. Chernyshov, P. M. Valetsky, E. A. Wilder, and R. J. Spontak, "Metal nanoparticles grown in the nanostructured matrix of poly(octadecylsiloxane)," Langmuir **16**(22), 8221-8225 (2000).

4. S. Porel, S. Singh, S. S. Harsha, D. N. Rao, and T. P. Radhakrishnan, "Nanoparticle-embedded polymer:In situ synthesis, free-standing films with

highly monodisperse silver nanoparticles and optical limiting," Chem. Mater. **17**(1), 9-12 (2005).

5. A. Dawn, P. Mukherjee, and A. K. Nandi, "Preparation of size-controlled, highly populated, stable, and nearly monodispersed Ag nanoparticles in an organic medium from a simple interfacial redox process using a conducting polymer," Langmuir **23**(10), 5231-5237 (2007).

6. K. Akamatsu, N. Tsuboi, Y. Hatakenaka, and S. Deki, "In situ spectroscopic and microscopic study on dispersion of Ag nanoparticles in polymer thin films," J. Phys. Chem. B **104**, 10168-10173 (2000).

7. K. Huber, T. Witte, J. Hollmann, and S. Keuker-Baumann, "Controlled formation of Ag nanoparticles by means of long-chain sodium polyacrylates in dilute solution," J. Am. Chem. Soc. **129**, 1089-1094 (2007).

8. B.-H. Sohn, J.-M. Choi, S. I. Yoo, S.-H. Yun, W.-C. Zin, J. C. Jung, M. Kanehara, T. Hirata, and T. Teranishi, "Directed self-assembly of two kinds of nanoparticles utilizing monolayer films of diblock copolymer micelles," J. Am. Chem. Soc. **125**, 6368-6369 (2003).

9. H. Xu, J. Xu, Z. Zhu, H. Liu, and S. Liu, "In-situ formation of silver nanoparticles with tunable spatial distribution oat the poly(N-isopropylacrylamide) corona of unimolecular micelles," Macromolecules **39**, 8451-8455 (2006).

10. M. Malenovska, S. Martinez, M.-A. Neouze, and U. Schubert, "Growth of metal nanoparticles in a sol-gel silica thin film," Eur. J. Inorg. Chem. **18**, 2609-2611 (2007).

11. R. G. Freeman, K. C. Grabar, K. J. Allison, R. M. Bright, J. A. Davis, A. P. Guthrie, M. B. Hommer, M. A. Jackson, P. C. Smith, D. G. Walter, and M. J. Natan, "Self-assembled metal colloid monolayers: an approach to SERS substrates," Science **267**, 1629-1632 (1995).

12. Y. Lu, G. L. Liu, and L. P. Lee, "High-density silver nanoparticle film with temperature-controllable interparticle spacing for a tunable surface enhanced Raman scattering substrate," Nano Lett. **5**(1), 5-9 (2005).

13. N. Horimoto, N. Ishikawa, and A. Nakajima, "Preparation of a SERS substrate using vacuum-synthesized silver nanoparticles," Chem. Phys. Lett. **413**, 78-83 (2005).

14. A. D. McFarland and R. P. V. Duyne, "Single silver nanoparticles as real-time optical sensors with zeptomole sensitivity," Nano Lett. **3**(8), 1057-1062 (2003).

15. K.-S. Lee and M. A. El-Sayed, "Gold and silver nanoparticles in sensing and imaging: Sensitivity of plasmon response to size, shape and metal composition," J. Phys. Chem. B **110**, 19220-19225 (2006).

16. S. Fan, P. R. Villeneuve, and J. D. Joannopoulos, "Large omnidirectional band gaps in metallodielectric photonic crystals," Phys. Rev. B **54**(16), 11245-11251 (1996).

17. Y. Yang, G. P. Wang, J. Xie, and S. Zhang, "Metal nanoparticles-embedded three-dimensional microstructures created by single-beam holography," Appl. Phys. Lett. **86**, 173108 (2005).

18. J. A. Dean, *Lange's Handbook of Chemistry,* 15 ed. (McGraw-Hill, 1999).

19. D. D. Evanoff and J. a. G. Chumanov, "Size-Controlled Synthesis of Nanoparticles. 1. “Silver-Only” Aqueous Suspensions via Hydrogen Reduction," J. Phys. Chem. B **108**, 13948 (2004).

20. D. D. Evanoff and J. a. G. Chumanov, "Size-controlled synthesis of nanoparticles. 2. measurement of extinction, scattering, and absorption cross sections," J. Phys. Chem. B **108**, 13957 (2004).

21. *Electronic Processes in Ionic crystals*, Mott, N. F. and Gurney, R. W., Dover Publications Inc. New York, 1964.

22. *Fundamentals of Photographic theory*, James T. H. and Higgins, G. C., John Wiley & Sons., New York, 1948.

23. R. S. Eachus, A. P. Marchetti, and A. A. Muenter, "The photophysics of silver halide imaging materials," Annu. Rev. Phys. Chem. **50**, 117-144 (1999).

24. K. Saravanamuttu, X. M. Du, S. I. Najafi, and M. P. Andrews, "Photoinduced structural relaxation and densification in sol-gel-derived nanocomposite thin films: implications for integrated optics device fabrication," Can. J. Chem. **76**(11), 1717-1729 (1998).Saravanamuttu, K.; Du, X.M.; Najafi, S. I.; Andrews, M.P. Can. J. Chem. **1998**, *76*, 1717.

25. R. Jin, Y. Cao, C. A. Mirkin, K. L. Kelly, G. C. Schatz, and J. G. Zheng, "Photoinduced conversion of silver nanospheres to nanoprisms," Science **294**, 1901 (2001).

26. *Sol-gel science: the physics and chemistry of sol-gel processing*, Brinker, C. J. and Scherer, G. W. Boston, 1990.

27. The band maximum was bathochromically shifted due to the greater refractive index of the film relative to sol.

28. M. Bockstaller, R. Kolb, and E. L. Thomas, "Metallodielectric photonic crystals based on diblock copolymers," Adv. Mater. **13**, 1783-1786 (2001).

29. A. Moroz, "Three-dimensional complete photonic-band-gap structures in the visible," Phys. Rev. Lett. **83**(25), 5274-5277 (1999).

Chapter 3 Optical self-trapping in a photopolymer doped with Ag nanoparticles: a single-step route to metallodielectric cylindrical waveguides

Liqun Qiu and Kalaichelvi Saravanamuttu

Reproduced by permission of OSA

J. Opt. Soc. Am. B., 2012(29), 1085-1093

Work presented in this chapter was conducted by Liqun Qiu, and supervised by Dr. Kalaichelvi Saravanamuttu

Abstract

A continuous wave, visible laser beam self-traps by initiating free-radical polymerization in the organosiloxane photopolymer doped with a well-characterized distribution of Ag nanoparticles. The self-trapped beam propagates over long distances (≫Rayleigh range) without diverging and permanently inscribes a cylindrical metallodielectric waveguide containing a dispersion of Ag nanoparticles. The self-trapped beam evolves from single-mode to multimode guidance over time; the effects of nanoparticle concentration on multimode dynamics were investigated. These findings open room temperature, soft polymer-based pathways where self-action effects including self-trapping and modulation instability can be exploited to spontaneously generate three-dimensional metallodielectric single or multiple cylindrical waveguides.

3.1 Introduction

The surface plasmon resonance of metal nanoparticles can be excited at visible wavelengths with resonance frequencies ranging with the size, shape, composition, spatial distribution and dielectric environment of the particles [1; 2; 3; 4; 5; 6]. Surface plasmons and their apparent enhancement of local electric fields cause giant increases in the signal to noise ratios of excitation processes [7; 8], such as Raman scattering [9;10;11], fluorescence [12;13;14] and luminescence through multiphoton–absorption [15]. Surface plasmons also elicit nonlinear responses [16;17] with $\sim 10^7$-fold enhancement of picosecond-scale third-order nonlinear response near the plasmon resonance frequency [18 ; 19]. Harnessing the extraordinary optical properties of metal nanoparticles into optical devices and technologies has stimulated extensive research in materials science and optical engineering. Particular effort has been devoted to generating stable dispersions of metal nanoparticles in soft dielectric matrices, which can then be facilely processed into optical device configurations. To this end, metal nanoparticles have been incorporated in dendrimers [20;21], polymers [22;23;24;25;26;27;28], surfactants [29;30] and sol-gel derived materials [31;32;33;34;35;36]. Such metallodielectric systems hold promise for surface-enhanced spectroscopic techniques [37;38;39], optical sensing and imaging [40; 41; 42], photonics [43; 44; 45] and optical switching devices [16; 46; 47]. Despite considerable progress, it remains challenging to efficiently transform soft metallodielectric composites into functional optical devices.

Here we report a single-step, room temperature *self-inscription* route to cylindrical, multimode polymer waveguides that are dispersed with Ag nanoparticles. Waveguides are the most fundamental, passive components of integrated-optics and photonics systems. When doped with Ag or Au nanoparticles, waveguides can exhibit nonlinear photo-responses, which

have enabled their application as ultrafast optical switches [16;86;87]. For the latter, nanoparticles were introduced into an optical fiber through a modified chemical vapour deposition (CVD) process combined with solution doping. Our method relies on optical self-trapping of a continuous wave, visible laser beam in a soft organosiloxane photopolymer doped with Ag nanoparticles [48] and consequent spontaneous inscription of a cylindrical metallodielectric waveguide.

A beam self-traps in a photoresponsive medium when it induces refractive index changes in the form of a waveguide and becomes entrapped as an optical mode [49;50;51]. Self-trapping is described by the nonlinear differential equation [52]:

$$ik_0 n_0 \frac{\partial E}{\partial z} + \frac{1}{2}\nabla_{\perp}^{2} E + k_0^2 n_0 \Delta n E + \frac{i}{2} k_0 n_0 \alpha E = 0 \quad \textbf{3-1}$$

where E represents the electric field amplitude, α is the attenuation coefficient of the medium, n_0 is the refractive index in the medium before exposure to light, and k_0, the free space wave. **Equation 3-1** describes the dynamic competition between the natural diffraction of the beam ($\nabla_{\perp}^{2} = (\partial^2/\partial x^2) + (\partial^2/\partial y^2)$) and self-induced refractive index change Δn. We previously demonstrated and extensively characterized the dynamics of self-trapped beams in photopolymerisable methacrylate-substituted siloxanes [53;54;55;56]. Refractive index changes in this medium originate from beam-induced free-radical polymerization of methacrylate substituents. Because refractive index changes due to polymerization are irreversible, the cylindrical waveguide inscribed by the self-trapped beam remains permanently inscribed in the medium.

The objectives of this study were to (i) demonstrate for the first time that nonlinear forms of light propagation, specifically self-trapping, can be elicited in a medium containing a dispersion of metal nanoparticles. The plasmon resonance of Ag nanoparticles employed in our study coincided with the excitation wavelength (532 nm) of the self-trapped beam [48] and this motivated the second objective of our work, which was (ii) to exploit this entirely new opportunity to examine the interactions between the self-trapped (and therefore extremely intense) optical field and resonant metal nanoparticles. Specifically, we examined the influence of the metal nanoparticles on the dynamics of self-trapping, including the modal evolution of the self-trapped beam. Because they originate from irreversible polymerization reactions, photoinduced refractive index changes are permanently inscribed in the medium [56]. Our final objective was (iii) the optical and structural characterization of the self-induced cylindrical waveguide in the medium and specifically, examination of the distribution of Ag nanoparticles in the waveguide. The self-induction of a metallodielectric cylindrical waveguide in a single, room temperature step would contrast sharply with previous metallodielectric waveguides, which have comparable metal content but must be fabricated through CVD processes [47].

3.2 Experimental

3.2.1 Preparation of organosiloxane sols doped with Ag nanoparticles

Organosiloxane sols were prepared based on a previously described method [48]. Sols were made through hydrolysis and condensation of 3-methacryloxypropyl trimethoxysilane (0.020 mol). The reaction was catalyzed with H_2O (0.0150 mol) acidified with HCl (0.0135 mmol). The majority of Cl^- ions in the resulting sol was precipitated by adding $AgNO_3$

solution (0.0100 mmol). The resulting AgCl precipitate was filtered out through a polytetrafluoroethylene (PTFE) membrane (0.2 μm pore size) resulting in residual $[Cl^-] = 7\times10^{-4}$ M. Various amounts of $AgNO_3$ solution were then added to prepare a series of sols with [AgCl] of $\sim7\times10^{-4}$ M and $[AgNO_3]$ of 1 mM and 2 mM, 4 mM, 6 mM and 8 mM. Because $[Ag^+][Cl^-]\sim10^{-6}$ in the sol is >> than the solubility product, $K_{sp} = [Ag^+][Cl^-]=1.77\times10^{-10}$ [57], AgCl existed as insoluble grains in the sol. Formation of larger AgCl particles was inhibited as the low saturation of AgCl increases the free energy barrier for crystal nucleation. Sols therefore remained stable and transparent for up to 2 days.

Ag nanoparticles in the organosiloxane sols were generated through photoreduction of AgCl grains to elemental Ag. Upon 1 hour of irradiation with a 23 W fluorescent light (Noma® mini spiral bulbs), the colourless sol turned dark brown. Formation of Ag nanoparticles was confirmed through absorption spectra (acquired with a Cary 50 Bio UV-Visible spectrometer), which contained an absorption band at ~ 437 nm (Figure 3.1a) characteristic of the dipolar SPRs of Ag nanoparticles [48]. Transmission electron microscopy (carried out with a Philips CM12 microscope) confirmed the presence of Ag nanoparticles with an average diameter of 20±11 nm in the sol (Figure 3.1b, c).

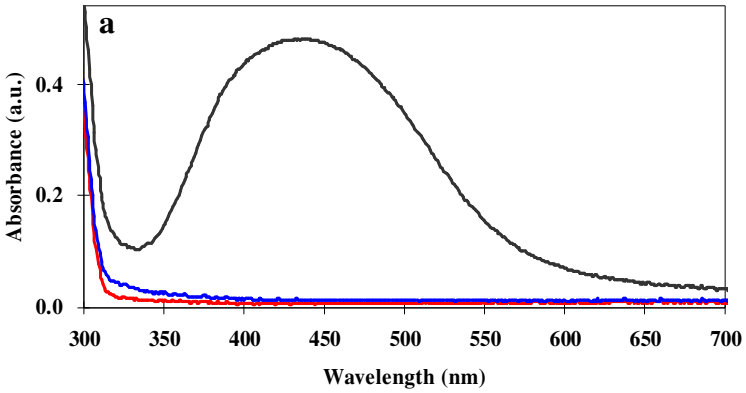
a
Absorbance (a.u.)
0.4
0.2
0.0
300
350
400
450
500
550
600
650
700
Wavelength (nm)

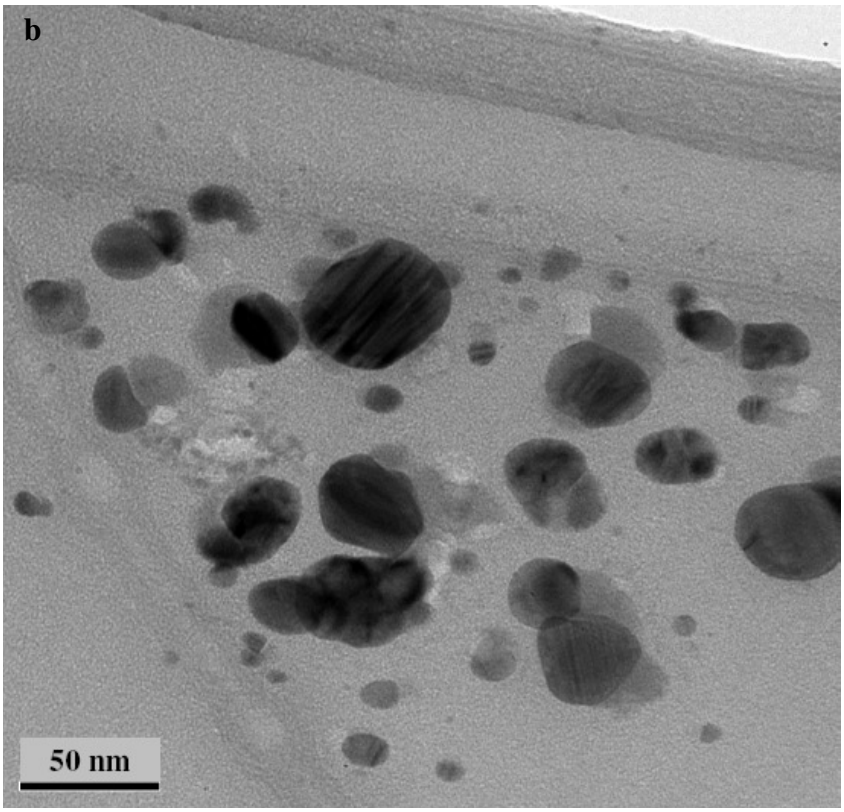
b
50 nm

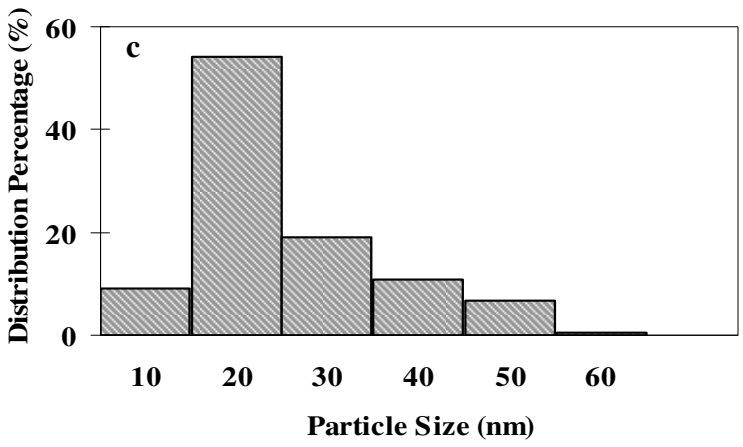

Figure 3.1 (a) Absorption spectra of organosiloxane sol that was undoped (red line) and doped with ~ 5 × 10^{-3} M Ag(I) (4 × 10^{-3} M $AgNO_3$ and 7 × 10^{-4} mM AgCl) before (blue line) and after (black line) irradiation with a 23 W fluorescent light. (b) TEM of Ag nanoparticles in the sol and (c) histogram of their size distribution (population analysed: 196 particles).

3.2.2 Preparation of samples for optical self-trapping

Prior to self-trapping experiments, 0.5 wt.% of the free-radical photo-initiator (bis(η^5cyclopentandienyl) bis(2,6-difluoro-3-(1H-pyrrol-yl)-phenyl) titanium(IV) (λ_{max} = 393 nm, 460 nm, Ciba Specialty Chemicals Inc., Canada) was added to the Ag nanoparticle-doped organosiloxane sol. The photoinitiator was first dissolved in organosiloxane sol that did not contain Ag nanoparticles and then mixed at a 1:1 volume ratio with the Ag-doped sols. The resulting sols had a total concentration [$Ag(I)_{initial}$] = 0.8 mM, 1 mM, 2 mM, 3 mM and 4 mM. The photosensitised sol was injected through a small perforation into a cylindrical cell (outer diameter = 16 mm, pathlength = 6 mm), which had two optically flat and transparent windows. The sample was uniformly irradiated with white light emitted by a quartz-tungsten-halogen lamp (400 nm - 740 nm, ~ 4 min at 8 mW· cm^{-2}) to induce partial

polymerization of methacrylate groups, which transformed the sol into a transparent brownish-orange gel.

3.2.3 Optical assembly

Self-trapping experiments were carried out on a previously described optical assembly (**Appendix I**) [56]. The excitation source was the TEM_{00} mode (Gaussian beam, M2 < 1.1) of continuous wave, visible (532 nm) light emitted by a diode-pumped solid-state laser (Verdi V5 Coherent, Inc., CA, USA). The output beam had a diameter and power of 2.25 mm and 100 mW, respectively. The beam was passed through half-wave plate, quarter-wave plate, a neutral density filter and polarizing beam splitter cubes; wave plate orientations were adjusted to obtain the desired intensity for experiments. The attenuated beam was steered by a pair of 45° elliptical mirrors onto a planoconvex lens (f.l. = 75.6 mm), which focused it to a diameter of 20 μm onto the entrance window of the cell containing the photopolymer.

The cross-sectional (x, y) intensity profile of the beam at the exit face of the cell was imaged by a pair of planoconvex lenses (f.l. = 100 mm and f.l. = 300 mm) onto a high-resolution charge-coupled device (CCD) camera (736(H) x 484(V) pixels, pixel size 4.80 μm (H) x 5.58 μm (V); LaserCam IIID 1/4", Coherent Inc, CA, USA). The camera was driven by the BeamView® Analyzer software (Version 3.2), which calculates beam diameter ($1/e^2$) [58], relative peak intensity [59], generates 2-D and 3-D intensity profiles and compensates for image magnification by the lenses (x 2.96). Combinations of neutral density filters (F) mounted on three separate rotatable wheels (VARM, Coherent Inc.) were placed between imaging lenses to prevent saturation of the CCD camera. All imaging optical components were mounted on carriers that could be translated along z with a resolution of 0.25 mm.

3.2.4 Characterisation of self-induced waveguide doped with Ag nanoparticles

Transmission optical micrographs of self-induced waveguides were acquired on an Olympus BX51 microscope. Focused ion beam(FIB) combined with field emission scanning electron microscopy (SEM) and energy-dispersive X-ray(EDX) spectroscopy of samples was carried out on a Zeiss NV 40 microscope that was equipped with an INCAx-act EDX spectrometer (Oxford Instruments). Transmission spectra of self-induced waveguides were acquired with an Ocean Optics portable spectrometer using a previously described method [54].

3.3 Results and discussion

3.3.1 Experimental evidence of self-trapping in an organosiloxane doped with Ag nanoparticles

We elicited self-trapping and self-induced waveguide formation with a continuous wave, visible laser beam (532 nm, 1.6 $\times 10^{-2}$ Wcm^{-2}) in an organosiloxane photopolymer doped with Ag nanoparticles ($[Ag(I)_{initial}]$ = 2 mM). In a typical experiment, the beam was focused to 20 μm onto the entrance face (z = 0.0 mm) of the transparent cell containing the photopolymer. Under linear conditions (in the absence of polymerization), the beam broadened through natural diffraction from 20 μm at the entrance face (z = 0.0 mm) to 88 μm at the exit face of the medium (z = 6.0 mm). However, the spatial intensity profile of the beam at z = 6.00 mm underwent a striking sequence of changes as it initiated free-radical polymerization and corresponding refractive index changes along its propagation path. Typical

results presented in **Figure 3.2** show that within 35 s, the beam narrowed into a tightly focused spot with a diameter 21 μm and a corresponding increase in relative peak intensity [59] from 1 % to 37 %. The beam-width now corresponded to its input width at z = 0.0 mm, confirming that it self-trapped and propagated without broadening through the medium.

a

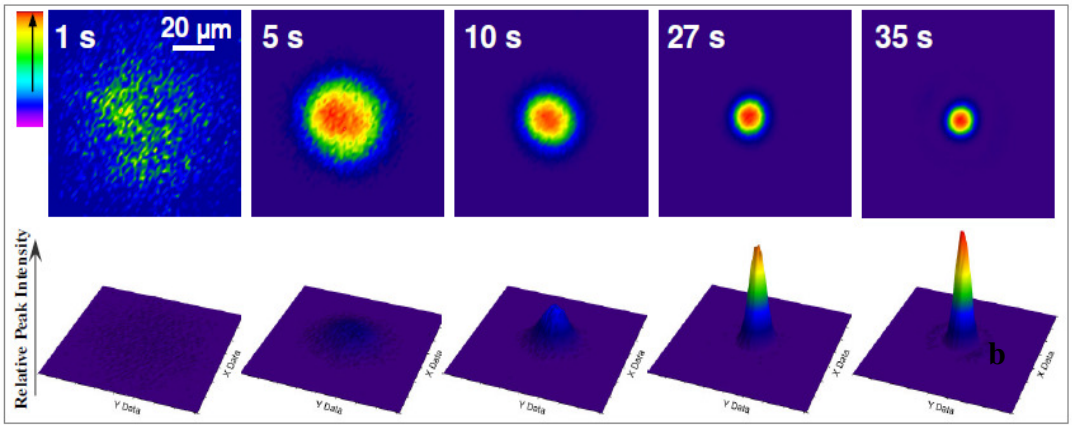

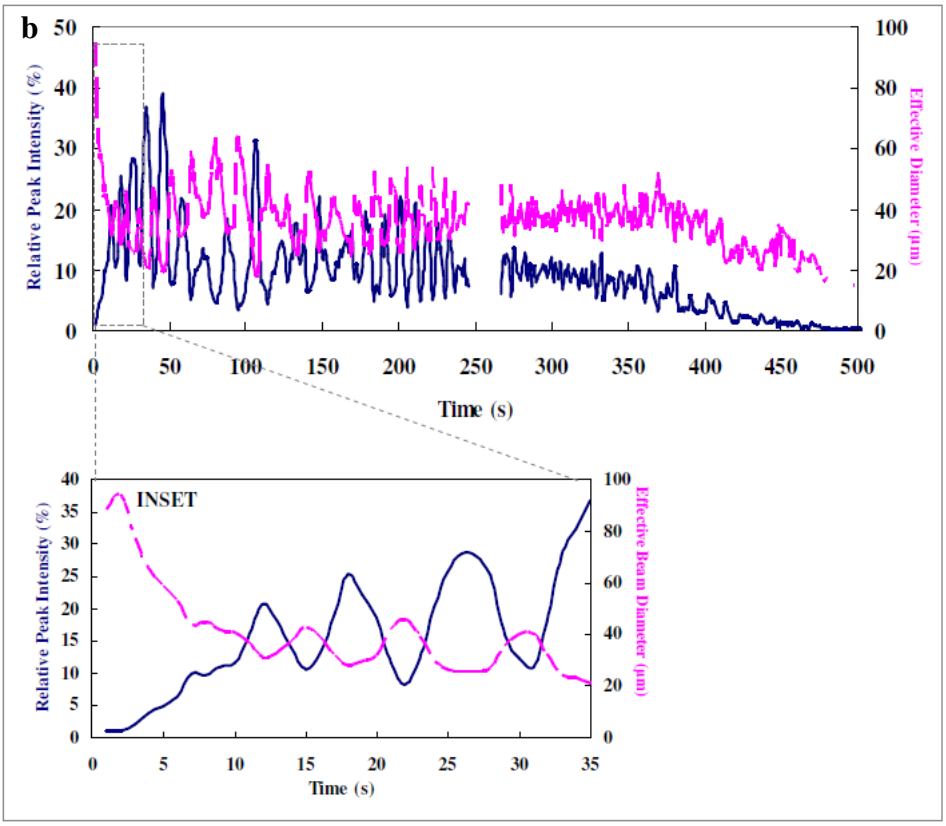

Figure 3.2 (a) 2-D (top) and 3-D (bottom) intensity profiles of a Gaussian laser beam (532 nm) at the exit face (z = 6.0 mm) of an organosiloxane doped with Ag nanoparticles ($[Ag(I)_{initial}]$ = 2 mM). (b) Plots of temporal relative peak intensity [59] (solid blue lines) and effective beam diameter [58] (dashed pink lines). Incident laser intensity = 1.6×10^{-2} W/cm^2. (A neutral density filter with optical density of 0.1 was placed before the CCD camera.)

3.3.2 Oscillations and multimode guidance of the self-trapped beam

Figure 3.2b contains temporal plots of the effective width and relative peak intensity, which trace the dynamics of the self-trapped beam over long times (500 s). The plots show that once self-trapped, the beam exhibited complementary oscillations in width and intensity. The aperiodic oscillations

were significant in amplitude, increased in frequency with time and persisted over ~280 s. From ~300 s, there was a gradual decrease in the relative peak intensity of the beam until it became negligible at 476 s. During this time, the beam remained self-trapped and did not revert to its initial, diffracted form. Attenuation is probably caused by polymerization-induced phase separation in the medium [53].

Strong oscillations of the self-trapped beam (**Figure 3.2 b**) were caused by the sequential excitation of high order modes in its self-induced waveguide. Analysis of its 2-D spatial intensity profiles showed that the self-trapped beam evolved rapidly from single-mode to multimode guidance: at early times (> 35 s), the self-trapped beam propagated only as the fundamental mode (LP_{01}) of its waveguide (**Figure 3.3**). Because the maximum refractive index change of the organosiloxane is relatively large (0.006) [56], the beam continued to initiate polymerization even when propagating as a guided mode in the self-induced waveguide. Consequent changes in the refractive index led to a non-trivial spatial and temporal variation in the modal composition of the self-induced waveguide (*vide infra*). At the detection plane, z = 6.00 mm, this was evidenced by the sequential appearance of high order, linearly polarized (LP) modes including LP_{11}, LP_{12}, LP_{21} and LP_{31} (**Figure 3.3**). Their striking spatial profiles were characteristic of those supported by circular waveguides such as optical fibers [60]. In addition to pure high order modes, superposed modes such as (LP_{01}+LP_{21}, LP_{01}+LP_{11}, LP_{02}+LP_{11}) were detected. Changes in the beam profiles were sufficiently slow that even intermediate profiles of transitions between modes could also be observed (**Figure 3.3 b**). As shown in **Figure 3.3 a**, the oscillations in intensity and width of the self-trapped beam are directly correlated with the excitation of multiple modes. For example, the characteristically circular and tightly focused profile of LP_{01} was observed as

a peak (valley) in relative intensity (width) while the more complex profiles of high-order modes, resulted in a smaller peak intensity and greater effective width. At relatively long times (230 s), the number of high order modes became too large and the superposed intensity profiles too complex that it was no longer possible to deconvolute the modal profile into its individual components.

Our experiment provides the extremely rare experimental opportunity to individually visualize high order guided modes as a self-trapped beam evolves from fundamental to multimode guidance. We previously detected multiple modes during self-trapping in an organosiloxane photopolymer that was not doped with Ag nanoparticles [56]. The mechanism of multimode excitation during self-trapping, which is based on detailed experimental studies and comparisons with theoretical models [52] is detailed elsewhere [56]. A brief outline is provided here: the beam initially self-traps by inducing a cylindrical waveguide that supports only the fundamental optical mode. This is observed in the early times of self-trapping where only the circular profile of the fundamental mode (LP_{01}) is observed. The guided beam continues to induce polymerization reactions within the confines of the waveguide and further increases the refractive index of the waveguide, which in turn transforms from single mode to multimode guidance. This is consistent with the appearance of increasingly high-order modes with time (**Figure 3.3**). However, changes in refractive index, which are dependent on optical intensity, are not uniform throughout the waveguide. Instead, they vary in a non-monotonic way along the path-length of the beam and in time. As a result, the propagation constants of each mode as well as the number and type of modes excited at any particular point along the waveguide changes over time. Results in **Figure 3.3** show the evolution of the modal structure of the self-induced waveguide at a single point (z = 6.00 mm) along

the propagation direction. At longer times as the refractive index change approach saturation, multiple modes are simultaneously supported by the waveguide and it no longer is possible to resolve individual modes.

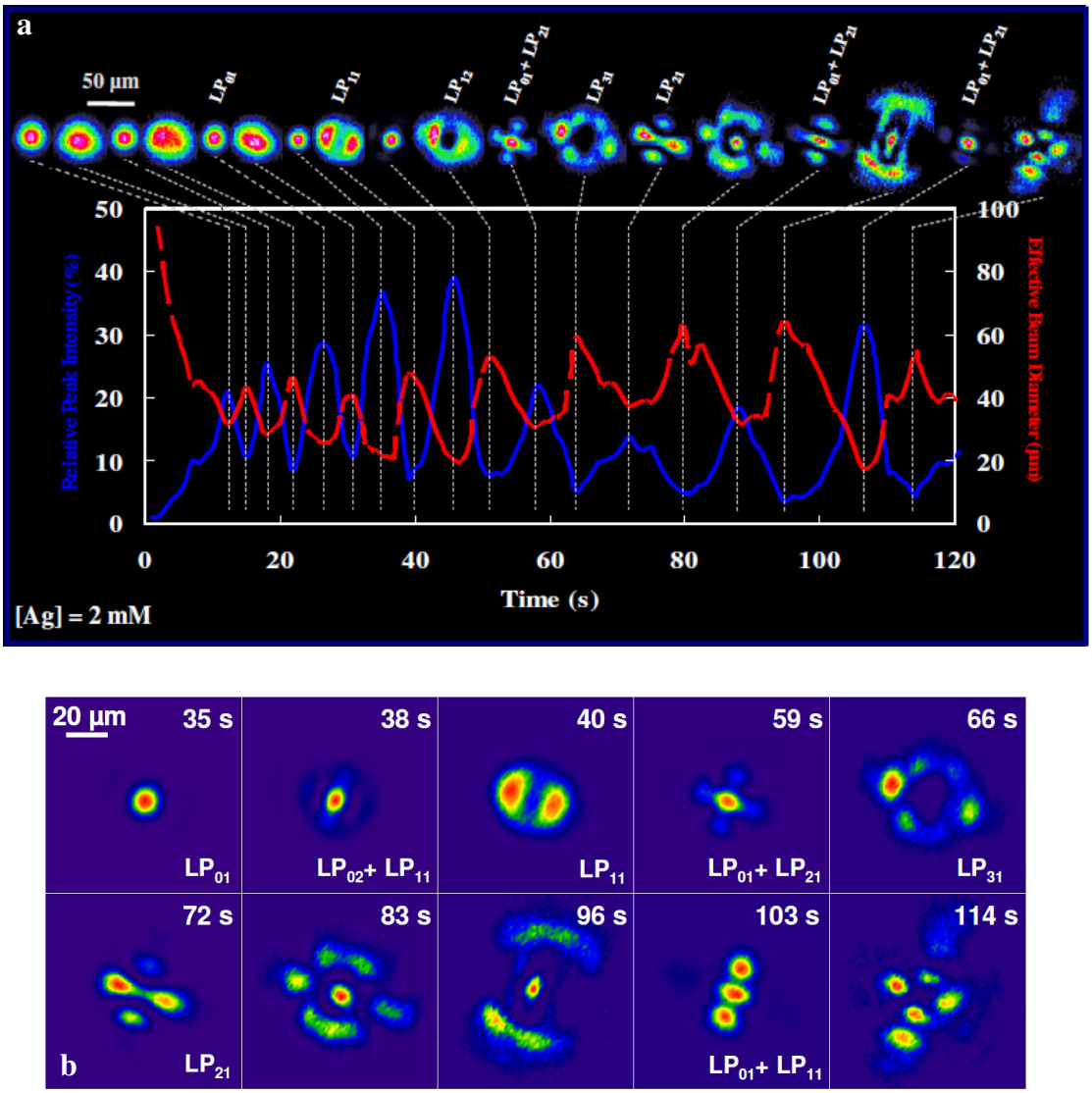

Figure 3.3 (a) Temporal plots of relative peak intensity (solid blue lines) and effective beam diameter (dashed red lines), and corresponding evolution of 2-D spatial intensity profiles of the beam at z = 6.0 mm within time period of 0~120 s; (b) Magnified images of the 2-D spatial intensity profiles showing clearly the evolution of various modes during optical self-trapping. Laser incident intensity = 1.6×10^{-2} W/cm^2; $[Ag(I)_{initial}] = 2 \times 10^{-3}$ M. (A neutral density filter with optical density of 0.1 was placed before the CCD camera).

3.3.3 Characterization of Ag nanoparticle-doped self-induced waveguide

Our experimental results and analyses demonstrate that the continuous wave, 532 nm laser beam self-traps in a photopolymer doped with Ag nanoparticles. Furthermore, the self-trapped beam exhibited the same multimode dynamics that characterizes its behavior in the undoped photopolymer. Critically, this confirms that Ag nanoparticles in the organosiloxane neither inhibited the self-trapping process nor completely attenuated the propagation of the self-trapped beam through the medium.

As previously described, self-trapping occurs when the beam inscribes a cylindrical waveguide and becomes entrapped as a guided mode. Because refractive index changes due to polymerisation in the organosiloxane are irreversible, this self-induced waveguide remained permanently imprinted in the medium. We first characterized the structure of the waveguide (formed after at least 245 s of self-trapping) and then confirmed that it contained a dispersion of Ag nanoparticles. Optical microscopy of the waveguide's longitudinal cross-section (along z) revealed a 6 mm-long cylindrical structure with diameter = 27 ± 2 μm (**Figure 3.4**). The transmission micrograph of its transverse cross-section ((x,y) plane) showed that the waveguide trapped and guided the microscope probe beam within a core area of 30 ± 1 μm in diameter.

The presence of Ag nanoparticles within the self-induced waveguide was confirmed through transmission optical spectroscopy [61], focused ion beam combined with field emission scanning electron microscopy (FIB/SEM) and energy-dispersive X-ray (EDX) spectroscopy. To acquire transmission spectra of the waveguide, white light from a quartz-tungsten-halogen lamp (400 nm - 740 nm) was coupled into and allowed to propagate through the 6 mm path-length of the waveguide; light at the output was focused into a

spectrometer. Spectra acquired under identical conditions of self-induced waveguides with and without Ag nanoparticles are presented in **Figure 3.4b**. The negligible transmission from 400 nm to 500 nm in both samples is due to the absorption of the residual photoinitiator (λ_{max} = 393 nm, 460 nm). However, in the Ag-doped waveguide, transmission remains negligible until 530 nm. This can be attributed to absorption due to the plasmon resonance band of Ag nanoparticles, which in the sol maximizes at 437 nm and spans from 366 nm to 524 nm (**Figure 3.1**). Transmission in the Ag-doped waveguide was in general significantly smaller than that of the undoped sample.

We directly observed Ag nanoparticles in the waveguide through FIB combined with SEM. The waveguide was etched with the focused ion beam to expose a transverse cross-section of the structure. The cross-section was then imaged by SEM, which revealed Ag particles as bright circular features, which were distributed throughout the cross-section. EDX spectroscopy carried out on the bright features confirmed them as elemental Ag (**Figure 3.4d**).

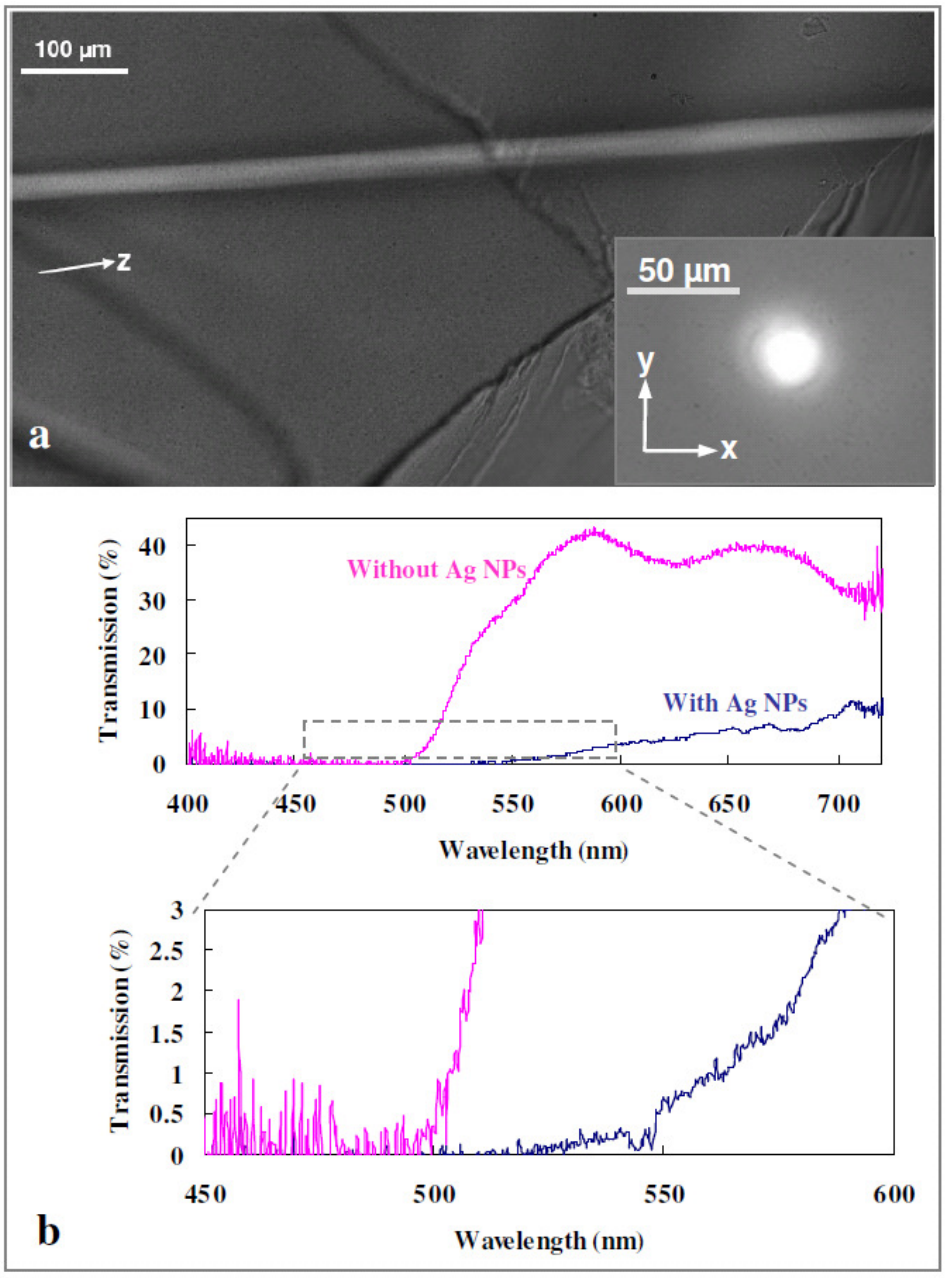
100 µm
z
50 µm
y
x
a
Without Ag NPs
With Ag NPs
Transmission (%)
Wavelength (nm)
b

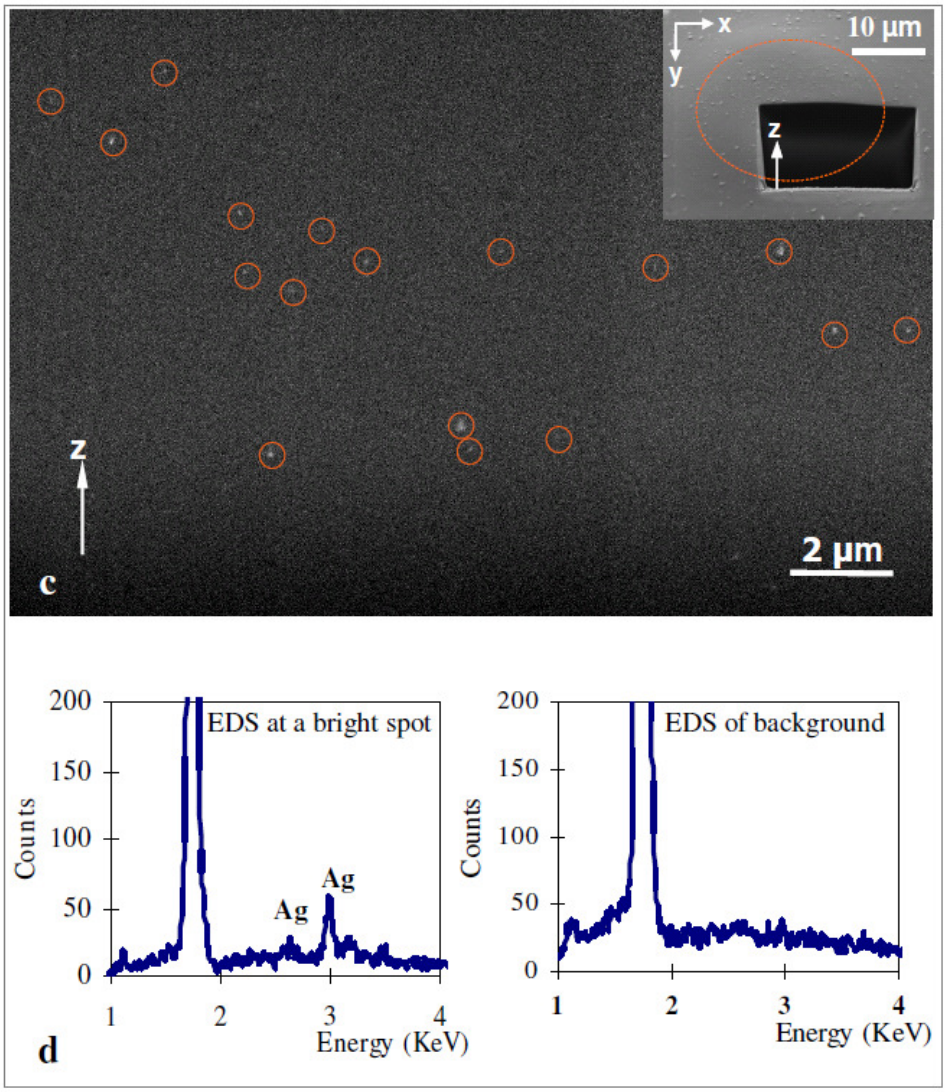

Figure 3.4 Characterisation of the self-induced metallodielectric waveguide. (a) Optical micrograph of the longitudinal cross-section (*z*) showed the cylindrical waveguide with a diameter of 27 ± 2 µm propagating through the sample. Inset: optical micrograph obtained in transmission mode at the exit face ((x, y) plane) of the waveguide showed that the microscope probe beam was confined within a core diameter of 30 ± 1µm. (b) Visible light transmission spectra of the Ag-doped (blue) and undoped (pink) waveguides. (c) FIB etching into the waveguide core followed by SEM revealed a dispersion of Ag nanoparticles (encircled in dashed red). Inset: SEM showing the FIB etched region of the self-induced waveguide; the dashed red circle traces the circular profile of the waveguide, which is only faintly visible. (d) Energy Dispersive X-ray (EDX) spectra confirmed that the bright features

(encircled in dashed red (c)) contained Ag content; no Ag content was detected in the surrounding area.

3.3.4 Effect of Ag nanoparticle doping concentration on optical self-trapping

We observed self-trapping of the 532 nm laser beam (1.6×10^{-2} Wcm^{-2}) in photopolymers with $[Ag(I)_{initial}]$ = 0.8 mM, 1 mM, 2 mM and 3 mM. In all cases, the diameter of the beam at z = 6.00 mm narrowed to approximately its input width at z = 0.00 mm with at least a 24-fold increase in intensity. To quantitatively compare self-trapping in the different materials, we calculated the maximum self-trapping efficiency, which is the ratio between the highest peak intensity and initial peak intensity [59], and self-trapped beam widths [58]. Results summarized in **Table 3-1** show that with the exception of the sample with $[Ag(I)_{intial}]$ = 3.0 mM, the diameter of the self-trapped beam in all samples was statistically identical. The efficiency in samples with $[Ag\ (I)_{initial}]$ = 0.8 mM, 1 mM and 2 mM was also statistically identical. However, relative to the undoped sample, the self-trapping efficiency decreased by approximately 41% in the presence of Ag nanoparticles. The excitation wavelength in our experiment, 532 nm, falls within the plasmon resonance band of the Ag nanoparticles (**Figure 3.1a**). The relative decrease in self-trapping efficiency, which measures the fold-increase in intensity, is due to the consequent absorption of the self-trapped beam caused by plasmon resonance excitation of the Ag nanoparticles (**Figure 3.4b**). Despite this attenuation, the beam still self-trapped efficiently in these three different samples. There was a critical change in self-trapping behavior when $[Ag(I)_{initial}]$ in the organosiloxane was increased to 3 mM. In this sample, there was a significant decrease in self-trapping efficiency (50 %) and a corresponding increase in the self-trapped beam width (28 ± 7 μm). Both

indicate that absorption of the propagating beam significantly decreased the rate of polymerization and in turn, the extent of narrowing of the beam. It is however important to note that even at these values, there is self-trapping of the beam with substantial increase in intensity and decrease in width relative to its initial profile at z = 6.0 mm.

Table 3-1 Summary of maximum self-trapping efficiency (ratio between the greatest peak intensity and the initial peak intensity), corresponding irradiation time and effective beam diameter at the maximum self-trapping efficiency in samples with different $[Ag(I)_{initial}]^{\alpha}$

pathlength	6 mm				
Ag doping concentration	0 mM	0.8 mM	1 mM	1 mM	3 mM
Maximum self-trapping efficiency	83±36	52±31	46±19	49±29	24±17
Eff. Beam diameter at maximum efficiency (μm)	14±4	17±4	16±3	15±4	28±7

$^{\alpha}$Results are averages of a minimum of 5 and maximum of 20 repeat experiments.

The self-trapped beam exhibited oscillations due to multimode excitation in all Ag-doped photopolymers. Temporal plots of relative intensity and width of the self-trapped beam in photopolymers with $[Ag(I)_{initial}]$ = 0.8 mM, 1mM, 3 mM and 2 mM are presented in **Figure 3.5** and **Figure 3.3a**, respectively; corresponding 2-D spatial intensity profiles of fundamental and high-order modes are included. Although modes were visible in the sample with $[Ag(I)_{initial}]$ = 3 mM, they appeared distorted and couldn't be easily resolved. This can be attributed to the scattering of light by the Ag nanoparticles in this sample, which is consistent with its relatively inefficient self-trapping behavior discussed above.

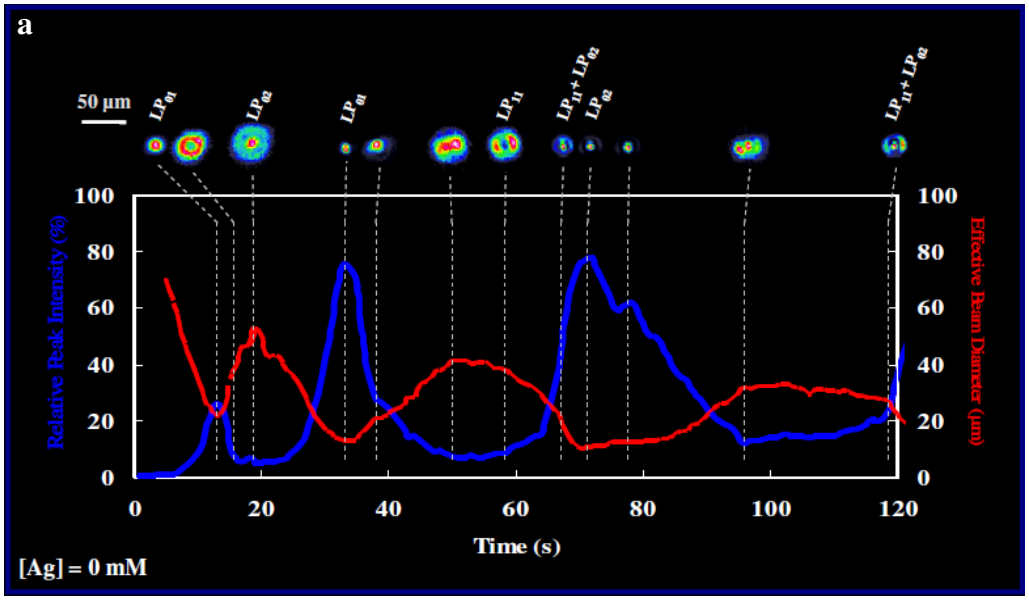
a
50 μm
LP01
LP02
LP03
LP11
LP11+LP02
LP12
LP11+LP03
Relative Peak Intensity (%)
Effective Beam Diameter (μm)
Time (s)
[Ag] = 0 mM

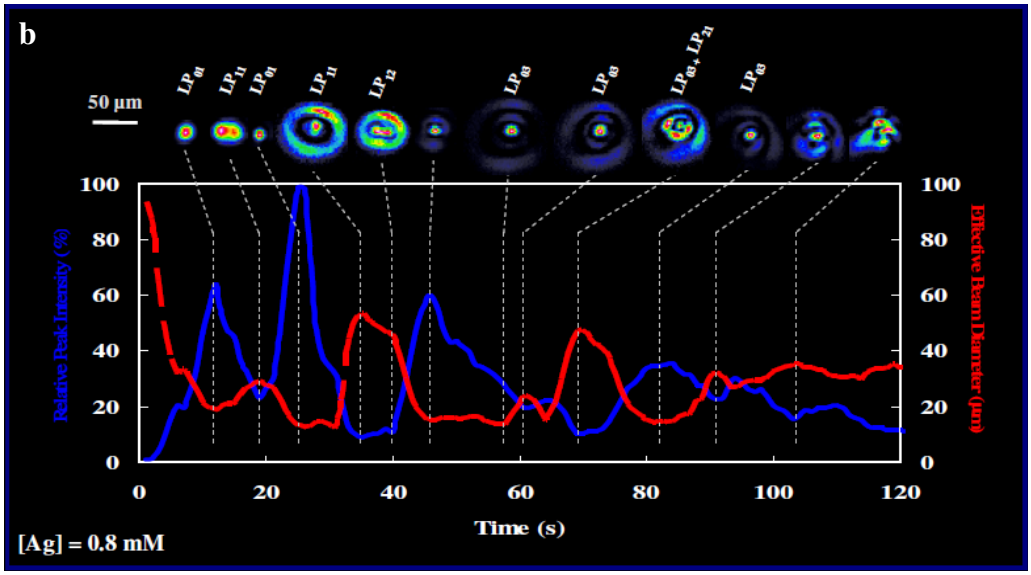
b
50 μm
LP01
LP11
LP02
LP11
LP12
LP03
LP03
LP03+LP21
LP13
Relative Peak Intensity (%)
Effective Beam Diameter (μm)
Time (s)
[Ag] = 0.8 mM

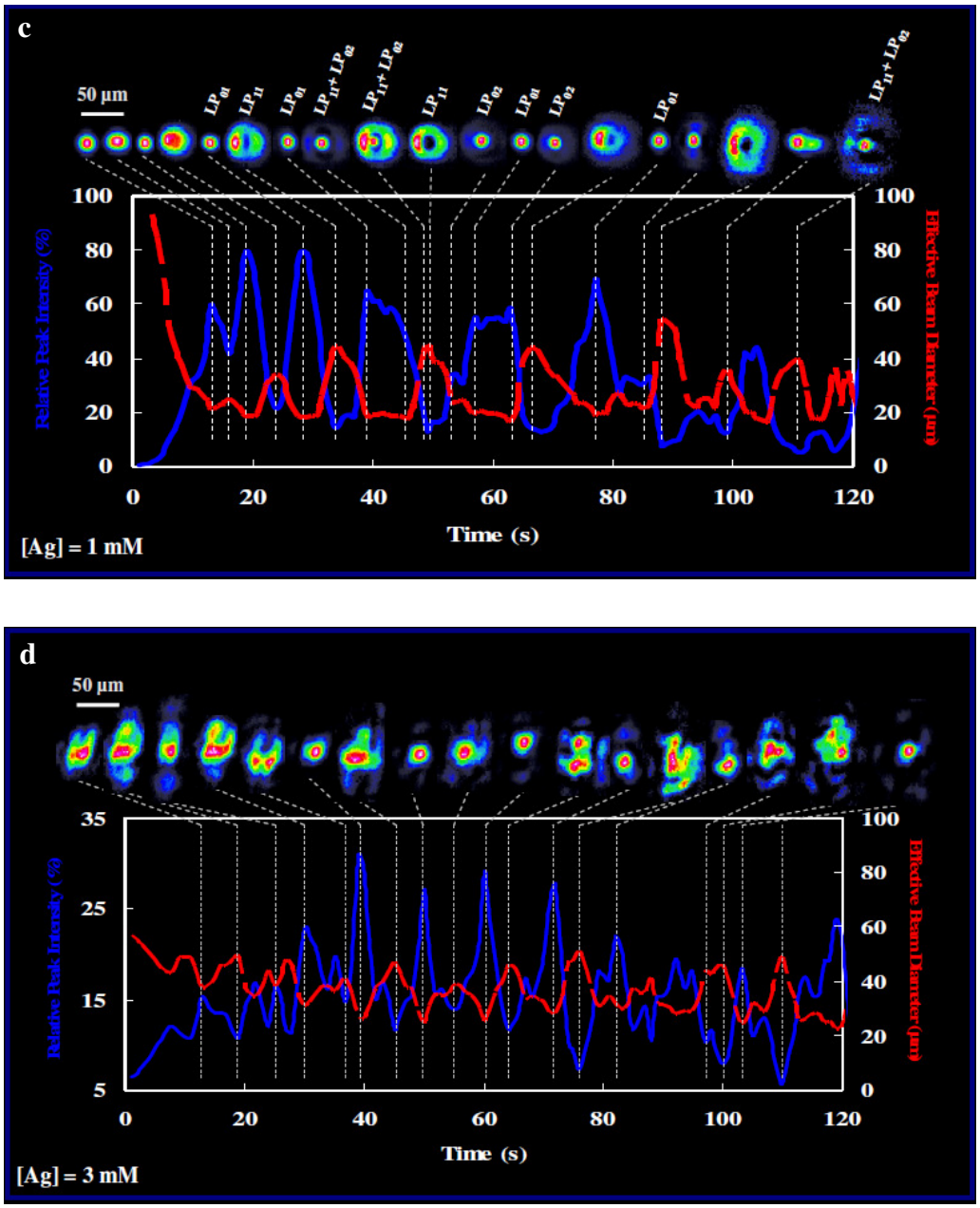

Figure 3.5 Temporal plots of relative peak intensity (%) (solid blue lines) and effective beam width (dashed red lines) and corresponding evolution of 2-D spatial intensity profiles of the self-trapped beam at z = 6.0 mm in (a) organosiloxane ($[Ag(I)_{initial}]$ = 0.0 mM) and (b-d) Ag-doped organosiloxane ($[Ag(I)_{initial}]$ = 0.8 mM, 1 mM, and 3 mM, respectively). Incident intensity = 1.6×10^{-2} W/cm^2. (Neutral density filters with optical density = 0.01, 0.035, 0.1, 1 were placed before the CCD camera for $[Ag(I)_{initial}]$ = 0.0 mM, 0.8 mM, 1 mM and 3 mM, respectively).

Comparison of the plots of all other photopolymer shows differences in the oscillatory behavior and types of high order modes that are excited in the self-trapped beam. In the undoped photopolymer and the photopolymer with $[Ag(I)_{initial}]$ = 0.8 mM, the frequency of the oscillations appears to be relatively small while higher order modes (e.g. LP_{02}, LP_{11}) were observed at early times (< 20 s). With increasing concentrations of $[Ag(I)_{initial}]$, the oscillatory frequency appeared to increase. In these materials (for example, the photopolymer with $[Ag(I)_{initial}]$ = 2.0 mM), the onset of high order modes was considerably more sequential in terms of the order of the modes; at early times, the fundamental mode LP_{01} was followed by LP_{11} at 40 s. Transitions between the modes were well resolved and the highest order mode observed was LP_{31}.

In the undoped photopolymer as well as samples with low concentrations of Ag nanoparticles, there is relatively little attenuation of the self-trapped beam. The rate of refractive index changes, which are directly proportional to the intensity of the optical field, therefore is relatively high. Once self-trapped in its cylindrical waveguide, the beam continues to rapidly induce refractive index changes. Its large refractive index in turn enables the waveguide to support the very high order modes observed in **Figure 3.5** [62]. At the same time, the fast evolution of its refractive index profile causes rapid changes in the modal profile of the waveguide. In this case, the sequential excitation of modes occurs too rapidly to be individually resolved. This results in the seemingly slow oscillations observed in **Figure 3.5**.

The modal evolution is better resolved at increasing concentrations of Ag nanoparticles (e.g. **Figure 3.3a** and **Figure 3.5c**). Here, the self-trapped beam suffers significant absorbance due to surface plasmon excitation. The rate of refractive index changes induced by the attenuated beam is smaller. Changes in the refractive index and modal profiles of the waveguide occur

more gradually allowing better resolution of the modal evolution of the waveguide. The current findings are consistent with our previous study of self-trapping in the undoped photopolymer [56]. We found that at small incident intensities, there was a relatively slow evolution of the refractive index profile and consequently, the modal composition of a self-trapped beam. This resulted in well-resolved oscillations of the beam and a clear sequential progression of high order modes. At greater intensities, the rapid changes in the refractive index of the waveguide led to broad, low frequency oscillations. These in fact were due to the overlap of fast oscillations caused by rapid changes in the modal profile of the waveguide.

3.4 Summary and outlook

A continuous wave, visible laser beam self-traps and permanently inscribes a metallodielectric cylindrical multimode waveguide in a Ag-nanoparticle doped organosiloxane photopolymer. The self-trapped beam exhibits multimode dynamics and evolves from single-mode to multimode guidance with increasing time. Self-trapping was achieved in photopolymers with $[Ag(I)_{initial}]$ ranging from 0.8 mM to 3 mM although a significant decrease in the efficiency of the process was observed at the greatest $[Ag(I)_{initial}]$ value. Differences in the modal evolution of the self-trapped beams in samples with varying values of $[Ag(I)_{initial}]$ were attributed to changes in the intensity of the self-trapped beam due to surface plasmon resonance.

Our findings identify a direct, room temperature, soft polymer route to self-induced metallodielectric waveguides in a soft photopolymer. This approach stands in contrast with the CVD-based routes that have been previously employed to generate metallodielectric waveguides. Based on absorbance due to the plasmon resonance of the metal nanoparticles, the

concentration of Ag nanoparticles in the polymer system appears comparable to that in the CVD-based systems [47]. This suggests that our waveguides could exhibit similar nonlinear optical responses. Furthermore, because the polymer waveguides result are induced by self-trapped beams, more complex metallodielectric waveguide architectures could be generated by exploiting other nonlinear forms of light propagation phenomena such as the pairwise interactions of self-trapped beams [63] or the interactions between large populations of self-trapped filaments, which lead to the spontaneous formation of 3-D waveguide lattices [64]. These studies are underway.

3.5 Acknowledgements

Funding from the Natural Sciences and Engineering Research Council, Canadian Foundation for Innovation, Ontario Institute of Technology and McMaster University is gratefully acknowledged. We thank CIBA GEIGY, Canada for generous donation of the photoinitiator IRGACURE-784®.

---

1. S. Link and M. A. El-Sayed, "Size and temperature dependence of the Plasmon absorption of colloidal gold nanoparticles," J. Phys. Chem. B **103**, 4212-4217 (1999).

2. C. Noguez, "Surface plasmons on metal nanoparticles: The influence of shape and physical environment," J. Phys. Chem. C **111**, 3806-3819 (2007).

3. M.-C. Daniel and D. Astruc, "Gold Nanoparticles: Assembly, supramolecular chemistry, quantum-size-related properties, and applications toward biology, catalysis, and nanotechnology," Chem. Rev. **104**, 293-346 (2004).

4. K. L. Kelly, E. Coronado, L. L. Zhao, and G. C. Schatz, "The Optical Properties of Metal Nanoparticles: The Influence of Size, Shape, and Dielectric Environment," J. Phys. Chem. B **107**, 668-677 (2003).

5. A. Moores and F. Goettmann, "The plasmon band in noble metal nanoparticles: an introduction to theory and applications," New. J. Chem. **30**, 1121-1132 (2006).

6. L. M. Liz-Marzán, "Nanometals formation and color," Materials Today **7**(2), 26-31 (2004).

7. M. Rycenga, C. M. Cobley, J. Zeng, W. Li, C. H. Moran, Q. Zhang, D. Qin, and Y. Xia, "Controlling the synthesis and assembly of silver nanostructures for plasmonic applications," Chem. Rev. **111**(6), 3669-3712 (2011).

8. V. Giannini, A. I. Fernández-Domínguez, S. C. Heck, and S. A. Maier, "Plasmonic nanoantennas: fundamentals and their use in controlling the radiative properties of nanoemitters," Chem. Rev. **111**(6), 3888-3912 (2011).

9. M. Moskovits, "Surface-enhanced spectroscopy," Rev. Mod. Phys. **57**(3), 783-826 (1985).

10. M. Moskovits, "Surface-enhanced Raman spectroscopy: a brief retrospective," J. Raman Spectrosc. **36**(6-7), 485-496 (2005).

11. E. C. L. Ru and P. G. Etchegoin, "Rigorous justification of the $|E|^4$ enhancement factor in Surface Enhanced Raman Spectroscopy," Chem. Phys. Lett. **423**(1-3), 63-66 (2006).

12. F. Tam, G. P. Goodrich, B. R. Johnson, and N. J. Halas, "Plasmonic enhancement of molecular fluorescence," Nano Lett. **7**(2), 496-501 (2007).

13. J.-W. Liaw, J.-H. Chen, C.-S. Chen, and M.-K. Kuo, "Purcell effect of nanoshell dimer on single molecule's fluorescence," Opt. Exp. **17**(16), 13532-13540 (2009).

14. A. Kinkhabwala, Z. Yu, S. Fan, Y. Avlasevich, K. Müllen, and W. E. Moerner, "Large single-molecule fluorescence enhancements produced by a bowtie nanoantenna," Nat. Photonics **3**, 654-657 (2009).

15. R. A. Farrer, F. L. Butterfield, V. W. Chen, and J. T. Fourkas, "Highly efficient multiphoton-abosorption-induced luminescence from gold nanoparticles," Nano Lett. **5**(6), 1139-1142 (2005).

16. A. Lin, X. Liu, P. R. Watekar, Y. Chung, and W.-T. Han, "Ag nanocrystal-incorporated germano-silicate optical fiber with high resonant nonlinearity," App. Phys. Lett. **93**, 021901 (2008).

17. D. C. Hutchings, M. Sheik-Bahae, D. J. Hagan, and E. W. V. Stryland, "Kramers-Krönig relations in nonlinear optics," Optical and Quantum Electronics **24**(1), 1-30 (1992).

18. F. Hache, D. Ricard, and C. Flytzanis, "Optical nonlinearities of small metal particles: surface-mediated resonance and quantum size effects," J. Opt. Soc. Am. B **3**(12), 1647-1655 (1986).

19. R. F. Haglund, Jr., L. Yang, R. H. Magruder III, J. E. Wittig, K. Becker, and R. A. Zuhr, "Picosecond nonlinear optical response of a Cu:silica nanocluster composite," Opt. Lett. **18**(5), 373-375 (1993).

20. A. Manna, T. Imae, K. Aoi, M. Okada, and T. Yogo, "Synthesis of dendrimer-passivated noble metal nanoparticles in a polar medium: Comparison of size between silver and gold particles," Chem. Mater. **13**, 1674-1681 (2001).

21. O. M. Wilson, R. W. J. Scott, J. C. Garcia-Martinez, and R. M. Crooks, "Separation of dendrimer-encapsulated Au and Ag nanoparticles by selective extraction," Chem. Mater. **16**(22), 4202-4204 (2004).

22. L. M. Bronstein, D. M. Chernyshov, P. M. Valetsky, E. A. Wilder, and R. J. Spontak, "Metal nanoparticles grown in the nanostructured matrix of poly(octadecylsiloxane)," Langmuir **16**(22), 8221-8225 (2000).

23. S. Porel, S. Singh, S. S. Harsha, D. N. Rao, and T. P. Radhakrishnan, "Nanoparticle-embedded polymer: In situ synthesis, free-standing films with highly monodisperse silver nanoparticles and optical limiting," Chem. Mater. **17**(1), 9-12 (2005).

24. A. Dawn, P. Mukherjee, and A. K. Nandi, "Preparation of size-controlled, highly populated, stable, and nearly monodispersed Ag nanoparticles in an organic medium from a simple interfacial redox process using a conducting polymer," Langmuir **23**(10), 5231-5237 (2007).

25. K. Akamatsu, N. Tsuboi, Y. Hatakenaka, and S. Deki, "In situ spectroscopic and microscopic study on dispersion of Ag nanoparticles in polymer thin films," J. Phys. Chem. B **104**, 10168-10173 (2000).

26. K. Huber, T. Witte, J. Hollmann, and S. Keuker-Baumann, "Controlled formation of Ag nanoparticles by means of long-chain sodium polyacrylates in dilute solution," J. Am. Chem. Soc. **129**, 1089-1094 (2007).

27. A. L. Stepanov and R. I. Khaibullin, "Optics of metal nanoparticles fabricated in organic matrix by ion implantation," Rev. Adv. Mater. Sci. **7**(2), 108-125 (2004).

28. M. Quinten, A. Heilmann, and A. Kiesow, "Refined interpretation of optical extinction spectra of nanoparticles in plasma polymer films," Appl. Phys. B: Lasers and Optics **68**(4), 707-712 (1999).

29. B.-H. Sohn, J.-M. Choi, S. II Yoo, S.-H. Yun, W-C. Zin, J. C. Jung, M. Kanehara, T. Hirata, and T. Teranishi, "Directed self-assembly of two kinds of nanoparticles utilizing monolayer films of diblock copolymer micelles," J. Am. Chem. Soc. **125**, 6368-6369 (2003).

30. H. Xu, J. Xu, Z. Zhu, H. Liu, and S. Liu, "In-situ formation of silver nanoparticles with tunable spatial distribution at the poly(N-isopropylacrylamide) corona of unimolecular micelles," Macromolecules **39**, 8451-8455 (2006).

31. M. Malenovska, S. Martinez, M.-A. Neouze, and U. Schubert, "Growth of metal nanoparticles in a sol-gel silica thin film," Eur. J. Inorg. Chem, **18**, 2609-2611 (2007).

32. V. I. Boev, J. Pérez-Juste, I. Pastoriza-Santos, C. J. R. Silva, M. D. J. M. Gomes, and L. M. Liz-Marzán, "Flexible ureasil hybrids with tailored optical properties through doping with metal nanoparticles," Langmuir **20**, 10268-10272 (2004).

33 . W. Schärtl, "Crosslinked spherical nanoparticles with core-shell topology," Adv. Mater. **12**, 1899-1908 (2000).

34. L. M. Liz-Marzán, M. Giersig, and P. Mulvaney, "Synthesis of nanosized gold-silica core-shell particles," Langmuir **12**, 4329-4335 (1996).

35. C. Graf and A. V. Blaaderen, "Metallodielectric colloidal core-shell particles for photonic applications," Langmuir **18**, 524-534 (2002).

36. C. Roos, M. Schmidt, J. Ebenhoch, F. Baumann, B. Deubzer, and J. Weis, "Design and synthesis of molecular reactors for the preparation of topologically trapped gold clusters," Adv. Mater. **11**(9), 761-766 (1999).

37. R. G. Freeman, K. C. Grabar, K. J. Allison, R. M. Bright, J. A. Davis, A. P. Guthrie, M. B. Hommer, M. A. Jackson, P. C. Smith, D. G. Walter, and M. J.

Natan, "Self-assembled metal colloid monolayers: an approach to SERS substrates," Science **267**, 1629-1632 (1995).

38. Y. Lu, G. L. Liu, and L. P. Lee, "High-density silver nanoparticle film with temperature-controllable interparticle spacing for a tunable surface enhanced Raman scattering substrate," Nano Lett. **5**(1), 5-9 (2005).

39. N. Horimoto, N. Ishikawa, and A. Nakajima, "Preparation of a SERS substrate using vacuum-synthesized silver nanoparticles," Chem. Phys. Lett. **413**, 78-83 (2005).

40. A. D. McFarland and R. P. V. Duyne, "Single silver nanoparticles as real-time optical sensors with zeptomole sensitivity," Nano Lett. **3**(8), 1057-1062 (2003).

41. K.-S. Lee and M. A. El-Sayed, "Gold and silver nanoparticles in sensing and imaging: Sensitivity of plasmon response to size, shape and metal composition," J. Phys. Chem. B **110**, 19220-19225 (2006).

42. A. Lin, D. H. Son, I. H. Ahn, G. H. Song, and W-T. Han, "Visible to infrared photoluminescence from gold nanoparticles embedded in germano-silicate glass fiber," Opt. Exp. **15**(10), 6374-6379 (2007).

43. S. Fan, P. R. Villeneuve, and J. D. Joannopoulos, "Large omnidirectional band gaps in metallodielectric photonic crystals," Phys. Rev. B **54**(16), 11245-11251 (1996).

44. Y. Yang, G. P. Wang, J. Xie, and S. Zhang, "Metal nanoparticles-embedded three-dimensional microstructures created by single-beam holography," Appl. Phys. Lett. **86**, 173108 (2005).

45. M. Bockstaller, R. Kolb, and E. L. Thomas, "Metallodielectric photonic crystals based on diblock copolymers," Adv. Mater. **13**, 1783-1786 (2001)

46. A. Lin, X. Liu, P. R. Watekar, W. Zhao, B. Peng, C. Sun, Y. Wang, and W.-T. Han, "All-optical switching application of germano-silicate optical fiber incorporated with Ag nanocrystals," Opt. Lett. **34**(6), 791-793 (2009).

47. A. Lin, B. H. Kim, S. Ju, and W.-T. Han, "Fabrication and third-order nonlinearity of germano-silicate glass fiber incorporated with Au nanoparticles," Proc. SPIE **6481**, 64810M (2007).

48. L. Qiu, J. Franc, A. Rewari, D. Blanc, and K. Saravanamuttu, "Photolytic formation of Ag nanoparticles in oligomeric organosiloxanes: new photolithographic routes to metallodielectric microperiodic structures," J. Mater. Chem. **19**, 373-378 (2009).

49. G. I. Stegeman and M. Segev, "Optical Spatial Solitons and Their Interactions: Universality and Diversity," Science **286**(5444), 1518-1523 (1999).

50. S. Trillo and W. Torruellas, *Spatial Solitons,* 1 ed. (Springer, New York, 2001).

51. A. W. Snyder and D. J. Mitchell, "Accessible Solitons," Science 276, 1538-1541 (1997)

52. T. M. Monro, C. M. De Sterke, and L. Poladian, "Topical review - Catching light in its own trap," Journal of Modern Optics **48**(2), 191-238 (2001);.

53. J. Zhang, K. Kasala, A. Rewari, and K. Saravanamuttu, "Self-Trapping of Spatially and Temporally Incoherent White Light in a Photochemical Medium," J. Am. Chem. Soc. **128**, 406-407 (2006).

54. J. Zhang and K. Saravanamuttu, "The dynamics of self-trapped beams of incoherent white light in a free-radical photopolymerizable medium," J. Am. Chem. Soc. **128**(46), 14913-14923 (2006).

55. J. Zhang and K. Saravanamuttu, "Nonlinear propagation of incoherent white light in a photopolymerizable medium: evidence of the co-existence

and competition between spontaneous pattern formation and self-trapping" J Mater Sci: Mater Electron **20**, 380-384 (2009).

56. A. B. Villafranca and K. Saravanamuttu, "An experimental study of the dynamics and temproal evolution of self-trapped laser beams in a photopolymerizable organosiloxane," J. Phys. Chem. C **112**, 17388-17396 (2008).

57. J. A. Dean, *Lange's Handbook of Chemistry,* 15 ed. (McGraw-Hill, 1999).

58. The effective beam diameter is the diameter of a circle with an area equal to the area of all pixels with intensity above 13.5% (that is, $1/e^2$) of the measured beam peak intensity in the CCD camera. It represents the actual beam diameter only for beam with Gaussian profile. For non Gaussian profiles, effective beam diameter recorded by the camera only indicates how wide the beam intensity spreads.

59. The relative peak intensity is the ratio between the greatest intensity on one or more pixels in an image and the saturation intensity of the camera.

60. J. A. Buck, *Fundamentals of Optical Fibers,* 2 ed., Wiley Series in Pure and Applied Optics (Wiley and Sons, 2004).

61. In order to obtain optical spectra of self-written waveguides, optical self-trapping was performed directly with the probing white light (400 - 740 nm). Spectra were collected after optical self-trapping had been successfully observed to make sure that the probing beam had been well confined within the formed waveguide. Set-up for optical self-trapping with incoherent white light was described in Ref 54.

62. T. M. Monro, C. M. de Sterke, and L. Poladian, "Investigation of waveguide growth in photosensitive germanosilicate glass," Journal of the Optical Society of America B: Optical Physics **13**(12), 2824-2832 (1996).

63. K. Kasala and K. Saravanamuttu, "An experimental study of the interactions of self-trapped white light beams in a photopolymer, " Appl. Phys. Lett. **93**(5), 051111 (2008).

64. I. B. Burgess, M. R. Ponte, and K. Saravanamuttu, "Spontaneous formation of 3-D optical and structural lattices from two orthogonal and mutually incoherent beams of white light propagating in a photopolymerisable material," J. Mater. Chem. **18**, 4133 (2008).

Chapter 4 Modulation instability of spatially and temporally incoherent white light in a photopolymer doped with Ag nanoparticles

Liqun Qiu and Kalaichelvi Saravanamuttu

Reproduced by permission of IOP
J. Opt. , 2012 (14), 125202, DOI: 10.1088/2040-8978/14/12/125202
Online abstract: iopscience.iop.org/2040-8986/14/12/125202

Work presented in this chapter was conducted by Liqun Qiu, and supervised by Dr. Kalaichelvi Saravanamuttu. Content of this chapter has been submitted to Journal of Optics.

Abstract

Modulation instability and spontaneous filamentation of a broad incandescent beam was elicited in the photopolymerisable medium containing a uniform distribution of Ag nanoparticles. Because photoinduced changes due to polymerisation are irreversible, the self-trapped filaments permanently inscribe the corresponding array of cylindrical waveguides dispersed with Ag nanoparticles. Careful examination of the dynamics of MI and calculations of parameters such as self-trapping efficiency and average separation distance of filaments reveals a strong dependence on the concentration of Ag nanoparticles as well as the pathlength of the sample. Microscopy of the photoinduced waveguide microstructures identified a

range of interactions between self-trapped filaments such as fusion, branching and repulsion.

4.1 Introduction

Metal nanoparticles are characterized by their surface plasmon resonance, which can be excited at visible wavelengths and tuned through composition, size, shape, and inter-particle coupling [1;2;3;4;5;6;7]. The apparent amplification of local fields due to surface plasmons has been attributed to the extraordinary enhancement of a variety of optical phenomena including photoluminescence [8;9], $\sim 10^7$-fold increases in third-order nonlinear optical responses [10;11], and increases in the spectroscopic signals of molecules at the particle surface. [7] Motivated by the optical properties imparted by metal nanoparticles, there has been considerable effort to incorporate them within dielectric media such as dendrimers [12;13], polymers [14;15;16;17;18], surfactant systems [19;20], and sol-gel derived composites[21], which can in turn be easily processed through lithography for example [22;29] into devices for spectroscopy [23;24;25], optical sensing and imaging [26;27], photonic crystals [28;29;30;31] and optica switches [28;32;33;34].

In this report, we show that a soft photopolymerisable organosiloxane medium containing a uniform distribution of Ag nanoparticles [35] elicits modulation instability (MI) and spontaneous division of a broad incandescent white beam into multiple self-trapped filaments [36;37]. We examine both the dependence of this nonlinear process on the metal nanoparticles and its potential as a single-step, room temperature and spontaneous route to large populations of cylindrical metallodielectric waveguides. MI of the incandescent beam and its consequent filamentation originate from refractive index changes due to photopolymerization along

the propagation path of the optical field. Because refractive index changes due to polymerisation are irreversible, the filaments permanently inscribe the corresponding array comprising thousands of cylindrical waveguides doped with Ag nanoparticles.

We previously showed that a broad incandescent beam emitted by a quartz-tungsten-halogen filament suffers MI in a (non-doped) photopolymerisable organosiloxane medium. Refractive index changes due to polymerisation are intensity-dependent, saturable and noninstantaneous, which enables nonlinear propagation including MI of a spatially and temporally incoherent and polychromatic wavepacket such as incandescent light [36;38;39;40;41;42;43;44;45;46]. This nonlinear form of light propagation occurs under the same conditions that enable a *narrow* beam of incandescent light to self-trap and propagate without diverging over long distances (>> Rayleigh range) [47;48]. Self-trapping originates from the dynamic competition between the natural divergence and self-induced refraction of a beam propagating in a photoresponsive medium [49;50] and is described by the nonlinear Schrödinger equation [51;52]:

$$ik_0 n_0 \frac{\partial E}{\partial z} + \frac{1}{2}\nabla_{\perp}^{2} E + k_0^2 n_0 \Delta n E + \frac{i}{2} k_0 n_0 \alpha E = 0 \qquad \textbf{4-1}$$

which expresses the counteraction between the beam divergence, $\nabla_{\perp}^{2} = (\partial^2/\partial x^2) + (\partial^2/\partial y^2)$, and refractive index changes, Δn, along its propagation path z. Here, α is the attenuation coefficient of the medium, n_0, the initial refractive index of the medium, and k_0, the free space wave vector. Equation **4-1** implies that noise that is normally negligible in a broad, uniform beam becomes amplified through the same competition between beam divergence and self-induced refractive index change that leads to self-

trapping. As a result, weak perturbations in intensity and refractive index along the propagation path of a broad beam grow and become amplified under the nonlinear conditions associated with photopolymerization. The resulting strong intensity modulations across the beam render it unstable and trigger its division into multiple, stable self-trapped filaments.

In this study, we show for the first time that MI of incandescent light can be elicited in a photopolymerisable system that is doped with Ag nanoparticles with plasmon resonances occurring in the visible spectrum (~450 nm). Detailed examination of the effects of the concentration of Ag nanoparticles and optical pathlength provided new insight into the dynamics of MI, which could not be elucidated from the non-doped system. Significantly, these findings also identify a fundamentally new and spontaneous lithographic route to generating large populations of metallodielectric waveguides.

4.2 Experimental

4.2.1 Preparing Ag nanoparticle-doped organosiloxane sols

Ag nanoparticle-doped organosiloxane sols were generated through previously described methods [35;53]. Briefly, organosiloxane sols were first prepared through the hydrolysis and condensation of 3-methacryloxypropyl trimethoxysilane (MAPTMS, 0.020 mol). The reaction was catalysed with H_2O (0.0150 mol) that was acidified with HCl (1.35×10^{-5} mol). After ~4 minutes of continuous stirring, the initially phase-separated mixture homogenized and became transparent. $AgNO_3$ solution (1.00×10^{-5} mol) was then added to precipitate the majority of Cl^- in the sol in the form of AgCl, which was then

filtered out through a polytetrafluoroethylene (PTFE) membrane (0.2 μm pore size, Pall Corporation). The sol contained a residual chloride concentration, $[Cl^-] = 7 \times 10^{-4}$ M. Different amounts of $AgNO_3$ solution were then added to prepare a series of sols with a constant $[AgCl] = 7 \times 10^{-4}$ M, and $[AgNO_3]$ ranging from 1×10^{-3} M to 8×10^{-3} M. Because $[Ag^+][Cl^-] \sim 10^{-6}$ in the sol is several orders greater than the solubility product, $K_{sp}=[Ag^+][Cl^-]=1.77\times10^{-10}$ [54], AgCl existed as insoluble grains. However, immediate aggregation and formation of AgCl precipitates were inhibited, as the low concentration of AgCl grains increased the free energy barrier for crystal nucleation and growth. Sols doped with AgCl therefore remained stable and transparent for up to 2 days when kept in the dark.

Ag nanoparticles were photolytically generated in the AgCl-doped sols by irradiating with white light (3 hrs, 23 W fluorescent light (Noma® mini spiral bulb)). Upon irradiation, the sols turned orange-brown; formation of Ag nanoparticles was confirmed through UV-VIS absorbance spectra (acquired with a Cary 50 Bio UV-visible spectrometer), which contained an absorption band maximising at ~450 nm (**Figure 4.1a**). This is characteristic of the dipolar plasmon resonance of Ag nanoparticles [35]. Transmission electron microscopy (carried out with a Philips CM12 microscope) further confirmed the presence of Ag nanoparticles with an average diameter of 52 ± 13 nm (**Figure 4.1b**).

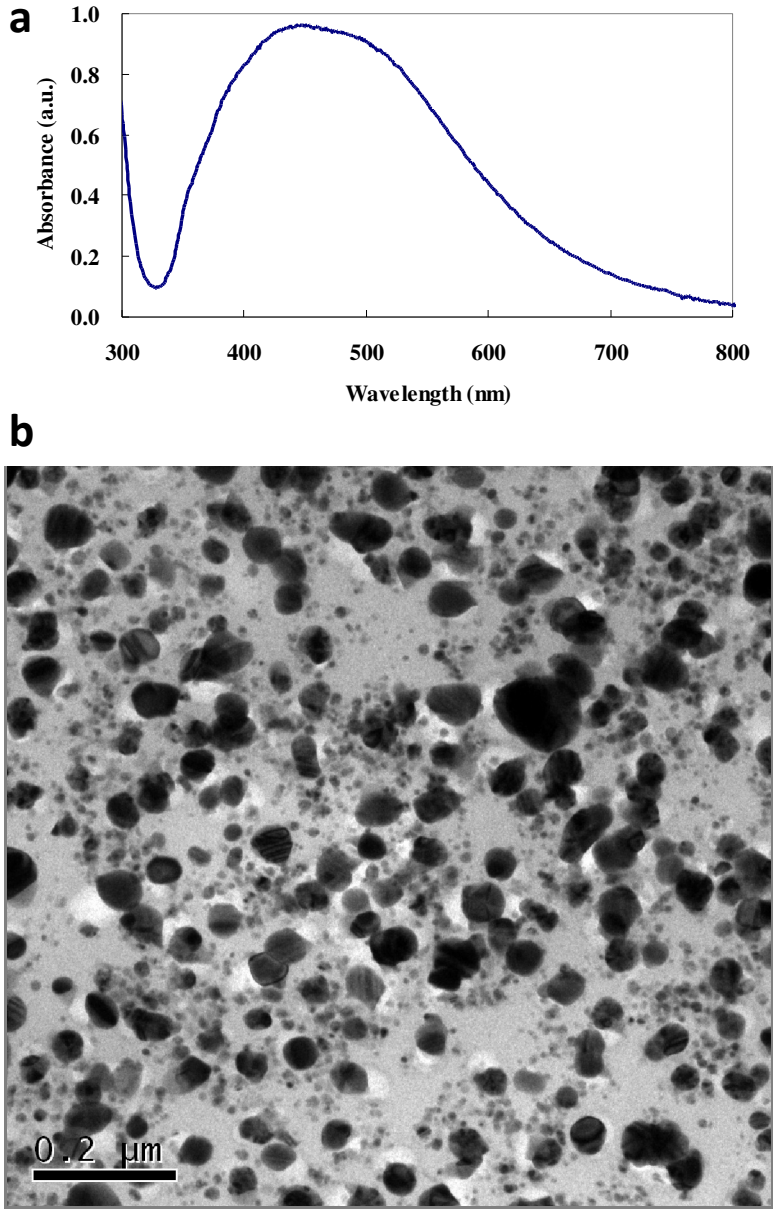

Figure 4.1 a) UV-Vis absorbance spectrum and (b) transmission electron micrograph of organosiloxane sol with Ag[I] = 8×10^{-3} M after irradiation for 3 hrs with the 23 W fluorescent light.

4.2.2 Sample preparation for optical experiments

Prior to optical experiments, Ag nanoparticle-containing sols were doped with 0.5 wt.% of the free-radical photo-initiator (bis(η^5-

cyclopentandienyl) bis(2,6-difluoro-3-(1H-pyrrol-yl)-phenyl) titanium(IV)) (λ_{max} = 393 nm, 460 nm, Ciba Specialty Chemicals Inc., Canada). This was achieved by dissolving the photoinitiator in an organosiloxane sol without Ag nanoparticles and mixing at a 1:1 volume ratio with the Ag nanoparticle-doped sol. Sols employed for optical experiments therefore typically had $[Ag(I)_{initial}] = 0.8 \times 10^{-3}$ M to 4.0×10^{-3} M. Samples for optical experiments were prepared by injecting the Ag nanoparticle-doped sol through a small perforation into a cylindrical sample cell (outer and inner diameter = 16 mm and 12 mm, respectively; pathlength = 2.0 mm, 4.0 mm, 6.0 mm, or 10.0 mm), which had two optically flat and transparent windows.

4.2.3 Optical assembly

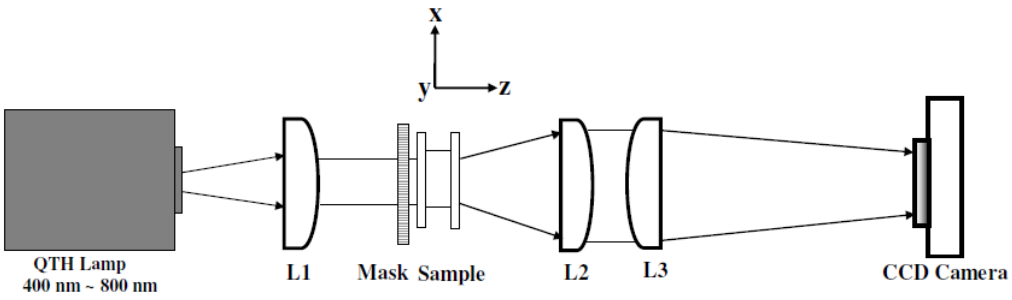

Figure 4.2 Scheme of the optical assembly employed for experiments of modulation instability (MI).

Figure 4.2 is a scheme of the optical assembly employed for experiments of modulation instability. Light from a quartz-tungsten-halogen lamp was collimated with a planoconvex lens (L_1) and passed through an amplitude mask, which imposed a 1-D modulation with a periodicity of 80 μm on the optical field. The modulated beam was launched into the sol-containing

sample cell and its spatial intensity profile at the exit face, imaged by a pair of planoconvex lenses (L_2, L_3) onto a CCD camera.

4.2.4 Characterization of Ag nanoparticle-doped microstructures

Transmission optical micrographs of photopolymerized microstructures generated through modulation instability were acquired with an OLYMPUS BX51 microscope. Scanning electron microscopy of the microstructures was carried out on a JEOL 7000F microscope (Oxford Instruments), which was equipped with an INCA-act Energy Dispersive X-ray spectrometer.

4.3 Results and Discussion

4.3.1 Experimental evidence of the modulation instability of incandescent light in Ag-nanoparticle doped organosiloxanes

In a typical experiment, a broad incandescent beam (22×10^{-3} Wcm^{-2}) with a weak, 1-D periodic (80 μm) intensity modulation (bright and dark stripes) was launched into a 2 mm-long cell containing Ag nanoparticle-doped organosiloxane ($[Ag(I)_{initial}] = 4\times10^{-3}$ M). Temporal changes in the spatial intensity profile of the beam at the exit face of the sample are presented in **Figure 4.3**. At very early times (**Figure 4.3 a**), the significant natural divergence of the incandescent beam reduced the contrast of the 1-D modulation so that at the exit face, the intensities of the bright and dark regions were 131±7 a.u. and 97±2 a.u., respectively. However, with time, the natural divergence of the beam was suppressed by refractive index changes (Δn) due to photopolymerization in the medium. Because the magnitude of Δn induced within a given period of time is proportional to intensity, greater values of Δn were induced by the bright stripes [36]. During this process, intensity became preferentially trapped within the high-index regions, enabling the bright stripes to propagate through the medium without diverging, *i.e.,* broadening or decreasing in intensity. At the sample output,

self-trapping of bright stripes was evidenced at 88 s by a significant decrease in their width from 66 ± 6 μm at 1 s to 33 ± 6 μm with a concomitant increase in intensity from 131 ± 7 to 222 ± 24 (**Figure 4.3 c**). As the bright stripes self-trapped and induced further increases in refractive index, they continually attracted intensity from the adjacent darker regions. Consequently, the increasing intensity of the bright stripes was accompanied by a depletion of intensity from adjacent dark stripes, which darkened from a relative intensity of 97 ± 2 at 1 s to only 39 ± 5 at 88 s (Figure 4.3 c).

With time, additional increases in Δn triggered the modulation instability (MI) of the bright stripes and their consequent division into multiple filaments. MI was initiated at 122 s, when the self-trapped bright stripes developed inhomogeneities in intensity, which amplified over time until at 160 s, each stripe divided *spontaneously* into discrete and stable spots (**Figure 4.3 d-f**). Each spot corresponded to a self-trapped filament of incandescent light, which propagated through the medium without diverging. The average width ($1/e^2$) of each filament was 27 ± 4μm (H) and 22 ± 5 μm (V); filaments were separated along the *y* axis by 33 ± 4μm. Along the *x* direction, the filaments were separated by 80 μm, which corresponded to the periodicity of the modulation originally imposed on the beam.

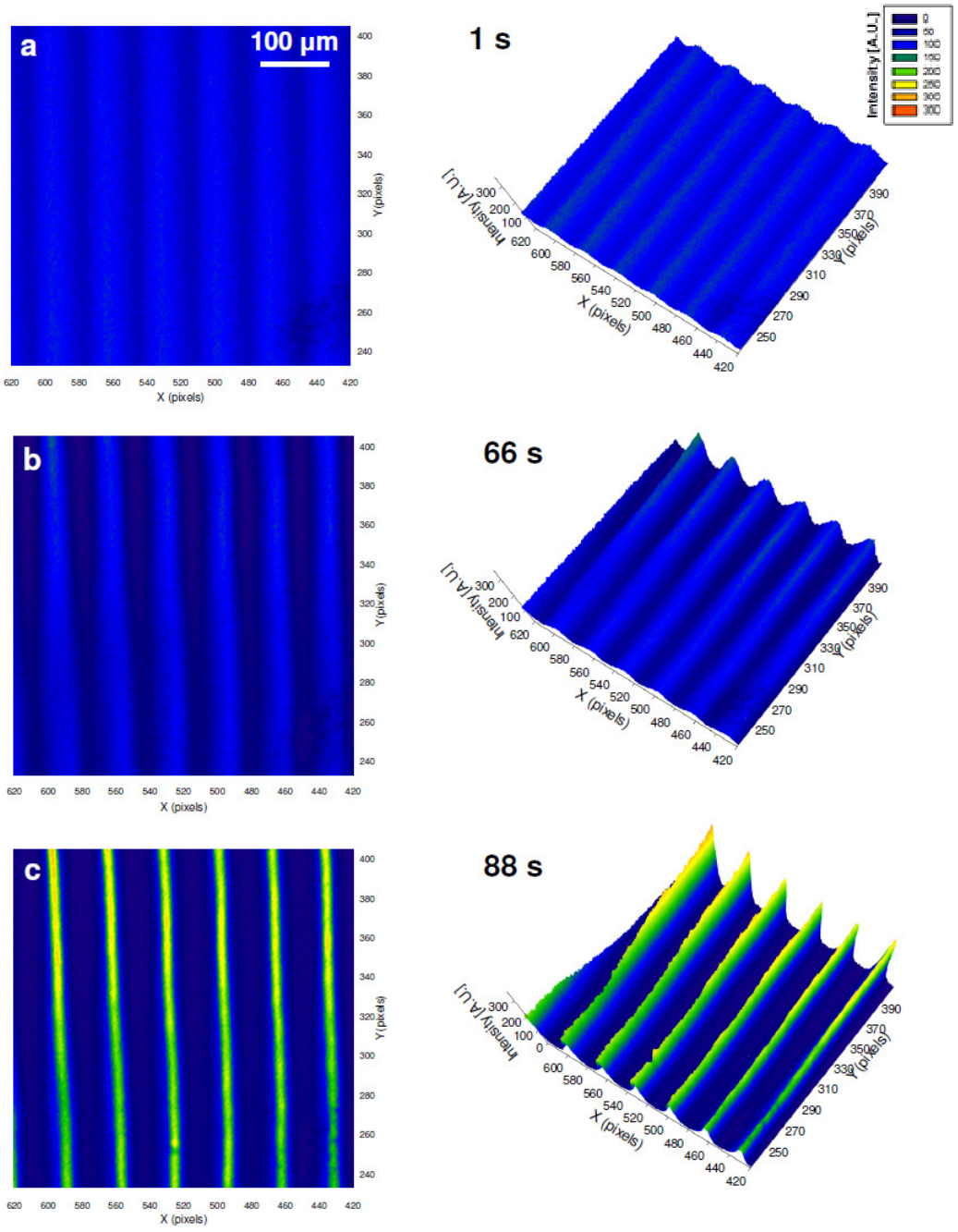
a
100 µm
b
c
1 s
66 s
88 s
X (pixels)
Y (pixels)
Intensity [A.U.]

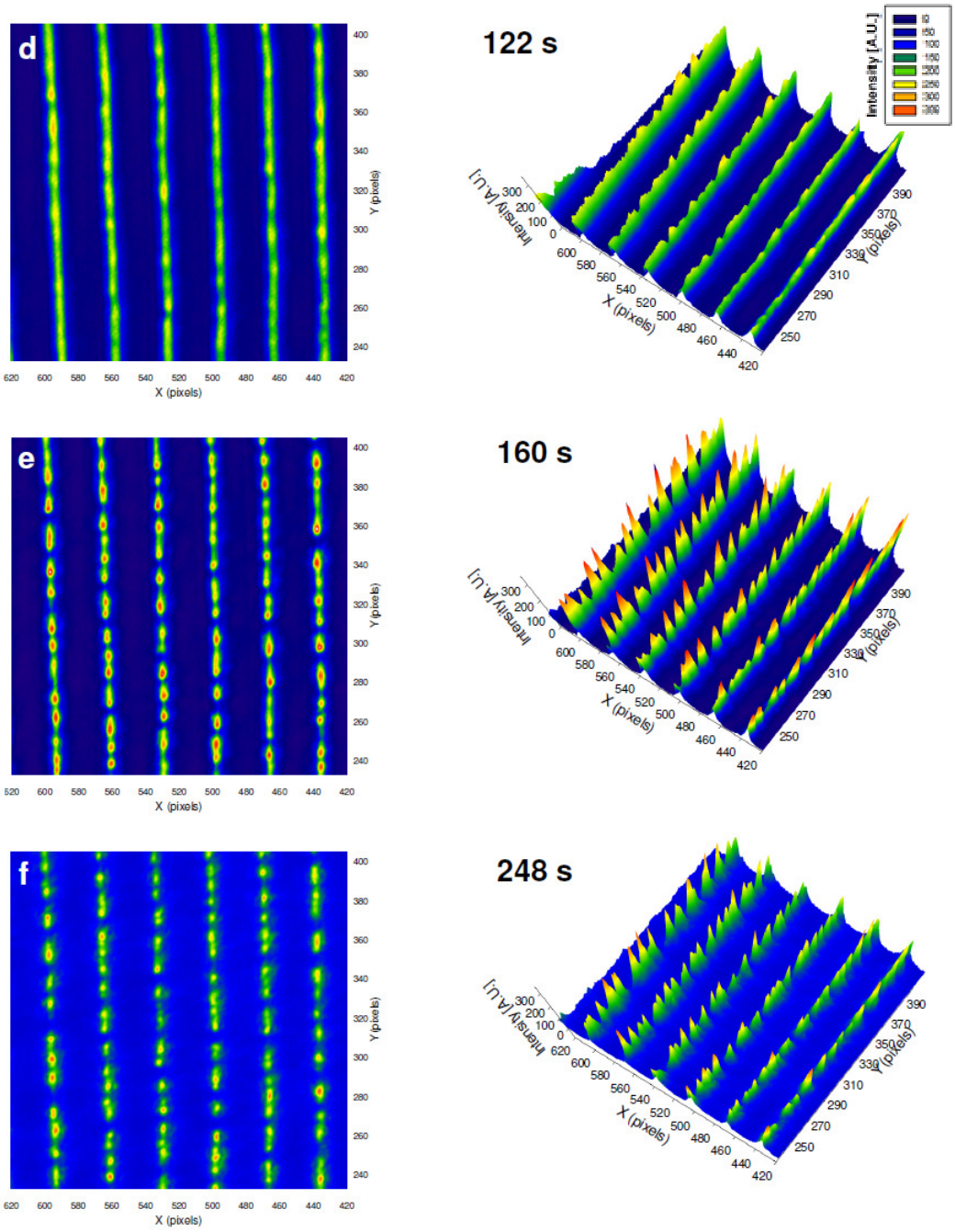

Figure 4.3 Temporal evolution of the spatial intensity profile of a weakly modulated incandescent beam (22 $\times 10^{-3}$ Wcm^{-2}) propagating through the Ag nanoparticle-doped photopolymeriable organosiloxane ([Ag(I)$_{initial}$]= 4 $\times 10^{-3}$ M). Profiles were acquired at the sample exit face (pathlength = 2 mm). In both 2-D and 3-D profiles, pixel size = 2.4 μm (*x*) x 2.8 μm (*y*).

4.3.2 Spontaneous generation of 3-D waveguide arrays doped with Ag nanoparticles

Because refractive index changes due to photopolymerization are irreversible, the cylindrical waveguides induced by self-trapped filaments were permanently inscribed in the medium. **Figure 4.4a** is a transverse cross-sectional optical micrograph, which shows that the photoinduced microstructure consisted of a periodic array of dotted lines. Each dot corresponds to the transverse cross-section of a cylindrical waveguide induced by a filament. The periodicity of the dotted lines was 71.8 ± 0.3 μm along the *x* direction, which was comparable to the periodicity of the 1-D amplitude mask [55]. The average separation distance between the dots was of 36 ± 3 μm, which was consistent with the average separation distance of self-trapped filaments (*vide supra*). An optical micrograph of the longitudinal cross-section acquired along the *z* (propagation) direction confirmed that the cylindrical waveguides propagated from the entrance to the exit face of the medium (**Figure 4.4b**).

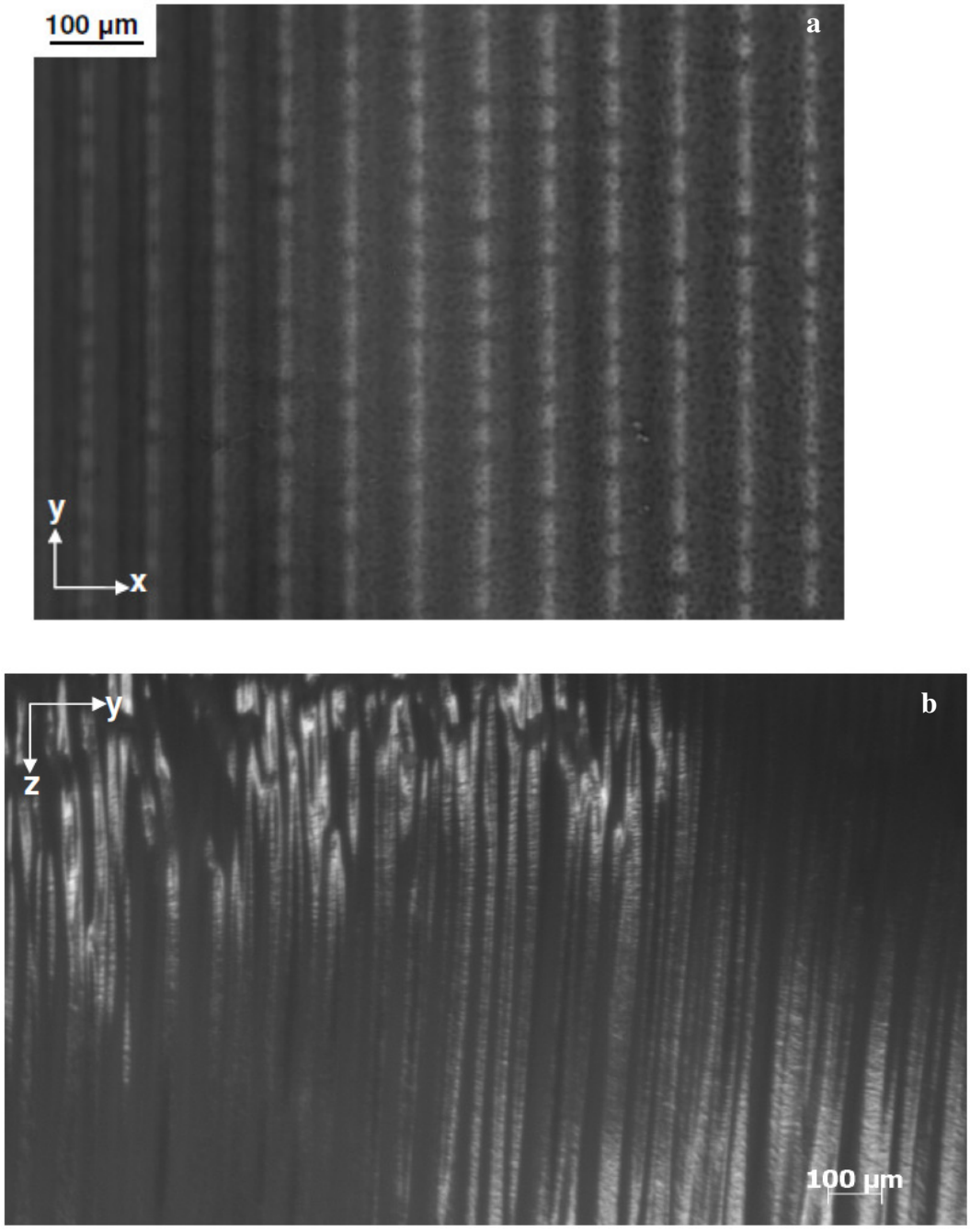

Figure 4.4 Optical micrographs of the 2-D array of cylindrical waveguides induced by self-trapped filaments of incandescent light in an organosiloxane doped with Ag nanoparticles ($[Ag(I)_{initial}]= 4 \times 10^{-3}$ M). (a) transmission micrograph of the transverse cross-section (sample pathlength = 2.0 mm) and (b) reflection micrograph of the longitudinal cross-section (sample pathlength = 4.0 mm) are presented. Optical intensity = 22×10^{-3} Wcm^{-2}.

The presence of Ag nanoparticles in the waveguide array shown in **Figure 4.4** was confirmed through transmission optical spectroscopy (**Figure 4.5**) [56] and scanning electron microscopy (SEM) coupled with energy dispersive X-ray spectroscopy (EDX) (**Figure 4.6**). Comparison of transmission spectra of waveguide arrays with and without Ag nanoparticles showed that there was negligible transmission from 400 nm to 480 nm in both samples (**Figure 4.5**). This can be attributed to the absorption of residual photoinitiator in the samples (λ_{max} = 393 nm, 460 nm). However, in the Ag-doped sample, transmission remained negligible until ~510 nm. This absorbance is associated with the excitation of plasmon resonance in the Ag nanoparticles; the plasmon resonance band maximizes at 450 nm and spans from 350 nm to 700 nm (see Section 2). It was also noted that the transmission of the waveguide arrays doped with Ag nanoparticles was in general smaller than that of the undoped array; this intensity loss is attributed to scatter from Ag nanoparticles embedded throughout the sample.

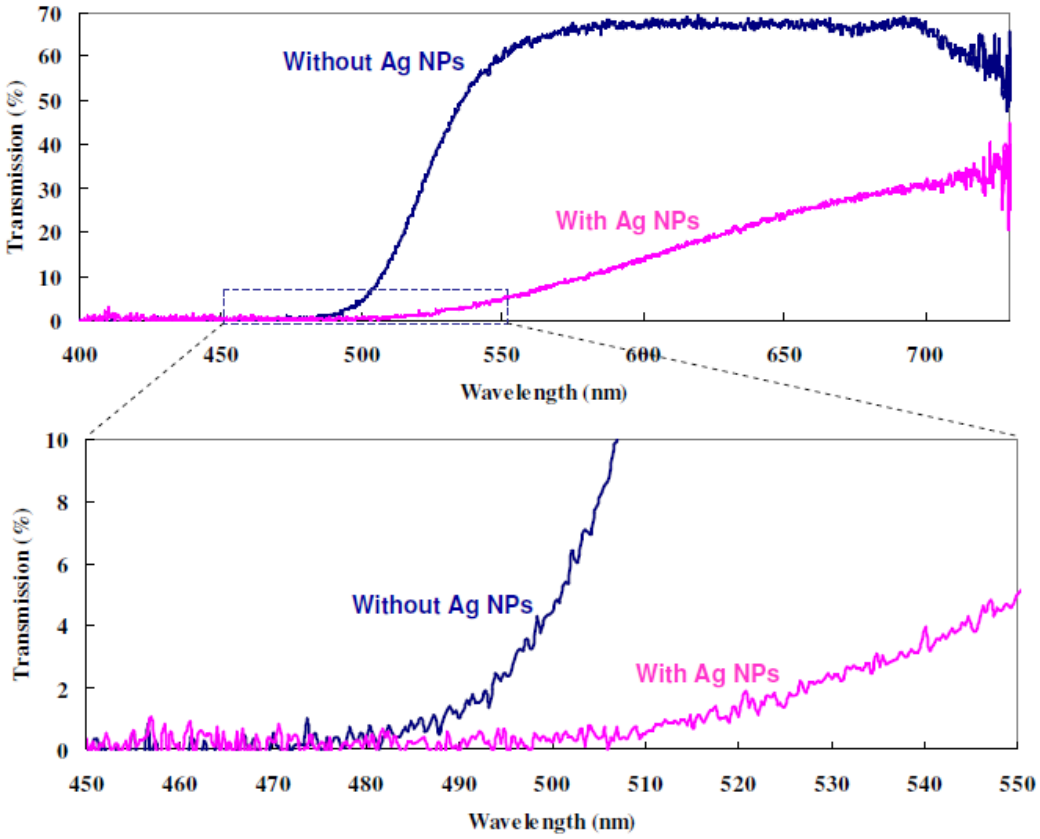

Figure 4.5 Optical transmission spectra of self-induced waveguide arrays that were non-doped (blue) and doped with Ag nanoparticles (pink).

We directly observed Ag nanoparticles embedded in the waveguide arrays as bright circular features in scanning electron micrographs(SEM). The particles were typically distributed uniformly throughout the sample (**Figure 4.6**). EDX spectroscopy confirmed the bright features to be elemental Ag (**Figure 4.6 i**). In the topological SEM acquired with secondary electrons in **Figure 4.6a**, self-induced filaments were observed as slightly brighter stripes. Magnified images comparing the bright (**Figure 4.6 f,h**) and dark regions (**Figure 4.6e, g**) showed that Ag nanoparticles in the bright regions were in general slightly larger than those in the dark region. The

appearance of larger particles in the bright areas suggests the photoinduced aggregation of Ag nanoparticles. In rare cases, SEM revealed chains of Ag nanoparticles that were preferentially aligned along the long axis of self-induced waveguides (**Figure 4.6 b, c**). Even in these cases, the rest of the sample contained a uniform distribution of discrete Ag nanoparticles.

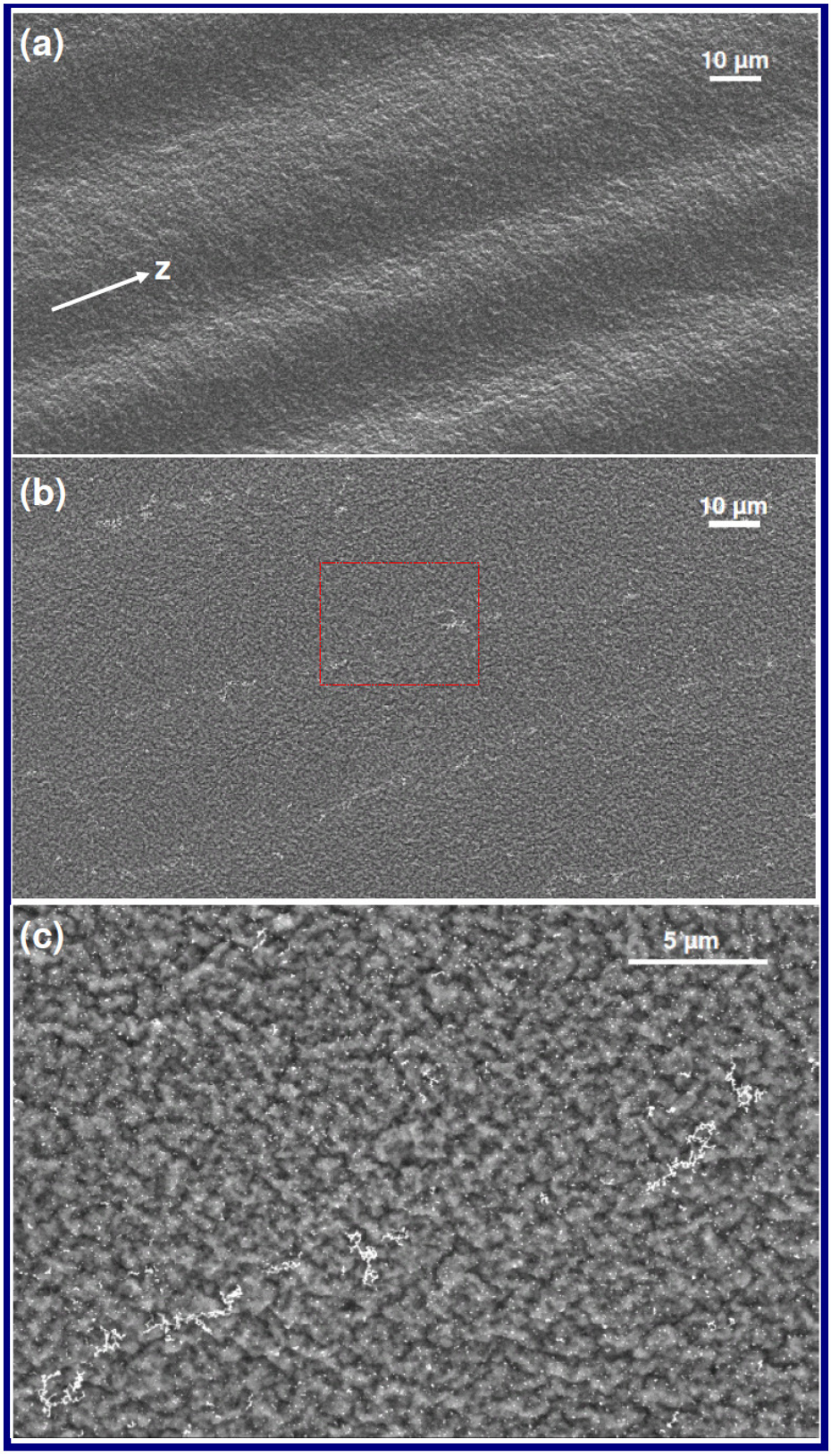
(a)
10 µm
z
(b)
10 µm
(c)
5 µm

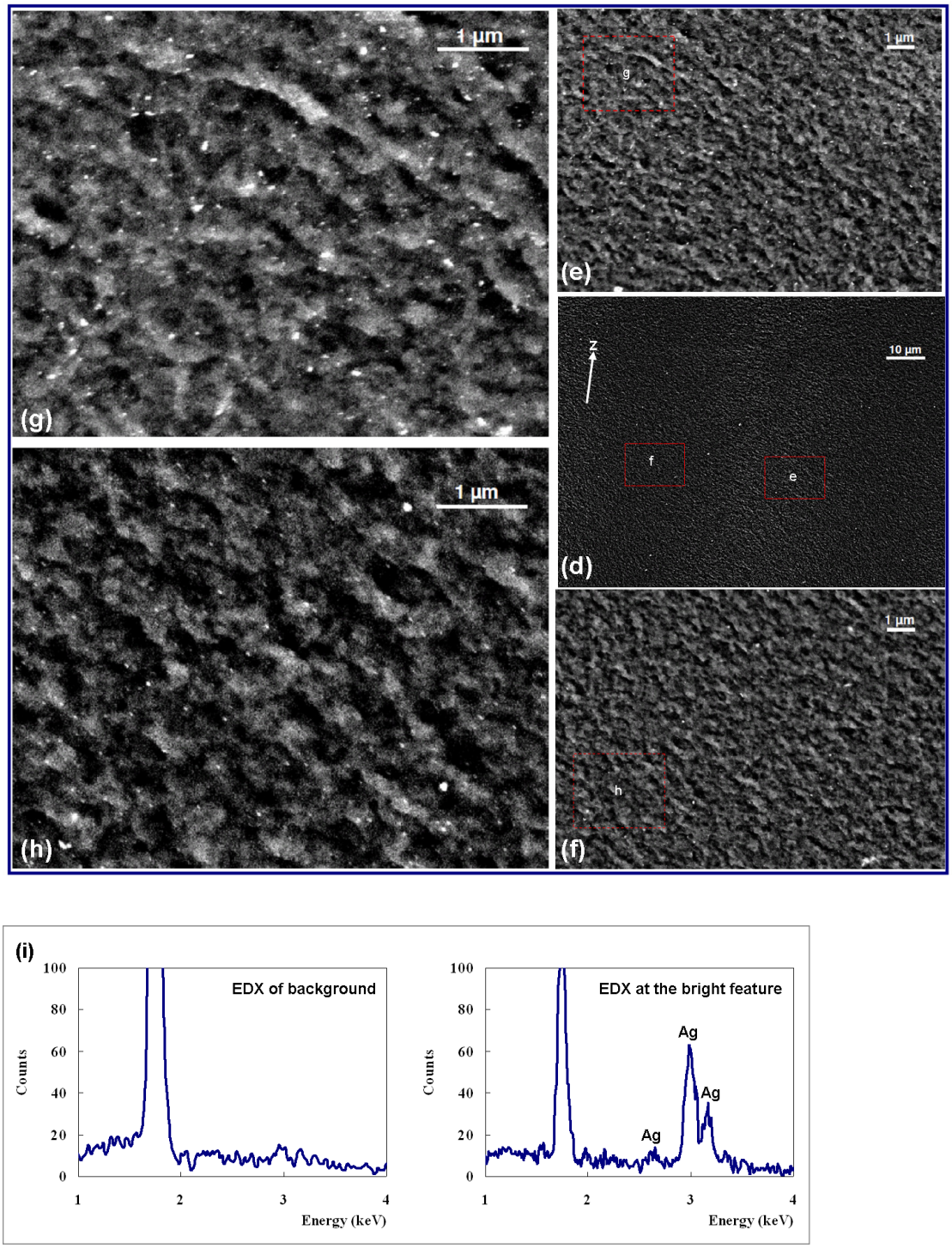

Figure 4.6 Scanning electron micrographs of self-induced waveguide arrays in a Ag nanoparticle-doped organosiloxane. (a) and (b) are respectively micrographs acquired through secondary electrons (for topological

information) and backscattered electrons (for elemental mapping) of the same sample area. (c) is a magnified region framed in red in (b). (e, g) and (f, h) are magnified images of bright and dark regions framed in red in (d). (i) Energy Dispersive X-ray (EDX) spectra of the bright (i) features (right) and surrounding area (left), respectively.

4.3.3 Effect of Ag nanoparticle concentration on modulation instability

We found that Ag nanoparticles played a critical role in eliciting modulation instability of the optical field. Significantly, the dynamics of the process was considerably different in the Ag-doped photopolymer compared to the non-doped system. For example, MI was not observed in a 2 mm-long photopolymer sample that did not contain Ag nanoparticles. In this case, although self-trapping of bright stripes was observed, filamentation did not occur (**Figure 4.7 a**). This was further confirmed in optical micrographs of longitudinal cross-sections of non-doped samples where self-induced waveguides were not observed until after a thickness of ~ 3 mm (**Figure 4.11**). Modulation instability is seeded by noise (normally negligible variations in amplitude or intensity) that is inherent to the sample [36]. In the non-doped system, susceptibility to noise increases with propagation distance; accordingly, samples with pathlengths ≥ 3 mm exhibited an inverse relationship between pathlength and the time at which MI is observed (**Figure 4.7 b-e**).

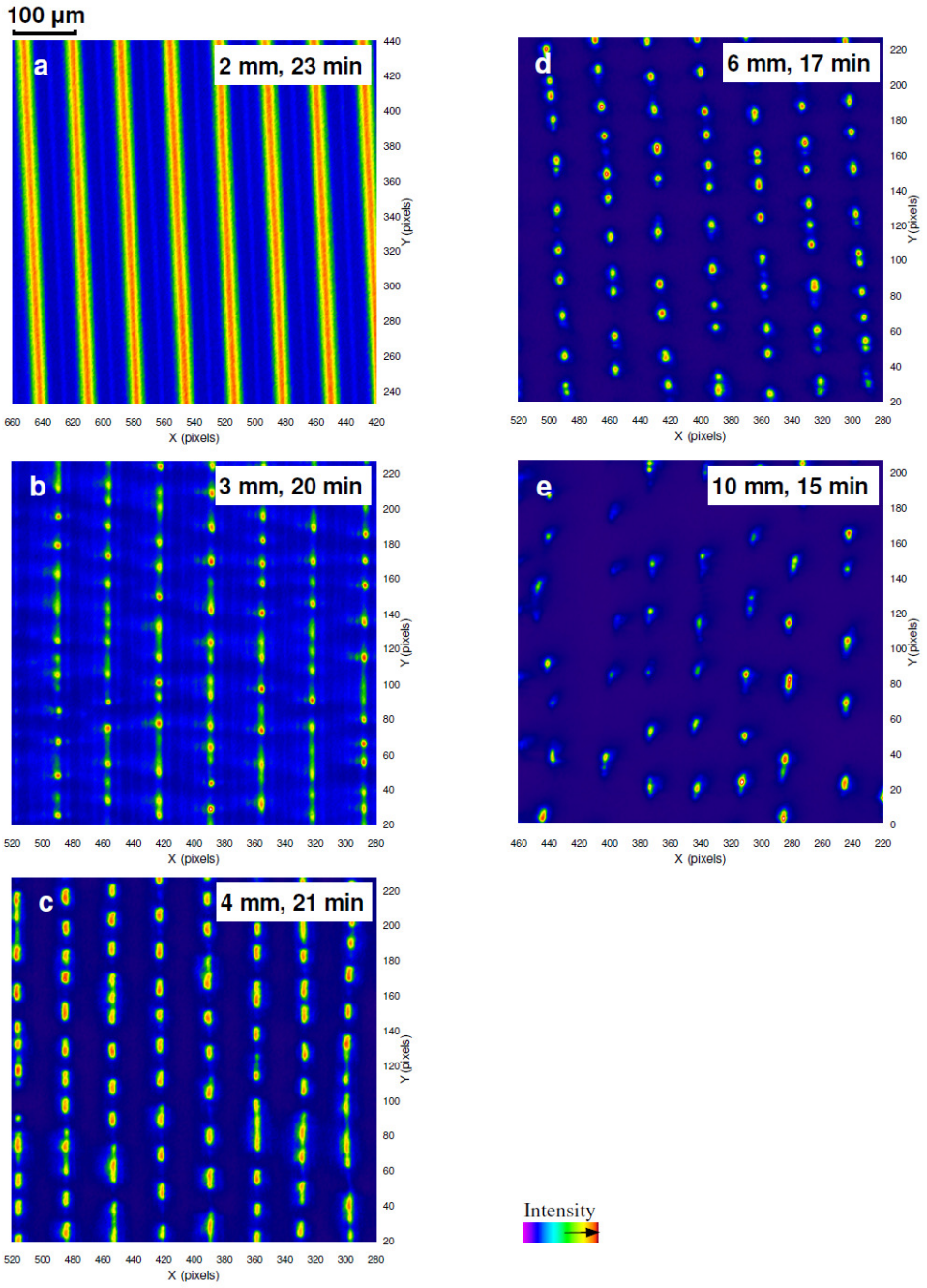

Figure 4.7 2-D spatial intensity profiles acquired at the exit face of non-doped organosiloxane samples with varying pathlength. No modulation instability was observed in (a) sample with pathlength = 2 mm even after 23 min. Modulation instability was observed in non-doped samples with pathlength (b) 3 mm (at 20 min.), (c) 4 mm (at 21 min.), (d) 6 mm (at 17 min.) and (e) 10 mm (at 15 min). In all cases, the incidence optical intensity= 6×10^{-3} Wcm^{-2}. Pixel size = 2.4 µm (x) × 2.8 µm (y).

The absence of filamentation in the non-doped sample with pathlength = 2 mm indicated that the Ag nanoparticles played an active role in triggering modulation instability of the optical field. Variations in the concentration of Ag nanoparticles showed that a threshold concentration of [Ag $(I)_{initial}$]= 0.8 $\times 10^{-3}$ M was necessary to elicit filamentation in a 2 mm-long sample. Increasing the concentration of Ag nanoparticles ([$Ag(I)_{initial}$] = 2 - 4 $\times 10^{-3}$ M) elicited modulation instability even in samples with a pathlength of 0.6 mm (**Figure 4.8**). In fact, in a sample with [$Ag(I)_{initial}$] = 4 $\times 10^{-3}$ M, optical microscopy showed that modulation instability and filamentation was initiated at only ~ 0.1 mm of the sample medium(**Figure 4.10 d**).

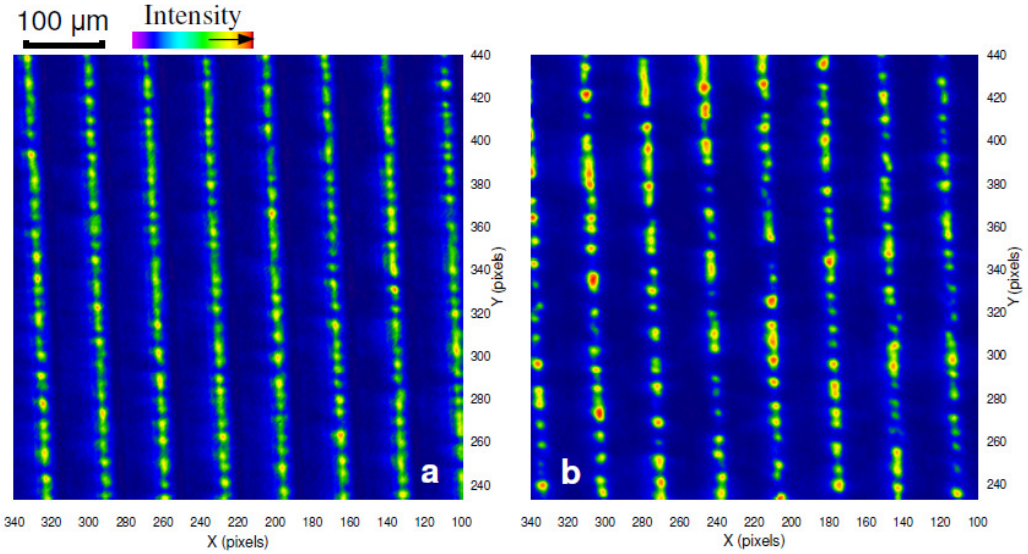

Figure 4.8 2-D spatial intensity profiles showing modulation instability in Ag nanoparticle-doped organosiloxane with pathlength = 0.6 mm. Modulation instability was observed in samples with (a) [$Ag(I)_{initial}$] = 4 $\times 10^{-3}$ M at 249 s at incident optical intensity = 22 $mWcm^{-2}$ and (b) [$Ag(I)_{initial}$] = 2 $\times 10^{-3}$ M at 346 s at incident optical intensity = 12 $mWcm^{-2}$. Pixel size =2.4 µm (x) × 2.8 µm (y).

Although Ag nanoparticles seeded modulation instability at propagation distances that were much smaller compared to non-doped samples, they also suppressed the propagation of self-trapped filaments over very long distances. In this case, extinction of the optical field both due to absorbance through plasmon resonance as well as scattering by Ag nanoparticles attenuated the beam [57]. This decreased the rate of photopolymerization and corresponding changes in refractive index, which is necessary to sustain modulation instability over long distances. For example, in a sample doped with Ag nanoparticles where $[Ag(I)_{initial}] = 4 \times 10^{-3}$ M, self-induced filaments could not propagate through samples with pathlength ≥ 3 mm. When the concentration of Ag nanoparticles was decreased however, self-induced filaments propagated over longer distances. For example, modulation instability was observed at the exit face of 4 mm-long samples with $[Ag(I)_{initial}] = 0.8 \times 10^{-3}$ M and 1×10^{-3} M (**Figure 4.9 a-b**). Although there was some break-up of the self-trapped bright stripes, the complete division of the optical field into discrete filaments did not occur when the pathlength of the same samples was increased to 6 mm (**Figure 4.9 c-d**). Interestingly, even in this case, the extent of break-up of the stripes was greater in the sample with $[Ag(I)_{initial}] = 0.8 \times 10^{-3}$ M (**Figure 4.9 d**) than in the sample with $[Ag(I)_{initial}] = 1 \times 10^{-3}$ M (**Figure 4.9 c**).

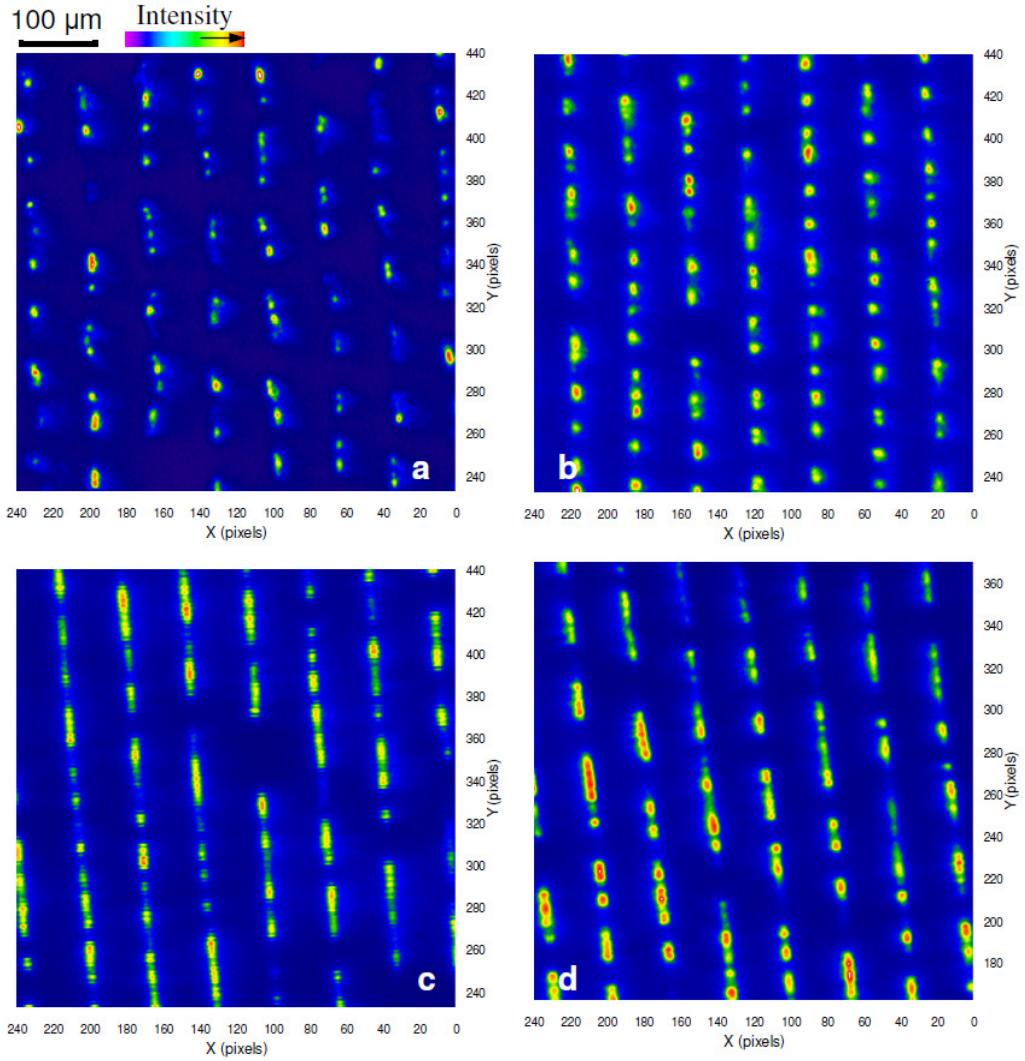

Figure 4.9 2-D spatial intensity profiles showing modulation instability in organosiloxane samples with low concentrations of Ag nanoparticles and pathlengths (a, b) 4 mm and (c, d) 6 mm. In (a) and (c), $[Ag(I)_{initial}]= 1 \times 10^{-3}$ M and in (b) and (d), $[Ag(I)_{initial}]= 0.8 \times 10^{-3}$ M. Incident optical intensity = 12 $\times 10^{-3}$ Wcm^{-2}. Modulation instability was observed at (a) 487 s (b) 445 s (c) 621 s and (d) 622 s. Pixel size = 2.4 µm (x) × 2.8 µm (y).

4.3.4 Dynamics and interactions of MI induced filaments

We characterized self-trapped filaments generated through MI in terms of their diameters, separation distance, efficiency of self-trapping and density. The dependence of these parameters on the concentration of Ag nanoparticles as well as the sample pathlength provided considerable insight into the mechanism and dynamics of MI.

Table 4-1 Filament widths observed in samples with varying concentrations of Ag nanoparticles. Results for each experiment were averaged over at least 100 filaments. Incident optical intensity = 12 $\times 10^{-3}$ Wcm^{-2} and 6 $\times 10^{-3}$ Wcm^{-2} for Ag nanoparticle-doped and non-doped samples, respectively.

$[Ag(I)_{initial}]$ ($x10^{-3}$ M)	**Filament diameter (1/e)**				
	Pathlength				
	0.6 mm	2.0 mm	4.0 mm	6.0 mm	10.0 mm
4.0	24±3µm (H) 16±3µm (V)	33±5µm (H) 20±6µm (V)			
2.0	27±3µm (H) 21±5µm (V)	30±5µm (H) 23±5µm (V)			
1.0		28±4µm (H) 22±4µm (V)	24±4µm(H) 26±5µm(V)		
0.8			27±3µm (H) 27±5µm(V)		
0.0			24±5µm (H) 26±5µm (V)	21±4µm(H) 24±5µm(V)	30±5µm (H) 31±5µm(V)

The widths ($1/e^2$) of self-trapped filaments did not vary significantly with sample pathlength, concentration of Ag nanoparticles or incident optical intensity. As summarised in **Table 4-1**, the average filament width, which ranged from 20 µm to 30 µm, were statistically identical. **Table 4-2** lists the average separation distance (D_{avg}) between filaments in samples with varying concentrations of Ag nanoparticles and pathlengths. For a given

pathlength, D_{avg} did not change significantly with the concentration of Ag nanoparticles. However, D_{avg} increased from <30 μm to ~80 μm when the pathlength increased from 0.6 mm to 10.0 mm. This in turn indicated that the spatial density of self-trapped filaments decreased with increasing pathlength of the sample.

Table 4-2 Summary of average separation distance (D_{avg}) between self-trapped filaments induced in photopolymer with varying concentrations of Ag nanoparticles. Incident intensity = 12 $\times 10^{-3}$ Wcm^{-2} and 6×10^{-3} Wcm^{-2} for Ag nanoparticle-doped and non-doped samples, respectively

$[Ag(I)_{initial}]$ ($x10^{-3}$ M)	D_{avg}				
	Pathlength				
	0.6 mm	2.0 mm	4.0 mm	6.0 mm	10.0 mm
4.0	22 ± 4 μm	38 ± 7 μm			
2.0	29±6 μm	38 ± 6 μm			
1.0		35 ± 4 μm	49 ± 9 μm		
0.8		38 ± 5 μm	47 ± 4 μm		
0.0			51 ± 6 μm	58 ± 5 μm	79 ± 9 μm

We measured the self-trapping efficiency of filaments by calculating the ratio (E) of the average peak intensity of filaments to the initial intensity of the optical field (both measured at the exit face of the sample). As listed in **Table 4-3**, E did not vary significantly with concentration of Ag nanoparticles for samples of the same pathlength. However, E differed significantly with sample pathlength, increasing by ~3-fold from 1.9 ± 0.1 to 6.1 ± 0.8 when the pathlength was increased from 0.6 mm to 10.0 mm (**Table 4-3**). However, the *product* of E and spatial density of filaments ($1/D_{avg}$) was comparable at all pathlengths (**Table 4-3**). This indicates that the *cumulative* self-trapping efficiency of the entire filament population is independent of pathlength, *i.e.*, at shorter pathlengths, there are a greater number of filaments with smaller

self-trapping efficiencies compared to longer pathlengths, where a smaller number of filaments self-trap with much greater efficiency.

Table 4-3 Summary of averaged ratios (E) of peak intensity (I_{MI}) of self-trapped filaments to initial intensity ($I_{initial}$) in samples with varying concentrations and pathlengths. The cumulative self-trapping efficiency of filament populations (product of E and $1/D_{avg}$) in samples with varying pathlengths is also listed. Incident intensity was 12 $\times 10^{-3}$ W/cm^{-2} and 6×10^{-3} W/cm^{-2} for Ag-nanoparticle doped samples, non- doped samples, respectively.*

$[Ag(I)_{initial}]$ ($x10^{-3}$ M)	E Pathlength				
	0.6 mm	2.0 mm	4.0 mm	6.0 mm	10.0 mm
4.0	1.5 ± 0.4	2.4 ± 0.3			
2.0	1.9 ± 0.03	2.4 ± 0.3			
1.0		2.7 ± 0.4	3.7 ± 0.6		
0.8			4.2 ± 0.2		
0.0			4.4 ± 1.5	5.5 ± 1.8	6.2±0.8
E/D_{avg} (μm^{-1})	0.067	0.067	0.084	0.090	0.077

*To calculate E/D_{avg}, for each pathlength, both E and D_{avg} were averaged over samples with different concentrations, as neither were dependent on $[Ag(I)_{initial}]$.

Analyses summarised in **Table 4-1**, **Table 4-2** and **Table 4-3** collectively show that modulation instability and filament formation in the Ag nanoparticle-doped organosiloxane is a dynamic process, which strongly depends on the pathlength of the sample. The ability to induce MI and self-induced waveguides at relatively short pathlengths compared with non-doped samples provides a unique opportunity to examine the behaviour of filaments at short propagation distances. Specifically, differences in the average filament separation distance D_{avg} suggest that the propagation, interactions and spatial organization of the filaments vary significantly with

pathlength (**Table 4-2**). We previously showed that interactions between a single pair of self-trapped incandescent white light beams depended on their separation distance [58]. Fusion was observed at separation distances corresponding to the width of each self-trapped beam whereas repulsion was observed at separation distances that were much greater than the beam width. Results of the current study show that interactions between the members of a large population of self-trapped incandescent filaments also varied with average separation distance. Direct evidence of these distance-dependent interactions was obtained through optical microscopy of the channel waveguide arrays induced by the self-trapped filaments (**Figure 4.10, Figure 4.11**).

Cross-sections of self-induced waveguide arrays obtained through modulation instability in the organosiloxane doped with Ag nanoparticles (**Figure 4.10**) and in a non-doped sample (**Figure 4.11**) were examined through optical microscopy. In the Ag nanoparticle-doped sample, self-trapped filaments formed after ~ 0.11 mm from the entrance face (**Figure 4.10b, d**). Waveguides within this short pathlength were tightly packed with a separation distance of ~14 μm; a magnified image in **Figure 4.10 c** provides evidence of the fusion of neighbouring filaments within this short propagation distance, which in turn caused the non-parallel propagation of the filaments. By comparison, waveguide arrays induced at sample pathlengths of 10 mm (in a non-doped sample) showed that the filament separation distance was much greater at 73 ± 2 μm (**Figure 4.11**). The greater separation distance also prevented fusion of filaments, which were observed to propagate in parallel through the sample (**Figure 4.11**). Because in this case, the separation distance of the filaments was greater than their average width (31 ± 5μm), repulsion is expected to be their dominant interaction [58]. This is consistent with the lack of fusion in these samples as

well as the parallel propagation of filaments, which maintain their large separation distance.

To account for the differences in the interactions between filaments, we first recall the mechanism of repulsion between an individual pair of self-trapped incandescent beams. A pair of self-trapping beams propagating in parallel repels by depleting the region in between of intensity. The increasing darkness (and decreasing refractive index) of this interstitial region prevents the flow of intensity between the two beams. Under these conditions, fusion, which requires a high-refractive index conduit between the two beams, is not possible. Instead, the interstitial region, which contains less intensity than it would under linear conditions, effectively causes repulsion of the beams. Because self-trapping efficiency (and thus intensity) of filaments is greater at longer pathlengths (**Table 4-3**), it is possible that they more rapidly deplete the interstitial regions of intensity. This would facilitate repulision, enabling their parallel propagation (**Figure 4.11**). By contrast, the less efficiently self-trapped (and less intense) filaments at smaller pathlengths cannot deplete the interstitial regions of intensity as effectively. This results in the two different types of interactions observed in proximal self-trapped beam pairs, fusion and filamentation (or branching).

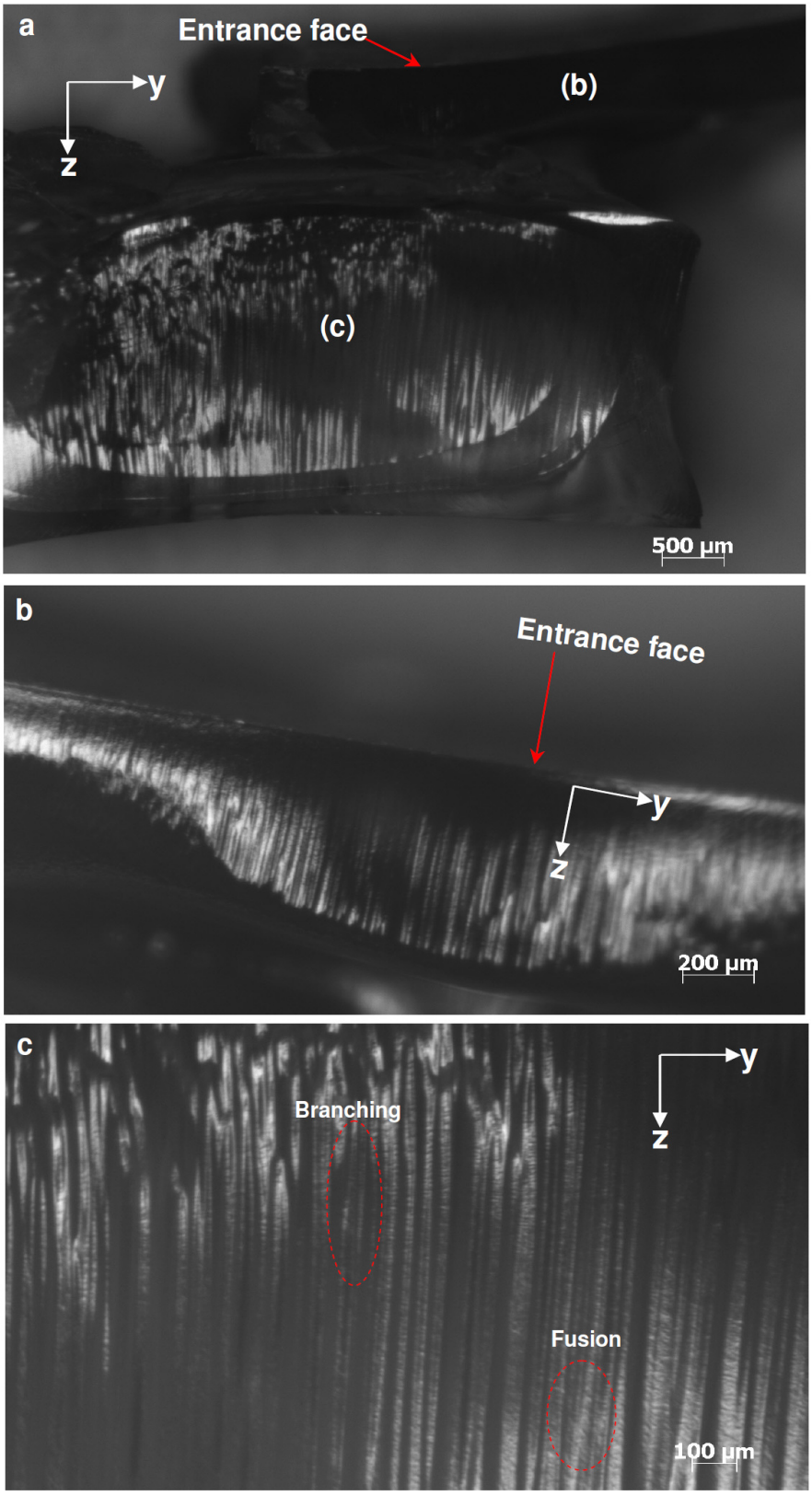
a
Entrance face
y
z
(b)
(c)
500 µm
b
Entrance face
y
z
200 µm
c
Branching
y
z
Fusion
100 µm

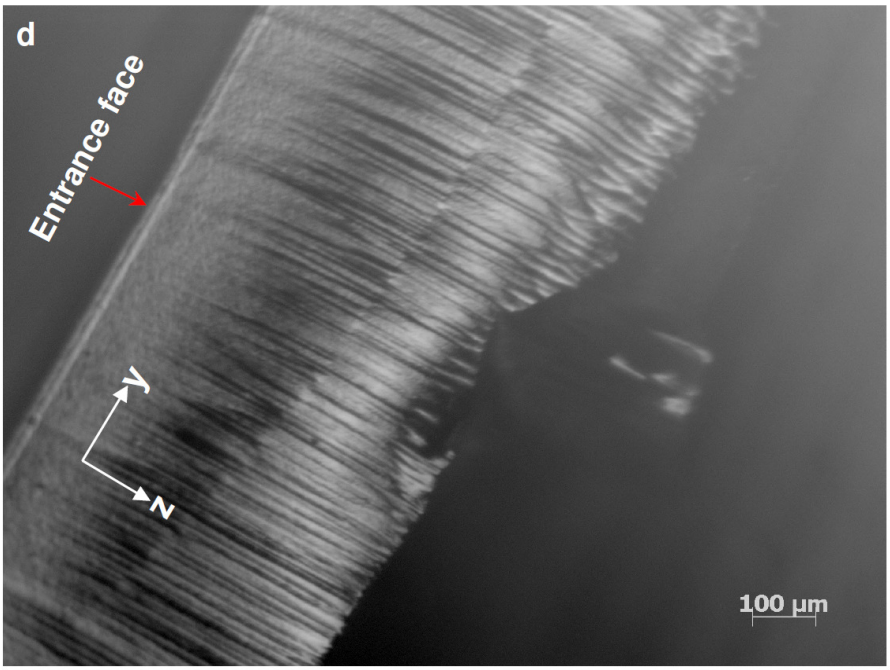

Figure 4.10 Transmission optical micrographs of waveguide arrays induced through modulation instability in an organosiloxane doped with Ag nanoparticles ($[Ag(I)_{initial}]$ = 4 ×10^{-3} M; sample pathlength = 4 mm. Incident intensity = 22 ×10^{-3} Wcm^{-2}. A low-magnification image (a) shows that the sample was split into two parts, which were then magnified in (b) and (c). The top edge of the thin piece (0.5 mm) of the sample in (b) corresponds to the entrance face of the sample. The bottom edge of image (c) is 2 mm from the sample entrance face. Image (d) is a cross-section close to the entrance face showing that MI filaments started to evolve after ~0.11 mm thickness in the Ag nanoparticle-doped sample.

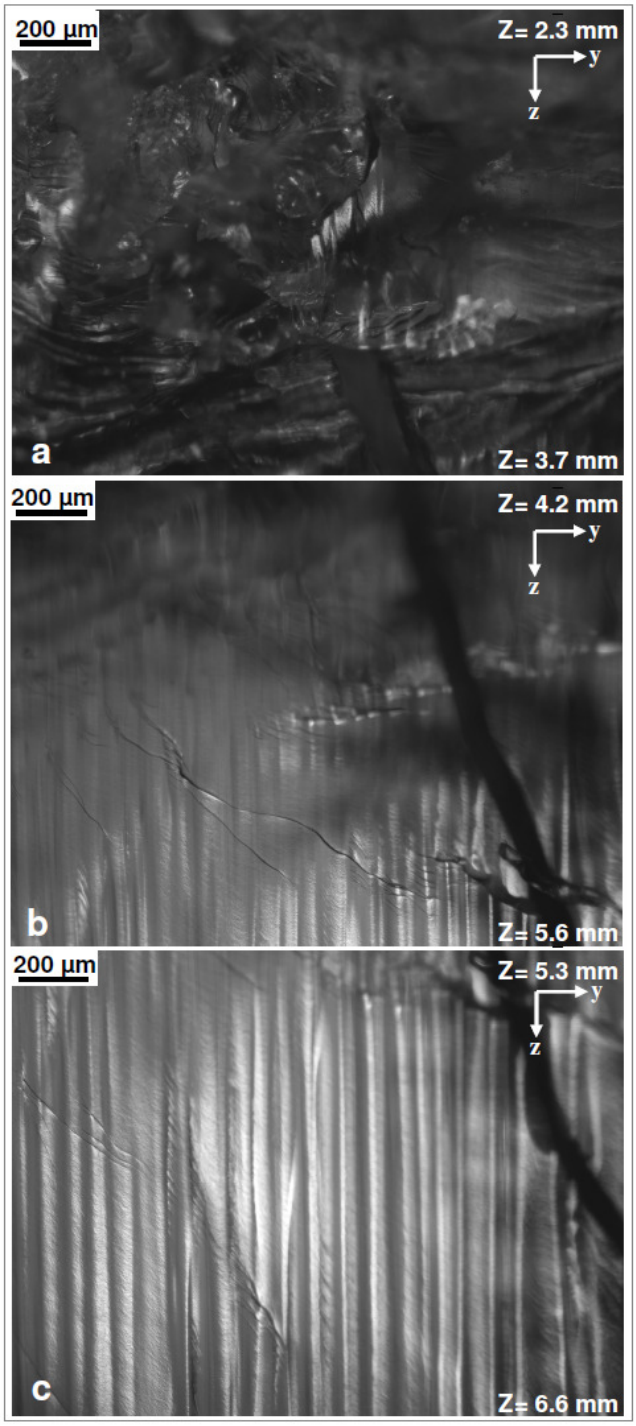

Figure 4.11 Transmission optical micrographs of waveguide arrays induced through modulation instability in an organosiloxane (sample pathlength = 10 mm. Incident intensity = 6×10^{-3} Wcm^{-2}.) (a) shows that self-induced

waveguides were not observed until after ~3 mm of propagation; (b) and (c) show that self-induced waveguides gradually appeared at longer distances and propagated in parallel over the rest of the sample.

4.4 Summary and outlook

We have demonstrated that arrays of metallodielectric waveguides can be obtained through MI of an incandescent beam propagating through a photopolmerisable Ag nanoparticle-doped medium. Careful examination of the dynamics of the nonlinear process as well as the resulting photoinduced metallodielectric microstructures showed that Ag nanoparticles play a critical role in eliciting MI. Specifically, MI and filamentation was observed at early pathlengths (~ 0.11 mm) in samples doped with metal nanoparticles whereas in non-doped samples, MI was observed only after ~ 3 mm. Conversely, self-trapped filaments in the metallodielectric samples did not propagate over very long distances (> 4.0 mm) due to attenuation of the beam resulting from scattering by Ag nanoparticles.

The ability to observed MI at very short pathlengths provided new opportunities to understand the dependence of MI dynamics on propagation distances. Specifically, the efficiency of self-trapping was found to be proportional to pathlength with filaments generated at short propagation paths carrying relatively less optical intensity. Interestingly, the population of filaments varied inversely with pathlength so that calculated values of the cumulative self-trapping efficiency for the entire filament population were constant at all propagation paths. Furthermore, micrographs of the waveguide arrays induced by the self-trapped filaments revealed a range of interactions such as fusion, branching and repulsion between filaments.

In addition to identifying an easily accessible route to arrays comprising thousands of metallodielectric cylindrical waveguides, our study provides fundamentally new insight into the dynamics of modulation instability and the interactions between a large population of spatially and temporally incoherent self-trapped filaments.

---

1. S. Link and M. A. El-Sayed, "Size and Temperature Dependence of the Plasmon Absorption of Colloidal Gold Nanoparticles," *J. Phys. Chem. B*, vol. 103, pp. 4212-4217, 1999.

2. C. Noguez, "Surface plasmons on metal nanoparticles: The influence of shape and physical environment," *J. Phys. Chem. C*, vol. 111, pp. 3806-3819, 2007.

3. M.-C. Daniel and D. Astruc, "Gold Nanoparticles: Assembly, supramolecular chemistry, Quantum-size-related properties, and applications toward biology, catalysis, and nanotechnology," *Chem. Rev.*, vol. 104, pp. 293-346, 2004.

4. K. L. Kelly, E. Coronado, L. L. Zhao, and G. C. Schatz, "The optical properties of metal nanoparticles: The influence of size, shape, and dielectric environment," *J. Phys. Chem. B* **107**(3), pp. 668-677 (2003).

5. A. Moores and F. Goettmann, "The plasmon band in noble metal nanoparticles: an introduction to theory and applications," *New. J. Chem.*, vol. 30, pp. 1121-1132, 2006.

6. L. M. Liz-Marzán, "Nanometals formation and color," *Materials Today*, vol. 7, pp. 26-31, 2004.

7. M. Rycenga, C. M. Cobley, J. Zeng, W. Li, C. H. Moran, Q. Zhang, D. Qin, and Y. Xia, "Controlling the synthesis and assembly of silver nanostructures for plasmonic applications," *Chem. Rev.*, vol. 111, pp. 3669-3712, 2011.

8. R. A. Farrer, F. L. Butterfield, V. W. Chen, and J. T. Fourkas, "Highly efficient multiphoton-abosorption-induced luminescence from gold nanoparticles," *Nano Lett.*, vol. 5, pp. 1139-1142, 2005.

9. A. Lin, D. H. Son, I. H. Ahn, G. H. Song, and W.-T. Han, "Visible to infrared photoluminescence from gold nanoparticles embedded in germano-silicate glass fiber," *Opt. Exp.*, vol. 15, pp. 6374-6379, 2007.

10. F. Hache, D. Ricard, and C. Flytzanis, "Optical nonlinearities of small metal particles: surface-mediated resonance and quantum size effects," *J. Opt. Soc. Am. B*, vol. 3, pp. 1647-1655, 1986.

11. J. R. F. Haglund, Jr., L. Yang, R. H. Magruder III, J. E. Wittig, K. Becker, and R. A. Zuhr, "Picosecond nonlinear optical response of a Cu:silica nanocluster composite," *Opt. Lett.*, vol. 18, pp. 373-375, 1993.

12. A. Manna, T. Imae, K. Aoi, M. Okada, and T. Yogo, "Synthesis of dendrimer-passivated noble metal nanoparticles in a polar medium: Comparison of size between silver and gold particles," *Chem. Mater.*, vol. 13, pp. 1674-1681, 2001.

13. O. M. Wilson, R. W. J. Scott, J. C. Garcia-Martinez, and R. M. Crooks, "Separation of dendrimer-encapsulated Au and Ag nanoparticles by selective extraction," *Chem. Mater.*, vol. 16, pp. 4202-4204, 2004.

14. L. M. Bronstein, D. M. Chernyshov, P. M. Valetsky, E. A. Wilder, and R. J. Spontak, "Metal nanoparticles grown in the nanostructured matrix of poly(octadecylsiloxane)," *Langmuir*, vol. 16, pp. 8221-8225, 2000.

15. S. Porel, S. Singh, S. S. Harsha, D. N. Rao, and T. P. Radhakrishnan, "Nanoparticle-embedded polymer: In situ synthesis, free-standing films with highly monodisperse silver nanoparticles and optical limiting," *Chem. Mater.*, vol. 17, pp. 9-12, 2005.

16. A. Dawn, P. Mukherjee, and A. K. Nandi, "Preparation of size-controlled, highly populated, stable, and nearly monodispersed Ag nanoparticles in an organic medium from a simple interfacial redox process using a conducting polymer," *Langmuir*, vol. 23, pp. 5231-5237, 2007.

17. K. Akamatsu, N. Tsuboi, Y. Hatakenaka, and S. Deki, "In situ spectroscopic and microscopic study on dispersion of Ag nanoparticles in polymer thin films," *J. Phys. Chem. B*, vol. 104, pp. 10168-10173, 2000.

18. K. Huber, T. Witte, J. Hollmann, and S. Keuker-Baumann, "Controlled formation of Ag nanoparticles by means of long-chain sodium polyacrylates in dilute solution," *J. Am. Chem. Soc.*, vol. 129, pp. 1089-1094, 2007.

19. B.-H. Sohn, J.-M. Choi, S. II. Yoo, S.-H. Yun, W.-C. Zin, J. C. Jung, M. Kanehara, T. Hirata, and T. Teranishi, "Directed self-assembly of two kinds of nanoparticles utilizing monolayer films of diblock copolymer micelles," *J. Am. Chem. Soc.*, vol. 125, pp. 6368-6369, 2003.

20. H. Xu, J. Xu, Z. Zhu, H. Liu, and S. Liu, "In-situ formation of silver nanoparticles with tunable spatial distribution at the poly(N-isopropylacrylamide) corona of unimolecular micelles," *Macromolecules*, vol. 39, pp. 8451-8455, 2006.

21. M. Malenovska, S. Martinez, M.-A. Neouze, and U. Schubert, "Growth of metal nanoparticles in a sol-gel silica thin film," *Eur. J. Inorg. Chem.*, vol. 18, pp. 2609-2611, 2007.

22. B. Zdyrko, M. K. Kinnan, G. Chumanov, and I. Luzinov, "Fabrication of optically active flexible polymer films with embedded chain-like arrays of silver nanoparticles " *Chem. Commun.* , pp. 1284, 2008.

23. R. G. Freeman, K. C. Grabar, K. J. Allison, R. M. Bright, J. A. Davis, A. P. Guthrie, M. B. Hommer, M. A. Jackson, P. C. Smith, D. G. Walter, and M. J.

Natan, "Self-assembled metal colloid monolayers: an approach to SERS substrates," *Science*, vol. 267, pp. 1629-1632, 1995.

24. Y. Lu, G. L. Liu, and L. P. Lee, "High-density silver nanoparticle film with temperature-controllable interparticle spacing for a tunable surface enhanced Raman scattering substrate," *Nano Lett.*, vol. 5, pp. 5-9, 2005.

25. N. Horimoto, N. Ishikawa, and A. Nakajima, "Preparation of a SERS substrate using vacuum-synthesized silver nanoparticles," *Chem. Phys. Lett.*, vol. 413, pp. 78-83, 2005.

26. A. D. McFarland and R. P. V. Duyne, "Single silver nanoparticles as real-time optical sensors with zeptomole sensitivity," *Nano Lett.*, vol. 3, pp. 1057-1062, 2003.

27. K.-S. Lee and M. A. El-Sayed, "Gold and silver nanoparticles in sensing and imaging: Sensitivity of plasmon response to size, shape and metal composition," *J. Phys. Chem. B*, vol. 110, pp. 19220-19225, 2006.

28. V. Morandi, F. Marabelli, V. Amendola, and M. Meneghetti, "Colloidal photonic crystals doped with gold nanoparticles: spectroscopy and optical switching properties," Adv. Funct. Mater. Vol. **17**, pp. 2779-2786, 2007.

29. Y. Tan, W. Qian, S. Ding, and Y. Wang, "Gold-nanoparticle-infiltrated polystyrene inverse opals: A three-dimensional platform for generating combined optical properties," Chem. Mater. Vol.18, pp. 3385-3389, 2006.

30. Y. Yang, G. P. Wang, J. Xie, and S. Zhang, "Metal nanoparticles-embedded three-dimensional microstructures created by single-beam holography," *Appl. Phys. Lett.*, vol. 86, pp. 173108, 2005.

31. M. Bockstaller, R. Kolb, and E. L. Thomas, "Metallodielectric photonic crystals based on diblock copolymers," *Adv. Mater.*, vol. 13, pp. 1783-1786, 2001.

32. A. Lin, X. Liu, P. R. Watekar, Y. Chung, and W.-T. Han, "Ag nanocrystal-incorporated germano-silicate optical fiber with high resonant nonlinearity," *App. Phys. Lett.*, vol. 93, pp. 021901, 2008.

33. A. Lin, X. Liu, P. R. Watekar, W. Zhao, B. Peng, C. Sun, Y. Wang, and W.-T. Han, "All-optical switching application of germano-silicate optical fiber incorporated with Ag nanocrystals," *Opt. Lett.*, vol. 34, pp. 791-793, 2009.

34. A. Lin, B. H. Kim, S. Ju, and W.-T. Han, "Fabrication and third-order optical nonlinearity of germano-silicate glass optical fiber incorporated with Au nanoparticles," *Proc. SPIE*, vol. 6481, pp. 64810M, 2007.

35. L. Qiu, J. Franc, A. Rewari, D. Blanc, and K. Saravanamuttu, "Photolytic formation of Ag nanoparticles in oligomeric organosiloxanes: new photolithographic routes to metallodielectric microperiodic structures," *J. Mater. Chem.*, vol. 19, pp. 373-378, 2009.

36. I. B. Burgess, W. E. Shimmell, and K. Saravanamuttu, "Spontaneous Pattern Formation Due to Modulation Instability of Incoherent White Light in a Photopolymerizable Medium," *J. Am. Chem. Soc.*, vol. 129, pp. 4738-4746, 2007.

37. I. B. Burgess, M. R. Ponte, and K. Saravanamuttu, "Spontaneous formation of 3-D optical and structural lattices from two orthogonal and mutually incoherent beams of white light propagating in a photopolymerisable material," *J. Mater. Chem.*, vol. 18, pp. 4133-4139, 2008.

38. T. Schwartz, T. Carmon, H. Buljan, and M. Segev, "Spontaneous pattern formation with incoherent white light," *Phys. Rev. Lett.*, vol. 93, pp. 223901, 2004.

39. H. Buljan, A. Siber, M. Soljacic, and M. Segev, "Propagation of incoherent "white" light and modulation instability in noninstantaneous nonlinear media," *Phys. Rev. E*, vol. 66, pp. 035601(R), 2002.

40. D. Kip, M. Soljacic, M. Segev, E. Eugenieva, and D. N. Christodoulides, "Modulation instability and pattern formation in spatially incoherent light beams," *Science*, vol. 290, pp. 495-498, 2000.

41. D. Kip, M. Soljacic, M. Segev, S. M. Sears, and D. N. Christodoulides, "(1+1)-Dimensional modulation instability of spatially incoherent light," *J. Opt. Soc. Am. B*, vol. 19, pp. 502-512, 2002.

42. M. Soljacic, M. Segev, T. Coskun, D. N. Christodoulides, and A. Vishwanath, "Modulation instability of incoherent beams in noninstantaneous nonlinear media," *Phys. Rev. Lett.* , vol. 84, pp. 467-470, 2000.

43. Z. Chen, J. Klinger, and D. N. Christodoulides, "Induced modulation instability of partially spatially incoherent light with varying perturbation periods," *Phys. Rev. E*, vol. 66, pp. 66601, 2002.

44. Z. Chen and K. McCarthy, "Spatial soliton pixels from partially incoherent light," *Opt. Lett.*, vol. 27, pp. 2019-2021, 2002.

45. S. M. Sears, M. Soljacic, D. N. Christodoulides, and M. Segev, "Pattern formation via symmetry breaking in nonlinear weakly correlated systems," *Phys. Rev. E*, vol. 65, pp. 036620, 2002.

46. M. Mitchell and M. Segev, "Self-trapping of incoherent white light," *Nature*, vol. 387, pp. 880-883, 1997.

47. J. Zhang, K. Kasala, A. Rewari, and K. Saravanamuttu, "Self-Trapping of Spatially and Temporally Incoherent White Light in a Photochemical Medium," *Journal of the American Chemical Society*, vol. 128, pp. 406-407, 2006.

48. J. Zhang and K. Saravanamuttu, "The dynamics of self-trapped beams of incoherent white light in a free-radical photopolymerizable medium," *J. Am. Chem. Soc.*, vol. 128, pp. 14913-14923, 2006.

49. G. I. Stegeman and M. Segev, "Optical Spatial Solitons and Their Interactions: Universality and Diversity," *Science*, vol. 286, pp. 1518-1523, 1999.

50. Trillo, S.; Torruellas, W., *Spatial Solitons*. New York, 2001.

51. T. M. Monro, C. M. De Sterke, and L. Poladian, "Topical review - Catching light in its own trap," *Journal of Modern Optics*, vol. 48, pp. 191-238, 2001.

52. A. W. Snyder and D. J. Mitchell, "Accessible Solitons," *Science*, vol. 276, pp. 1538-1541, 1997.

53. L. Qiu and K. Saravanamuttu, "Optical self-trapping in a photopolymer doped with Ag nanoparticles: a single-step route to metallodielectric cyclindrical waveguides," *J. Am. Opt. Soc. B*, vol. 29, pp. 1085-1093, 2012.

54. J. A. Dean, *Lange's Handbook of Chemistry,* 15 ed. (McGraw-Hill, 1999).

55. Measurements from optical micrographs of the microstructured samples were approximate and usually smaller than the measurement from the intensity profiles captured during the experiment, due to surface inhomogeneities that developed when samples were extracted from the sample cell and to shrinkage of the sample caused by condensation of residual silicon alkoxide and silanol groups upon exposure to atmosphere moisture.

56. Incidence light for MI experiment (irradiated from Lamp A) was applied as the probing beam for transmission spectroscopy. Spectra were collected at the exit face of the sample.

57. In this study, overlap between absorption by photoinitiator and Ag nanoparticles was dominant. By avoiding such overlap (e. g, by using a beam of shorter wavelength), waveguide should be able to form over longer distance despite the high doping concentration.

58. K. Kasala and K. Saravanamuttu, "An experimental study of the interactions of self-trapped white light beams in a photopolymer," *Appl. Phys. Lett.*, vol **93**(5), 051111, 2008.

Chapter 5 Effect of Ag nanoparticles on diffraction rings induced by spatial self-phase modulation

Abstract

Another form of nonlinear light propagation — spatial self-phase modulation induced diffraction rings, was elicited in the photopolymerisable organosiloxane containing Ag nanoparticles. Effect of Ag nanoparticles on developing of diffraction rings has been examined: Presence of Ag nanoparticles shortened the sample distance (comparing to non-Ag doped sample) where the diffraction rings induced from spatial self-phase modulation can be fully developed without being affected by near-field diffractions. And it was found that by increasing the doping concentration, the sample pathlength within which diffraction rings could be well developed was shortened. On the other hand, in samples with longer pathlength, presence of Ag nanoparticles enhanced the effect from the competitive optical self-trapping, causing incomplete developing of diffraction rings.

5.1 Introduction

One efficient and simple approach to micro-structured photopolymers, that has been demonstrated by work in our group [1;2;3;4;5;6], is through spontaneous self-inscriptions induced by nonlinear forms of light propagation, which rely on the refractive index change induced by photo-induced polymerisation in a photopolymerisable medium. Furthermore, by doping Ag nanoparticles in the photopolymerisable material [7], micro-structured metallodielectric composites have been subsequently fabricated through the nonlinear forms of light propagation. Specifically, Ag nanoparticle doped 1-D optical fiber waveguides have been created through a narrow beam self-trapping [8]; Ag nanoparticle doped 2-D arrays of optical

waveguides have been produced through the spontaneous filamentation induced by modulation instability of a broad beam [9]. At the same time, the influence on those two forms of nonlinear light propagation, i.e. optical self-trapping and modulation instability, from doped Ag nanoparticles has been examined. Here, we further studied effects of Ag nanoparticles on another form of nonlinear light propagation in the photopolymerisable system: diffraction rings induced by spatial self-phase modulation.

Below is a brief introduction of diffraction rings induced by spatial self-phase modulation.

In a medium which shows localized refractive index response to optical intensity, upon incidence with a coherent Gaussian beam, a corresponding Gaussian refractive index profile is induced. The nonlinear phase buildup across the transverse direction of the beam ($\Delta\psi(\rho)$) due to induced refractive index change can be expressed as [10;11]:

$$\Delta\psi(\rho) = \Delta\psi_0 \exp(-\frac{2\rho^2}{\omega^2}) \qquad \textbf{5-1}$$

Where ρ denotes the radial coordinate, $\Delta\psi_0$ the maximum value of phase shift and ω is the beam radius at the entrance face of the medium.

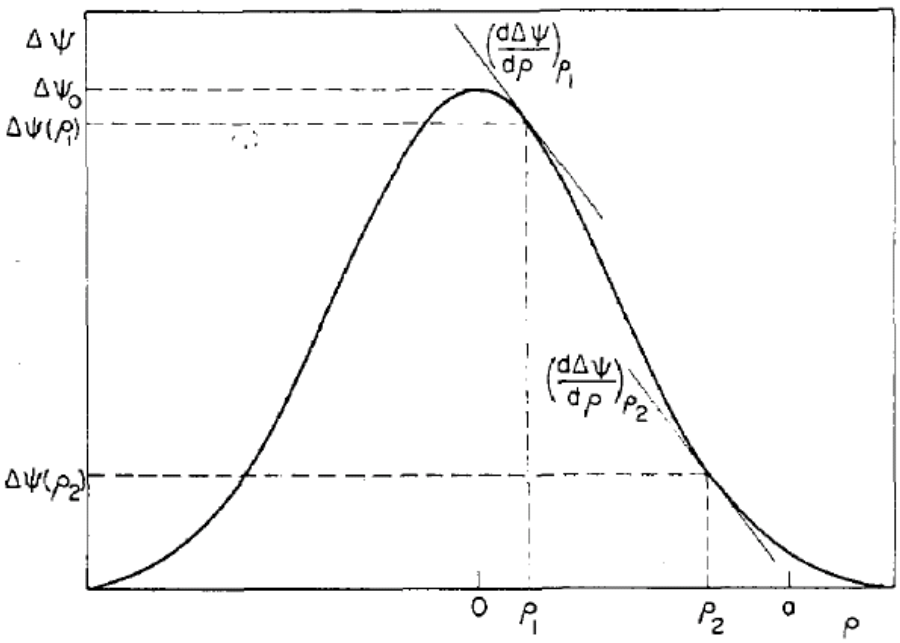

Figure 5.1 Schematic of the phase shift profile induced by a Gaussian beam in nonlinear medium. Besides, Light from position r_1 and r_2 have the same slope (that is, same transverse wavevector), and therefore interfere. Figured is reprinted from [11]. Reprinted with permission of OSA.

Based on **Equation 5-1,** Durbin *et al.* plotted the phase shift profile of a Gaussian beam propagating in a nonlinear medium (**Figure 5.1**). The slope at each point along the profile is corresponding to the transverse wavevector $k_\perp = (d\Delta\psi/d\rho)_\rho$ of the light scattered there. As illustrated in **Figure 5.1**, light at ρ_1 and ρ_2 have the same transverse wavevector, and therefore interfere with each other. The maximum interference occurs where $\Delta\psi(r_1) - \Delta\psi(r_2) = m\pi$. Depending on whether even or odd the integer *m* is, constructive or destructive interference forms, respectively. The former results in enhancement of brightness, while the latter a decrease (or complete cancelation) of the intensity. Bright and dark concentric interference cones are thus induced from the cylindrically symmetric profile

of $\Delta\psi(\rho)$, which are shown as diffraction rings when observed at transverse plane at far-field plane (i.e. distance ≫ Rayleigh range (z_R)). Theoretically, the number of diffraction rings is proportional to the maximum phase shift $\Delta\psi_0$, i.e.

$$N \approx \frac{\Delta\psi_0}{2\pi} \qquad \textbf{5-2}$$

Self-phase modulation induced diffraction rings have been studied in various materials, such as glasses or liquids with thermally dependent refractive response [10;12;13;14], atomic vapours [15;16;17;18], dye-doped materials [19;20;21], liquid crystals [11;22;23], Kerr media [24;25], and photorefractive crystals [26].

Our group has reported self-phase modulation induced diffraction rings with a Gaussian beam (532 nm) in photopolymerisable organosiloxanes, in which refractive index change originates from the photo-initiated free radical polymerization [6]. The empirically derived expression of refractive index change through photopolymerization at an optical field E is [27]:

$$\Delta n(\rho,z,t) = \Delta n_s \left\{1-\exp[-\frac{1}{U_0}\int_0^{t-\tau}\left|E(\rho,z,t)\right|^2 dt]\right\}, \qquad \textbf{5-3}$$

where Δn_s is the maximum refractive index change (that is achieved at saturation of polymerization), U_0 the critical exposure required to initiate photopolymerization, τ the monomer-radical lifetime, and $E(\rho,z,t)$ the amplitude of the optical field at a particular point (ρ,z) at time t. This equation indicates that refractive index change Δn increases with light exposure, until the maximum refractive index change Δn_s is reached, and it

takes short (long) time to reach the maximum refractive index change Δn_s with high (low) intensity beams. According to **Equation 5-2**, in order to form diffraction rings, the maximum phase shift has to satisfy $\Delta\psi_0 \geq 2\pi$. According to previous experiments carried out by Villafranca in non-Ag doped organosiloxanes, diffraction rings occur only within certain intensity range: at low intensity, where $\Delta\psi_0$ is insufficient ($< 2\pi$), only self-trapping/self-focusing occur; whereas, at very high intensities, $\Delta\psi_0$ can be also lost due to the overall saturation of polymerisation across the beam [5].

Spatial self-phase modulation for diffraction rings originates at the very beginning of the sample medium [28]. In nonlinear media with virtually instantaneous refractive responses (e.g. the femtosecond response in a Kerr medium), developing of diffraction rings is prevented in thick samples (where optical path length > Rayleigh length (Z_R)) due to the disruption from the simultaneous self-focusing/trapping of the beam. Diffraction rings can be induced only in thin samples and be observed at a far-field plane out of the sample media (e.g. in air). On the contrary, the non-instantaneous refractive responses due to photopolymerization (which ranges from milliseconds to seconds) allows diffraction rings to be observed in thick samples, due to the delay of the onset of the competitive self-focusing/trapping of the beam. According to Villafranca's explaination [6], it can be assumed that at the very early time of irradiation, the refractive index change and the corresponding phase shift of the beam occurs mainly near the entrance face (where optical path length < Z_R) and index changes beyond this range are negligible; as a result, the self-phase modulation induced interference cones that originate near the entrance face propagate and diverge linearly through the rest of the sample medium and are observed as rings on the exit face.

The relatively slow refractive responses in the photopolymerisable medium also made it possible to conduct dynamic studies of the diffraction rings by observing their temporal evolutions [6].

5.2 Experimental

5.2.1 Preparation of organosiloxane sols doped with Ag nanoparticles

Ag nanoparticle-doped organosiloxane sols were prepared through the same methods as described in previous chapters [7;8;9]. Briefly, hydrolysis and condensation of 3-methacryloxypropyl trimethoxysilane (MAPTMS, 0.020 mol) was initiated by catalyzing with H_2O (0.0150 mol) acidified with HCl (0.0135 mmol). The majority of Cl^- ions in the resulting sol were precipitated by adding $AgNO_3$ solution (0.0100 mmol). The resulting AgCl precipitate was filtered out through a polyetrafluoroethylene (PTFE) membrane (0.2 μm pore size), resulting in residual $[Cl^-] = 7\times10^{-4}$ M. A series of sols with [AgCl] of $\sim7\times10^{-4}$ M and $[AgNO_3]$ of 1 mM, 2 mM, and 8 mM were then prepared by adding various amounts of $AgNO_3$. Because $[Ag^+][Cl^-]\sim10^{-6}$ in the sol is >> than the solubility product, $K_{sp} = [Ag^+][Cl^-]=1.77\times10^{-10}$ [29], AgCl existed as insoluble grains in the sol. The immediate formation of AgCl precipitates was inhibited due to the high free energy barrier for crystal nucleation at the low concentration of AgCl. The resulting sols therefore remained stable and transparent for up to 2 days.

Ag nanoparticles in the organosiloxane sols were generated through photoreduction of AgCl grains to elemental Ag. Upon 3 hours' irradiation with a 23 W fluorescent light (Noma® mini spiral bulbs), the colourless sol turned dark brown. Formation of Ag nanoparticles was confirmed through absorption spectrum (acquired with a Cary 50 Bio UV-Visible spectrometer), The resulting sol was orange brown, with extinction band peaking at 454 nm (**Chapter 4, Figure 4.1 a)**, which mainly corresponds to the dipolar mode

plasmon of Ag nanoparticles; TEM micrographs show that the average size of Ag nanoparticles were 53± 15 nm (**Chapter 4, Figure 4.1** b).

5.2.2 Preparation of samples for diffraction rings

Prior to optical experiments, the free-radical photo-initiator (bis(η^5cyclopentandienyl) bis(2,6-difluoro-3-(1H-pyrrol-yl)-phenyl) titanium(IV) (λ_{max} = 393 nm, 460 nm, Ciba Specialty Chemicals Inc., Canada), which had been dissolved with the hydrolyzed MAPTMS sol, was introduced into the Ag-nanoparticle doped sol to photosensitize the methacrylate substitutes of the organosiloxanes. Volume ratio between the Ag-nanoparticle doped and photo-initiator dissolved sol was 1:1, and the concentration of photo-initiator in the resulting mixture was 0.5% wt. The sols then had a total concentration [$Ag(I)_{initial}$] = 0.8 mM ~ 4 mM.

For optical experiment, sample was injected through a small perforation into a cylindrical sample cell (inner diameter = 12 mm, cell pathlength varied from 2.0 mm to 6.0 mm), which was made by gluing microscope coverslips to either side of a plastic (Delrin) ring.

TO achieve localized optical responses in the sample medium, the initial liquid sample sol was partially gelled by a partial photopolymerization, with a uniform irradiation of white light emitted by a quartz-tungsten-halogen lamp (400 nm - 740 nm， ~ 4 min at 8 mW· cm^{-2}).

5.2.3 Optical assembly

Self-phase modulation induced diffraction rings was carried out on the same optical assembly used for optical self-trapping [as described in Chapter 2, and illustrated in **Appendix I**] [5;8]. Briefly, the TEM_{00} mode (Gaussian beam, M2 < 1.1), continuous wave, visible (532 nm) light emitted by a diode-

pumped solid-state laser (Verdi V5 Coherent, Inc., CA, USA) was employed as the irradiation source. The beam diameter and output power were 2.25 mm and 100 mW, respectively. The beam was attenuated to 5 μw after passing it through a half-wave plate, a quarter-wave plate, a neutral density filter and a set of polarizing beam splitter cubes. Before incidence to sample, the beam was focused by a planoconvex lens to a spot of 20 μm (in diameter) onto the entrance window of the sample cell and the resulting incidence intensity was 1.6 W/cm^2. To avoid the effect from wavefront curvature of the input beam [30;31], the entrance face of the sample was positioned at the center of the beam waist (where curvature of the beam $R \rightarrow \infty$).

The 2-D (x, y) intensity profile of the beam at the exit face of the cell was projected and imaged by a pair of planoconvex lenses onto a high-resolution charge-coupled device (CCD) camera (736(H) x 484(V) pixels, pixel size 4.80 μm (H) x 5.58 μm (V); LaserCam IIID 1/4", Coherent Inc, CA, USA). Combinations of neutral density filters (F) mounted on three separate rotatable wheels (VARM, Coherent Inc.) were placed between imaging lenses L2 and L3 to prevent over exposure of the CCD camera.

5.3 Results and discussion

5.3.1 Experimental evidence and temporal evolution of spatial self-phase modulation induced diffraction rings

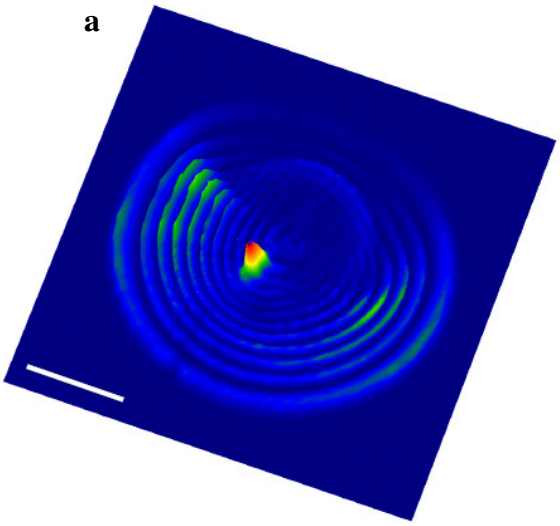

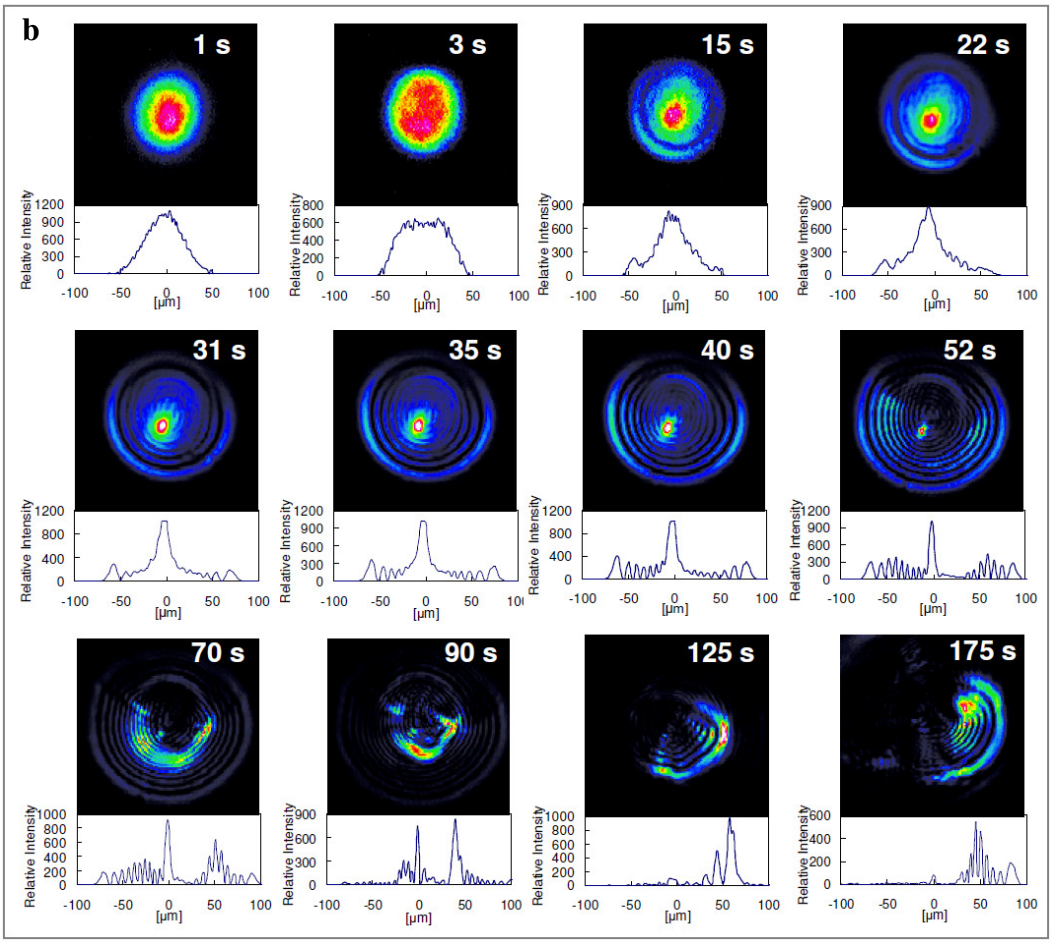
b
1 s
3 s
15 s
22 s
31 s
35 s
40 s
52 s
70 s
90 s
125 s
175 s
Relative Intensity
[μm]

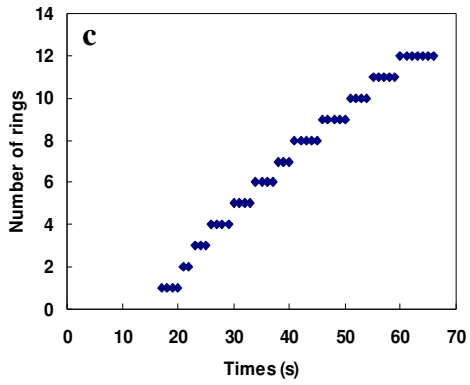
c
Number of rings
Times (s)

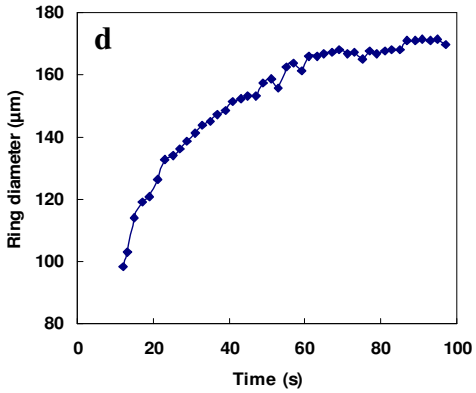
d
Ring diameter (μm)
Time (s)

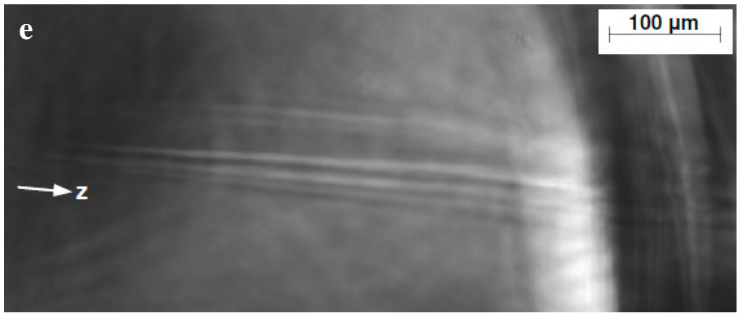

Figure 5.2 (a) 3-D spatial intensity profile of the diffraction rings induced by spatial self-phase modulation of the continuous wave, visible laser beam (532 nm) in the Ag-nanoparticle doped photopolymerisable organosiloxane (scale bar = 50 µm). The image was obtained at the 52th second of irradiation. (b) A set of the temporal 2D and corresponding 1D intensity profiles of the beam showing the temporal evolution of the diffraction rings. (c) Variation of the number of diffraction rings and (d) diameter of the outmost ring observed at the exit face as a function of the irradiation time. (e) The transmission optical micrograph of the longitudinal cross-section (i.e. along the direction of beam propagation) of the sample obtained after the diffraction-ring experiment. For the diffraction-ring experiment, optical intensity = 1.6 W/cm^2, [Ag(I)$_{initial}$] = 1 × 10^{-3} M, and sample pathlength = 4.0 mm.

Figure 5.2a demonstrates the intensity profile of the diffraction rings formed at the exit face of the Ag-nanoparticle doped organosiloxane, with the incidence of an continuous wave, visible laser beam (532 nm). As forming of diffraction rings requires a maximum phase shift across the beam $\Delta\psi_0 \geq 2\pi$, relatively higher input beam intensity (1.6 W/cm^2) has to be applied, which was 2~3 orders of the intensity required to induce optical self-trapping [5, 8]. In this typical experiment, the beam was focused to 20 µm at the entrance face (z = 0.0 mm) of the transparent cell (pathlength = 4.0 mm) containing the Ag-nanoparticle doped photopolymer ([Ag(I)$_{initial}$] = 1 ×10^{-3} M.

Due to the non-instantaneous photoresponse in the photopolymerisable organosiloxane, temporal evolution of the diffraction rings could be traced

and recorded. As shown in **Figure 5.2b**, the focused beam initially diverged from 20 μm at the entrance face to ~88 μm at the exit face (z = 4.0 mm); within 15 s, a single bright ring developed from the outer edge of the beam, indicating that the photopolymerization induced Δn had been sufficient to induce a maximum phase shift $\Delta\psi_0 \geq 2\pi$, and a constructive interference had been enabled from the inflection point of the $\Delta\psi(\rho)$ curve [11]. Overtime, an increasing number of diffraction rings were observed, until after 60 s, a maximum of 12 rings formed [**Figure 5.2b, c**]. According to **Equation 5-3**, this is due to the continuous increase of the maximum phase shift $\Delta\psi_0$ that was induced by the continuously increased refractive index change Δn during photopolymerization. Similarly, the eventual saturation of the number of diffraction rings indicated the saturation of the photopolymerization of the methacrylate groups in the organosiloxane matrix. As the maximum phase shift $\Delta\psi_0$ was increasing, the slope at the inflection point of the phase-shift profile curve (Figure 5.1), i.e. $(d\Delta\psi / d_{\triangle}\rho)_{\max}$ was also increasing, which was reflected by the increasing diameter (D) of the outermost ring (**Figure 5.2**d), as D is related to half-angle [32]

$$\beta = \arctan(D/2z) \approx (d\Delta\psi(\rho)/d\rho)_{\max}\lambda/2\pi, \qquad \textbf{5-4}$$

where z is the distance from the origin of the diffraction rings to the observing plane, which is approximately the sample pathlength in our experiment. The steepening of the gradient at the inflection point of the phase-shift profile curve(i.e. increasing slope) was expected for a Gaussian beam incidence to a medium with localized and intensity dependent refractive index response, since a faster change of refractive index Δn is induced at closer to the center of the beam where the beam is more intense.

Developing of diffraction rings was accompanied with the self-focusing/trapping of the beam [**Figure 5.2b**, 15 s ~ 70 s], which started at as

early as the 10th second. it appeared as the high intensity spot near the center of the diffraction rings, which continuously narrowed down to 14 μm at the 55th s (recall that diameter of the beam was ~88 μm at the very beginning of incidence, and the diameter of the outmost ring was ~ 150 μm at this time), and increased from 650 in intensity to >988 (camera detector saturated at this point). The center self-trapping beam stayed until ~the 70th s, when it crashed to multiple large speckles scattered off the center. Despite the crashing of self-trapping, the overall optical intensity turned to be more and more confined near beam center, resulting in simultaneous decreasing of intensity in the outer layer rings [**Figure 5.2 b**, 70 s, and 90 s], which became invisible after 125 s [**Figure 5.2 b**, 125 s]. However, the inner layer of diffraction rings kept being illuminated by the crashed beam and stayed visible until the 175th s.

After the laser beam irradiation, transmission optical micrograph of the longitudinal cross-section of the sample indicated the formation of multi-layered cone structures within the sample (**Figure 5.2 e**).

5.3.2 Comparing with spatial self-phase modulation induced diffraction rings in non-Ag- nanoparticles doped organosiloxanes

To investigate effect of doped Ag- nanoparticle on developing of diffraction-rings, controlled experiments were performed in non-Ag nanoparticle doped organosiloxanes.

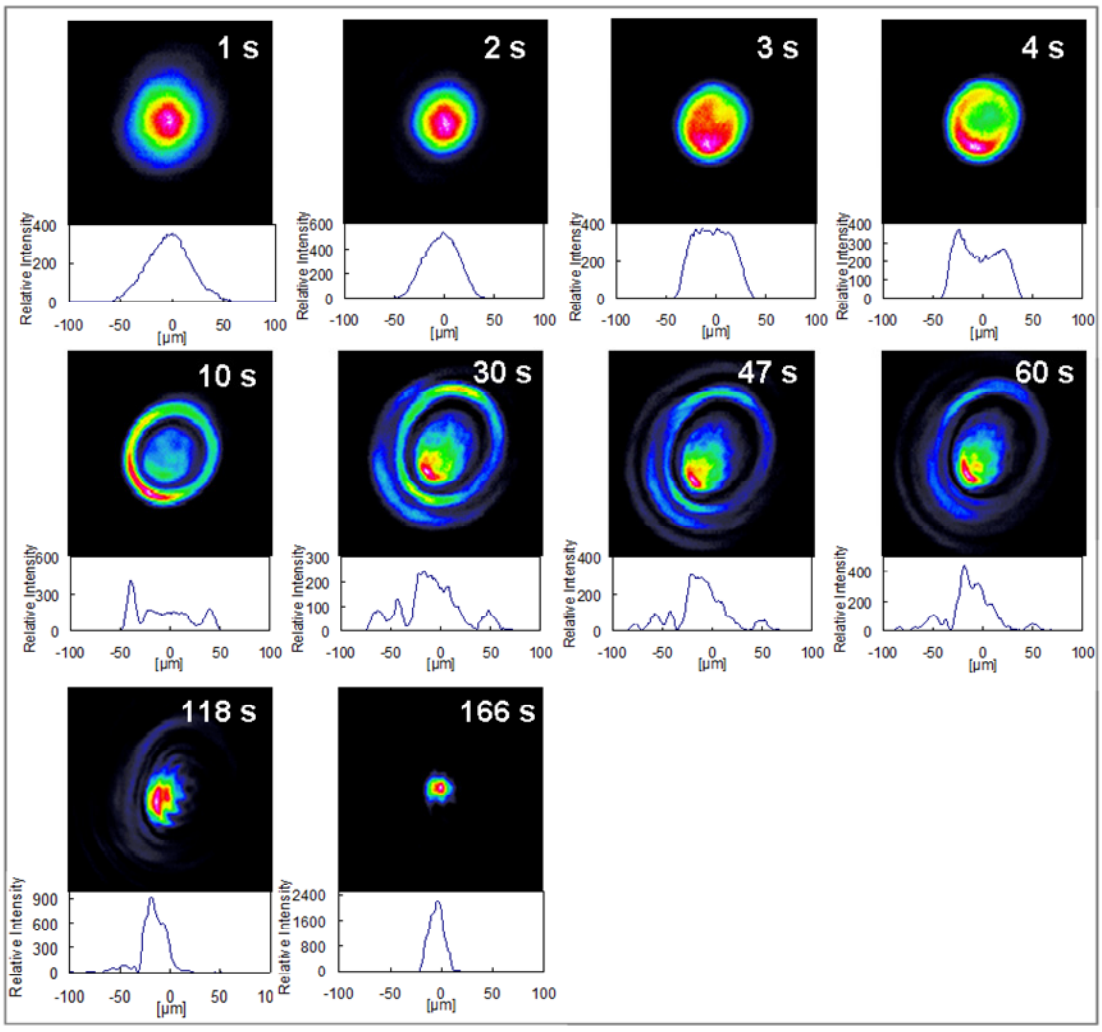

Figure 5.3 Temporal evolution of diffraction rings in non-Ag doped organosiloxane with sample pathlength of 4.0 mm. Temporal variations of 2-D and 1-D spatial intensity profiles of the beam at the exit face are presented. For the diffraction-ring experiment, optical intensity = 1.6 W/cm^{-2}; $[Ag(I)_{initial}] = 0$.

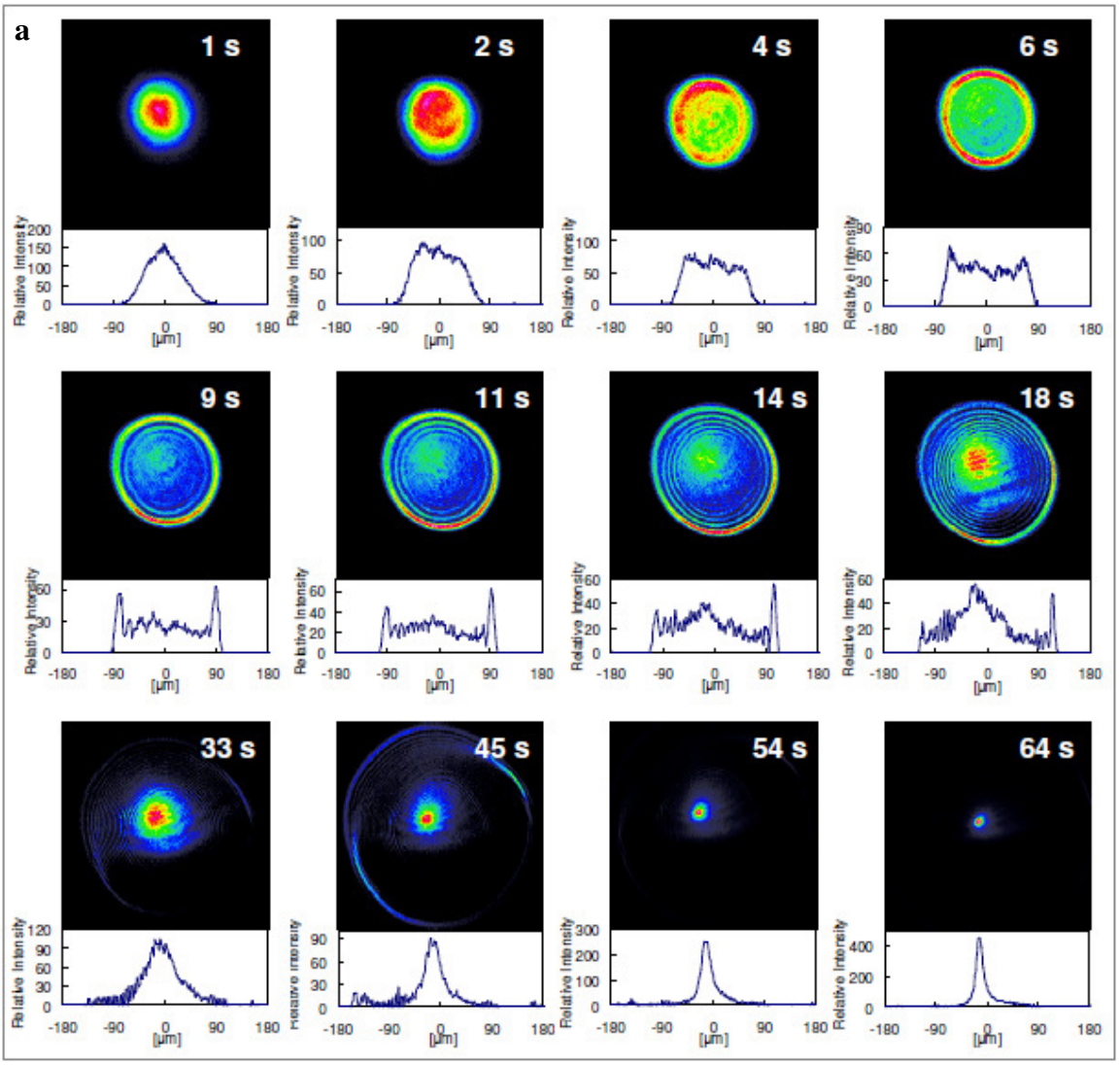
a
1 s
2 s
4 s
6 s
9 s
11 s
14 s
18 s
33 s
45 s
54 s
64 s
Relative Intensity
[μm]

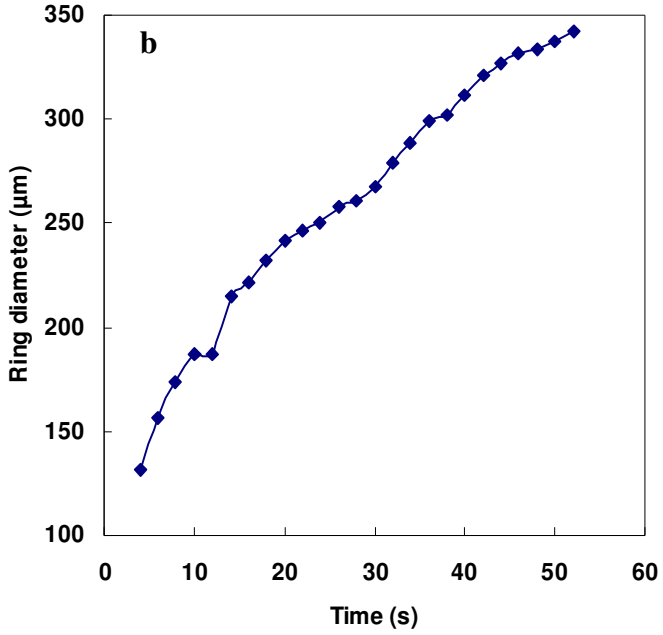

Figure 5.4 (a) Temporal evolution of diffraction rings in non-Ag doped organosiloxane with sample pathlength of 6.0 mm. Temporal variations of 2-D and 1-D spatial intensity profiles of the beam at the exit face are presented. (b) Diameter of the outermost ring at the exit-face of the sample as a function of irradiation time. For the diffraction-ring experiment, optical intensity = 1.6 W/cm^2; [Ag(I)$_{initial}$] = 0.

Figure 5.3 shows a typical diffraction ring experiment in non-Ag-nanoparticle doped organosiloxanes with a sample pathlength of 4 mm, where less diffraction rings (the maximum of 6 rings) formed comparing with the maximum of 11 rings observed in the Ag-nanoparticle doped organosiloxanes with the same sample pathlength. Besides, the developed rings appeared to be thicker than rings developed in Ag-nanoparticle doped sample. In this sample, self-focusing and self-trapping developed rather slowly, and the bright narrow spot didn't appear until ~118 s [**Figure 5.3**, 118 s]. Overtime, optical intensity of the propagating beam continued to be concentrated to the bright spot, which by 166s, had narrowed down in diameter from ~39 μm (at 118 s) to 29 μm, and increased in intensity from

~900 (at 118 s) to ~2350. At this moment, self-trapping became the only dominant process that could be observed by the camera [**Figure 5.3** 166 s].

As mentioned in the introduction section, the major refractive index change contributing to self-phase modulation for diffraction rings originates from the very beginning of the nonlinear sample medium (<< Z_R) [6; 11; 28]. Previous experiments by Villafranca proved that diffraction rings can be induced in the photopolymerisable organosiloxane within a thickness ≤ 0.56 mm: when the diffraction-ring experiment was carried out in a thin sample with a pathlength of only 0.56 mm, and the spatial intensity profile of the beam at a far-field plane (which was 46 mm to the entrance plane, and therefore in air) was captured, similar maximum number of diffraction rings was observed, comparing with that observed at the exit face of a sample with 6 mm pathlength [6]. However, previous studies also showed that evolving of diffraction rings is impeded at near-field, where Fresnel diffraction dominates: formation of diffraction rings is affected by the wavefront curvature of the beam, resulting in either non-developing or partial developing of the diffraction rings [6]. According to Villafranca's observation, near-field diffraction takes significant effect within 4 mm pathlength in the non-Ag doped organsiloxane [6]. As shown in **Figure 5.3**, diffraction-rings were only partially developed with a broad bright center. In contrast, in sample(non-Ag doped) with pathlength of 6 mm, far-field diffraction dominated, therefore, more rings (maximum number of 19 rings) with finer structures were observed at the exit face (**Figure 5.4 a**).

Comparing **Figure 5.2**, **Figure 5.3**, and **Figure 5.4a,** evolving of diffraction rings in Ag-nanoparticle doped sample with 4 mm pathlength seems to be more similar to that in non-Ag nanoparticle doped sample with 6 mm pathlength, where far-field (Fraunhofer) diffractions dominates. This indicates that presence of Ag nanoparticles in the medium shortens the near-

field range. Besides diffraction rings, self-focusing/trapping which later became dominant over diffraction rings (e.g., **Figure 5.3** 166 s and **Figure 5.4a** 54 s) is also affected by Ag nanoparticles: In Ag-nanoparticle doped sample, though self-focusing started as early as the 10^{th} second, it crashed at ~the 70^{th} s before it became dominant over diffraction rings [**Figure 5.2b**] .

5.3.3 Pathlength dependence on developing of diffraction-rings in Ag – nanoparticle doped organosiloxane

To further investigate propagation of diffraction-rings in organosiloxanes doped with Ag-nanoparticles, experiments were then carried out at other sample-pathlengths, specifically, 2 mm and 6 mm.

As shown in **Figure 5.5a**, when pathlength of the Ag-nanoparticle doped sample ($[Ag(I)_{initial}] = 1 \times 10^{-3}$ M) was decreased to 2 mm, developing of diffraction rings appeared to be hindered, which, as explained by Villafranca's study, was due to the dominant near-field diffraction within this short pathlength [6]. In rare cases, where diffraction rings did developed (as shown in **Figure 5.5b**, where a maximum of 4 rings were observed), an inhomogeneity of the medium (either due to an uneven pre-irradiation induced non-uniform prepolymerization of the organosiloxane medium, or due to a local high concentration or aggregation of Ag nanoparticles) is assumed, as evidenced by both the non-centered ring structures and the strong filamentation (**Figure 5.5 b**, 117 s).

a) Pathlength = 2 mm, $[Ag(I)_{initial}] = 1 \times 10^{-3}$ M

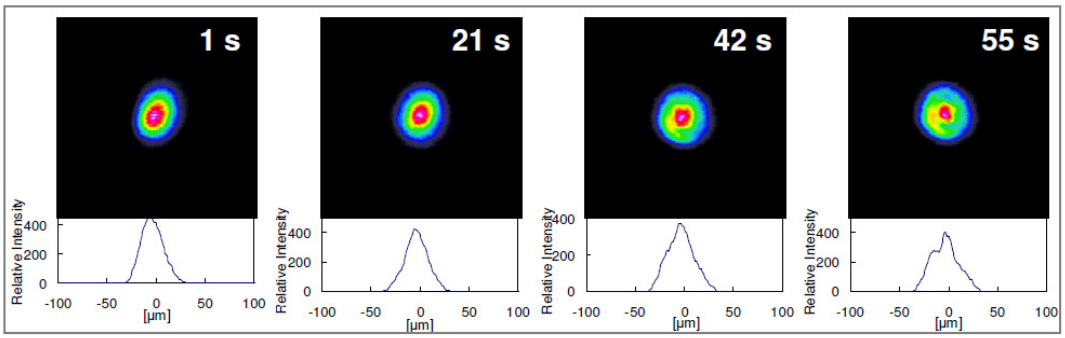

b) Pathlength = 2 mm, $[Ag(I)_{initial}] = 1 \times 10^{-3}$ M

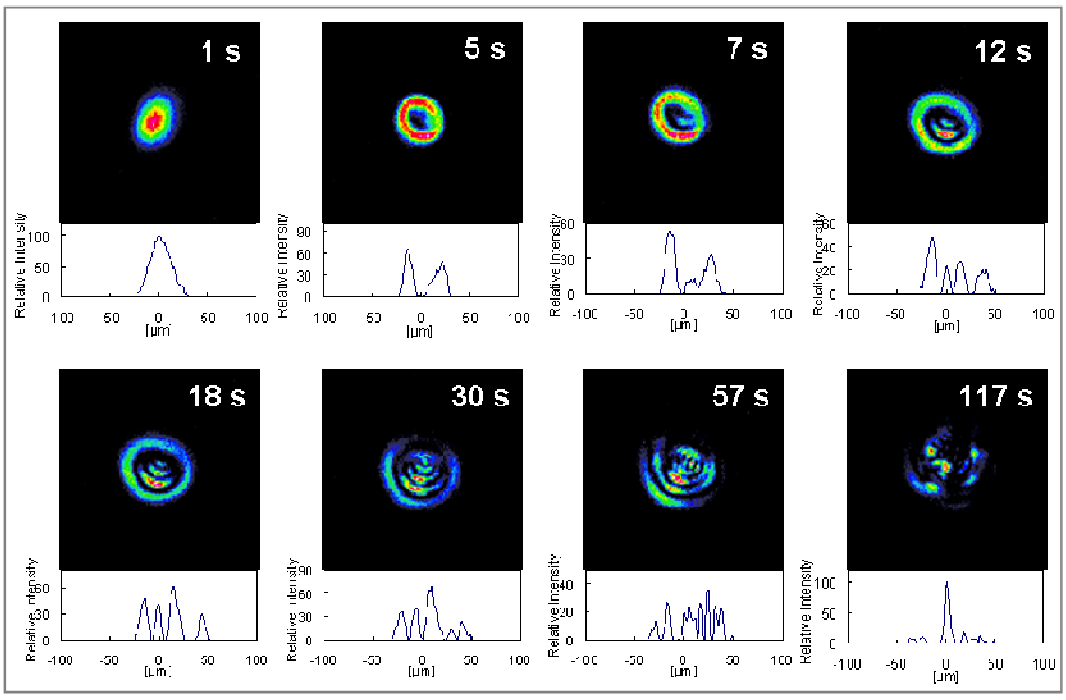

Figure 5.5 Temporal evolution of diffraction rings in organosiloxanes doped with Ag nanoparticles ($[Ag(I)_{initial}] = 1 \times 10^{-3}$ M) with a sample pathlength of 2.0 mm. Temporal variations of 2-D and 1-D spatial intensity profiles of the beam at the exit face are presented. a) shows the result as observed in most experiments, where no diffraction rings were observed; b) shows the rare case where a few diffraction rings appeared. For the diffraction-ring experiment, optical intensity=1.6 W/cm^2.

In the Ag nanoparticle doped sample, while at short pathlength (e.g., 2 mm), the formation of diffraction-ring is affected by the near-field diffraction, at long sample pathlength (e.g., 6 mm), complete evolving of diffraction rings is significantly hindered by the competitive self-focusing/trapping process. The two sets of temporal spatial intensity profiles as shown in **Figure 5.6**, respectively corresponding to two different types of diffraction rings evolved in the Ag-nanoparticle doped sample ($[Ag(I)_{initial}] = 1 \times 10^{-3}$ M) with 6 mm pathlength, were neither completely developed.

In **Figure 5.6a**, upon incidence, the beam initially expanded and developed a diffraction ring with diameter of 122 μm within 3 seconds. From the 11th second, diffraction rings started to shrink quickly from 118 μm to 62 μm at the 31th second (**Figure 5.6b**). It continued shrinking until at the 44th s, the whole beam was focused to a spot of 28 μm in width.

In **Figure 5.6c**, the beam spot at the exit face had shrunk significantly from 117 μm to 79 μm[1] before diffractions rings appeared (**Figure 5.6c** 3 s-10 s, **Figure 5.6d)**. Two diffraction rings firstly evolved simultaneously at the 10th second. Diameter of the outmost ring stayed above 67 μm until the 14th s (**Figure 5.6**c 14 s). Then it narrowed down quickly to ~ 35 μm within the next 14 s (**Figure 5.6**c, 18s~28 s). After that, it oscillated between 49 μm and 38 μm until the 64th s (**Figure 5.6**c 31~64 s), and then further narrowed down to ~ 29 μm at the 78th s (**Figure 5.6**c 78 s). After that, the shrunk rings continued oscillating in size between 38 μm and 56 μm until the beam completely crashed and broke into multiple speckles after 114th s (not shown

[1] In order to compare beam size with diameter of the outmost diffraction ring, instead of using efficient beam width ($1/e^2$), diameter of the edge of the beam spot was used.

here). During this experiment, while two rings initially appeared simultaneously, unlike the outmost ring, which stayed until self-trapping became dominant, the inner ring oscillated in and out. Besides, there appeared a center bright spot at the 21th second, which also oscillated in and out. Oscillation of the inner ring and the center bright spot indicated there was a simultaneous mode oscillation of the self-trapping beam, which overlapped with diffraction rings. This is evidenced by the obvious optical mode, for example, the LP_{21} mode at the 55th s (**Figure 5.6 c** 55s).

In both cases, shrinking (**Figure 5.6**b and d) of the diffraction rings occurred, which was not observed in either Ag-doped organosiloxane with shorter sample pathlengths (**Figure 5.2, Figure 5.5**) or the non-Ag doped organosiloxanes at all sample pathlengths under study (**Figure 5.3**, **Figure 5.4**, and **Ref 30)**. Complete development of diffraction rings was thus hindered and much less number of rings was observed, probably due to the much more competitive optical self-trapping in the Ag-doped medium with long sample-pathlength.

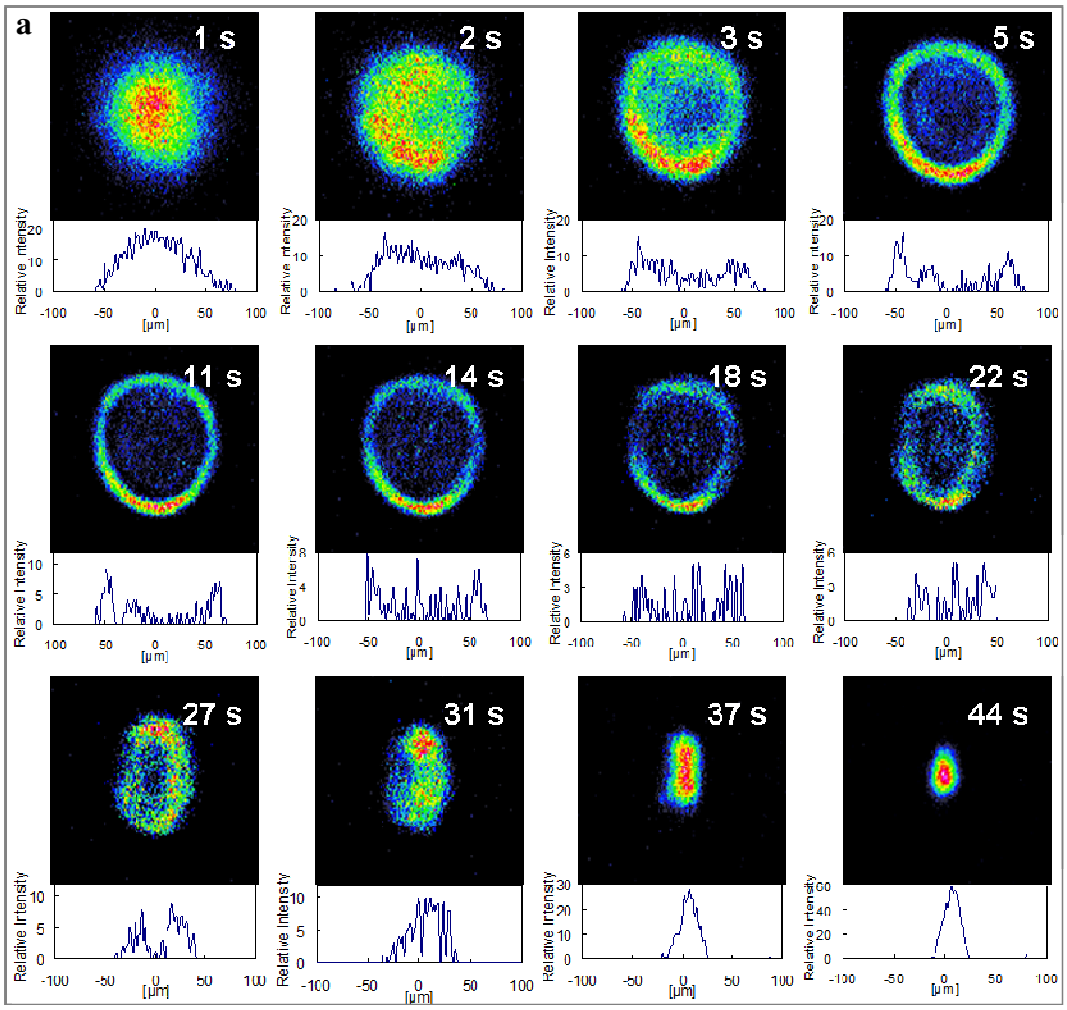
a
1 s
2 s
3 s
5 s
11 s
14 s
18 s
22 s
27 s
31 s
37 s
44 s
Relative Intensity
[μm]

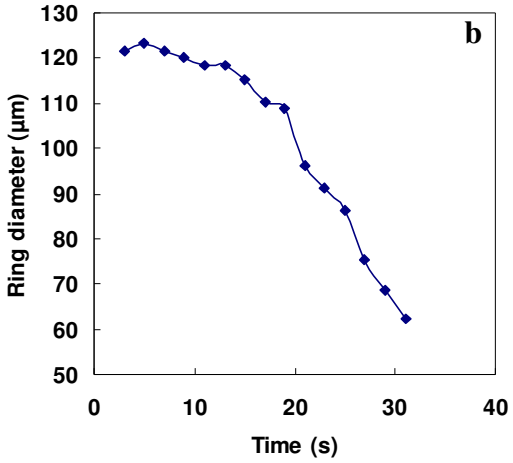
b
Ring diameter (μm)
Time (s)
130
120
110
100
90
80
70
60
50
0
10
20
30
40

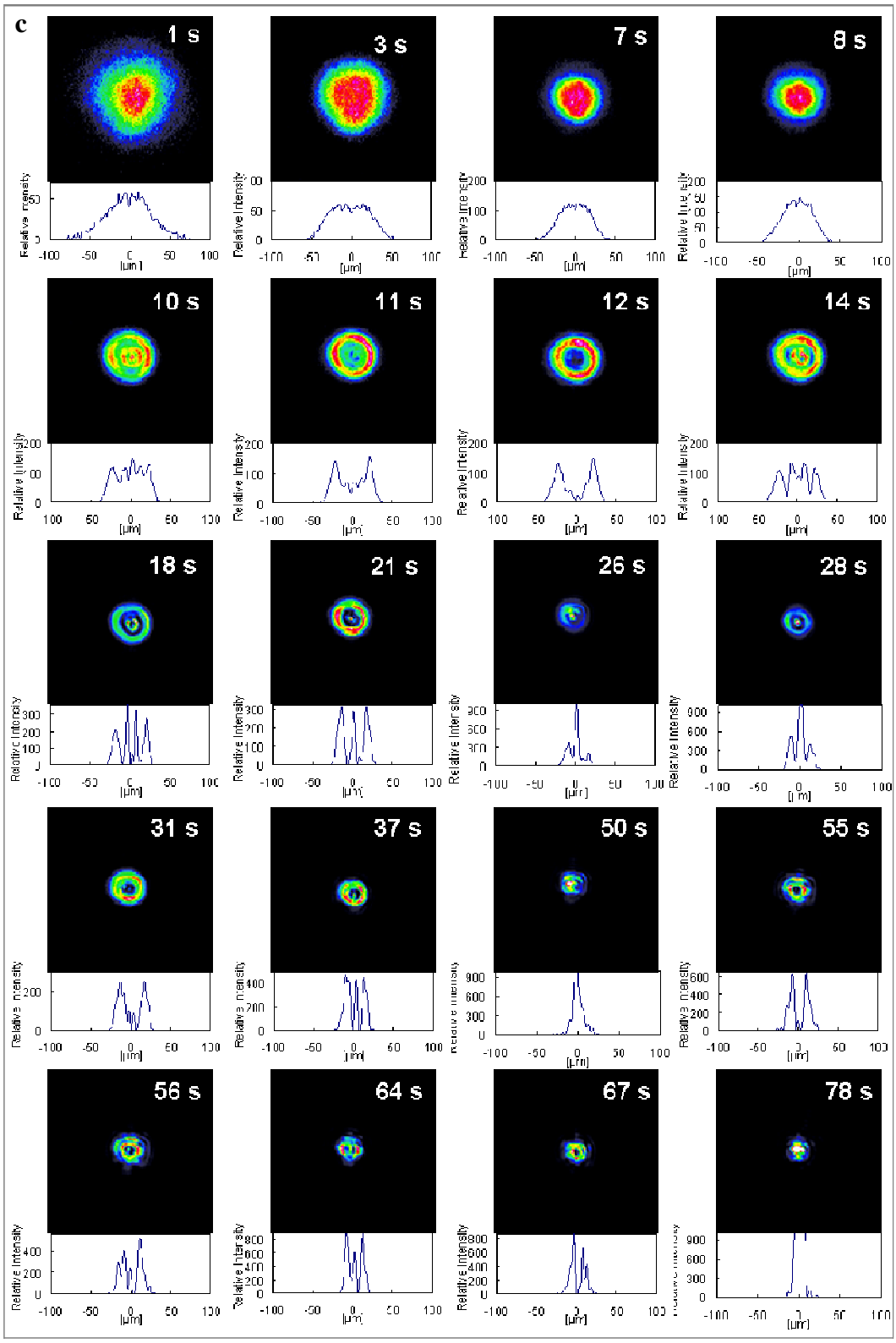
c
1 s
3 s
7 s
8 s
10 s
11 s
12 s
14 s
18 s
21 s
26 s
28 s
31 s
37 s
50 s
55 s
56 s
64 s
67 s
78 s
Relative Intensity
[μm]

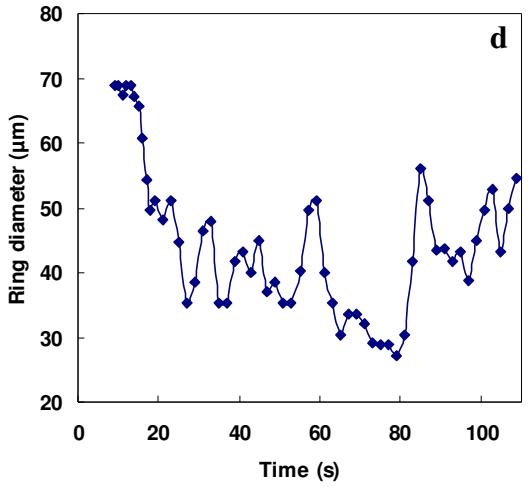

Figure 5.6 Temporal evolution of diffraction rings in organosiloxanes doped with Ag nanoparticles ($[Ag(I)_{initial}] = 1 \times 10^{-3}$ M) with a sample pathlength of 6.0 mm. Temporal variations of 2-D and 1-D spatial intensity profiles of the beam at the exit face are presented. Different types of diffraction rings have been observed as demonstrated respectively in (a) and (c); (b) and (d) are temporal plots of the diameter of the outmost ring in (a) and (c), respectively. Optical intensity=1.6 W/cm^2.

5.3.4 Evolving of diffraction rings in sample with high doping concentration of Ag –nanoparticles

As described above, unlike in un-doped sample, where evolving of diffraction rings was affected by near-field diffraction up to a pathlength of 4 mm, in sample doped with Ag nanoparticles ($[Ag(I)_{initial}] = 1 \times 10^{-3}$ M), well developed diffraction rings have been observed at sample pathlength of 4 mm [**Figure 5.2**]. However, when sample pathlength was shortened to 2 mm, near-field diffraction became dominated in the Ag-nanoparticle doped sample (at a doping concentration of $[Ag(I)_{initial}] = 1 \times 10^{-3}$ M) and hindered developing of diffraction rings. Here, to further investigate the effect from the doping concentration of Ag nanoparticles on the diffraction-ring formation, the diffraction-ring experiment was further performed in 2 mm sample with high doping concentration of $[Ag(I)_{initial}] = 4 \times 10^{-3}$ M. As shown in **Figure**

5.7a, ring-structures appeared at 11th s and expanded continuously within the next 82s to reach a maximum number of >23 rings with the diameter of the outmost ring of 278 μm, which can be assumed as from the dominant far-field diffraction. On the other hand, high doping concentration of Ag nanoparticles caused fragmentation of diffraction rings. Especially, serious filamentation occurred at near the center of the beam. Besides, as shown in **Figure 5.7b**, upon beam incidence, a > 411 times decreasing in optical intensity of beam at the exit face of the sample medium occurred within the first 91 seconds. Such dramatic intensity decrease indicated significant increase of optical extinction from Ag nanoparticles. This is very possibly due to the strong optical field induced aggregation of Ag nanoparticles at such high doping concentration. The very broken rings (filamentation/fragmentation of the beam) as mentioned above also indicated the poor homogeneity of the sample medium caused by aggregation of Ag nanoparticles.

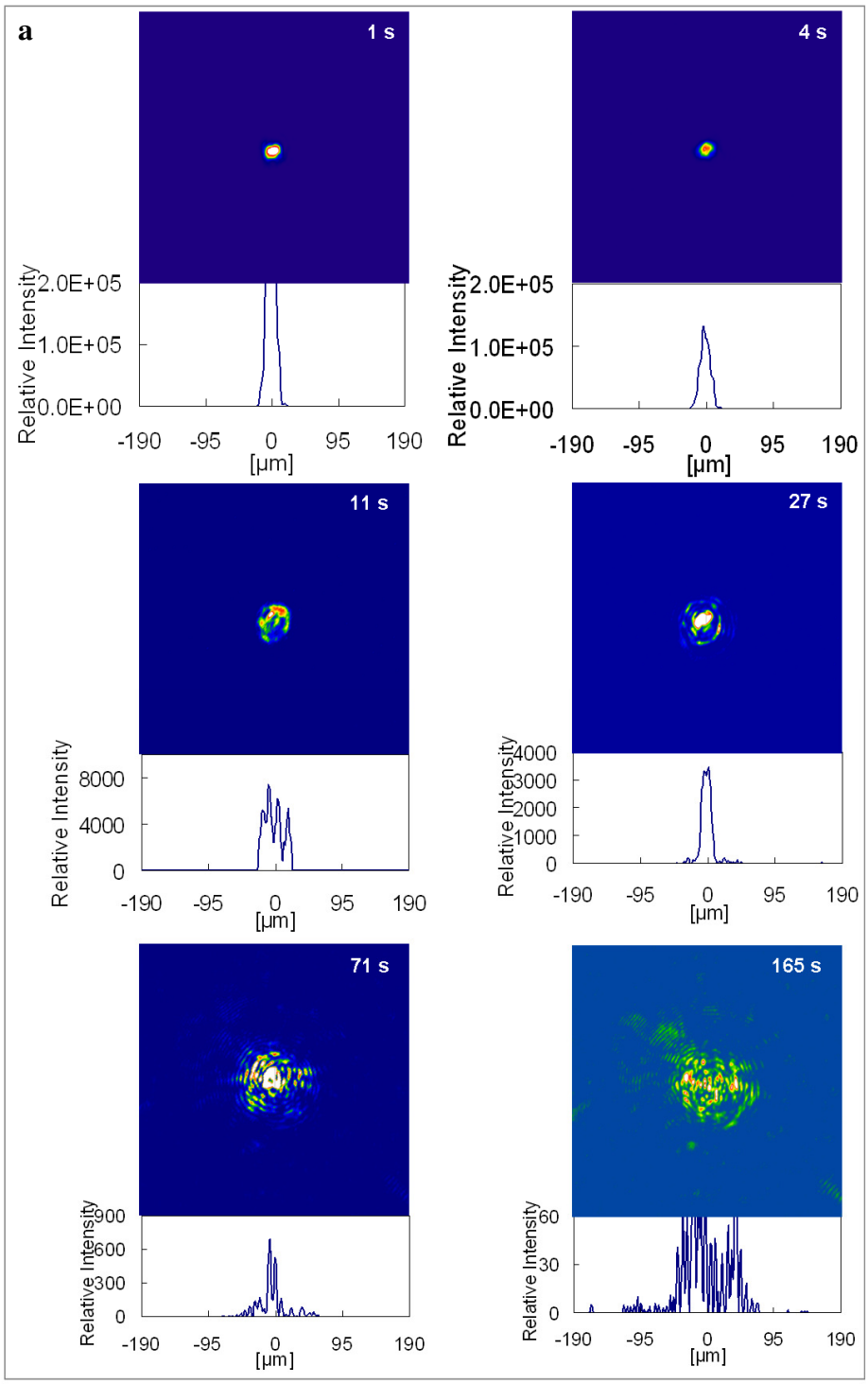
a
1 s
4 s
11 s
27 s
71 s
165 s
Relative Intensity
2.0E+05
1.0E+05
0.0E+00
8000
4000
0
4000
3000
2000
1000
900
600
300
60
30
-190
-95
0
95
190
[µm]

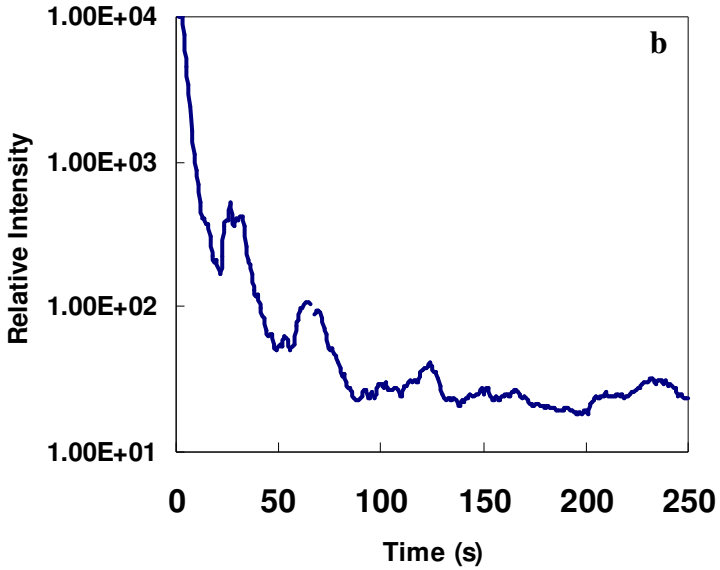

Figure 5.7 (a)Temporal evolution of diffraction rings in organosiloxanes doped with Ag nanoparticles ($[Ag(I)_{initial}] = 4 \times 10^{-3}$ M) with a sample pathlength of 2.0 mm; (b) Plot of the temporal intensity during beam incidence. Optical intensity = 1.6 W/cm^2.

5.4 Summary

Here, we studied effect of doped Ag-nanoparticles on spatial self-phase modulation induced diffraction rings. In a previous study by Villafranca in non-Ag nanoparticle doped organosiloxanes, complete formation of diffraction-rings was found to be hindered by near-field diffraction at pathlengths of up to 4 mm. Doping of Ag-nanoparticles in the medium shortened the distance where the near-field diffraction took in-ignorable effect, and well developed diffraction rings have been observed in sample with pathlength of 4 mm at doping concentration of $[Ag(I)_{initial}] = 1 \times 10^{-3}$ M. When further increasing doping concentration to $[Ag(I)_{initial}] = 4 \times 10^{-3}$ M, complete evolving of diffraction rings were even observed in sample with 2 mm sample-length. On the other hand, when sample pathlength of the Ag-nanoparticle doped sample was increased to 6 mm, evolving of diffraction

rings was seriously affected by the competitive self-focusing/trapping, and the few developed rings quickly shrunk without further development of diffraction rings. This had never been observed in the non-Ag doped organosiloxanes of pathlength up to 10 mm.

---

1. J. Zhang, K. Kasala, A. Rewari, and K. Saravanamuttu, "Self-Trapping of Spatially and Temporally Incoherent White Light in a Photochemical Medium," Journal of the American Chemical Society **128**, 406-407 (2006).
2. J. Zhang and K. Saravanamuttu, "The dynamics of self-trapped beams of incoherent white light in a free-radical photopolymerizable medium," J. Am. Chem. Soc. **128**(46), 14913-14923 (2006).
3. I. B. Burgess, W. E. Shimmell, and K. Saravanamuttu, "Spontaneous Pattern Formation Due to Modulation Instability of Incoherent White Light in a Photopolymerizable Medium," J. Am. Chem. Soc. **129**, 4738 (2007).
4. I. B. Burgess, M. R. Ponte, and K. Saravanamuttu, "Spontaneous formation of 3-D optical and structural lattices from two orthogonal and mutually incoherent beams of white light propagating in a photopolymerisable material," J. Mater. Chem. **18**, 4133 (2008).
5. A. B. Villafranca and K. Saravanamuttu, "An experimental study of the dynamics and temproal evolution of self-trapped laser beams in a photopolymerizable organosiloxane," J. Phys. Chem. C **112**, 17388-17396 (2008).
6. A. B. Villafranca and K. Saravanamuttu, "Diffraction rings due to spatial self-phase modulation in a photopolymerizable medium," J. Opt. A: Pure Appl. Opt. **11**, 125202 (2009).
7. L. Qiu, J. Franc, A. Rewari, D. Blanc, and K. Saravanamuttu, "Photolytic formation of Ag nanoparticles in oligomeric organosiloxanes: new

photolithographic routes to metallodielectric microperiodic structures," J. Mater. Chem. **19**, 373-378 (2009).

8. L. Qiu and K. Saravanamuttu, "Optical self-trapping in a photopolymer doped with Ag nanoparticles: a single-step route to metallodielectric cyclindrical waveguides," J. Am. Opt. Soc. B (2012), accepted.

9. L. Qiu and K. Saravanamuttu, Paper in manuscript.

10. F. W. Dabby, T. K. Gustafson, J. R. Whinnery, Y. Kohanzadeh, and P. L. Kelley, "Thermally self-induced phase modulation of laser beams," Appl. Phys. Lett. **16**(9), 362-365 (1970).

11. S. D. Durbin, S. M. Arakelian, and Y. R. Shen, "Laser-induced diffraction rings from a nematic-liquid-crystal film," Opt. Lett. **6**(9), 411-413 (1981).

12. X. Yang, S. Qi, C. Zhang, K. Chen, X. Liang, G. Yang, T. Xu, Y. Han, and J. Tian, "The study of self-diffraction of mercury dithizonate in polymer film," Opt. Comm. **256**, 414-421 (2005).

13. W. R. Callen, B. G. Huth, and R. H. Pantell, "Optical patterns of thermally self-defocused light," Appl. Phys. Lett. **11**(3), 103-105 (1967).

14. R. G. Harrison, L. Dambly, D. Yu, and W. Lu, "A new self-diffraction pattern formation in defocusing liquid media," Opt. Comm. **139**(1-3), 69-72 (1997).

15. M. L. Berre, E. Ressayre, A. Tallet, K. Tai, H. M. Gibbs, M. C. Rushford, and N. Peyghambarian, "Continuous-wave off-resonance rings and continuous-wave on-resonance enhancement," J. Opt. Soc. Am. B **1**(4), 591-605 (1984).

16. D. Grischkowsky, "Self-focusing of light by potassium vapor," Phys. Rev. Lett. **24**(6), 866-869 (1970).

17. A. C. Tam, "Strong amplification of sidebands in self-focused laser beams in an atomic vapor," Phys. Rev. A **19**(5), 1971-1977 (1979).

18. Y. H. Meyer, "Multiple conical emissions from near resonant laser propagation in dense sodium vapor," Opt. Comm. **34**(3), 439-444 (1980).

19. G. R. Kumar, B. P. Singh, and K. K. Sharma, "Continuous-wave self-diffraction in dye-doped glasses," J. Opt. Soc. Am. B **8**(10), 2119-2127 (1991).
20. M. Trejo-Durán, J. A. Andrade-Lucio, A. Martínez-Richa, R. Vera-Graziano, and V. M. Castaño, "Self-diffracting effects in hybrid materials," Appl. Phys. Lett. **90**, 091112 (2007).
21. R. M. Sundari and P. K. Palanisamy, "Self-diffraction and Z-scan studies in organic dye doped thin films," Appl. Surf. Sci. **252**, 2281-2287 (2006).
22. N. F. Pilipetski, A. V. Sukhov, N. V. Tabiryan, and B. Y. Zel'Dovich, "The orientational mechanism of nonlinearity and the self-focusing of He-Ne laser radiation in nematic liquid crystal mesophase (theory and experiment)," Opt. Comm. **37**(4), 280-284 (1981).
23. E. Santamato and Y. R. Shen, "Field-curvature effect on the diffraction ring pattern of a laser beam dressed by spatial self-phase modulation in a nematic film," Opt. Lett. **9**(12), 564-566 (1984).
24. H.-J. Zhang, J.-H. Dai, P.-Y. Wang, and L.-A. Wu, "Self-focusing and self-trapping in new types of Kerr media with large nonlinearities," Opt. Lett. **14**(13), 695-696 (1989).
25. C. M. Nascimento, M. A. R. C. Alencar, S. Chávez-Cerda, M. G. A. d. Silva, M. R. Meneghetti, and J. M. Hickmann, "Experimental demonstration of novel effects on the far-field diffraction patterns of a Gaussian beam in a Kerr medium," J. Opt. A: Pure Appl. Opt. **8**, 947-951 (2006).
26. W. Wan, S. Jia, and J. W. Fleischer, "Dispersive superfluid-like shock waves in nonlinear optics," Nature Physics **3**, 46-51 (2006).
27. A. S. Kewitsch and A. Yariv, "Self-focusing and self-trapping of optical beams upon photopolymerization," Optics Letters **21**(1), 24-26 (1996).

28. M. L. Berre, E. Ressayre, A. Tallet, K. Tai, H. M. Gibbs, M. C. Rushford, and N. Peyghambarian, "Continuous-wave off-resonance rings and continuous-wave on-resonance enhancement," J. Opt. Soc. Am. B **1**(4), 591-605 (1984).

29. J. A. Dean, *Lange's Handbook of Chemistry,* 15 ed. (McGraw-Hill, 1999).

30. A. B. Villafranca and K. Saravanamuttu, "Diversity and slow dynamics of diffraction rings: a comprehensive study of spatial self-phase modulation in a photopolymer," (2012), Manuscript in preparation.

31 . A. Villafranca, "Laser induced self-action phenomena in a photopolymerisable medium," (McMaster University, Hamilton, Ontario, 2010).

32. C. H. Skinner and P. D. Kleiber, "Observation of anomalous conical emission from laser-excited barium vapor," Phys. Rev. A **21**(1), 151-156 (1980).

Chapter 6 Conclusions and future work

6.1 General conclusions

One primary motivation of this thesis was to develop simple-step, room-temperature, and soft polymer-based pathways to Ag-nanoparticle doped metallodielectric microstructures. Such metallodielectric systems hold promises in a wide range of applications, including photovoltaic cells, photonics, optical switching devices and optical sensing/imagings. Soft metallodielectric composites were synthesized by photolytically generating Ag nanoparticles in the oligomeric organosiloxanes, which could be gelled through the photo-initiated free-radical polymerization of the methacrylate substituents. Besides conventional optical lithography, three different forms of nonlinear light propagation (i.e. optical self-trapping, modulation instability, and spatial self-phase modulation) were for the first time elicited in the Ag-nanoparticle doped photopolymerisable media, resulting in spontaneously self-induced metallo-dielectric microstructures. This led to the other major objective of this thesis: to investigate the effects of Ag nanoparticles on the dynamics of these nonlinear forms of light propagation. The main contributions of this thesis are summarized below.

A method has been developed to photolytically generate and stabilize Ag nanoparticles in oligomeric organosiloxane sols, through the well-established AgCl-photoreduction method [Chapter 2].

Growth of Ag nanoparticles was examined as a function of the doping concentration of Ag(I) ($[Ag(I)_{initial}]$ ranged from 1×10^{-3} M to 8×10^{-3} M), the irradiation duration, and the viscosity of the medium. A short term (within 2 hrs' irradiation) investigation by UV-Vis spectroscopy revealed that the

formation of Ag nanoparticles was initiated with a nucleation process which was followed by a continuous growth process. Both processes rely on the reciprocal electronic and ionic events: electrons excited and released upon photo-irradiation become rapidly trapped by lattice defects of AgCl grains; the trapped negative electrons then Coulombically attract mobile Ag^+ ions, which in turn attract more electrons. At $[Ag(I)_{initial}] = 8\times10^{-3}$ M, within 3 hrs' irradiation, size and aspect ratio given by TEMs of the Ag nanoparticles were 40 ± 10 nm and 1.4 ± 0.3, respectively. Increasing polydispersity in size and aspect ratio of Ag particles was observed in samples with long term irradiation: particles with length scales ranging from 20 nm to 156 nm, and aspect ratio up to 4 were observed after 72 hrs' irradiation. Such increasing polydispersity was accompanied with the appearance of polygonal Ag nanoparticles (e.g. triangles and hexagons). Formation of larger particles was also confirmed by UV-Vis absorption spectroscopy, which showed broadening and red shifting of the dipolar plasmon resonance, and the emergence of quadrupolar plasmon resonance. Formation of larger polygonal particles was assumed to rely on interactions between the seed particles formed in early stages. This assumption was evidenced by the lack of large faceted particles in samples where particle-interaction was inhibited due to either low concentration or poor mobility of Ag particles.

By irradiating the Ag(I)-containing organosiloxane film through photomasks, Ag(I) ions were spatial-selectively photo-reduced to Ag nanoparticles, forming gratings with periodicities of a few micrometers. Alternatively, gratings with periodicity ranging from 500 nm to 700 nm were created through interference lithography based on photopolymerization of the organosiloxane matrix [Chapter 2].

Nonlinear forms of light propagation, including optical self-trapping, modulation instability, and spatial self-phase modulation induced diffraction rings, have been elicited in the Ag-nanoparticle doped organosiloxanes.

Since these nonlinear forms of light propagation originate from photopolymerization of the photosensitized organosiloxanes, photoinduced refractive index changes were permanently inscribed in the Ag nanoparticle doped medium. Optical waveguides with a diameter of ~30 μm have been created by eliciting optical self-trapping with a narrow continuous wave, coherent visible laser at low intensity 1.6×10^{-2} W/cm^2 [Chapter 3]; concentric cones have been produced by eliciting spatial self-phase modulation, with the same kind of laser beam, but at a relatively high intensity(1.6 W/cm^2) [Chapter 5]; arrays of waveguides have been created by eliciting modulation instability with a broad beam of incoherent white light(Chapter 4). The formed microstructures have been characterized with optical micrography, and the presence of Ag nanoparticles within the resulting structures has been confirmed with both UV-Vis spectroscopy and SEM-EDX spectroscopy.

Dynamics of nonlinear forms of light propagation in the Ag nanoparticle doped medium has been examined, and the influence from the doped Ag nanoparticles has been evaluated.

As in the non-Ag nanoparticle doped organosiloxanes, the self-trapped beam exhibited multimode dynamics and evolved from single-mode guidance to multi-mode with increasing time. However, when the doping concentration [$Ag(I)_{initial}$] was increased to ≥ 3 mM, optical modes were seriously disturbed. At smaller doping concentrations (i.e. [$Ag(I)_{initial}$] ≤ 2mM), slower rates in modal evolution were observed in sample with higher doping concentration. This can be explained by the slower refractive index

change induced by the propagating beam that was more attenuated from the extinction of Ag nanoparticles.

For self-phase modulation, comparing with the non-Ag doped medium, the sample pathlength required to form well-developed diffraction rings without significant disturbance by the near-field diffraction was shortened in the presence of Ag nanoparticles: in the non-Ag doped sample, fully developed diffraction rings were observed in samples with a pathlength ≥ 6 mm, while in the Ag-nanoparticle doped medium with $[Ag(I)_{initial}] = 1 \times 10^{-3}$ M, fully developed diffraction rings were observed in sample with 4 mm pathlength. Further increase of the doping concentration $[Ag(I)_{initial}]$ to 4×10^{-3} M allowed diffraction rings to be observed in samples with pathlength of only 2 mm. On the other hand, in Ag nanoparticle doped sample, evolving of diffraction rings was found to be more affected by the competitive self-focusing/trapping process. When the sample pathlength was increased to 6 mm, very few diffraction rings which were evolved at the early stage of the beam incidence, quickly shrunk with the self-focusing/trapping beam, leaving no complete developing of diffraction rings.

For modulation instability, the presence of Ag nanoparticles shortened the distance where MI started to grow: While MI in the non-Ag doped organosiloxanes didn't appear until after ~3.5 mm, it took only ~0.11 mm for the MI to appear in the Ag-nanoparticle doped sample. On the other hand, due to optical extinction by SPRs, the presence of Ag nanoparticles also shortened the propagation distance of the MI induced filaments. In the non-doped organosiloxanes, complete MI filamentation has been observed in sample with 10 mm pathlength. In the Ag-nanoparticle doped samples, complete MI filamentation could be elicited at a maximum pathlength of only 4 mm.

The ability to elicit MI at very short pathlengths provided new opportunities for a systematic study of the dependence of MI dynamics on propagation distances. By analysing MI experiments at short pathlengths (0.6 mm to 4 mm) in the Ag-nanoparticle doped samples, and at long pathlengths (4 mm to 10 mm) in the non-doped samples, a direct pathlength dependence has been observed. The self-trapping efficiency of the MI induced filaments was found to be proportional to pathlength. At the same time, the population of filaments varied inversely with the pathlength. As a result, the cumulative self-trapping efficiency for the entire filament population at all propagation pathlengths was statistically constant. A self-adjustment of filaments' separation over distance has been observed, which was realized through various interactions (i.e. fusion and branching at short pathlength, and expulsion at long pathlength) among the self-trapping filaments.

In summary, the work in this thesis is a cross disciplinary study involving both chemistry (material fabrication) and physical optical (nonlinear propagations). For material fabrication, major contributions include: a photolytical method has been developed for in-situ producing and stabilizing Ag nanoparticles in organosiloxanes which can be further structured through photopolymerization; based on that, simple-step, room-temperature routes have been developed for various metallodielectric microstructures, through not only the conventional photomask and interference lithography, but more significantly, through the spontaneous self-inscription based on nonlinear forms of light propagation. For nonlinear forms of light propagation, major contributions include: nonlinear forms of light propagation, including optical self-trapping, modulation instability and spatial self-phase modulation induced diffraction rings have been for the first time elicited in the Ag-nanoparticle doped medium; effects of Ag nanoparticles these different forms of nonlinear propagation have been investigated; besides, due to the ability

to elicit MI in short distances in the Ag-nanoparticle doped medium, a systematic study on distance dependence of MI dynamics has been carried out .

6.2 Future work

Following the work from this thesis, further work could proceed in several directions.

Firstly, more metallodielectric microstructures for optical devices could be achieved through nonlinear forms of light propagation in the Ag-nanoparticle doped organosilxoanes. For example, 3D lattice structures can be produced by eliciting MI with multiple beams. The initial work has been carried out with a 2-angled beam irradiation, as demonstrated in **Appendix II**. A spontaneous-alignment of the MI induced filaments along the direction parallel to the 2- beam plane has been observed. Based on that, various 3D metallodielectric lattices can be created by simply varying the number and the direction of the incident beams. As shown in **Appendix II**, one problem in the Ag-nanoparticle doped sample is that the propagation distance of the MI filaments is highly limited. This may be improved by using shorter wavelengths which are away from the SPRs wavelength of Ag nanoparticles, so that the attenuation of the beam(s) by extinctions from Ag nanoparticles can be reduced.

In this thesis, all the three forms of nonlinear light propagation, i.e. self-trapping, modulation instability (MI) and spatial self-phase modulation were carried out at optical wavelengths that were overlapping with the SPRs wavelengths of the doped Ag nanoparticles, so that the influence from SPRs of metal nanoparticles on nonlinear forms of light propagation could be well evaluated. However, in terms of material fabrication, incidences without such overlap (e.g. a UV light) may enable longer pathlengths of the self-induced

microstructures. Besides, experimental results with off-SPRs incidences would be very useful to achieve a more comprehensive understanding of the effect from metal nanoparticles on nonlinear forms of light propagation.

We have demonstrated in Chapter 4 a rare case where chains of Ag nanoparticles formed and were aligned along the direction of the self-trapping filaments. This is likely caused by the phase separation caused by the highly non-uniform photopolymerization induce by beam self-trapping. More work is required to achieve controlled confinement and alignment of Ag nanoparticles within the system. Furthermore, our group has recently conducted self-trapping of a *black* beam, which induced a dark channel where much less polymerization occurred than the surrounding area [1]. By eliciting the black-beam self-trapping in the Ag-nanoparticle doped medium, an efficient confinement of Ag nanoparticles could probably occur within the self-induced dark channel.

As mentioned in Chapter 1 and Chapter 3, due to the large third order nonlinearity that can be induced near SPRs of the doped Ag nanoparticles [2], our self-induced optical waveguides have great potential in all-optical switches. Their nonlinear responses need to be measured for the actual applications.

The Ag-nanoparticle doped organosiloxanes have great potential in photovoltaic cells, to improve its light harvesting efficiency, allowing considerable reduction in the physical thickness of the photovoltaic absorber layers [3]. Traditional photovoltaic absorber materials, such as crystalline silicon wafers, have limited optical absorption and therefore, a large thickness of absorber layers is required, which on the other hand, increases the collection length of charge carriers, causing low collection of charge carriers due to bulk re-combination. Therefore, thin film solar-cell within

which solar light can be efficiently trapped and absorbed are very important. By coating the Ag-nanoparticle doped organosiloxanes onto the photovoltaic absorber layer, multiple scattering of the propagating light waves can be induced within the absorber layer. As a result, the effective optical path length of the absorber layer can be increased. Besides, Ag nanoparticles can function as subwavelength antennas, trapping and concentrating light into strong localized plasmoic near-field, which can be coupled to the photovoltaic absorber elements. Furthermore, presence of Ag nanoparticles enables sunlight to be trapped from a wider range of incident angles. Further improvement can be made by integrating the material with arrays of optical waveguides along various directions, which can be created within the photopolymerisable organosiloxanes through the MI filamentation induced by optical beams propagating at many different directions. Work in creating self-inscribed waveguides to enhance sunlight trapping has been initiated in our group.

Besides photovoltaics, many other photo-responsive processes, such as Raman scattering, and fluorescence can be enhanced by SPRs of metal nanoparticles. Therefore, the Ag-nanoparticle doped composites can be further developed and functionalized by incorporating other photo-responsive components, such as quantum dots and dye molecules. Further chemical modification of either the functional components or the organosiloxane matrix is required to improve their compatibility, allowing homogeneous and stable dispersion of the functional components within the material.

Since SPRs have a direct dependence on particle shape, doping of non-spherical metal nanoparticles within the dielectric material would be another research direction. Although non-spherical polygonal Ag nanoparticles have been created during the long-time irradiation of the Ag doped

organosiloxanes [Chapter 2], further modification of the synthesis system is necessary for sufficient control of the particle size and shape. Abundant previous researches have shown that with the aid of proper surfactants/salts, shape of Ag nanoparticles can be optically controlled with the irradiation source [4;5;6;7;8;9]. Alternatively, metal particles can be pre-made to desired shapes before being dispersed into the dielectric matrices. In this case, further chemical modification of either metal particles or the organosiloxanes would be necessary to ensure homogeneous dispersion.

---

1. K. Kasala and K. Saravanamuttu, "A black beam borne by an incandescent field self-traps in a photopolymerizing medium," J. Am. Chem. Soc., Just accepted, DOI: 10.1021/ja305671b (2012).

[2] A. Lin, X. Liu, P. R. Watekar, W. Zhao, B. Peng, C. Sun, Y. Wang, and W.-T. Han, "All-optical switching application of germano-silicate optical fiber incorporated with Ag nanocrystals," *Opt. Lett.*, vol. 34, pp. 791-793, 2009.

3. H. A. Atwater and A. Polman, "Plasmonics for improved photovoltaic devices," *Nat. Mater.*, vol. 9, pp. 205-213, 2010.

4. R. Jin, Y. Cao, C. A. Mirkin, K. L. Kelly, G. C. Schatz, and J. G. Zheng, "Photoinduced conversion of silver nanospheres to nanoprisms," Science **294**, 1901 (2001).

5. R. Jin, Y. C. Cao, E. Hao, G. S. Métraux, G. C. Schatz, and C. A. Mirkin, "Controlling anisotropic nanoparticle growth through plasmon excitation," Nature **425**, 487-490 (2003).

6. M. Maillard, P. Huang, and L. Brus, "Silver nanodisk growth by surface plasmon enhanced photoreduction of adsorbed [Ag^+]," Nano Lett. **3**(11), 1611-1615 (2003).

7. A. R. Tao, S. Habas, and P. Yang, "Shape control of colloidal metal nanocrystals," Small **4**(3), 310-325 (2007).

8. K. G. Stamplecoskie and J. C. Scaiano, "Light emitting diode irradiation can control the morphology and optical properties of silver nanoparticles," J. Am. Chem. Soc. **132**(6), 1825 (2010).

9. C. Xue and C. A. Mirkin, "pH-Switchable silver nanoprism growth pathways," Angewandte Chemie International Edition **46**, 2036 (2007).

Appendix I Optical set-up for experiments of optical self-trapping and spatial self-phase modulation

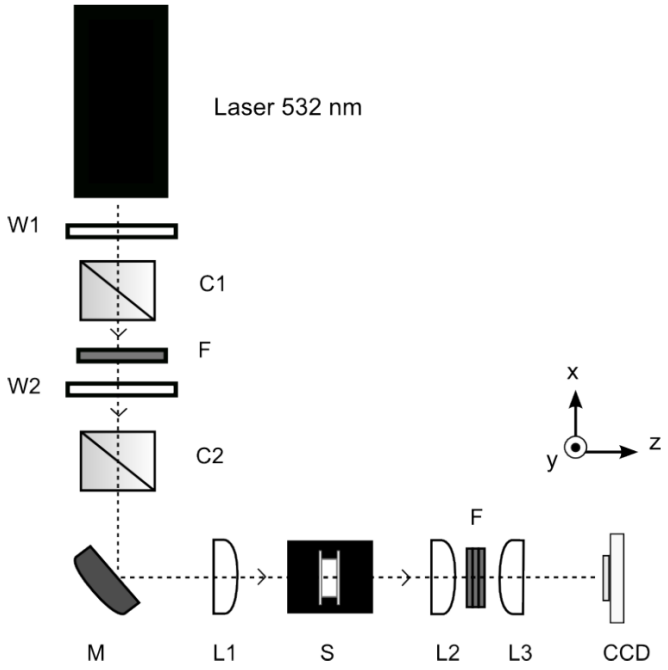

Figure I. 1 Optical assembly for self-trapping experiments. A c.w. 532 nm laser beam was attenuated through a combination of half-wave plate (W1), a neutral density filter (F), quarter-wave plate (W2) and polarizing beam cubes (C1 and C2), reflected by 45° mirrors (M) and focused through a plano-convex lens (L1) onto the entrance face of the sample-containing cell (S). Intensity profiles of the beam were attenuated by a set of neutral density filters (F) and projected by a plano-convex lens pair (L2 and L3) onto a CCD camera. Illustration reprinted from [1] with permission from Villafranca.

---

1 . A. Villafranca, "Laser induced self-action phenomena in a photopolymerisable medium," (McMaster University, Hamilton, Ontario, 2010).

Appendix II MI with two-angled beams propagating in Ag-nanoparticle doped photopolymer

In **Chapter 4**, alignment of the self-induced filaments with a single broad beam along the vertical direction (y) was achieved by imposing a 1-D intensity modulation with an amplitude mask. As shown in **Figure II. 1a**, without the mask, the single broad beam itself only results in randomly arranged filamentation in the medium.

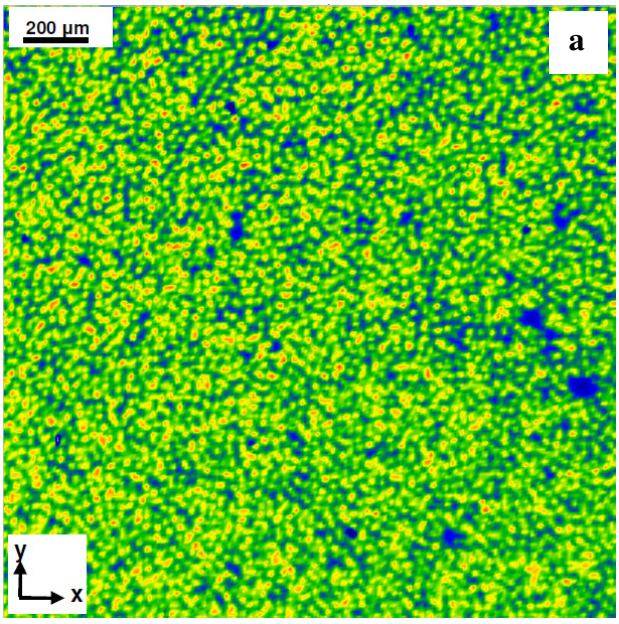

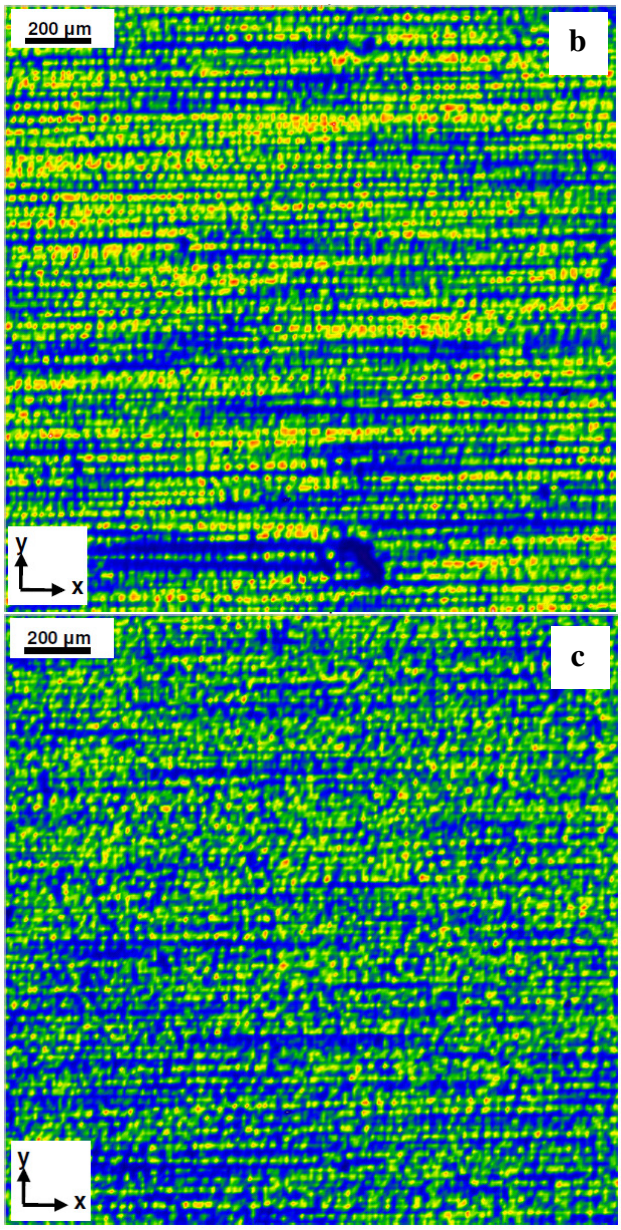

Figure II. 1 2D spatial intensity profiles at the exit face of Ag-nanoparticle doped organosiloxanes of MI elicited with (a) one single broad beam, and (b),(c) two angled broad beams of white light (Beam I propagated along z direction; Beam II was 46° to Beam I). Doping concentration $[Ag(I)_{Initial}]$ was 1×10^{-3} M in (a) and (b), and 3.5×10^{-3} M in (c). For single beam irradiation, the optical intensity = 6 mW/cm^2; for two-beam irradiation, the two beams were horizontally leveled (along x direction), and the optical intensity of each beam = 3.1 mW/cm^2.

However, the alignment of the filaments was observed, when a second beam, which propagates in an angled direction to the primary beam, was added to the irradiation source. As shown in **Figure II. 1b**, the alignment was along the direction parallel to the plane of the two-angled beams. For the 2-beam experiment, a second quartz-tungsten-halogen lamp was added to the one-beam setup (**Figure 4.2**)**.** Beam from the second lamp (Beam II) was horizontally levelled and angled (46°) with the primary beam (Beam I). Irradiation intensities of the two beams were set identical. Simultaneous incidence of the two beams to the Ag-nanoparticle doped organosiloxanes (doping concentration $[Ag(I)]_{initial}$ = 1 mM, pathlength =2 mm) resulted in horizontally (x direction) aligned MI filaments, despite that in some area , the alignment was disturbed, which was probably due to the inhomogeneity of the sample medium(**Figure II. 1 b**). The average distance between the lines of filaments (y direction) and filaments along the lines (x direction) were 32 ± 3 μm and 31 ± 3 μm, respectively, which were close to the average splitting distance of the filaments observed in one-beam MI experiments in 2 mm sample cells (**Table 4-2**). In another experiment where doping concentration $[Ag(I)_{initial}]$ was raised to 3.5 mM, increasing disturbance of the MI filaments alignment along horizontal direction was observed(**Figure II. 1 c**). The average distance between self-induced filaments along x and y directions were 33 ± 2 μm and 31 ± 2 μm, respectively, which were similar as the separation observed in the sample with lower doping concentration ($[Ag(I)_{initial}]$ = 1 mM).

Furthermore, when an amplitude mask was set right before the entrance face of the sample medium, with its 1D modulation (80μm periodicity) along the x direction (horizontal), the alignment of the MI filaments along both x and y directions is expected(**Figure II. 2 a**). As shown in **Figure II. 2 b** for a sample with doping concentration $[Ag(I)_{initial}]$ = 1 mM, the resulting MI

filaments were highly aligned along the y direction, and partially aligned along the x direction. The periodicity of the MI filaments along x direction was 80 μm, which was corresponding to the periodicity of the imposed 1D intensity modulation. The periodicity of the MI filaments along the y direction was 43 ± 5 μm, which was mainly affected by the sample pathlength. The lattice structure of the resulting sample with the MI filaments induced by the 2-angled beams, as proposed in **Figure II. 2a**, was evident in optical micrographs of the resulting samples (**Figure II. 2 c-e**). The transmission micrograph at the exit face (xy plane) of the sample showed bright spots aligned along both the x and y directions, with better alignment and smaller periodicity (32 ± 3 μm) along the y direction, and certain disturbance and larger periodicity (74.0 ± 0.2 μm) along the x direction. The reflection image at the xz plane clearly showed both MI filaments induced by the normal incidence from Beam I and MI filaments induced by the angled incidence from Beam II, which was 46° to Beam I. The angle between the two sets of filaments was 30 ± 1°, which agreed with the theoretical expectation according to Snell's law, assuming that refractive index of the polymerized organosiloxane was 1.43. Periodicities of the filaments induced by Beam I and Beam II were P_I = 75.1 ± 0.5 μm and P_{II} = 63.9 ± 0.3 μm, respectively, both imposed by the 1-D intensity modulation from the photomask. The smaller value of P_{II} of filaments at 30 ± 1° was as expected, as $P_{II} = P_I \sin 30°$. To observe the longitudinal yz plane, the sample had to be cut. However, random cracking and distortion usually occurred upon cutting of the fragile sample. Therefore, the cross section as shown in Figure II. 2d could be slightly off the yz plane, with a periodicity of ~90 μm along z direction and a periodicity of ~25 μm along y direction. However, it's still close to the structure as predicated in **Figure II. 2a**.

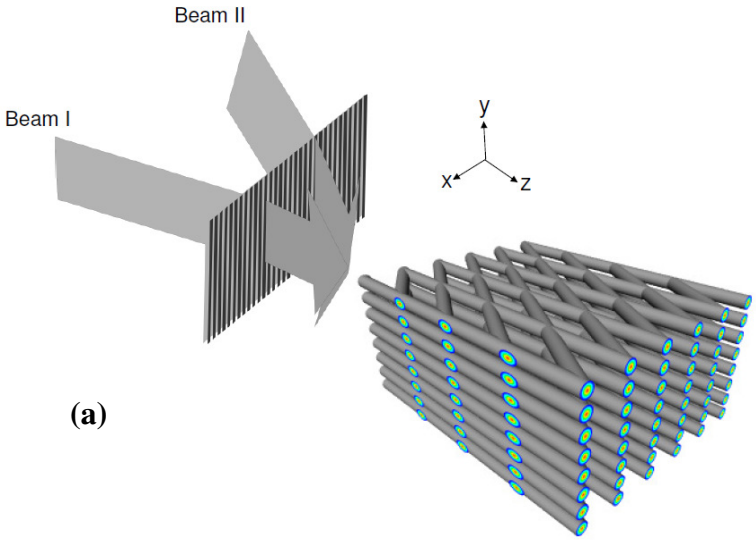

(a)

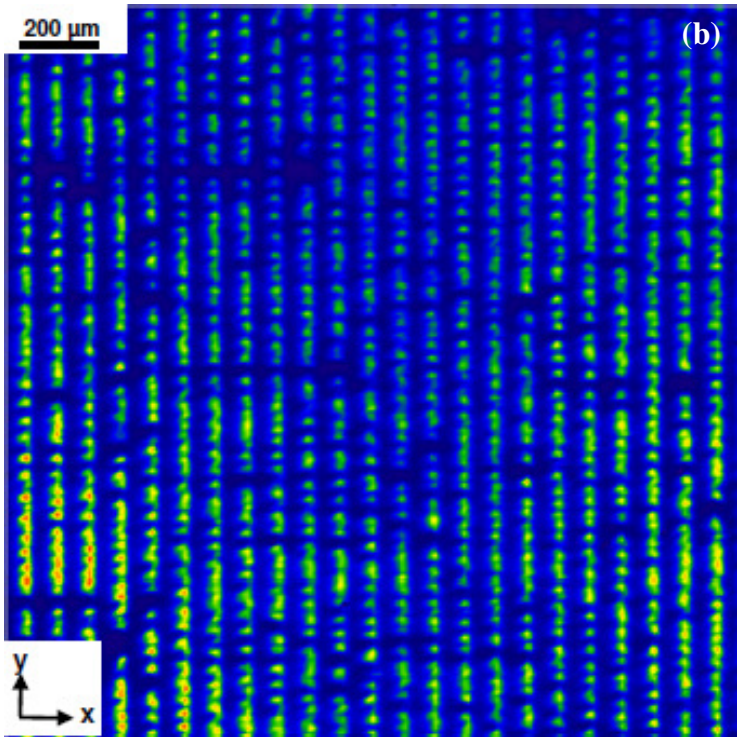

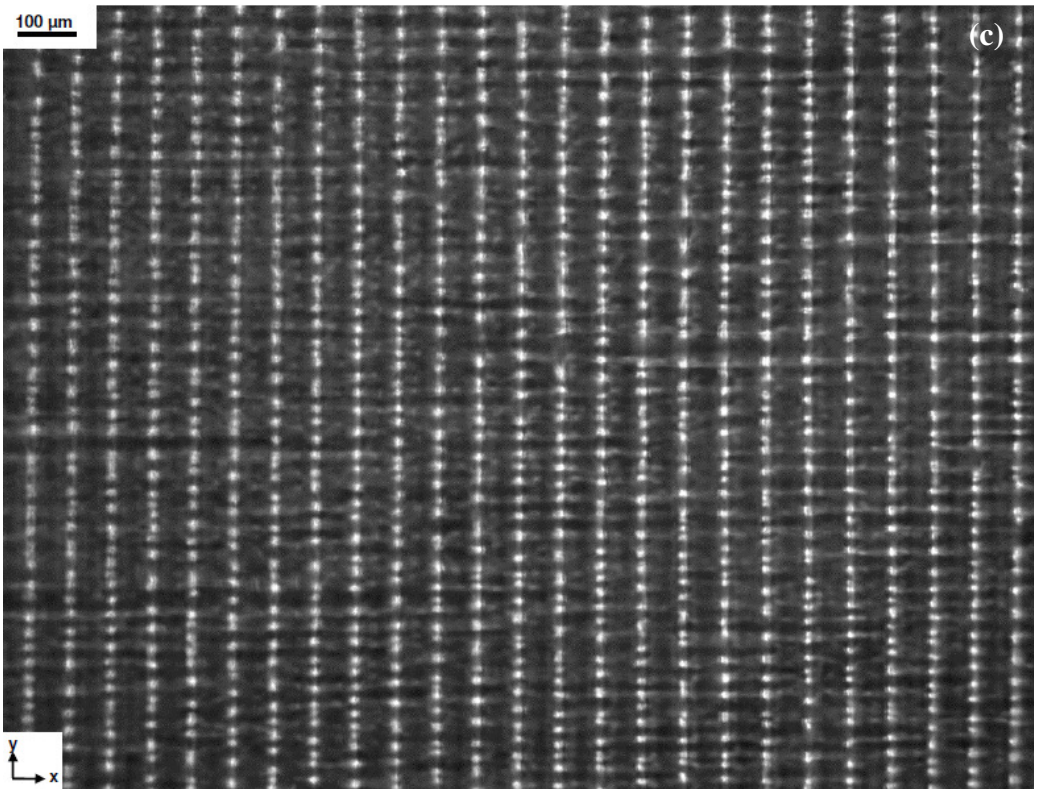
100 µm
(c)
y
x

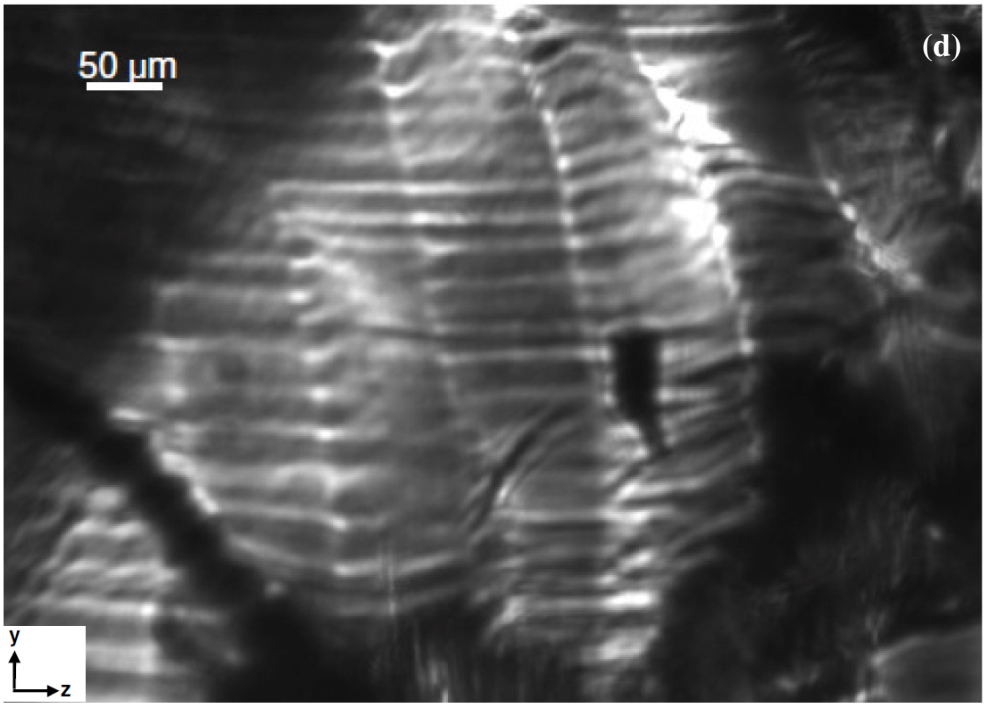
50 µm
(d)
y
z

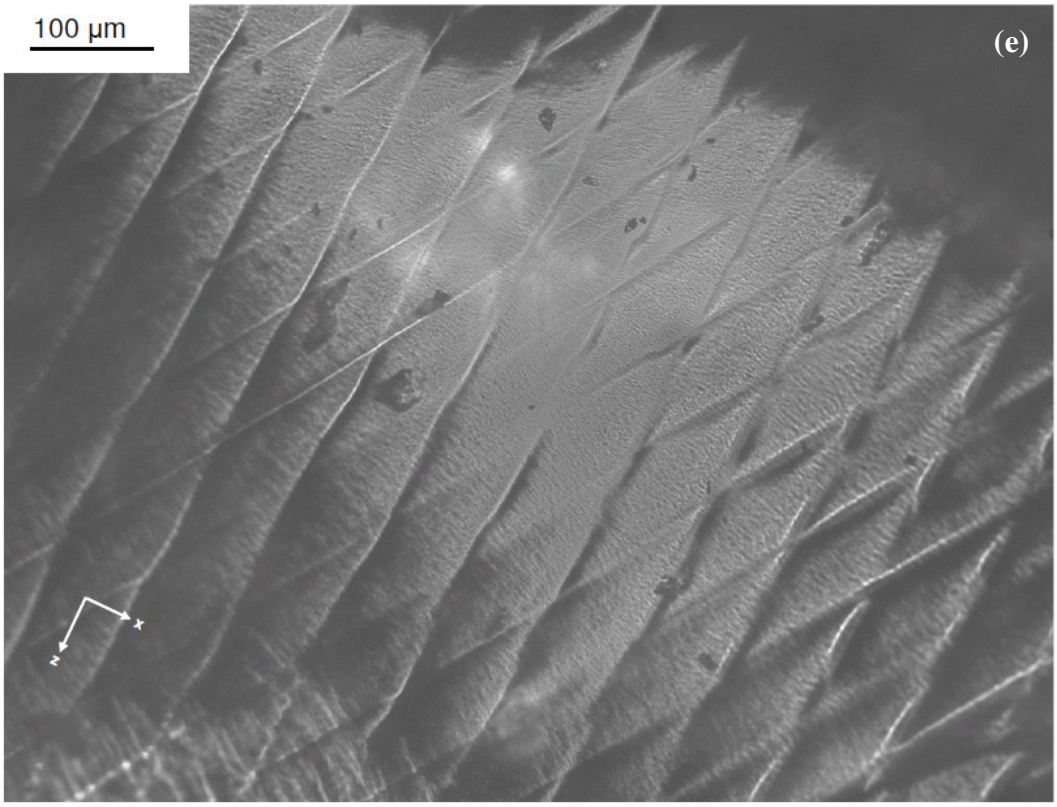

Figure II. 2 (a) Schematic representation of the 3D filamentation structure self-formed due to MI induced by the 2-angled beams that have been horizontally levelled: Beam I propagated along z direction; Beam II was 46° and horizontally leveled to Beam I; both beams passed the photomask with 1D modulation (80 µm periodicity) along x direction. (b) 2D intensity profile at the exit face of Ag-nanoparticle doped organosiloxanes after filaments had evolved through MI. (c) The transmission image the exit face (xy plane). Reflection images (d) at near the yz plane and (e), at the xz plane. For the 2-beam experiment, [Ag] = 1 $\times 10^{-3}$ M; optical intensity of each beam = 3.1 mW/cm^2.

As mentioned before, high Ag doping concentration causes severe disturbance of the horizontal alignment of the self-induced filaments. As shown in the sample with doping concentration [Ag $(I)_{initial}$] =3.5 mM, while the vertical alignment along the y direction due to the 1-D stripes of the photomask stayed, the horizontal alignment along the x direction was completely lost at this high concentration. (**Figure II. 3**)

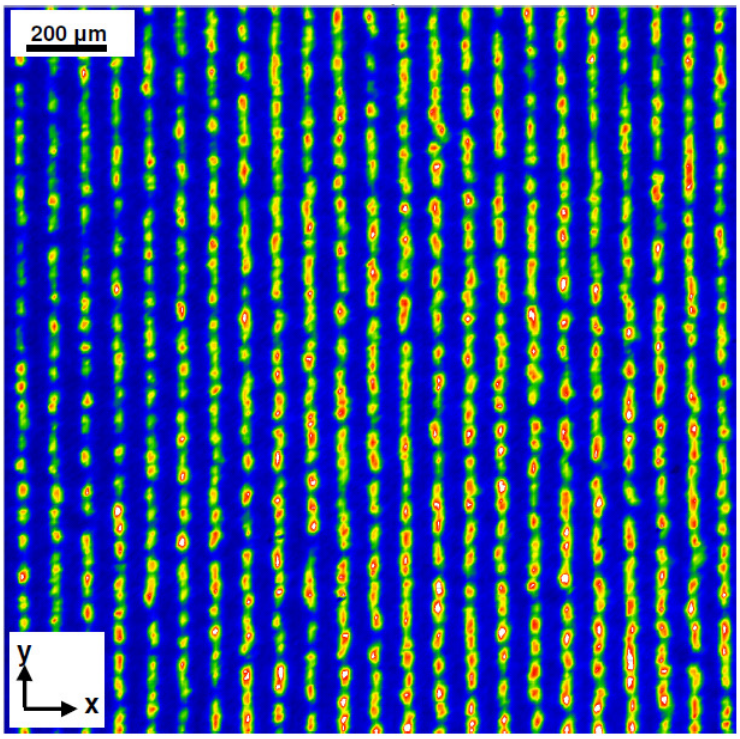

Figure II. 3 The 2D spatial intensity profile at the exit face of the Ag-nanoparticle doped organosiloxanes of the MI filaments induced by two-angled broad beams of white light with the 1D intensity modulation (80 µm periodicity) imposed along the x direction. $[Ag(I)_{initial}] = 3.5 \times 10^{-3}$ M; optical intensity of each beam = 5.1 mW/cm^2.

All experiments for two angled beam MI in Ag nanoparticle doped organsiloxanes were carried out in samples with 2 mm pathlength. Similar as in the one-beam MI experiment, Ag nanoparticles prohibited propagation of MI filaments over long distance. On the contrary, organosiloxanes without Ag nanoparticles allows MI filaments to propagate over longer distance (at least 10 mm). MI result as shown in **Figure II. 4** was obtained in a 6 mm sample

without doping Ag nanoparticle. The larger periodicity (71 ± 2 μm) of the MI filaments along the y direction comparing with that in Ag-doped samples, was due to the longer pathlength of the non-doped sample.

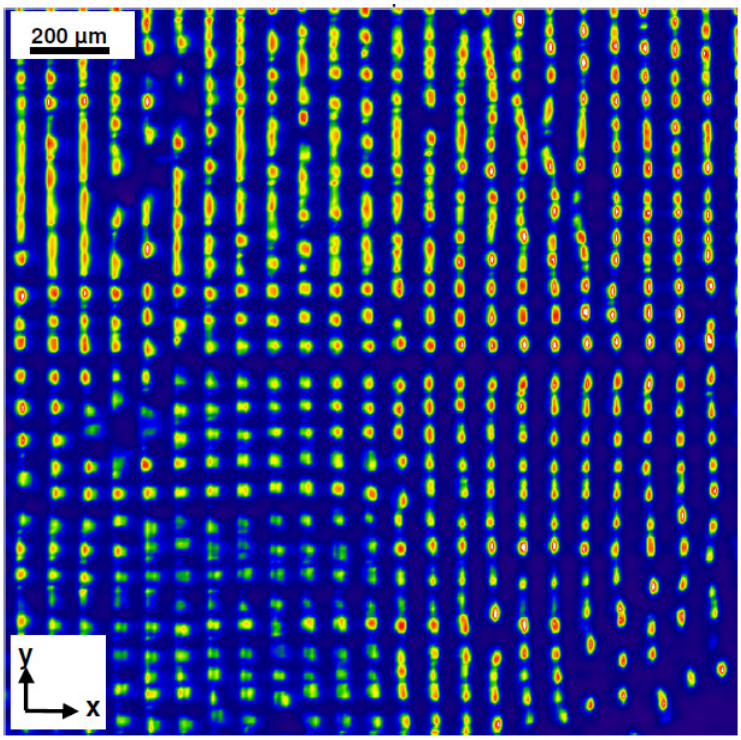

Figure II. 4 The 2D spatial intensity profile at the exit face of non-Ag doped organosiloxanes after self-induced filaments have evolved through MI of two-angled broad beams of white light with 1D intensity modulation (80 μm periodicity) along x direction (horizontal). Incident intensity of each beam = 3.1 mW/cm^2.